Extraction of Polarised Quark Distributions of the Nucleon from Deep Inelastic Scattering at the HERMES Experiment

Marc Beckmann

FAKULTÄT FÜR PHYSIK
ALBERT-LUDWIGS-UNIVERSITÄT FREIBURG

Extraction of Polarised Quark Distributions of the Nucleon from Deep Inelastic Scattering at the HERMES Experiment

INAUGURAL–DISSERTATION
zur
Erlangung des Doktorgrades
der
Fakultät für Physik
der
Albert-Ludwigs-Universität Freiburg im Breisgau

vorgelegt von

Marc Beckmann

aus Nürnberg

Mai 2000

Dekan:	Prof. Dr. Kay Königsmann
Leiter der Arbeit:	Prof. Dr. Kay Königsmann
Referent:	Prof. Dr. Kay Königsmann
Korreferent:	Prof. Dr. Andreas Bamberger
Tag der Verkündigung des Prüfungsergebnisses:	26. Juni 2000

The HERMES Experiment at HERA

Spin Structure of the Nucleon

Deutsches Elektronen-Synchrotron DESY

Contents

List of Figures

List of Tables

1 Introduction

Soon after the advent of deep inelastic scattering in the late sixties, the up to then only mathematical concept of quarks [Gel 64] quickly became a description of the fundamental components of hadronic matter. The early SLAC–MIT experiments [Fri 72] revealed a scaling property of the cross section for the scattering of high energy electrons off nucleons. This experimental observation could be explained by hard, pointlike scattering centres in the nucleon, which were identified with the quarks. In the Standard Model, which represents the current understanding of the structure of matter, elementary fermions (quarks and leptons), which interact by the exchange of gauge bosons (photons, gluons and the charged and neutral weak bosons) are the fundamental components of matter. In hadrons, the quarks are bound together by the gluons, which are the mediators of the strong force.

For high–energy processes, which probe the structure and interaction of particles at short distances, the interplay of the quarks and gluons is extremely well described in the framework of **Q**uantum **C**hromo **D**ynamics (QCD), the quantum field theory of the strong interaction. The strong force becomes weaker at short distances and vanishes in the limit of zero distance, a feature called asymptotic freedom. The smallness of the strong coupling constant allows the calculation of QCD processes by perturbative expansions. However, at low energies the perturbative expansions diverge due to the rise of the coupling constant. Thus QCD does not allow quantitative predictions for processes like the confinement of quarks inside hadrons. The study of non–perturbative processes will be part of this thesis.

Like the quarks, a nucleon is a fermion characterised by a spin of $1/2$ in units of $\hbar$. Spin is a very important quantity as it poses symmetry requirements on the wavefunction used to describe a particle in quantum mechanics. In a naive model the nucleon is composed of only three valence quarks, which are bound together by gluons. The total spin of the nucleon could be explained by the simple vector sum of the spins of the three valence quarks. This model also describes the measured magnetic moments of the proton and the neutron remarkably well. It came thus as a surprise when the EMC experiment [Ash 88] revealed that only little of the proton's spin was due to the spin of the quarks.

In a general approach, the spin of the nucleon can be decomposed into contributions from quarks, gluons, and orbital angular momenta. They represent the individual terms in the sum rule for the helicity s_z^N of the nucleon:

$$s_z^N/\hbar \;=\; \frac{1}{2} \;=\; \frac{1}{2}\Delta\Sigma + \Delta g + L_q + L_g \,. \tag{1.1}$$

Neglecting heavy quarks

$$\Delta\Sigma \;=\; \Delta u + \Delta\overline{u} + \Delta d + \Delta\overline{d} + \Delta s + \Delta\overline{s} \tag{1.2}$$

is the contribution from the quark spins, Δg is the component due to the gluon spin, and L_q and L_g are the orbital angular momenta of the quarks and the gluons, respectively.

Stimulated by the EMC result, several experiments were carried out which provided accurate data on the spin structure function g_1 of the proton and the neutron in inclusive polarised deep inelastic lepton–nucleon scattering. From the results on g_1 values for $\Delta\Sigma$ were extracted using additional experimental information on weak decays of baryons. These analyses obtain a value of $\Delta\Sigma \simeq 0.3$ for the total contribution of the quark spins to the nucleon spin in leading order QCD. This result amounts to about 40% of the value expected from relativistic quark models of the nucleon. Furthermore, assuming $SU(3)$ flavour symmetry, the contributions by the individual flavours in Eqn. (1.2) can be separated. Little is known experimentally on the gluon contribution Δg, and no measurements exist on L_q or L_g. The continued experimental effort to provide precise data on the separate contributions will help to gain

> "... a deeper understanding of the nucleon, an object we thought we knew so well, but which reveals a new face when it spins." [Ell 96]

The HERMES experiment at DESY was designed to the disentangle the contributions from the different quark flavours to the nucleon's spin in *semi inclusive* deep inelastic scattering reactions. In such reactions, hadrons are detected in coincidence with the scattered lepton. The flavour of the quark probed in the scattering process can be deduced from the charge and the type of the observed hadron in a statistical analysis. This method allows a direct separation of the spin contributions by the individual quark flavours without requiring $SU(3)$ flavour symmetry.

HERMES features two novel experimental techniques: a gaseous target of polarised pure hydrogen, deuterium or ^{3}He atoms, internal to the beam line vacuum of the HERA accelerator, and a high current, longitudinally polarised positron beam with an energy of 27.5 GeV. Positrons and hadrons from deep inelastic scattering processes are detected in a large acceptance spectrometer downstream of the interaction region. The spectrometer was designed to provide a good particle identification for the analysis of semi inclusive scattering events.

HERMES has been taking data since 1995. This thesis reports on the analysis of semi inclusive DIS events on a polarised proton target, recorded in the years 1996 and 1997. Together with semi inclusive asymmetries on a polarised ^{3}He target used in 1995, polarised valence and sea quark distributions in the kinematic range $0.023 < x < 0.6$ and $1\,\mathrm{GeV}^2 < Q^2 < 10\,\mathrm{GeV}^2$ are extracted from the HERMES data. The extracted results represent the currently most precise measurements of polarised quark distributions.

The outline of this thesis is as follows: Chapter 2 reviews the theoretical framework of polarised deep inelastic scattering. In Chapter 3 the HERMES experimental apparatus is described. The mandatory experimental prerequisite of a polarised beam and the measurement of its degree of polarisation is covered in Chapter 4. This chapter also describes the Longitudinal Polarimeter, which was the specific hardware responsibility of the author. The analysis of HERMES data from the years 1996 and 1997 to obtain inclusive and semi inclusive charged hadron cross section asymmetries on the nucleon is presented in Chapter 5. Finally, in Chapter 6 a formalism is introduced to extract quark spin densities from the measured asymmetries. Polarised quark distributions as a function of x are presented and compared to other experimental results and theoretical predictions.

2 Polarised Deep Inelastic Scattering

2.1 Kinematics

In the deep inelastic scattering (DIS) process an incoming lepton $\ell = e^{\pm}, \mu^{\pm}, \nu_{e,\mu}, \overline{\nu}_{e,\mu}$ interacts with a nucleon N in such a way that the nucleon is broken up and forms a final hadronic state X:

$$\ell + N \to \ell' + X \; . \tag{2.1}$$

In inclusive DIS processes only the scattered lepton ℓ' is detected, while in semi inclusive processes at least one of the final state hadrons X is measured in coincidence with the lepton.

The DIS process is mediated by the exchange of a virtual boson (γ^*, $W^{\pm}$, Z^0) between the lepton ℓ and one of the partons inside the target nucleon. For energy transfers ν from the lepton to the nucleon, which are small compared to the masses[i] of the weak gauge bosons ($\nu \ll m_{Z^0}, m_{W^{\pm}}$), contributions from weak current interactions can be neglected. In this case deep inelastic scattering can be described in lowest order by the exchange of a single virtual photon γ^*, as depicted in Fig. 2.1.

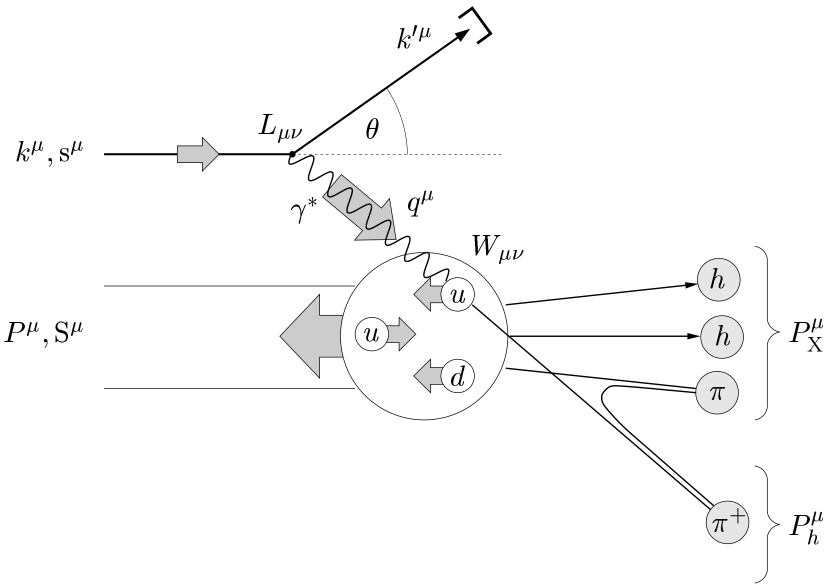

Figure 2.1: Sketch of the deep inelastic scattering process in the one–photon approximation as seen in the laboratory system. The shaded arrows indicate the spins of the particles.

The kinematic quantities used in the following treatment are defined in Table 2.1. In this discussion only the special case is considered, for which an incoming positron with four–momentum $k^{\mu} = (E, \vec{k})$ is scattered off a target nucleon with four–momentum $P^{\mu} = (M, \vec{0})$, which is at rest in the laboratory (lab) system, where M denotes the rest mass of the target nucleon. Furthermore it is assumed, that the energies of the incident and scattered positron are much larger than the positron rest mass m_e, which is neglected in the following expressions.

[i] Unless noted otherwise, throughout this text the convention $\hbar = c = 1$ is used.

Table 2.1: A legend of kinematic quantities used in the description of deep inelastic positron nucleon scattering.

Positron	
$k^\mu = (E, \vec{k})$	Four–momentum of the incident positron
$k'^\mu = (E', \vec{k}')$	Four–momentum of the scattered positron
θ, ϕ	Polar and azimuthal positron scattering angles in the lab system
$\mathrm{s}^\mu \overset{\mathrm{Lab}}{=} \frac{1}{m_e}(\lvert\vec{k}\rvert, \hat{\vec{k}}E); \quad \hat{\vec{k}} := \frac{\vec{k}}{\lvert\vec{k}\rvert}$	Spin four–vector of the incident positron in the lab system for **longitudinal** polarisation.
Target nucleon	
$P^\mu \overset{\mathrm{Lab}}{=} (M, \vec{0})$	Four–momentum of the target nucleon
$\mathrm{S}^\mu \overset{\mathrm{Lab}}{=} (0, \hat{\vec{S}})$	Spin four–vector of the target nucleon
Detected final state hadrons	
$P_h^\mu = (E_h, \vec{P}_h)$	Four–momentum of a detected final state hadron h
Inclusive DIS	
$\nu = \frac{P_\mu q^\mu}{M} \overset{\mathrm{Lab}}{=} E - E'$	Energy transfer to the target
$q^\mu = k^\mu - k'^\mu = (\nu, \vec{q})$	Four–momentum transfer to the target
$Q^2 = -q_\mu q^\mu \overset{\mathrm{Lab}}{\simeq} 4EE' \sin^2\frac{\theta}{2}$	Squared invariant mass of the virtual photon
$s = (P^\mu + k^\mu)^2 \overset{\mathrm{Lab}}{=} 2ME + M^2$	Squared centre of mass energy
$W^2 = (P^\mu + q^\mu)^2 \overset{\mathrm{Lab}}{=} M^2 + 2M\nu - Q^2$	Squared mass of the final hadronic state
$x = \frac{Q^2}{2P_\mu q^\mu} \overset{\mathrm{Lab}}{=} \frac{Q^2}{2M\nu}$	Bjørken scaling variable
$y = \frac{P_\mu q^\mu}{P_\mu k^\mu} \overset{\mathrm{Lab}}{=} \frac{\nu}{E}$	Fractional energy transfer of the virtual photon
Semi inclusive DIS	
$P_\parallel^* = \vec{P}_h \cdot \frac{\vec{q}}{\lvert\vec{q}\rvert}\Big\rvert_{\gamma^* N\text{–system}}$	Longitudinal momentum of a hadron h in the γ^*–N centre of mass system
$x_\mathrm{F} = \frac{P_\parallel^*}{\lvert\vec{q}\rvert} \simeq \frac{2P_\parallel^*}{W}$	Feynman scaling variable
$z = \frac{P_\mu P_h^\mu}{P_\mu q^\mu} \overset{\mathrm{Lab}}{=} \frac{E_h}{\nu}$	Fraction of the virtual photon energy carried by a hadron h

From the measured azimuthal scattering angle θ and the energy E' of the scattered positron, the kinematic quantities x, y, and Q^2 can be calculated. The negative of the squared invariant mass of the virtual photon, Q^2, is a measure of the spatial resolution in the scattering process. In analogy to diffraction in optics, the virtual photon can resolve objects, whose extension perpendicular to the direction of the photon is comparable to or larger than the reduced wavelength $\lambdabar$ of the photon. This quantity $\lambdabar$ is not Lorentz–invariant, but depends on the reference frame. In the so–called *Breit* frame, where no energy is transfered from the virtual photon to the target ($\nu = 0$), the reduced wavelength of the virtual photon is simply given by

$$\lambdabar = \frac{1}{|\vec{q}|} \overset{\nu=0}{\equiv} \frac{1}{\sqrt{Q^2}} . \tag{2.2}$$

In the laboratory system, this expression becomes modified. However, in either of these reference frames the spatial resolution of the virtual photon increases for larger values of Q^2.

The dimensionless variable x is called *Bjørken scaling variable*, and is a measure of the inelasticity of the scattering process. In an elastic scattering process the target nucleon remains intact, and consequently $W^2 = M^2$, which implies $2M\nu = Q^2$ or $x = 1$. For inelastic processes, $W^2 > M^2$ and $0 < x < 1$. As will be shown in Sect. 2.4, the variable x can be identified for large values of Q^2 with the fractional momentum of the target nucleon carried by the struck quark.

The second dimensionless variable y $(0 \leq y \leq 1)$ is the fractional energy transfer from the incident lepton to the target nucleon. In elastic scattering processes, only the quantity Q^2 is not fixed, while $x = 1$ and $y = 0$. For inelastic scattering processes, one additional degree of freedom is obtained, so that two of the three variables x, y, and Q^2 become independent. The kinematics of an inclusive inelastic scattering process hence are fully determined by any combination of two of the before mentioned variables.

In semi inclusive scattering processes, additional kinematic variables are required for each detected hadron. In the lab system, the Lorentz–invariant, dimensionless variable z gives the fraction of the energy of the virtual photon, which is carried by the detected hadron. The *Feynman scaling variable* x_{F} is defined in the centre of mass system of the virtual photon and the nucleon, and scales the longitudinal component of the hadron's momentum to its maximum possible value. The kinematically allowed ranges for the above quantities are $0 \leq z \leq 1$ and $-1 \leq x_{\mathrm{F}} \leq 1$. For large values of the invariant hadronic mass in the final state ($W^2 \gg M^2$), hadrons going backwards[ii] in the γ^*–N reference frame ($x_{\mathrm{F}} < 0$) have small values of z, while for hadrons with a large forward momentum in this frame, x_{F} and z become roughly equal.

2.2 Cross Sections and Nucleon Structure Functions

Assuming one photon exchange, the differential cross section for the detection of the scattered positron in a solid angle $\mathrm{d}\Omega$ and in an energy range $[E', E' + \mathrm{d}E']$ may be written as [Ans 95]:

$$\begin{aligned} \frac{\mathrm{d}^2\sigma}{\mathrm{d}\Omega\,\mathrm{d}E'} &= \frac{\alpha^2}{M\,Q^4}\,\frac{E'}{E}\,L_{\mu\nu}W^{\mu\nu} \\ &= \frac{\alpha^2}{M\,Q^4}\,\frac{E'}{E}\left[L^{(\mathrm{S})}_{\mu\nu}\,W^{\mu\nu\,(\mathrm{S})} - L^{(\mathrm{A})}_{\mu\nu}\,W^{\mu\nu\,(\mathrm{A})}\right] . \end{aligned} \tag{2.3}$$

[ii] In this context, the **forward** direction is defined along the direction of the virtual photon

Here, α denotes the electromagnetic coupling constant, and $L_{\mu\nu}$ and $W_{\mu\nu}$ are the lepton and hadron tensors, respectively. They represent the vertex factors for the leptonic and hadronic parts of the DIS process, as shown in Fig. 2.1. The lepton and hadron tensors can be split into two parts, which are symmetric (anti–symmetric) under parity transformations:

$$L_{\mu\nu} = L^{(\mathrm{S})}_{\mu\nu} + iL^{(\mathrm{A})}_{\mu\nu} , \tag{2.4}$$

$$W_{\mu\nu} = W^{(\mathrm{S})}_{\mu\nu} + iW^{(\mathrm{A})}_{\mu\nu} . \tag{2.5}$$

As the electromagnetic interaction conserves parity, only terms with like symmetry contribute to the DIS cross section in Eqn. (2.3).

Due to the pointlike nature of the positrons the lepton tensor can be calculated in QED from

$$L_{\mu\nu}(k,\mathrm{s};k',\mathrm{s}') = \left[\overline{u}'(k',\mathrm{s}')\,\gamma_\mu\,u(k,\mathrm{s})\right]^* \left[\overline{u}'(k',\mathrm{s}')\,\gamma_\nu\,u(k,\mathrm{s})\right] , \tag{2.6}$$

where the $u(k,\mathrm{s})$ $[u'(k',\mathrm{s}')]$ are the Dirac spinors for spin–1/2 particles with four–momentum k $[k']$ and spin four–vector s $[\mathrm{s}']$, describing the incident [scattered] positron. Summing over the spin four–vector s' of the scattered positron, whose polarisation is not observed in the experiment, one obtains the following expressions for the symmetric and anti–symmetric part of the lepton tensor:

$$L^{(\mathrm{S})}_{\mu\nu}(k;k') = 2\,\left[k_\mu k'_\nu + k'_\mu k_\nu - g_{\mu\nu}(k\cdot k' - m_e^2)\right] , \tag{2.7}$$

$$L^{(\mathrm{A})}_{\mu\nu}(k,s;k') = 2\,m_e\,\varepsilon_{\mu\nu\lambda\sigma}\,\mathrm{s}^\lambda\,\left(k-k'\right)^\sigma . \tag{2.8}$$

The anti–symmetric part depends on the spin s^λ of the incident positron, while the symmetric part is spin–independent. In the above expressions, m_e denotes the positron mass, $g_{\mu\nu}$ is the metric tensor, and $\varepsilon_{\mu\nu\lambda\sigma}$ is the totally anti–symmetric Levi–Civita tensor of rank four.

In contrast to the lepton tensor, the hadron tensor $W_{\mu\nu}$ which describes the interaction at the virtual photon–nucleon vertex is unknown. It represents the internal structure of the nucleon, whose understanding in a specific aspect is the aim of this thesis. The internal nucleon structure, and hence the hadronic tensor, can be parameterised by a set of structure functions, which will be discussed in the following two sections.

2.2.1 The Unpolarised Cross Section

Imposing additional symmetry requirements as Lorentz covariance, gauge invariance and the standard symmetries of the strong interaction under C and P transformations, the spin–independent part of the hadron tensor $W^{(\mathrm{S})}_{\mu\nu}$ can be expressed in terms of two scalar, dimensionless structure functions, $F_1(x,Q^2)$ and $F_2(x,Q^2)$:

$$W^{(\mathrm{S})}_{\mu\nu}(q;P) = 2\left(-g_{\mu\nu} - \frac{q_\mu\,q_\nu}{Q^2}\right)F_1(x,Q^2) + \left(P_\mu + \frac{P_\lambda\,q^\lambda}{Q^2}q_\mu\right)\left(P_\nu + \frac{P_\lambda\,q^\lambda}{Q^2}q_\nu\right)\frac{F_2(x,Q^2)}{P_\lambda\,q^\lambda} . \tag{2.9}$$

The structure functions $F_1(x,Q^2)$ and $F_2(x,Q^2)$ are Lorentz–invariant and reflect the internal structure of the nucleon. They depend on the two independent Lorentz scalars x and Q^2 in DIS.

By contracting the symmetric parts of the lepton and hadron tensors, and averaging over the spin of the initial positron, one obtains the unpolarised differential cross section in the lab system from Eqn. (2.3) (see e.g. [Ans 95]):

$$\frac{\mathrm{d}^2\overline{\sigma}}{\mathrm{d}x\,\mathrm{d}Q^2} = \left(\frac{\mathrm{d}\overline{\sigma}}{\mathrm{d}\Omega}\right)_{\mathrm{Mott}} \cdot \frac{1}{EE'}\,\frac{\pi}{x}\left[F_2(x,Q^2) + \frac{2\nu}{M}F_1(x,Q^2)\,\tan^2\left(\frac{\theta}{2}\right)\right] , \tag{2.10}$$

where

$$\left(\frac{\mathrm{d}\overline{\sigma}}{\mathrm{d}\Omega}\right)_{\mathrm{Mott}} = \frac{4\alpha^2 E'^2}{Q^4}\cos^2\left(\frac{\theta}{2}\right) . \tag{2.11}$$

The unpolarised structure functions parameterise the deviation of the observed experimental cross section from the Mott cross section for the scattering of a relativistic spin–1/2 particle from a pointlike central potential. They are thus the analogy to the electric and magnetic form factors in elastic electron–nucleon scattering, which describe the Fourier transform of the electric charge distribution and the magnetic moment of the nucleon, respectively.

Precise measurements of the proton and deuterium structure functions F_2^{p} and F_2^{d} have been performed by numerous fixed target (BCDMS [Ben 89], E665 [Ada 96], NMC [Arn 95], SLAC [Whi 92]) and collider experiments (H1 [Aid 96] and ZEUS [Der 96]), covering a broad kinematic range of $2\cdot 10^{-6} \leq x \leq 0.85$, and $0.1 \leq (Q^2/\mathrm{GeV}^2) \leq 5\cdot 10^3$. In Fig. 2.2 a compilation of world data on the proton structure function F_2^{p} in the kinematic range relevant to HERMES is shown. In [Cas 98] a similar plot with data extending to much higher values of Q^2 from the collider experiments can be found. For values of $x \lesssim 0.18$ and $x \gtrsim 0.3$ the structure function shows a significant dependence on Q^2, which is not expected from the naive quark model. This Q^2–dependence is a consequence of QCD effects, which will be discussed in Sect. 2.5.

The unpolarised cross section can alternatively be expressed in terms of the photo absorption cross sections $\sigma_{\mathrm{T}}(x,Q^2)$ and $\sigma_{\mathrm{L}}(x,Q^2)$ for transversely and longitudinally polarised virtual photons on a nucleon:

$$\frac{\mathrm{d}^2\overline{\sigma}}{\mathrm{d}x\,\mathrm{d}Q^2} = \Gamma\left[\sigma_{\mathrm{T}}(x,Q^2) + \varepsilon\,\sigma_{\mathrm{L}}(x,Q^2)\right] . \tag{2.12}$$

Here, Γ gives the flux of virtual photons, which originate from the lepton beam. Neglecting the positron rest mass m_e, the degree of longitudinal polarisation ε of the virtual photons is given by

$$\varepsilon \overset{Q^2 \gg 2\,m_e^2}{\simeq} \frac{1 - y - \frac{1}{4}\gamma^2 y^2}{1 - y + \frac{1}{4}y^2(\gamma^2+2)} , \tag{2.13}$$

where

$$\gamma^2 := \frac{Q^2}{\nu^2} = \frac{4M^2x^2}{Q^2} . \tag{2.14}$$

Introducing the ratio $R(x,Q^2)$ of the photo absorption cross sections,

$$R(x,Q^2) = \frac{\sigma_{\mathrm{L}}(x,Q^2)}{\sigma_{\mathrm{T}}(x,Q^2)} , \tag{2.15}$$

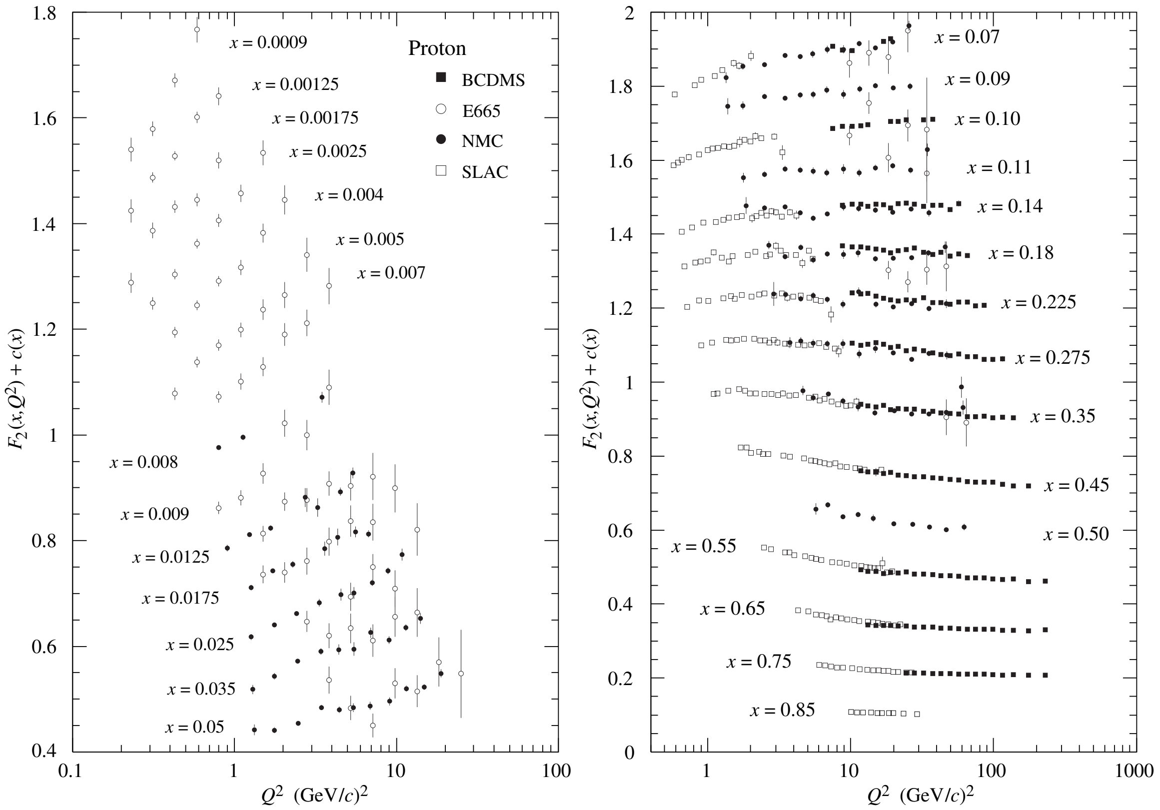

Figure 2.2: The unpolarised proton structure function $F_2^{\mathrm{p}}(x,Q^2)$, measured in deep inelastic scattering of electrons (SLAC [Whi 92]) and muons (BCDMS [Ben 89], E665 [Ada 96], NMC [Arn 95]) off fixed targets. The data are shown as a function of Q^2 for fixed values of x. Only statistical errors are shown. For the purpose of plotting, a constant $c(x) = 0.1\,i_x$ is added to $F_2^{\mathrm{p}}(x_i,Q^2)$, where i is the number of the x–bin, ranging from 1 ($x = 0.05$) to 14 ($x = 0.0009$) on the left–hand figure, and from 1 ($x = 0.85$) to 15 ($x = 0.07$) on the right–hand figure. This plot has been reproduced from [Cas 98].

the structure functions $F_1(x,Q^2)$ and $F_2(x,Q^2)$ can be related to each other by the longitudinal structure function $F_{\mathrm{L}}(x,Q^2)$:

$$R(x,Q^2) \;=\; \frac{F_{\mathrm{L}}(x,Q^2)}{2x\,F_1(x,Q^2)} \;:=\; \frac{(1+\gamma^2)\,F_2(x,Q^2) - 2x\,F_1(x,Q^2)}{2x\,F_1(x,Q^2)}\,, \tag{2.16}$$

or

$$F_1(x,Q^2) \;=\; F_2(x,Q^2)\cdot\frac{1+\gamma^2}{2x\,[1+R(x,Q^2)]}\,. \tag{2.17}$$

The cross section ratio R has been measured in the HERMES kinematic range by several experiments in DIS and found to be identical for proton and neutron targets within the experimental uncertainties. In [Abe 99] a combined analysis of the world data on $R(x,Q^2)$ can be found; Figure 5.9 in Sect. 5.8.4 shows a compilation of the available data on R as a function of x in different bins of Q^2.

In the Bjørken limit, where $Q^2 \to \infty$ and $\nu \to \infty$, such that $x = Q^2/2M\nu$ remains constant, the photo absorption cross section σ_L for longitudinally polarised photons vanishes as a consequence of the requirement of helicity conservation at the virtual photon–quark scattering vertex. In this limit, $R \to 0$, and Eqn. (2.17) simplifies to yield the Callan–Gross relation [Cal 69]:

$$2x\,F_1(x) = F_2(x)\;. \tag{2.18}$$

2.2.2 The Polarised Cross Section

Information about the spin structure of the nucleon can be obtained from deep inelastic scattering of longitudinally polarised leptons off a polarised nucleon target. The cross section for polarised DIS hence depends on both the symmetric and anti–symmetric parts of the lepton and hadron tensors in Eqn. (2.3). Demanding the same symmetry requirements as for the unpolarised case in the previous section, the anti–symmetric hadron tensor $W^{(A)}_{\mu\nu}$ can be parameterised by two other, dimensionless spin–dependent structure functions, $g_1(x, Q^2)$ and $g_2(x, Q^2)$:

$$W^{(A)}_{\mu\nu}(q; P, S) \;=\; \varepsilon_{\mu\nu\lambda\sigma}\, q^\lambda\, \frac{1}{\nu}\left[S^\sigma\, g_1(x, Q^2) + \left(S^\sigma - \frac{S_\rho\, q^\rho}{P_\rho\, q^\rho}\, P^\sigma\right) g_2(x, Q^2)\right]\;. \tag{2.19}$$

Like in the unpolarised case, the structure functions g_1 and g_2 are Lorentz–invariant scalars, and depend only on x and Q^2.

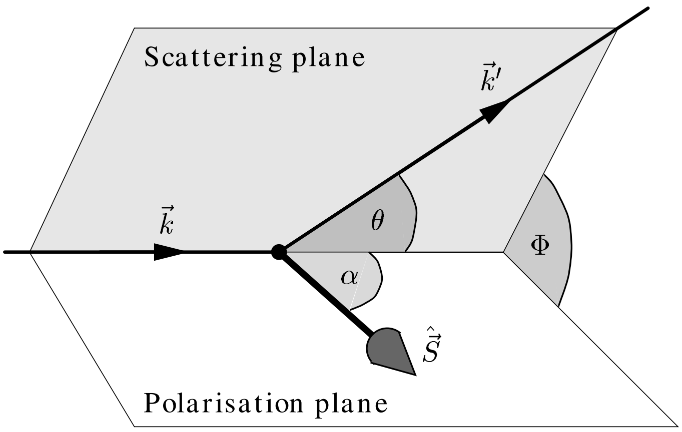

Figure 2.3: Definition of the angles in polarised inclusive deep inelastic scattering in the laboratory system.

In order to access the spin–dependent structure functions, one measures *cross section differences* between two different relative orientations of the beam and target spins, for which the contributions from the unpolarised, spin–independent structure functions cancel out. Experimentally, either the beam or target spin orientation is flipped. The experiments at SLAC (E142 [Ant 96], E143 [Abe 98], E154 [Abe 97a], ...) use the first variant, while the experiments at CERN (EMC [Ash 88], SMC [Ada 97], COMPASS [COM 96]) and at DESY (HERMES [Ack 98a]) cycle the orientation of the target spin. In Fig. 2.3 the angles are defined, which are relevant for the following discussion of the case, when the orientation of the target spin is flipped. Note, that the angle α gives the orientation of the target spin with respect to the *momentum of the incident positron*. The angle Φ between the scattering plane, which is defined by the incident and scattered positron momenta, and the polarisation plane, given by the target spin vector and the momentum of the incident positron, is undefined in the case when $\alpha = 0, \pi$, i.e. when the target spin is aligned parallel or anti–parallel to the momentum of the incident positron.

For a *longitudinally* polarised lepton beam, the cross section difference between two opposite orientations of the target spin is

$$\begin{aligned}\frac{\mathrm{d}^2[\sigma(\alpha+\pi)-\sigma(\alpha)]}{\mathrm{d}x\,\mathrm{d}Q^2} &= \frac{8\pi\alpha^2}{Q^4}\,\frac{y}{E}\cdot\Big[\big(E\cos\alpha + E'\cos\Theta\big)\;g_1(x,Q^2)\\ &\qquad + \frac{2EE'}{\nu}\,(\cos\Theta-\cos\alpha)\;g_2(x,Q^2)\Big]\,, \end{aligned}\tag{2.20}$$

with $\cos\Theta = \sin\theta\,\sin\alpha\,\cos\Phi + \cos\theta\,\cos\alpha$. Θ is the angle between the scattered positron direction, $\vec{k}'$, and the direction of the target spin $\hat{\vec{S}}$ (see Fig. 2.3).

If the target and beam spins are aligned parallel ($\rightrightarrows$) or anti–parallel ($\rightleftarrows$) to each other, i.e. $\alpha = 0$, the expression for the cross section difference simplifies to:

$$\frac{\mathrm{d}^2(\sigma^{\rightleftarrows}-\sigma^{\rightrightarrows})}{\mathrm{d}x\,\mathrm{d}Q^2} = \frac{8\pi\alpha^2}{Q^4}\,\frac{y}{E}\cdot\Big[\big(E+E'\cos\theta\big)\;g_1(x,Q^2)\;-\;\frac{Q^2}{\nu}\,g_2(x,Q^2)\Big]\,. \tag{2.21}$$

The result is independent of the angle Φ in Fig. 2.3, which is undefined in this configuration, as already noted earlier.

For a second special case, where the target spin is oriented perpendicular to the lepton beam momentum ($\alpha = \pi/2$), one obtains a different kinematic weighting of g_1 and g_2 in the expression for the cross section difference:

$$\frac{\mathrm{d}^2(\sigma^{\rightarrow\Uparrow}-\sigma^{\rightarrow\Downarrow})}{\mathrm{d}x\,\mathrm{d}Q^2} = \frac{8\pi\alpha^2}{Q^4}\,\frac{y}{E}\cdot E'\cdot\sin\theta\cos\Phi\left[g_1(x,Q^2)+\frac{2E}{\nu}\,g_2(x,Q^2)\right]\,. \tag{2.22}$$

In this configuration the cross section becomes dependent on the azimuthal scattering angle with respect to the orientation of the target spin. This corresponds to an azimuthal cross section asymmetry for scattering longitudinally polarised leptons on a transversely polarised target.

It is worthwhile to note, that the longitudinal polarisation of the lepton beam is crucial, as for transverse orientation of the beam spin, all cross section differences are suppressed by a factor m_ℓ/E, which approaches zero in the limit of infinite energy E of the incident lepton beam.

Figure 2.4 shows a compilation of the world data on the spin–dependent structure function $g_1(x)$ on the proton and the neutron at a fixed value of $Q_0^2 = 5\ \mathrm{GeV}^2$, measured in polarised DIS. Measurements with similar accuracy exist for the deuteron ([Abe 98], [Ade 98b], [Ant 99b]). Like the unpolarised structure functions, the polarised structure function $g_1(x,Q^2)$ varies with Q^2 for fixed values of x. The data shown in Fig. 2.4 have been measured at different values of Q^2 in every x–bin. As the experiments were carried out at different beam energies, also the mean values of Q^2 differ between the experiments for a given value of x. The evolution of the data to a common fixed value of Q_0^2 was performed under the assumption, that the ratio of the polarised and unpolarised

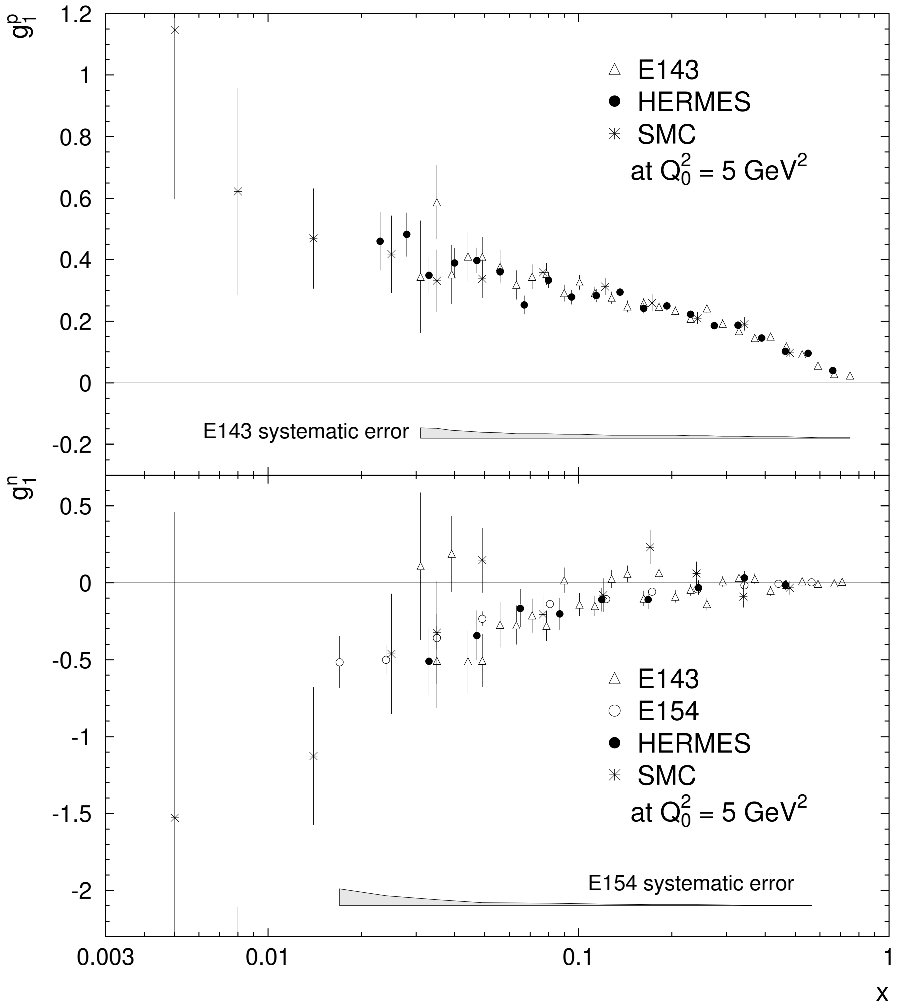

Figure 2.4: The spin–dependent structure functions $g_1^{\rm p}(x)$ on the proton and $g_1^{\rm n}(x)$ on the neutron, measured in deep inelastic scattering of polarised electrons (E143 [Abe 98], E154 [Abe 97a]), positrons (HERMES [Ack 97]), and muons (SMC [Ade 98b], [Ada 95]). The data are shown as a function of x for a fixed value of $Q_0^2 = 5$ GeV^2. Only the statistical errors are shown with the data points; as an example, the systematic error of the most precise experiment is shown in each panel, indicated by the shaded band.

structure functions is approximately independent of Q^2:

$$\frac{g_1(x,Q^2)}{F_1(x,Q^2)} \simeq \frac{g_1(x,Q_0^2)}{F_1(x,Q_0^2)} \, . \tag{2.23}$$

Using this relation together with Eqn. (2.17), the polarised structure function g_1 can be evolved to the fixed scale Q_0^2 according to

$$g_1(x,Q_0^2) \simeq \frac{F_2(x,Q_0^2)}{F_2(x,Q^2)} \cdot \frac{\left[1+R(x,Q^2)\right]\left(1+\frac{4M^2x^2}{Q_0^2}\right)}{\left[1+R(x,Q_0^2)\right]\left(1+\frac{4M^2x^2}{Q^2}\right)} \cdot g_1(x,Q^2)\, , \tag{2.24}$$

where parametrisations for $F_2(x,Q^2)$ [Arn 95] and $R(x,Q^2)$ [Abe 99] are taken.

Relation (2.23) is not strict, as will be shown in Sect. 2.5, and the evolution procedure presented here is under some criticism in the literature (e.g. [Ans 95]). However, for the comparatively small range of $1 \lesssim (Q^2/\mathrm{GeV}^2) \lesssim 60$ covered by the data, the deviations from Eqn. (2.23) are negligible compared to the experimental uncertainties of the data currently available. No systematic differences are visible between the results on $g_1(x,Q_0^2)$ from the SMC experiment and from the HERMES experiment, which differ most in their measured range in Q^2.

The second spin–structure function $g_2(x,Q^2)$ can be split in two parts [Wan 77]:

$$g_2(x,Q^2) \;=\; g_2^{\mathrm{WW}}(x,Q^2) + \hat{g}_2(x,Q^2)\,, \tag{2.25}$$

where

$$g_2^{\mathrm{WW}}(x,Q^2) \;=\; -g_1(x,Q^2) + \int_x^1 \frac{\mathrm{d}x'}{x'}\, g_1(x',Q^2) \tag{2.26}$$

is the so–called *Wandzura–Wilczek* term. The second term $\hat{g}_2(x,Q^2)$ in Eqn. (2.25) arises from a twist–3 contribution in the the Operator Product Expansion (OPE) of matrix elements, which describe the nucleon structure in terms of the electromagnetic current distributions $J_\mu(x)$.

Experimentally, g_2 has been measured in polarised DIS on proton ([Ada 94, Abe 98, Ant 99a]), deuteron ([Abe 98, Ant 99a]), and neutron ([Ant 96, Abe 98, Abe 97b]) targets, covering a kinematic range of $0.01 \le x \le 0.8$ and $1 \le Q^2/\mathrm{GeV}^2 \le 30$. Figure 5.10 in Sect. 5.8.5 shows the data on $x \cdot g_2(x)$ for the proton from the SLAC experiments E143 and E155. In all measurements, the size of $g_2(x)$ has been found to be very small or even zero in a wide kinematic range, following the prediction $g_2(x) \equiv 0$ of the naive quark model. Furthermore, the data are compatible with the leading twist Wandzura–Wilczek term Eqn. (2.26), albeit the experimental uncertainties on g_2 are considerably larger than for the measurements of g_1.

2.3 Double Spin Asymmetries

In principle, the spin–dependent structure functions g_1 and g_2 can be determined by measuring the cross section differences for a longitudinally ($\alpha = 0, \pi$) and a transversely ($\alpha = \frac{\pi}{2}, \frac{3\pi}{2}$) polarised target. Rather than measuring cross section *differences*, it is advantageous from an experimental point of view to measure the following cross section *asymmetries*:

$$A_\parallel(x,Q^2) \;\equiv\; A_\parallel \;:=\; \frac{\sigma^{\rightleftarrows} - \sigma^{\rightrightarrows}}{\sigma^{\rightleftarrows} + \sigma^{\rightrightarrows}}\,, \tag{2.27}$$

$$A_\perp(x,Q^2) \;\equiv\; A_\perp \;:=\; \frac{\sigma^{\rightarrow\Uparrow} - \sigma^{\rightarrow\Downarrow}}{\sigma^{\rightarrow\Uparrow} + \sigma^{\rightarrow\Downarrow}}\,. \tag{2.28}$$

Here, $\sigma^{\rightleftarrows(\rightrightarrows)}$ is a short notation for the differential cross sections $\frac{\mathrm{d}^2\sigma^{\rightleftarrows(\rightrightarrows)}}{\mathrm{d}x\,\mathrm{d}Q^2}$ for parallel (anti–parallel) alignments of beam and target spin, which have been introduced in the previous section. The $\sigma^{\rightarrow\Uparrow}$, $\sigma^{\rightarrow\Downarrow}$ are defined accordingly. Provided the time intervals between the flipping of the target or beam spin are short enough, efficiency and acceptance effects, which are not correlated to the relative orientation of the beam and target spins, cancel out by measuring cross section asymmetries instead of cross section differences. Hence, asymmetry measurements are less susceptible to systematic effects than measurements of differences of absolute cross sections.

In lowest order, the fundamental process in deep inelastic scattering is the interaction of a virtual photon γ^* with the target nucleon N. In the virtual photon–nucleon reference frame, the cross section differences can be expressed in terms of the two asymmetries A_1 and A_2:

$$A_1(x,Q^2) \equiv A_1 := \frac{\sigma_{\frac{1}{2}} - \sigma_{\frac{3}{2}}}{\sigma_{\frac{1}{2}} + \sigma_{\frac{3}{2}}} = \frac{g_1 - \gamma^2 g_2}{F_1}\,, \tag{2.29}$$

$$A_2(x,Q^2) \equiv A_2 := \frac{2\,\sigma_{\mathrm{I}}}{\sigma_{\frac{1}{2}} + \sigma_{\frac{3}{2}}} = \frac{\gamma(g_1 + g_2)}{F_1}\,, \tag{2.30}$$

where the dependence of the structure functions and cross sections on the kinematical quantities x and Q^2 has been omitted for clarity. In these definitions, $\sigma_{\frac{1}{2}}$ ($\sigma_{\frac{3}{2}}$) denotes the cross section for the absorption of a virtual photon by the nucleon, when the projection of the total angular momentum of the virtual photon–nucleon system along the momentum of the photon is $\frac{1}{2}$ ($\frac{3}{2}$). $\sigma_{\mathrm{T}} = \frac{1}{2}(\sigma_{\frac{1}{2}} + \sigma_{\frac{3}{2}})$ is the total transverse photo absorption cross section, while σ_{I} arises from the interference of longitudinal and transverse photo absorption amplitudes. Like in the above definitions for $A_{||}$ and $A_{\perp}$, the σ_j are short notations for the corresponding differential cross sections with respect to x and Q^2. The interference cross section term has to obey the triangular relation $\sigma_{\mathrm{I}} \leq \sqrt{\sigma_{\mathrm{L}}\,\sigma_{\mathrm{T}}}$, thus leading to a positivity limit for the absolute value of the asymmetry A_2:

$$|A_2| = \left|\frac{\sigma_{\mathrm{I}}}{\sigma_{\mathrm{T}}}\right| \leq \sqrt{\frac{\sigma_{\mathrm{L}}\,\sigma_{\mathrm{T}}}{\sigma_{\mathrm{T}}^2}} = \sqrt{R(x,Q^2)}\,, \tag{2.31}$$

which is given by the square root of the cross section ratio R introduced in Sect. 2.2.1.

The virtual photon asymmetries A_1 and A_2 are related to the experimental asymmetries $A_{||}$ and $A_{\perp}$ by

$$A_{||} = D\,(A_1 + \eta A_2)\,, \tag{2.32}$$

$$A_{\perp} = D\left(\xi A_2 - \frac{\eta}{\xi} A_1\right)\,. \tag{2.33}$$

$D = D(x,Q^2)$ is the depolarisation factor of the virtual photon, which depends on the kinematical quantities and the cross section ratio R, while η and ξ are purely kinematical factors:

$$D = \frac{1-(1-y)\,\varepsilon}{1+\varepsilon\,R}\,, \tag{2.34}$$

$$\eta = \frac{\varepsilon\,\gamma\,y}{1-(1-y)\,\varepsilon}\,, \tag{2.35}$$

$$\xi = \sqrt{\frac{2\,\varepsilon}{1+\varepsilon}}\,, \tag{2.36}$$

and ε is the degree of longitudinal polarisation of the virtual photon, already defined in Eqn. (2.13).

Rewriting Eqn. (2.29) and using the definition in Eqn. (2.32), the virtual photon asymmetry A_1 can be expressed as

$$A_1 = \frac{A_{\|}}{D(1+\eta\gamma)} - \frac{\eta\gamma(1+\gamma^2)}{1+\eta\gamma}\,\frac{g_2}{F_1} \overset{g_2=0}{\simeq} \frac{A_{\|}}{D(1+\eta\gamma)}\,. \tag{2.37}$$

This allows to approximately extract the virtual photon asymmetry A_1 from a measurement of the longitudinal asymmetry $A_{\|}$ alone, under the assumption that the polarised structure function g_2 vanishes. The contribution from g_2 in Eqn. (2.37) is additionally suppressed by a factor, which varies between $1.4\cdot 10^{-3}$ and 0.15 for the kinematic range covered by the HERMES data used in this analysis (see Chapter 5). The uncertainty arising from neglecting g_2 is considered in the calculation of the systematic uncertainties on the extracted values of the virtual photon asymmetry A_1 in Sect. 5.8.5.

2.4 Structure Functions in the Quark Parton Model

Quarks were initially a mathematical construct, invented to group members of the baryon and meson multiplets according to resembling properties [Gel 64]. They became only generally accepted as the fundamental constituents of hadronic matter (besides the gluons, which are the gauge bosons of the strong interaction, coupling the quarks into bound states) after the experimental observation in the early seventies at SLAC [Fri 72] that the structure function $F_2(x)$ is independent of Q^2 for a fixed value of x. This feature had been predicted in [Bjø 69a].

In the quark parton model (QPM), which was invented by Bjørken [Bjø 69b] and Feynman [Fey 69], the nucleon is composed of hard, pointlike scattering centres, called partons. In DIS, mediated by the exchange of a virtual photon, only the charged partons, which are identified with the spin–1/2 quarks, couple to the photon and contribute to the scattering process.

The QPM is formulated in the *infinite momentum frame*, where a nucleon moves with infinite linear momentum, so that rest masses of the partons and the nucleon itself, as well as momenta transverse to the direction of motion, can be neglected. In this frame the four–momentum of a nucleon is given by $P^\mu = (P, 0, 0, P)$, and a parton inside the nucleon carries the four–momentum $p^\mu \equiv \zeta P^\mu = (\zeta P, 0, 0, \zeta P)$, where ζ is the *Nachtmann* variable and gives the fractional momentum of the nucleon carried by the parton. In the *scaling limit* $\zeta^2 P^2 \ll Q^2$ this variable can be expressed as $\zeta = Q^2/(2M\nu)$, which is identical to the Bjørken–x variable defined in inclusive DIS (see Tab. 2.1). For large enough values of Q^2, the Bjørken–x variable can thus be interpreted as the fractional momentum of the nucleon carried by the struck quark.

Furthermore, in the QPM deep inelastic scattering can be described by the incoherent sum of elastic scattering processes of the virtual photon off non–interacting quarks. The structure functions are thus obtained by summing over the quark (and anti–quark) flavours f and integrating over the momentum fractions ζ:

$$F_1(x) = \tfrac{1}{2}\sum_f \int_0^1 \mathrm{d}\zeta\; e_f^2\, q_f(\zeta)\,\delta(\zeta - x) = \frac{1}{2}\sum_f e_f^2\, q_f(x)\,, \tag{2.38}$$

$$F_2(x) = \sum_f \int_0^1 \mathrm{d}\zeta\; \zeta\, e_f^2\, q_f(\zeta)\,\delta(\zeta - x) = \sum_f x\, e_f^2\, q_f(x)\,. \tag{2.39}$$

The quantity $q_f(x)$ in this expression is the *parton density function* (PDF) for a quark of flavour f and with the fractional electric charge e_f. $q_f(x)\,\mathrm{d}x$ gives the probability to find a quark with flavour f in the nucleon within the momentum range $[x, x+\mathrm{d}x]$. The sum over f is performed over all quark flavours with rest masses less than the value of Q^2 in the measurement. At HERMES kinematics, $f = u, \overline{u}, d, \overline{d}, s, \overline{s}$.

From Eqns. (2.39) and (2.38) one obtains the Callan–Gross relation Eqn. (2.18), which holds in the given form for pointlike constituents of the nucleon with a spin component of 1/2 along a quantisation axis [Cal 69]. For spin 0 quarks, the Callan–Gross relation would read instead (see e. g. [Gri 87], p. 270):

$$\frac{2x\,F_1(x)}{F_2(x)} = 0\,, \tag{2.40}$$

which has clearly been ruled out by data from early DIS experiments at SLAC [Fri 72], thus confirming a second assumption of the initially hypothetical quark model.

As the parton density functions give the number densities of quarks inside the nucleon, certain sum rules can be formulated. In the case of a proton, they write as:

$$\int_0^1 \left[u(x) - \overline{u}(x)\right]\,\mathrm{d}x =: \int_0^1 u_\mathrm{v}(x)\,\mathrm{d}x = 2\,, \tag{2.41}$$

$$\int_0^1 \left[d(x) - \overline{d}(x)\right]\,\mathrm{d}x =: \int_0^1 d_\mathrm{v}(x)\,\mathrm{d}x = 1\,, \tag{2.42}$$

$$\int_0^1 \left[s(x) - \overline{s}(x)\right]\,\mathrm{d}x = 0\,, \tag{2.43}$$

where $u_\mathrm{v}(x)$ and $d_\mathrm{v}(x)$ are the *valence quark* distributions. In a static picture of the nucleon, a proton is composed of two up quarks, one down quark, and carries no net strangeness, which gives the constraints on the individual flavour integrals in the above sum rules. In the following discussion, the parton density functions will be assumed to be defined on the proton. For a neutron, the corresponding PDFs can be obtained from a conjugation of the I_3 isospin component:

$$u^\mathrm{p}(x) \equiv d^\mathrm{n}(x)\,, \quad d^\mathrm{p}(x) \equiv u^\mathrm{n}(x)\,, \quad s^\mathrm{p}(x) \equiv s^\mathrm{n}(x)\,. \tag{2.44}$$

Furthermore, as the electrically neutral gluons do not interact with the virtual photon in lowest order, only the quarks are "seen" by the virtual photon probe. The integral over the fractional momenta,

$$\int_0^1 \mathrm{d}x\; x\left[u(x) + \overline{u}(x) + d(x) + \overline{d}(x) + s(x) + \overline{s}(x)\right] = 1 - \epsilon_g\,, \tag{2.45}$$

yields the total momentum of the nucleon minus the fraction ϵ_g, which is carried by the gluons. Experimentally, a value of ϵ_g around $\frac{1}{2}$ has been determined.

Similarly to the unpolarised structure functions, the *polarised* structure function $g_1(x)$ can be expressed in terms of *polarised* parton densities $\Delta q_f(x)$ in the QPM:

$$g_1(x) = \frac{1}{2}\sum_f e_f^2\,\left[q_f^+(x) - q_f^-(x)\right] =: \frac{1}{2}\sum_f e_f^2\,\Delta q_f(x)\,. \tag{2.46}$$

We denote $q_f^{+(-)}(x)$ as the number density for quarks with flavour f in the nucleon and parallel (anti–parallel) orientation of the quark spin with respect to the nucleon spin. The unpolarised PDFs defined above are hence given by $q_f(x) \equiv q_f^+(x) + q_f^-(x)$.

This allows a transparent probabilistic interpretation of the polarised structure function $g_1(x)$ in the QPM: in the photo absorption process of a virtual photon by a quark, the virtual photon can only couple to quarks, whose spin is aligned opposite to the spin of the photon. In the virtual photon–quark reference frame, the orbital angular momentum is zero, and hence the total angular momentum equals the sum of the spin projections of the two particles. After the absorption process only a quark with spin $\frac{1}{2}$ remains in the final state, thus requiring a total angular momentum of $\frac{1}{2}$ in the initial state also, to obey angular momentum conservation. When measuring the photo absorption cross section $\sigma_{\frac{1}{2}}$, the spin of the parent nucleon is anti–parallel to the spin of the virtual photon and thus the quark distribution $q_f^+(x)$ is probed. Accordingly, measuring the cross section $\sigma_{\frac{3}{2}}$, one probes the $q_f^-(x)$ quark distribution. In the approximation $g_2(x) \approx 0$,

$$g_1(x) \;\propto\; \sigma_{\frac{1}{2}} - \sigma_{\frac{3}{2}} \,, \tag{2.47}$$

and the definition of the polarised structure function $g_1(x)$ in the QPM in Eqn. (2.46) becomes obvious.

For the second spin structure function g_2 no such simple and transparent interpretation exists and g_2 vanishes in the QPM:

$$g_2(x) \;\equiv\; 0 \,. \tag{2.48}$$

2.5 Parton Densities in Quantum Chromodynamics

In the simple quark parton model the pointlike nature of the quarks as scattering centres implies that the structure functions should be independent of Q^2. This feature, called *Bjørken–scaling*, is not reproduced by the data, as can be seen in Fig. 2.2, except for a small kinematic range of $0.18 \lesssim x \lesssim 0.275$, where scaling is approximately fulfilled. Without having to abandon the successful quark model, the observed behaviour can be explained impressively well in the framework of Quantum Chromodynamics (QCD).

QCD is a non–Abelian quantum field theory of the strong interaction, embedded in the Standard Model. In QCD, quarks posses three different charges, which couple to the strong interaction, named *colour* charges. The formal symmetry of the strong interaction under the exchange of the colour charges is expressed in the $SU(3)_\mathrm{c}$ symmetry group. The field quanta of the strong interaction, which couple to the colour charges, are the gluons. The gluons carry one unit of colour and one unit of anti–colour themselves, which provides them with the possibility to couple among each other. This is a unique feature, not present in the field theory of electromagnetism, where the photons are electrically neutral and do not couple to each other. The coupling strength $g_\mathrm{s} = \sqrt{4\pi\,\alpha_\mathrm{s}}$ in the strong interaction is determined by the coupling constant, which in leading order perturbative QCD calculation is given by

$$\alpha_\mathrm{s}(\mu^2) \;=\; \frac{4\pi}{\beta_0\,\ln(\mu^2/\Lambda^2)} \,, \tag{2.49}$$

with $\beta_0 \;=\; 11 - \frac{2}{3}n_f$ and n_f the number of quark flavours with rest masses less than the energy scale μ. In DIS, the scale μ is usually identified with $\mu^2 = Q^2$. The parameter Λ is the QCD scale parameter, which gives a lower limit for the applicability of the perturbative calculation. This parameter depends on the chosen renormalisation scheme and on the number of quark flavours involved. Since a heavy virtual quark–anti-quark pair has a very short live time, it can only be resolved at very high values of Q^2. Hence, n_f depends on Q^2 and ranges from $n_f = 3$ to $n_f = 6$. For $n_f = 4$ a value of $\Lambda = (305 \pm 25_{\text{stat.}} \pm 50_{\text{syst.}})$ MeV is obtained [Cas 98], valid in the $\overline{\text{MS}}$ renormalisation scheme [Bar 78].

The value of the strong coupling "constant" $\alpha_s(Q^2)$ depends on Q^2, corresponding to a dependence on the spatial separation. In the limit $Q^2 \to \infty$, α_s vanishes logarithmically. This behaviour is called asymptotic freedom and implies that for very short distances the quarks can indeed be treated as free, pointlike particles, thus reproducing the QPM in this limit. Due to the running coupling constant, also the quark and gluon distributions become Q^2–dependent.

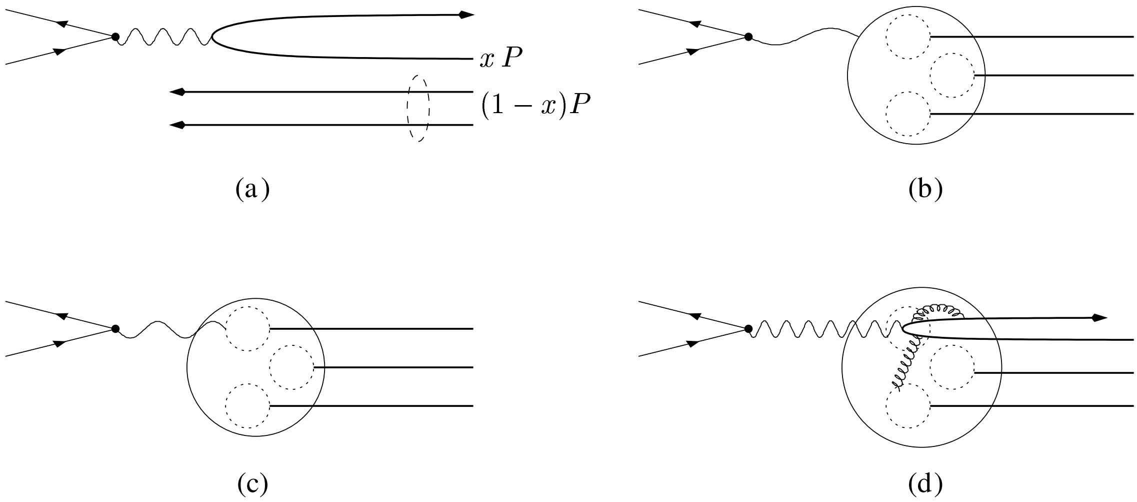

Figure 2.5: Evolution of the scattering process with Q^2 (after [Tip 99]): (a) The quark parton model in the infinite momentum frame describes the elastic scattering of the virtual photon off free, non–interacting quarks. For long wavelengths of the virtual photon, corresponding to low Q^2 values (b), the entire nucleon as a whole is probed. With increasing Q^2 individual quarks are being resolved (c), which are still "shielded" by a cloud of gluons and virtual quark–anti-quark pairs. In the limit of very high values of Q^2 (d) the pointlike quarks become apparent, resembling the scattering process in the QPM.

Figure 2.5 tries to illustrate this behaviour: for increasing values of Q^2 the spatial resolution of the virtual photon probe increases, thus resolving smaller structures. The so–called *constituent quarks*, which become apparent at moderate values of $Q^2 \approx 1$ GeV^2 (see Fig. 2.5 (c)), are themselves composed of one of the three *current* quarks plus an undetermined number of gluons and quarks, originating from splitting of gluons into virtual quark–anti-quark ($q\overline{q}$) pairs. With increasing resolution, more and more of these quarks become visible. As a quark can radiate off gluons (comparable to electromagnetic bremsstrahlung), it may lose part of its momentum to gluons, which in turn can split into $q\overline{q}$ pairs, as sketched in Fig. 2.6 a,b. Each of these virtual *sea* quarks carries a fraction of the initial gluon momentum. This process leads to a depletion of the quark density at high values of x with increasing Q^2, compensated by an increase at low values of x. Correspondingly, also the gluon distribution grows at low x with increasing Q^2. This Q^2–dependence becomes visible in the unpolarised structure function $F_2(x, Q^2)$, which is proportional to the quark distributions (see Eqn. (2.39)), as shown in Fig. 2.2.

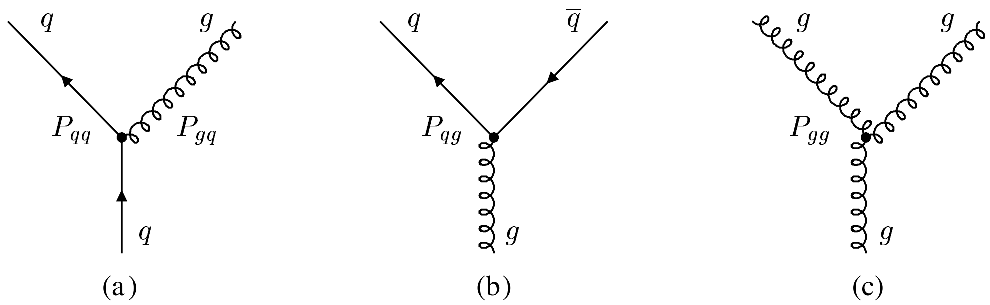

Figure 2.6: Fundamental Feynman diagrams in lowest order for the strong interaction. The time is oriented upwards in these diagrams. A quark q can emit a gluon g (a), thus producing a quark and a gluon with lower momenta in the final state. A gluon in the initial state can create a virtual $q\overline{q}$ pair (b) or radiate off another gluon (c). The P_{mn} are the splitting functions, which are explained in the text.

Quantitatively, the logarithmic dependence of the parton density functions on Q^2 is described by the coupled Dokshitser–Gribov–Lipatov–Altarelli–Parisi (DGLAP) equations [Dok 77, Gri 72, Lip 75, Alt 77]:

$$\frac{\partial}{\partial(\ln Q^2)}\, q^{\mathrm{NS}}(x,Q^2) \;=\; \frac{\alpha_{\mathrm{s}}(Q^2)}{2\pi}\,\left[P_{qq}^{\mathrm{NS}} \otimes q^{\mathrm{NS}}\right](x,Q^2)\,, \tag{2.50}$$

$$\frac{\partial}{\partial(\ln Q^2)}\begin{pmatrix}\Sigma(x,Q^2)\\ g(x,Q^2)\end{pmatrix} \;=\; \frac{\alpha_{\mathrm{s}}(Q^2)}{2\pi}\left[\begin{pmatrix}P_{qq}^{\mathrm{S}} & 2n_f\,P_{qg}\\ P_{gq} & P_{gg}\end{pmatrix} \otimes \begin{pmatrix}\Sigma\\ g\end{pmatrix}\right](x,Q^2)\,, \tag{2.51}$$

where $\otimes$ denotes a convolution integral:

$$[a \otimes b]\,(x,Q^2) \;:=\; \int_x^1 \frac{\mathrm{d}y}{y}\, a\!\left(\frac{x}{y},Q^2\right)\, b(y,Q^2)\,. \tag{2.52}$$

Here, $q^{\mathrm{NS}}(x,Q^2), \Sigma(x,Q^2)$, and $g(x,Q^2)$ are the flavour *non–singlet* and *singlet* quark distributions, and the gluon distribution, respectively. The non–singlet and singlet quark distributions are defined as

$$q^{\mathrm{NS}}(x,Q^2) \;:=\; \sum_{f=u,\overline{u},d,\overline{d},\ldots}\left(\frac{e_f^2}{\langle e^2\rangle} - 1\right)\, q_f(x,Q^2)\,, \tag{2.53}$$

$$\Sigma(x,Q^2) \;:=\; \sum_{f=u,\overline{u},d,\overline{d},\ldots} q_f(x,Q^2)\,, \tag{2.54}$$

where $\langle e^2\rangle := \sum_f e_f^2/n_f$.

The coefficients P_{mn} in Eqns. (2.50) and (2.51) are called *splitting functions*, which depend on the ratio $\frac{x}{y}$ of the fractional momenta of the parton n in the initial state and the parton m in the final state. In Figure 2.6 the leading order combinations for

mn are sketched. The probability that a quark with momentum fraction x originates from a parent quark with a larger momentum fraction y (see Fig. 2.6 a) is proportional to $\alpha_s(Q^2)\, P_{qq}(\frac{x}{y})$. In the same process also a gluon with fractional momentum x' is radiated off the initial state quark. The probability for this process is proportional to $\alpha_s(Q^2)\, P_{gq}(\frac{x'}{y})$. Accordingly, the splitting function P_{qg} is related to the process shown in Fig. 2.6 b, where a gluon splits up into a virtual $q\overline{q}$ pair. Finally, the probability for the coupling of three gluons among each other (Fig. 2.6 c) is proportional to P_{gg}. The polarised parton distributions evolve formally equivalent to the unpolarised ones, with the replacements $q^{\rm NS} \to \Delta q^{\rm NS}$, $\Sigma \to \Delta\Sigma$, $g \to \Delta g$, and $P_{mn} \to \Delta P_{mn}^{(\rm NS/S)}$ in Eqns. (2.50) and (2.51).

It should be noted, that the non–singlet distribution $q^{\rm NS}(x,Q^2)$ evolves independently from the gluon distribution, while $\Sigma(x,Q^2)$ and $g(x,Q^2)$ couple to each other. This behaviour may be exploited in principle to determine the gluon distribution from measuring the Q^2–dependence of the singlet and non–singlet quark distributions via combinations of related structure functions. From the evolution of the non–singlet part (Eqn. (2.50)), the value of $\alpha_s(Q^2)$ can be determined, which is used in a next step to derive the gluon distribution $g(x,Q^2)$ from the evolution of the singlet distribution $\Sigma(x,Q^2)$ (Eqn. (2.51)).

In perturbative QCD, the resulting expressions for the unpolarised and polarised structure functions $F_1(x,Q^2)$ and $g_1(x,Q^2)$ are given by

$$F_1(x,Q^2) \;=\; \frac{1}{2}\,\langle e^2\rangle\,\left\{C_{\rm NS}\otimes q^{\rm NS} + C_{\rm S}\otimes\Sigma + C_g\otimes g\right\}\;, \tag{2.55}$$

$$g_1(x,Q^2) \;=\; \frac{1}{2}\,\langle e^2\rangle\,\left\{\Delta C_{\rm NS}\otimes \Delta q^{\rm NS} + \Delta C_{\rm S}\otimes\Delta\Sigma + \Delta C_g\otimes \Delta g\right\}\;. \tag{2.56}$$

The $C_{\rm NS,S,\mathit{g}}$ ($\Delta C_{\rm NS,S,\mathit{g}}$) denote the unpolarised (polarised) flavour non–singlet, singlet, and gluon *coefficient functions*. The splitting and the coefficient functions depend on the ratio $\frac{x}{y}$ and on the coupling constant $\alpha_s(Q^2)$, and can be expanded in power series in α_s:

$$P\left(\frac{x}{y},Q^2\right) \;=\; P^{(0)}\left(\frac{x}{y}\right) + \frac{\alpha_s(Q^2)}{2\pi}\,P^{(1)}\left(\frac{x}{y}\right) + \mathcal{O}\{\alpha_s^2(Q^2)\}\,, \tag{2.57}$$

$$C\left(\frac{x}{y},Q^2\right) \;=\; C^{(0)}\left(\frac{x}{y}\right) + \frac{\alpha_s(Q^2)}{2\pi}\,C^{(1)}\left(\frac{x}{y}\right) + \mathcal{O}\{\alpha_s^2(Q^2)\}\,.$$

In leading order (LO), the unpolarised and polarised coefficient functions are equal and

$$(\Delta)C_{\rm NS}^{(0)}\left(\frac{x}{y}\right) \;=\; (\Delta)C_{\rm S}^{(0)}\left(\frac{x}{y}\right) \;=\; \delta\left(1-\frac{x}{y}\right)\;,\quad (\Delta)C_g^{(0)}\left(\frac{x}{y}\right) \;=\; 0\,. \tag{2.58}$$

Consequently, the structure functions F_1 and g_1 decouple from the gluon contributions and from Eqns. (2.55) and (2.56) one obtains in leading order:

$$F_1(x,Q^2) \;=\; \frac{1}{2}\sum_f e_f^2\, q_f(x,Q^2)\,, \tag{2.59}$$

$$g_1(x,Q^2) \;=\; \frac{1}{2}\sum_f e_f^2\, \Delta q_f(x,Q^2)\,. \tag{2.60}$$

These equations resemble the expressions obtained in the QPM, where the unpolarised and polarised quark distributions have been replaced by effective Q^2–dependent parton density functions.

Beyond LO, the splitting and coefficient functions depend on the chosen renormalisation scheme (see [Alt 82], e.g.). Full next–to–leading order (NLO) calculations of the unpolarised [Alt 82] and polarised splitting [Zij 94, Mer 96, Vog 96] and coefficient functions [Kod 79] are available. As the unpolarised and polarised splitting functions are different, with the exception of P_{qq} and ΔP_{qq}, the ratio g_1/F_1 becomes dependent on Q^2 in QCD. However, in the kinematic region dominated by valence quarks, this Q^2–dependence is expected to be small [Geh 95, Lam 95]. The approximate Q^2–independence of the structure function ratio g_1/F_1 in a limited range of Q^2 was exploited in Sect. 2.2.2 for the evolution of the polarised structure function $g_1(x,Q^2)$ to a fixed value of Q_0^2. Over the range in Q^2 currently accessible in measurements, no significant Q^2–dependence is observed within the precision of the data [Ade 98b].

2.6 Model Predictions

Up to now, theoretical models can not predict the x–dependence of the spin structure functions satisfactory. However, many models allow to make statements about the values of certain moments of the spin structure functions, which give insight into the nucleon's spin structure. The first moment Γ_1 of the spin structure function g_1 is defined as

$$\Gamma_1(Q^2) \;:=\; \int_0^1 g_1(x,Q^2)\,\mathrm{d}x\;, \tag{2.61}$$

and can be related to expectation values from current algebra for a proton (neutron) as [Ans 95]

$$\Gamma_1^{\mathrm{p(n)}}(Q^2) \;=\; \frac{1}{12}\left[\overset{+}{\scriptstyle(-)}\,a_3 + \frac{a_8}{3}\right]\,\Delta\mathcal{C}_{\mathrm{NS}}(Q^2) + \frac{1}{9}\,a_0(Q^2)\,\Delta\mathcal{C}_{\mathrm{S}}(Q^2)\;. \tag{2.62}$$

In this expression, the minus sign refers to Γ_1^{n}, while in the proton case a_3 contributes with a positive sign. The a_i are the expectation values of axial vector currents on the proton:

$$2M\,a_0\,S_\mu \;=\; \langle P,S|J^0_{5,\mu}|P,S\rangle\;, \tag{2.63}$$

$$M\,a_j\,S_\mu \;=\; \langle P,S|J^j_{5,\mu}|P,S\rangle\;,\quad j=3,8\;. \tag{2.64}$$

Here, the $J^0_{5,\mu}$ and $J^j_{5,\mu}$ are the flavour singlet current, and the non–vanishing elements of the flavour octet axial vector currents, respectively. The definitions of these currents can be found in [Ans 95], e.g.

The $\Delta\mathcal{C}_{\mathrm{NS,S}}$ in Eqn. (2.62) denote the first moments of the coefficient functions, introduced in the previous section:

$$\Delta\mathcal{C}_{\mathrm{NS(S)}}(Q^2) \;:=\; \int_0^1 \Delta C_{\mathrm{NS(S)}}(x,Q^2)\,\mathrm{d}x\;. \tag{2.65}$$

Like the coefficient functions, they depend on the number n_f of active flavours. For $n_f=3$, the flavour non–singlet and the flavour singlet coefficients are given up to third (second) order in $\alpha_s(Q^2)$ by [Lar 94]:

$$\Delta\mathcal{C}_{\rm NS}(Q^2) \;=\; 1 - \frac{\alpha_s(Q^2)}{\pi} \;-\; 3.5833\left(\frac{\alpha_s(Q^2)}{\pi}\right)^2 - \;20.2153\left(\frac{\alpha_s(Q^2)}{\pi}\right)^3 , \qquad (2.66)$$

$$\Delta\mathcal{C}_{\rm S}(Q^2) \;=\; 1 - \frac{\alpha_s(Q^2)}{\pi} \;-\; 1.0959\left(\frac{\alpha_s(Q^2)}{\pi}\right)^2 , \qquad (2.67)$$

valid in the $\overline{\rm MS}$ renormalisation scheme.

Under the assumption of $SU(3)_f$ flavour symmetry for the axial vector currents in the spin–$\frac{1}{2}$ baryon octet, the matrix elements a_3 and a_8 can be related to the constants F and D from weak decays:

$$a_3 \;=\; F + D\,, \qquad a_8 \;=\; 3F - D\,. \qquad (2.68)$$

The values for F and D have been determined experimentally from hyperon decays [Roo 82]:

$$F \;=\; 0.477 \pm 0.012\,, \qquad D \;=\; 0.756 \pm 0.011\,. \qquad (2.69)$$

From isospin symmetry, the matrix element a_3 equals the ratio $|g_{\rm A}/g_{\rm V}|$ of the axial vector $(g_{\rm A})$ to the vector $(g_{\rm V})$ coupling constants. The axial singlet matrix element, a_0, can not be related to the decay constants.

The matrix elements a_i can also be related to the first moments Δq_f of the polarised quark and anti–quark distributions in the QPM:

$$a_0 \;=\; \Delta\Sigma \;:=\; \Delta u + \Delta\overline{u} + \Delta d + \Delta\overline{d} + \Delta s + \Delta\overline{s}\,, \qquad (2.70)$$

$$a_3 \;=\; \Delta q_3 \;:=\; \Delta u + \Delta\overline{u} - (\Delta d + \Delta\overline{d})\,, \qquad (2.71)$$

$$a_8 \;=\; \Delta q_8 \;:=\; \Delta u + \Delta\overline{u} + \Delta d + \Delta\overline{d} - 2(\Delta s + \Delta\overline{s})\,, \qquad (2.72)$$

with $\Delta q_f \;:=\; \int_0^1 \Delta q_f(x)\,{\rm d}x$. Hence, in the QPM, the singlet axial charge a_0 gives the contribution $\Delta\Sigma$ of all quarks to the nucleon's spin.

In QCD this statement is not true in general. Depending on the chosen factorisation scheme, $a_0(Q^2)$ also gets a contribution from the first moment $\Delta g(Q^2)$ of the polarised gluon distribution. In the gauge invariant $\overline{\rm MS}$ scheme [Bar 78], for instance, gluons do not contribute to $\Gamma_1(Q^2)$, which means that the QPM statement, $a_0 = \Delta\Sigma$, remains valid. In the chiral invariant Adler–Bardeen (AB) [Adl 69b] scheme, however, gluons do contribute to $\Gamma_1(Q^2)$ and one obtains

$$a_0^{\rm (AB)}(Q^2) \;=\; \Delta\Sigma - n_f\,\frac{\alpha_s(Q^2)}{2\pi}\,\Delta g(Q^2)\,. \qquad (2.73)$$

This gluon contribution is called the Adler–Bell–Jackiw anomaly [Adl 69a, Bel 69], which corresponds to a pointlike interaction between the singlet axial current and the gluon density [Ans 95]. In the AB factorisation scheme, $\Delta\Sigma$ is independent of Q^2, but cannot be obtained from the measured value of $a_0(Q^2)$ without knowledge of $\Delta g(Q^2)$ [Ans 95, Rit 97].

2.6.1 The Bjørken Sum Rule

The Bjørken sum rule [Bjø 66] was derived already in the year 1966, prior to the existence of QCD, from current algebra. This sum rule relates the difference of the first moments of the spin structure functions $g_1^{\mathrm{p,n}}$ on a proton and a neutron target to the decay constant $g_a = |g_{\mathrm{A}}/g_{\mathrm{V}}| = 1.2670 \pm 0.0035$ [Cas 98] from neutron β–decay. Including QCD corrections, the Bjørken sum rule writes

$$\Gamma_1^{\mathrm{Bj}}(Q^2) \;\equiv\; \Gamma_1^{\mathrm{p}}(Q^2) - \Gamma_1^{\mathrm{n}}(Q^2) \;=\; \frac{1}{6}\left|\frac{g_{\mathrm{A}}}{g_{\mathrm{V}}}\right| \, \Delta\mathcal{C}_{\mathrm{NS}}(Q^2)\,, \tag{2.74}$$

where $\Delta\mathcal{C}_{\mathrm{NS}}(Q^2)$ is given in Eqn. (2.66).

At a scale of $Q_0^2 = 5\ \mathrm{GeV}^2$ and using an input value for the strong coupling constant $\alpha_{\mathrm{s}}(m_{Z^0}) = 0.118 \pm 0.003$ at the mass of the neutral Z^0 boson, one obtains a value for the Bjørken sum rule of $\Gamma_1^{\mathrm{Bj}}(Q_0^2) = 0.182 \pm 0.003$. From the combined results of EMC, SMC, and E143 data, an experimental value of $\Gamma_{1,\mathrm{exp.}}^{\mathrm{Bj}}(Q_0^2) = 0.170 \pm 0.012$ [Abe 98] was obtained, thus confirming the theoretical prediction within the experimental and theoretical uncertainties. Alternatively, under the assumption that the Bjørken sum rule is accurate, Eqn. (2.74) can be solved for $\alpha_{\mathrm{s}}(Q^2)$ (using Eqn. (2.66)) to obtain a rather precise value of $\alpha_{\mathrm{s}}(m_{Z^0}) = 0.123\,^{+0.010}_{-0.006}$ [Abe 98]. Figure 2.7 shows a summary of experimental results on $\Gamma_{1,\mathrm{exp}}^{\mathrm{p,n}}$ and a comparison with the predictions from the Bjørken sum rule and the Ellis–Jaffe sum rule, which will be explained in the following section.

2.6.2 The Ellis–Jaffe Sum Rule

Since the axial singlet charge a_0 can not be related to the decay constants, separate sum rules for Γ_1^{p} and Γ_1^{n} require assumptions about this quantity. Ellis and Jaffe assumed that the strange sea quarks and the gluons carry no net polarisation: $\Delta s + \Delta\overline{s} \equiv \Delta g \equiv 0$ [Ell 74]. Using the relations of the current matrix elements to the decay constants introduced above, the QCD–corrected Ellis–Jaffe sum rule for the proton (neutron) becomes:

$$\Gamma_1^{\mathrm{p(n)}}(Q^2) \;=\; \frac{1}{12}\left[\overset{\,}{\scriptstyle(}\!\overset{+}{-}\!\scriptstyle{)}\,(F+D) + F - \frac{D}{3}\right]\Delta\mathcal{C}_{\mathrm{NS}}(Q^2) \;+\; \frac{3F-D}{9}\,\Delta\mathcal{C}_{\mathrm{S}}(Q^2)\,, \tag{2.75}$$

or separately for the proton and the neutron:

$$\Gamma_1^{\mathrm{p}}(Q^2) \;=\; \frac{1}{18}\left[(3F+D)\,\Delta\mathcal{C}_{\mathrm{NS}}(Q^2) + 2\,(3F-D)\,\Delta\mathcal{C}_{\mathrm{S}}(Q^2)\right]\,, \tag{2.76}$$

$$\Gamma_1^{\mathrm{n}}(Q^2) \;=\; \frac{1}{9}\left[-D\,\Delta\mathcal{C}_{\mathrm{NS}}(Q^2) + (3F-D)\,\Delta\mathcal{C}_{\mathrm{S}}(Q^2)\right]\,. \tag{2.77}$$

At the same scale $Q_0^2 = 5\ \mathrm{GeV}^2$ and using the same value for the strong coupling constant $\alpha_{\mathrm{s}}(m_{Z^0}) = 0.118 \pm 0.003$ as in the previous section, one obtains values of $\Gamma_1^{\mathrm{p}}(Q_0^2) = 0.164 \pm 0.005$ and $\Gamma_1^{\mathrm{n}}(Q_0^2) = -0.018 \pm 0.004$ from the above Eqns. (2.76) and (2.77). A comparison with the combined experimental results $\Gamma_{1,\mathrm{exp}}^{\mathrm{p}}(Q_0^2) = 0.129 \pm 0.010$ and $\Gamma_{1,\mathrm{exp}}^{\mathrm{n}}(Q_0^2) = -0.034 \pm 0.017$ [Abe 98] shows a significant violation of the Ellis–Jaffe sum rule. This violation implies that there might be a $SU(3)$ symmetry breaking, or there is a significant contribution from strange quarks and/or gluons to the spin of the nucleon. The violation of the Ellis–Jaffe sum rule is also visualised in Fig. 2.7.

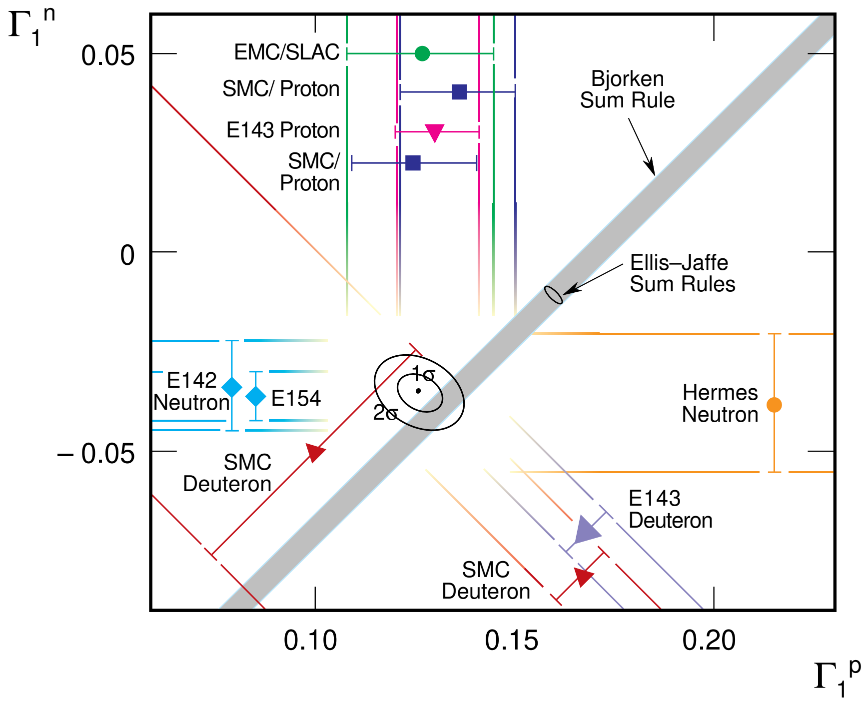

Figure 2.7: Summary of experimental tests of the Bjørken and Ellis–Jaffe sum rules. The horizontal and vertical axis are the integrals Γ_1^p and Γ_1^n, respectively. The prediction of the Bjørken sum rule is indicated by the shaded diagonal band, the predictions from the Ellis–Jaffe sum rules for Γ_1^p and Γ_1^n are indicated by the small ellipse within the band of the Bjørken sum rule. Also shown is the overall best fit for $\Gamma_{1,\mathrm{exp}}^{\mathrm{Bj}}$ using all experimental data, together with the 1σ and 2σ contours. This figure has been reproduced from [Hug 99].

2.7 Semi Inclusive Polarised Deep Inelastic Scattering

As laid out in the previous sections, inclusive polarised DIS provides a useful tool to access information on the spin structure of the nucleon. Further insight into the contributions from the individual quark flavours to the nucleon's spin may be obtained from the analysis of polarised semi inclusive DIS events, for which at least one final state hadron is detected in coincidence with the scattered lepton ℓ'. Under the assumption of local parton–hadron duality, the measured flow of hadron quantum numbers reflects the flow of parton quantum numbers in the scattering process. Hadrons observed final in the state may thus be correlated to the initial quarks, providing more information on the nucleon structure.

2.7.1 Fragmentation Functions

In the framework of the quark model, the semi inclusive DIS process is described in terms of a single quark which is struck by the virtual photon and ejected from the nucleon (see Fig. 2.1). In the lab frame the struck quark absorbs the energy of the virtual photon and is ejected along the direction of the virtual photon. Due to the confinement properties of QCD, which demand that only colour neutral (colour singlet) states may exist as free particles, both the struck quark and the target remnants have to form a set of colour neutral final state hadrons. This process, which is called hadronisation, can not be described in perturbative QCD, because it involves long–range interactions between the struck quark and the target remnant as they move apart. At a certain distance the strong coupling constant $\alpha_{\mathrm{s}}(Q^2)$ becomes larger than unity, thus inhibiting the perturbative expansion in powers of α_{s}. Instead, the hadronisation process is parameterised by *fragmentation functions* $D_f^h(Q^2, z)$, which give the probability density that a struck quark of flavour f, probed at a particular scale Q^2, produces a final state hadron h with fractional energy z.

Hadrons produced in the fragmentation of the struck quark are defined as *current fragments*, while those originating from the target remnant are called *target fragments*. The probabilistic interpretation of the fragmentation functions given above is valid for the current fragments. At finite values of the energy transfer ν by the virtual photon, no unambiguous separation of the two classes of hadrons is possible. However, there are several methods discussed in literature to enhance current fragments in a given sample of hadrons. For instance, current fragments are preferably selected (a) by requiring forward momenta in the γ^*–N system, corresponding to positive values of x_{F}, or (b) by requiring fast hadrons in the lab system, identified by a cut on $z > z_{\mathrm{min}}$ (e.g. $z_{\mathrm{min}} = 0.2$). The separation of current from target fragments by these cuts is enhanced for larger values of the hadronic final state mass squared, W^2.

The fragmentation functions are normalised to conserve energy and particle multiplicities n_h:

$$\sum_h \int_0^1 \mathrm{d}z\; z \cdot D_f^h(Q^2, z) \;=\; 1\;, \tag{2.78}$$

$$\sum_f \int_0^1 \mathrm{d}z\; D_f^h(Q^2, z) \;=\; n_h(Q^2)\;. \tag{2.79}$$

Since the fragmentation process proceeds by the strong interaction, charge conjugation and isospin invariance reduce the number of independent fragmentation functions significantly. This is illustrated in the example of fragmentation of quarks into charged pions. For three different flavours of quarks and anti–quarks, the total number of twelve possible combinations can be reduced to three independent fragmentation functions, using charge conjugation symmetry $[D_u^{\pi^+}(z) = D_{\bar{u}}^{\pi^-}(z)]$ and isospin symmetry $[D_u^{\pi^+}(z) \;=\; D_d^{\pi^-}(z)]$:

$$D_+(z) \;\equiv\; D_u^{\pi^+}(z) \;=\; D_{\bar{u}}^{\pi^-}(z) \;=\; D_{\bar{d}}^{\pi^+}(z) \;=\; D_d^{\pi^-}(z)\;, \tag{2.80}$$

$$D_-(z) \;\equiv\; D_u^{\pi^-}(z) \;=\; D_{\bar{u}}^{\pi^+}(z) \;=\; D_{\bar{d}}^{\pi^-}(z) \;=\; D_d^{\pi^+}(z)\;, \tag{2.81}$$

$$D_{\mathrm{s}}(z) \;\equiv\; D_s^{\pi^+}(z) \;=\; D_{\bar{s}}^{\pi^-}(z) \;=\; D_{\bar{s}}^{\pi^+}(z) \;=\; D_s^{\pi^-}(z)\;, \tag{2.82}$$

where the dependence on Q^2 has been omitted. The $D_+(z)$, $D_-(z)$, and $D_{\mathrm{s}}(z)$ are called *favoured*, *unfavoured*, and *strange* fragmentation functions, respectively. They obey the hierarchical relationship $D_+(z) \;\geq\; D_-(z) \;\geq\; D_{\mathrm{s}}(z)$. The favoured fragmentation functions relate to pions, which have the initial quark in their ground state wavefunction. Such processes are more probable than the unfavoured or strange quark cases, described by $D_-(z)$ and $D_{\mathrm{s}}(z)$.

The factorisation theorem in QCD, which is valid in the Bjørken limit, implies two other features of fragmentation functions. Factorisation demands that the hadronisation process be independent of the hard photon–quark scattering process, and hence should be independent of x and Q^2. Secondly, the fragmentation process is assumed to be universal, i.e. independent of the original environment of the initial quark, which starts the hadronisation process. This *environmental independence* implies that fragmentation functions determined in DIS should equally well describe hadronisation processes from $q\overline{q}$ pair production in $e^+ e^-$ collisions, which has been confirmed experimentally [Adl 97, Bre 99]. The same DIS data support the independence from x at finite values of Q^2, while already earlier data showed [Arn 86, Jon 91] that fragmentation functions vary with Q^2. In [Bin 95] LO and NLO QCD expressions for the fragmentation functions are presented, which describe the measured Q^2–dependence very well.

2.7.2 Semi Inclusive Asymmetries and Structure Functions

The differential cross section for the unpolarised semi inclusive scattering process is related to the expression for unpolarised inclusive DIS, given in Eqn. (2.10), by

$$\frac{\mathrm{d}^3\overline{\sigma}^h}{\mathrm{d}x\,\mathrm{d}Q^2\,\mathrm{d}z} = \frac{\sum_f e_f^2\, q_f(x,Q^2)\, D_f^h(Q^2,z)}{\sum_f e_f^2\, q_f(x,Q^2)} \cdot \frac{\mathrm{d}^2\overline{\sigma}}{\mathrm{d}x\,\mathrm{d}Q^2}\,. \tag{2.83}$$

Furthermore, using Eqns. (2.59) and (2.60), the unpolarised and polarised semi inclusive structure functions F_1^h and g_1^h are defined in LO as

$$F_1^h(x,Q^2,z) = \frac{1}{2}\sum_f e_f^2\, q_f(x,Q^2)\, D_f^h(Q^2,z)\,, \tag{2.84}$$

$$g_1^h(x,Q^2,z) = \frac{1}{2}\sum_f e_f^2\, \Delta q_f(x,Q^2)\, D_f^h(Q^2,z)\,. \tag{2.85}$$

The definition of g_1^h is valid under the assumption that the fragmentation process is independent of the relative orientation of the spin of the struck quark with respect to the spin of the target nucleon.

Using the same assumption $g_2^h = 0$ as in the inclusive case, the semi inclusive photon asymmetry A_1^h is obtained from

$$A_1^h(x,Q^2) \overset{g_2^h=0}{\simeq} \frac{\int_{z_{\min}}^1 \mathrm{d}z\, g_1^h(x,Q^2,z)}{\int_{z_{\min}}^1 \mathrm{d}z\, F_1^h(x,Q^2,z)} = \frac{\sum_f e_f^2\, \Delta q_f(x,Q^2)\, \int_{z_{\min}}^1 \mathrm{d}z\, D_f^h(Q^2,z)}{\sum_f e_f^2\, q_f(x,Q^2)\, \int_{z_{\min}}^1 \mathrm{d}z\, D_f^h(Q^2,z)}\,, \tag{2.86}$$

where the integration is performed over the range in z, as used for the identification of current fragments. Given the integrated fragmentation functions and the unpolarised quark distributions $q_f(x,Q^2)$, Eqn. (2.86) will be the basis for the extraction of the polarised quark distributions $\Delta q_f(x,Q^2)$ from a set of semi inclusive asymmetries (see Chapter 6).

2.8 Fragmentation Models

As already mentioned earlier, perturbative QCD fails to calculate the hadronisation process due to long–range interactions involved. For this reason, phenomenological models of the fragmentation process have been developed. Below, two important models, the independent fragmentation model and the LUND string fragmentation model, will be discussed in more detail. Both models have been implemented into the JETSET Monte Carlo generator [Sjö 94], which is used in the analysis presented in this thesis. The models contain parameters, which have to be adapted to the kinematical domain of the experiment. In a recursive tuning procedure, described in [Gei 98, Tal 98], these model parameters have been adjusted to reproduce measured particle multiplicities and event shapes optimally.

2.8.1 The Independent Fragmentation Model

The **I**ndependent **F**ragmentation (IF) model was invented already in 1978 by Field and Feynman [Fie 78]. This model is based on an hierarchical process, in which each parton fragments into a cascade, independent of other partons of the same generation in other branches of the cascades. In the fragmentation process, each parton picks up $q\overline{q}$ pairs from the vacuum, until a certain energy cut–off is reached. The primary quark q_0 in the cascade combines with the anti–quark $\overline{q}_1$ from the first generated $q\overline{q}$ pair to form a meson state with energy fraction z_0, while the remaining energy fraction $z_1 = 1 - z_0$ is assigned to the secondary quark q_1. This process is repeated until the energy fraction z_l of the left over quark falls below the fixed energy cut–off, when the last remaining quark is neglected. The produced mesons may be unstable and decay to long–lived particles after their formation.

The fragmentation process is controlled by few parameters. One of them controls the scaling function $f(z)$, which in turn gives the probability that the energy fraction z is left to the remaining cascade after a $q\overline{q}$ pair was produced. A second parameter γ gives the relative probabilities for the production of quark–anti-quark pairs of a certain flavour. Using isospin symmetry and neglecting heavier quarks, one obtains $\gamma \equiv \gamma_u = \gamma_d$ for the production of $u\overline{u}$ and $d\overline{d}$ pairs, leaving the probability $\gamma_s = 1 - 2\gamma$ for the production of an $s\overline{s}$ pair. From the measured multiplicity ratio of K/π [Arn 84], γ has been set to $\gamma = 0.435$, corresponding to $\gamma_s = 0.3\gamma$. A third parameter $\langle p_\perp^2 \rangle$ controls the width of the transverse momentum distribution of the produced $q\overline{q}$ pairs. In the IF model, this distribution is assumed Gaussian.

Despite some conceptual weaknesses, the independent fragmentation model describes many features of hadronisation remarkably well. Yet the model lacks Lorentz–invariance since the fragmentation process is explicitely carried out in the hadronic centre of mass frame. The transformation into a different reference frame does not conserve the relative momenta and hence the multiplicities of produced particles change. Furthermore, the colour and flavour quantum numbers are not conserved, because the last quarks below the energy cut–off are neglected.

2.8.2 The String Fragmentation Model

The LUND **S**tring **F**ragmentation (SF) model [And 83] shares some fundamental ideas with the IF model. However, it employs the concept of linear confinement, motivated by QCD. The main difference to the IF model is that the initial partons are not treated independently, but they are connected via the colour field stretching in between them. This colour field is assumed to possess a constant field energy density κ per unit length, leading to a linear rising potential $V(r) = \kappa r$ for two partons separated by a distance r.

As the struck parton moves apart from its partner, the energy stored in the colour *string* exceeds the mass of a $q\overline{q}$ pair. At this point the string breaks up and forms a $q\overline{q}$ pair, connecting now two strings to the initial pair of partons. These new substrings continue to break independently, until a string–connected quark–anti-quark pair is close to the mass shell of a colour singlet hadron. The LUND SF model has up to date proven to be a very successful model for the description of experimental data.

The SF model shares a number of parameters with the IF model. These control the probabilities for the production of different flavours (γ_u, γ_d, and γ_s), the width of the distribution of the transverse momenta, the ratio between quark and di–quark production, and the ratio between pseudo–scalar and scalar final state mesons. The latter have not been mentioned before, but are also present in the IF model. In the SF model, the string breaking is governed by a quantum mechanical tunnelling mechanism. The production probability of a $q\overline{q}$ pair in this tunnelling mechanism is controlled by two free parameters a and b, which have to be determined by tuning the model to experimental distributions.

As a main advantage over the IF model, the LUND string model conserves all quantum numbers and it is invariant under Lorentz transformations. It has been implemented in the JETSET Monte Carlo package [Sjö 94], which was widely used in this work (see Chapter 6). The default parameters of this model were optimised to describe the high energy data of collider experiments at LEP and HERA. For a satisfactory description of the hadron multiplicities measured at HERMES they had to be tuned, as described in [Gei 98, Tal 98].

3 The HERMES Experiment

During the winter break 1994/95 the HERMES experiment was set up and commissioned as the third experiment at the HERA positron–proton[i] collider ring at DESY, Hamburg. HERA provides two interaction areas where the positron and proton beams are brought into collision. Around the two interaction points the experiments H1 and ZEUS were built which investigate the internal structure of the proton in deep inelastic scattering processes at highest values of Q^2.

The HERMES experiment is located in the HERA East Hall and operates a gaseous fixed target internal to the beam line of the HERA positron machine. The main focus of the HERMES research program are the polarised structure functions of the nucleon and the decomposition of the contributions of the spins from the different quark flavours to the nucleon spin. HERMES does not use the HERA proton beam.

The fourth experiment HERA–B was set up in 1997 in the HERA West Hall and uses a fixed target in the HERA proton beam halo to study the *CP* violation in the B meson system. Fig. 4.1 shows a sketch of the HERA storage rings with the locations of the four experiments.

3.1 The Internal Gas Target

The HERMES experiment uses a gas target internal to the positron beam line. While internal gas targets are superior to external gaseous, liquid or solid targets with respect to the purity of the target material and the background from scattering events at the target material containment, they suffer from much a smaller area thickness compared to external targets. To enhance the target thickness without losing the advantages of an internal gas target, the novel technique of a storage cell is being used at HERMES. In the year 1995 the HERMES experiment was operated with a polarised ^{3}He target while a polarised hydrogen target was used in the years 1996 and 1997. Additionally, unpolarised target gases of any species, which are compatible with the HERA beam line vacuum requirements, can be used. In the following sections the storage cell and the sources for polarised ^{3}He and hydrogen will be explained in more detail. Table 3.1 shows the parameters of the two different target types used between 1995 and 1997.

Table 3.1: Parameters of the polarised ^{3}He and hydrogen targets used in the HERMES experiment until 1997. The numbers given are typical values for normal data taking.

	^{3}He target	H target	Unit
Years of operation	1995	1996, 1997	
Target thickness	1.0×10^{15}	$0.7 \ldots 1.0 \times 10^{14}$	nucleons/cm^2
Average nuclear polarisation $\|P_z\|$	0.46	0.78 ... 0.89	
Spin flip interval	600	60	s
Cell operating temperature	25	100	K

[i] Initially designed as an electron–proton collider, HERA for technical reasons has been operated with positrons instead, except for a period between March 1998 and May 1998.

3.1.1 The Storage Cell

The storage cell is an open–ended tube with an elliptical cross section of 29.0 mm width by 9.8 mm height and 400 mm in length. The positron beam is steered along the central axis of the tube. Figure 3.1 shows a sketch of the storage cell used with the polarised hydrogen target. The cell used for the ^{3}He target has a different feed tube geometry and no sampling tube. Not shown in Fig. 3.1 is an extension mounted at the downstream end of the cell. This ensures that scattered positrons always have to penetrate the same amount of material independent of the location of the scattering vertex within the storage cell. The cell extension has the same cross section and wall thickness as the storage cell itself and is equipped with apertures outside the acceptance of the spectrometer to pump out the gas atoms.

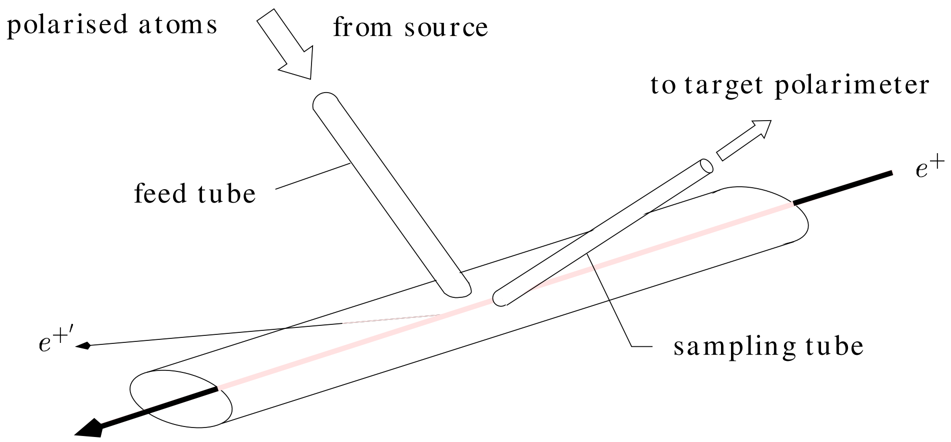

Figure 3.1: Schematic representation of the target storage cell used with the polarised hydrogen target. The polarised atoms from the source enter the cell through the feed tube. A small fraction of the injected gas atoms is extracted through the sampling tube and fed into the target polarimeter. Scattered positrons ($e^{+'}$) have to penetrate the cell wall which is made of 75 μm thick pure aluminium.

Polarised gas atoms from a source are injected into the storage cell through a feed tube which is installed perpendicular to the beam axis in the centre of the cell. The injected gas atoms perform wall collisions at thermal velocities and diffuse into the surrounding ultra high vacuum of the HERA positron machine through the open cell ends. During the diffusion process the target atoms cross the positron beam path many times and hence substantially increase the effective target thickness by approximately two orders of magnitude as compared to a free gas jet. The target gas atoms which have left the cell are pumped away by a powerful high speed differential pump system around the target area to ensure a marginal reduction of the live time of the stored positron beam due to the target gas in the beam path. This is necessary as the HERMES experiment has to be operated simultaneously with the two other HERA experiments which use the positron beam.

In order to further increase the target thickness, the thermal velocity of the target gas atoms is reduced by cryogenically cooling the storage cell. For the polarised ^{3}He target the cell was operated at a temperature of $\sim$25 K, while for the polarised hydrogen target a higher temperature of $\sim$100 K was chosen, in order to minimise depolarising effects during wall collisions. Because of the coupling of the spin of the single electron to the proton spin in hydrogen, polarised hydrogen is sensitive to flips of the electron spin. Wall collisions can flip the electron spin due to varying local magnetic fields the atom encounters while it is in close proximity to the wall surface. The electron spins in the ground state ^{3}He atom couple to spin zero and do not interact with the nuclear spin. Hence wall depolarisation is not a critical issue for the operation of the ^{3}He target.

In front of the storage cell and behind the cell extension so–called wake–field suppressors are installed which provide a smooth transition between the cross section of the HERA beam tube and the storage cell in the target chamber. The bunched positron beam in HERA induces mirror currents in the walls of the beam pipe which cause the emission of strong radio frequency (rf) fields at discontinuities in the impedance of the pipe. These rf fields can deposit a sizeable amount of energy in the target area, which both heats up the storage cell and the feedback with the positron beam itself destabilises the beam orbit. Thanks to the wake–field suppressors only a marginal load of rf fields is generated in the target area.

3.1.2 The Polarised ^{3}He Target

The polarised ^{3}He target [DeS 98] was used during the 1995 data taking period. A sample of ^{3}He gas atoms is polarised by resonant optical pumping on the transition $2^3\,S_1 \rightarrow 2^3\,P_0$. A small fraction of the gas atoms is brought into the long–lived metastable $2^3\,S_1$ state by a weak rf discharge within a pumping volume. Metastability exchange collisions with unpolarised ground state ^{3}He atoms transfer the electron spin from the polarised metastable atoms to the nuclear spin of the ground state atoms. The process of polarising ^{3}He by metastability–exchange optical pumping is described in detail in [Col 63].

Circularly polarised light with a wavelength of 1083 nm from a continuous Nd:LNA laser is incident on a pumping cell made of quartz and polarises the ^{3}He atoms by the process described above. Unpolarised ^{3}He atoms are fed into the pumping cell through a capillary tube. The polarised gas atoms can flow through a second capillary tube into the target storage cell. A homogeneous magnetic target holding field of 3.4 mT over the volume of the pumping and the storage cells, which was oriented parallel to the positron beam axis, provided the quantisation axis for the polarised atoms. Switching the helicity of the pump laser light from left–handed to right–handed (and vice versa) allowed for changing the sign of the ^{3}He atomic polarisation.

The degree of polarisation was measured with two independent optical target polarimeters inside the pumping cell and with lower statistical accuracy also inside the storage cell. The orientation of the polarisation axis was flipped every 10 minutes during data taking. The average polarisation over the 1995 data taking period inside the storage cell was 46% at a target areal density of 1.0×10^{15} nucleons/cm^2.

3.1.3 The Polarised Proton Target

During the data taking periods in the years 1996 and 1997 an **A**tomic **B**eam **S**ource (ABS) [Gol 96] was used as polarised proton target (see Fig. 3.2). Molecular hydrogen is dissociated by an rf discharge in a glass tube. A cooled nozzle at one end of this tube forms a beam of hydrogen atoms which passes through a skimmer and collimator into the first stage of a differential vacuum chamber system. A sixtupole magnet system focuses the atoms in the two states[ii] $|1> := |m_s, m_I> = |+\frac{1}{2}, +\frac{1}{2}>$ and $|2> := |+\frac{1}{2}, -\frac{1}{2}>$ with the same electron spin polarisation $m_s = +\frac{1}{2}$ on the beam axis into the entrance to the next vacuum chamber while defocusing the two other states $|3> := |-\frac{1}{2}, -\frac{1}{2}>$ and $|4> := |-\frac{1}{2}, +\frac{1}{2}>$ with opposite electron spin which are pumped away.

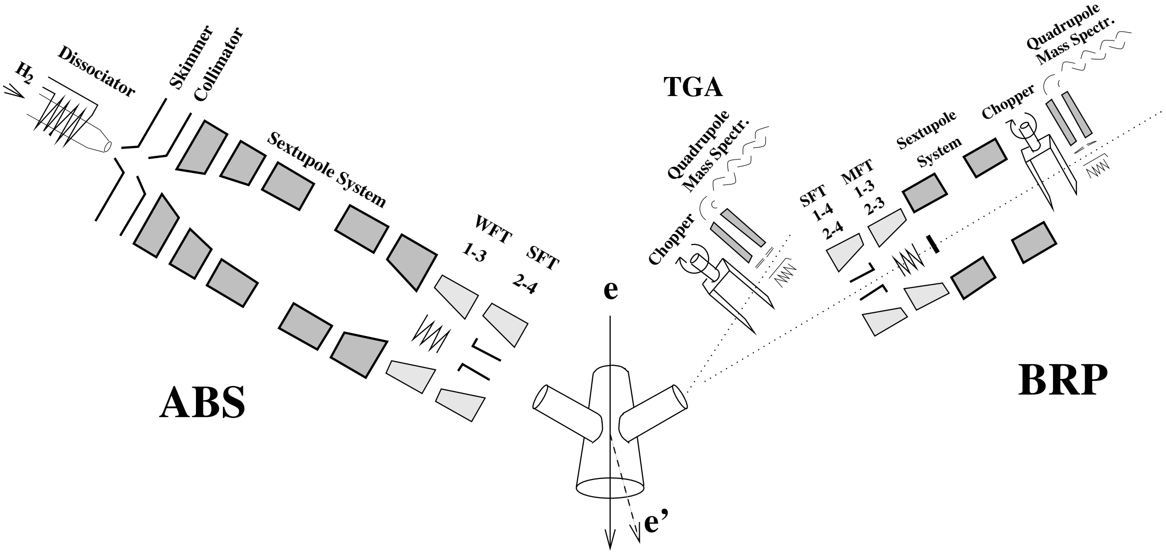

Figure 3.2: A schematical representation of the Atomic Beam Source (ABS) for polarised hydrogen with the Breit Rabi Polarimeter (BRP) and the Target Gas Analyser (TGA) [Bra 96b].

The electron spin polarisation of the atoms is transfered to the nuclear spin by radio frequency transitions ("Weak Field Transition", WFT, and "Strong Field Transition", SFT in Fig. 3.2) after the sixtupole magnet system. The rf transitions allow to interchange the occupation numbers of the hyperfine states $|1> \leftrightarrow |3>$ and $|2> \leftrightarrow |4>$, respectively, and hence populate states with nuclear spin polarisation $m_I = \pm\frac{1}{2}$. By activating either one of the rf transitions the orientation of the nuclear spin with respect to the magnetic target holding field can be reversed quickly. On average, the orientation of the target spin is reversed every 60 seconds to keep systematic influences on the asymmetry measurements from drifts at a minimum level.

To measure the nuclear and electron spin polarisation of the atoms in the storage cell a small fraction of the target atoms is extracted through the sampling tube and analysed in a **B**reit **R**abi **P**olarimeter (BRP) [Bra 96b]. Like the ABS, the BRP is consisting of rf transitions and a sixtupole magnet system which allows to isolate single hyperfine states entering a quadrupole mass spectrometer. From the measured relative occupation numbers of the hyperfine states of the target atoms their polarisation can be calculated.

[ii]At the pole tips of the sixtupole magnet system the magnetic field strength $B_{\max} = 1.5\mathrm{T}$ is much stronger than the critical magnetic field strength for hydrogen $B_c^{\mathrm{H}} = 50.7\mathrm{mT}$, so that the hydrogen atoms are described in a basis with decoupled electron and nuclear spins.

The **T**arget **G**as **A**nalyser (TGA) allows to measure the degree of dissociation of the hydrogen atoms in the storage cell as well as the composition of the residual gas in the target chamber. It is mounted under an angle of 7° with respect to the axis of the sampling tube in front of the entrance to the BRP.

Both the TGA and the BRP are sampling the target gas atoms in the centre of the storage cell. As the analysed atoms undergo a different number of wall collisions during their transport through the sampling tube compared to the atoms remaining in the storage cell, the values measured by the BRP and TGA have to be corrected to obtain the effective values for the target atoms. In Sect. 5.5 the calculation of the effective target polarisation including these corrections is detailed.

For the polarised hydrogen target, a superconducting magnet generates a holding field of $B = 335$ mT with an uniformity at the level of $\frac{\Delta B}{B} = \pm 1.5\%$ along the cell axis at the working point. At this rather high value of the magnetic field, the nuclear and electron spins of the hydrogen are almost completely decoupled and nuclear depolarisation due to wall collisions is reduced. The storage cell was additionally coated with Drifilm to further suppress wall depolarisation and recombination of the hydrogen atoms. The bunched HERA positron beam induces transient magnetic fields in the target region which can depolarise the target atoms by resonant interaction if harmonics from the spectrum of the transient field match the frequency of a transition between two hyperfine states of the hydrogen atom. Scans of the magnetic holding field have revealed such resonant interactions [Ack 99a] which result in a depolarisation of the target. The good homogeneity of the magnetic field ensures that the working point can be chosen between two resonances such that no beam induced resonant depolarisation occurs anywhere in the storage cell.

3.1.4 The Unpolarised Gas Feed System

In addition to the targets for polarised ^{3}He and hydrogen described in the previous sections, a gas feed system allows to inject various species of unpolarised gases into the storage cell. During the years 1995 to 1997 samples of $^1H_2$, $^2H_2$, ^{3}He and $^{14}N_2$ gases were used as unpolarised targets to perform measurements on the flavour asymmetry of the unpolarised light sea quark distribution in the nucleon [Ack 98b], on nuclear effects on the formation and decay of vector mesons [Ack 99b], on single spin azimuthal asymmetries in pion electroproduction [Air 00] and on nuclear effects on the cross section ratio $R = \sigma_L/\sigma_T$ [Ack 00].

3.2 The Spectrometer

The HERMES experiment uses an open forward magnetic spectrometer which consists of two identical halves [Ack 98a]. Figure 3.3 shows a 3–D model of the spectrometer as it has been in use during the 1995 data taking period. The two halves are symmetrical about a horizontal plane which is defined by the HERA storage ring. As the beam lines have to traverse the spectrometer magnet, they are guided in a massive shielding plate made from iron to shield them against the magnetic field of the magnet. To compensate for remaining field components from the spectrometer magnet, an additional correction coil has been installed around the positron beam line inside the shielding plate.

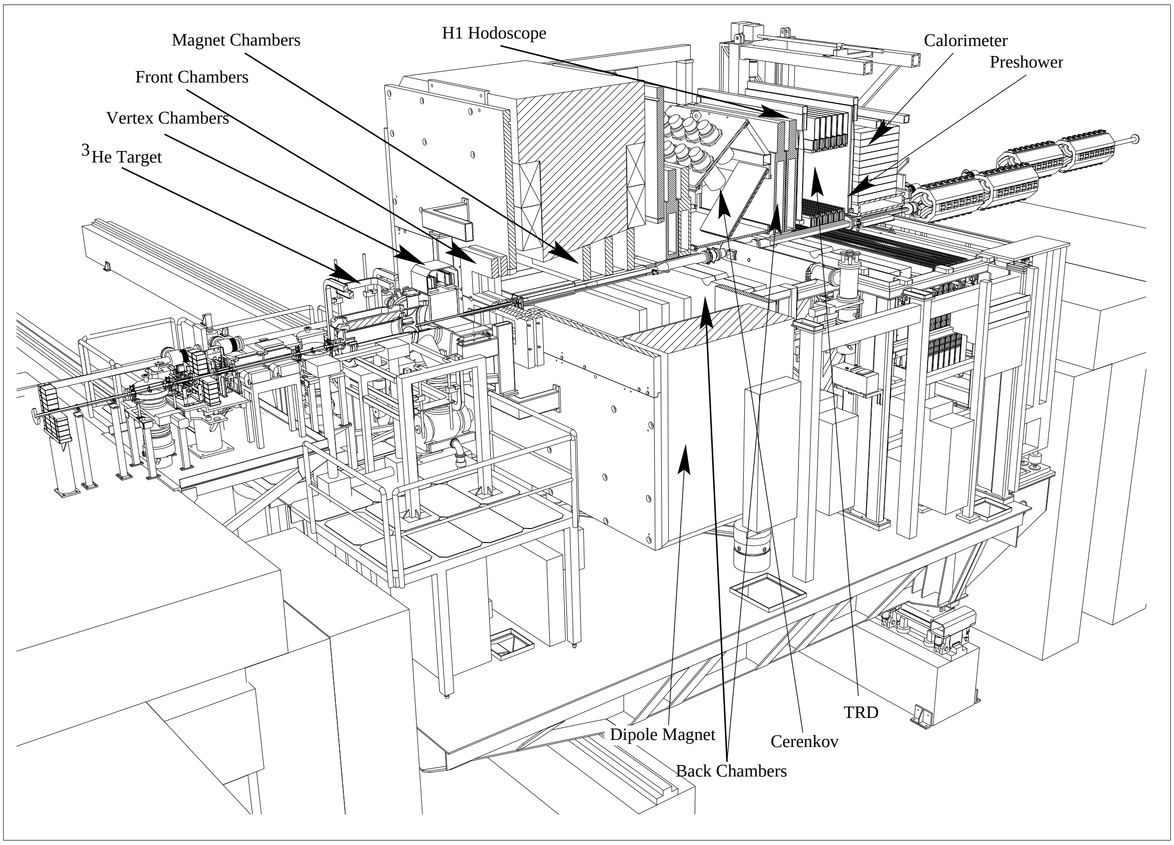

Figure 3.3: A three dimensional CAD drawing which represents the configuration of the HERMES spectrometer during the 1995 data taking period.

3.2.1 The Spectrometer Magnet

The spectrometer magnet is operated at a deflecting power of $\int B \, \mathrm{d}l = 1.3$ T m during data taking although it is capable of delivering up to 1.5 T m. The gap between the magnet's pole faces encloses the geometrical acceptance of the spectrometer to $\pm(40 \ldots 140)$ mrad in the vertical direction and to ±170 mrad in the horizontal direction. The lower limit on the vertical acceptance is given by the shielding plate in the horizontal symmetry plane of the spectrometer. The deflecting magnetic dipole field is oriented vertically and charged particles are only deflected horizontally during the passage through the magnetic field. Starting from the centre of the magnet, the horizontal acceptance is increased by ±50 mrad to maintain good acceptance for particles with low momenta. As the pole faces of the magnet are tilted matching the vertical acceptance, the field inside the magnet is inhomogeneous over the entire volume. Three dimensional model calculations of the magnetic field distribution have been verified by a Hall probe scan within an accuracy of 10^{-3} .

3.2.2 The Tracking System

The tracking system of the HERMES spectrometer consists of a total of five tracking chambers upstream, three chambers inside and four chambers downstream of the magnet. Their locations are shown in Fig. 3.4. All tracking chambers consist of several planes with three different wire orientations, adding up to a total number of 57 planes. The wires in one plane are oriented along the vertical axis, the wires in the two other planes are tilted by $+30°$ and $-30°$ with respect to the vertical axis. This arrangement allows the reconstruction of both horizontal and vertical tracking information without wires oriented in the horizontal plane. The lateral extension of the large back drift chambers, which are described below, precluded the use of horizontally strung wires. The identical arrangement of wire planes in each of the tracking detectors simplifies the reconstruction code significantly [Wan 96].

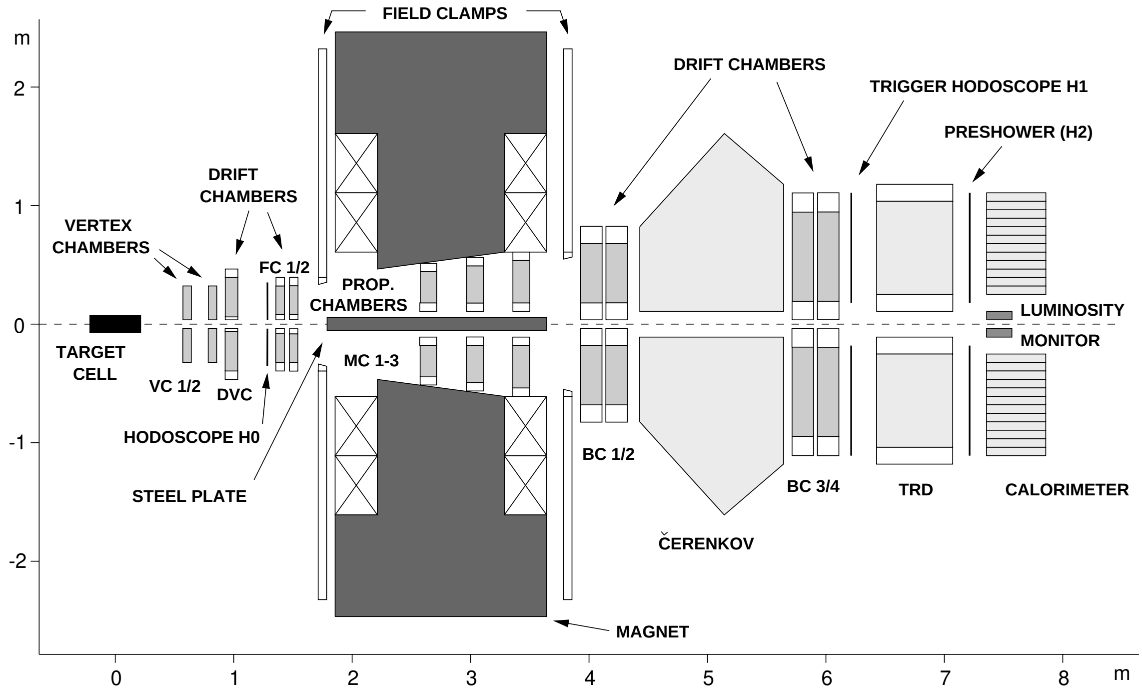

Figure 3.4: A two dimensional cut of the HERMES spectrometer in the configuration used during 1996 and 1997 data taking. The setup of two (upper and lower) identical detector halves is visible. The drift vertex chambers (DVC) and front hodoscope H0 are available since the 1996 data taking period. After the end of the 1997 data taking period the threshold Čerenkov counter shown in this picture was converted into a dual radiator Ring Imaging Čerenkov (RICH) counter. In addition an iron wall instrumented with tracking hodoscopes for muon identification was installed downstream of the calorimeter.

The first set of tracking chambers next to the target are the Vertex Chambers (VC) [Blo 99]. The VCs consist of two modules of micro strip gas chambers (MSGCs) with three planes each. In this type of chambers, thin metal strips on a carrier material with low conductivity form drift cells which are very small compared to conventional wire chambers. In the case of the HERMES chambers, the cells are 193 μm wide, and are formed by 7 μm wide anode and 85 μm wide potential strips on a 200 μm thick glass substrate. Due to the small pitch, the VCs count a large number of channels: 6014 and 6386 channels are available in the first and the second module, respectively. This large number of channels requires special readout electronics, which buffer the analogue signals for each wire from every positron bunch crossing in analogue pipelines. In the case a trigger was generated, these pipelines are then read out, pre–amplified, discriminated and finally sent to a front end receiver of the data acquisition system (DAQ). The readout electronics of the VCs is implemented in so–called Analogue Pipeline Chips (APCs). During the first year of data taking in 1995 an early batch of these chips, which did not work stably, prevented the successful use of the VCs for the event reconstruction. For the 1996 data taking period the chips in the upper half, and for the 1997 data taking all remaining chips were replaced by an improved version which turned out to fulfil the expectations. Since 1997 the VCs provided front tracking with efficiencies around 95% and a spatial resolution of $\sim$90 μm per plane.

Due to the initial problems with the operation of the VCs a second set of vertex chambers, the Drift Vertex Chambers (DVCs) were installed between the 1995 and 1996 data taking periods. The DVCs are located 1.1 m downstream of the target centre and consist of 6 planes of conventional drift chambers with a drift cell size of 6 mm. The DVCs provide a total number of 544 channels per detector half and achieve a resolution of 220 μm per plane.

The next set of chambers are the Front Chambers (FCs) which are installed right in front of the magnet field clamp, about 1.6 m downstream from the target centre. Like the DVCs they are drift chambers, arranged in two modules with six planes each. The drift cells are 7 mm wide and their resolution is 225 μm per plane.

Behind the magnet, four sets of drift chambers which are combined in two groups form the back tracking devices. Each of the so–called Back Chambers (BCs) [Ber 98] consists of six planes with a cell width of 15 mm and provides a resolution of 275 μm and 300 μm per plane for the first and second set, respectively.

To resolve ambiguities in the track matching between front and back tracks a set of proportional chambers, which are called Magnet Chambers (MCs), was installed inside the magnet between the pole faces. Due to the operation in the high field inside the magnet, these chambers have been realised as multi–wire proportional chambers (MWPCs) with a cell width of 2 mm. Each of the three MC modules consists of three planes which provide a resolution of 700 μm per plane. The large number of 5504 channels per detector half and the stringent space limitations inside the magnet also necessitated the use of a readout electronics system which reduces the amount of information sent to the DAQ at an early stage and is mounted on the chamber frames within the magnet. The MCs are particularly useful for the tracking of low energy particles (mainly pions), which are deflected so they leave the acceptance of the backward part of the spectrometer or even hit the magnet inner walls.

The tracking system has been simulated with the detailed HERMES Monte Carlo (HMC) program [HMC 96] which is based on the GEANT [CER 94] software package. The momentum resolution of the HERMES spectrometer is 0.7 – 1.25% over the measured kinematical range and the angular resolution is better than 0.6 mrad everywhere. Figure 3.5 shows the resolution in the corresponding kinematical variables x and Q^2 over the measured ranges as derived from HMC studies.

3.2.3 The Particle Identification Detectors

The HERMES detector was designed to provide a very clean separation of the scattered positron track from hadron tracks which mainly originate from photo production background. This is achieved by four different particle identification (PID) detectors, which

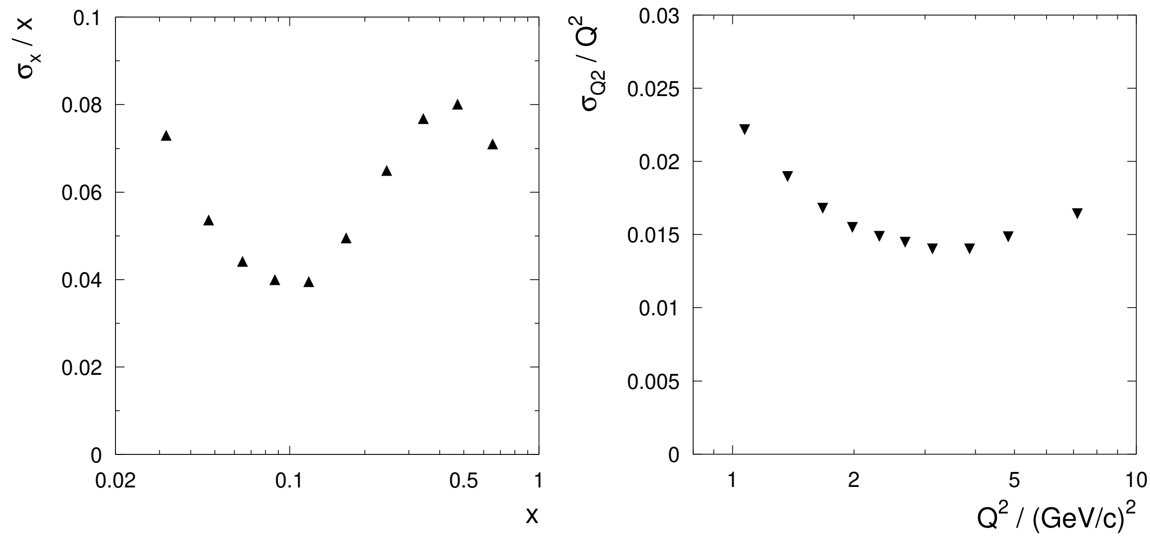

Figure 3.5: Resolution of the HERMES spectrometer in the kinematic variables Bjørken–x (left plot) and Q^2 (right plot), obtained from a Monte Carlo simulation of the detector [Gut 99a].

are described in detail in this subsection.

The electromagnetic calorimeter marks the downstream end of the spectrometer. It is used in the trigger for DIS events, to measure the total energy of scattered positrons and photons, and to suppress pions both online and offline. Each calorimeter half is built out of 420 blocks of radiation resistant F101 lead glass, arranged in a 42×10 array. The lead glass blocks have a depth of 50 cm, equivalent to about 18 radiation lengths, and are read out individually by 7.62 cm diameter photo multipliers. From test beam measurements of a smaller prototype of the calorimeter an energy linearity of 1% over the range 1 ... 30 GeV and an energy resolution of $\sigma(E)/E[\%] = (5.1\pm1.1)/\sqrt{E[\mathrm{GeV}]}\oplus(1.5\pm0.5)$ was determined [Ava 98], where $\oplus$ denotes the quadratic sum of the two terms.

In the lead glass blocks, positrons create an electromagnetic shower, which is almost fully contained. In contrast, pions and hadrons in general deposit only a fraction of their energy in the calorimeter blocks due to nuclear interaction and ionisation losses $\mathrm{d}E/\mathrm{d}x$. This allows a positron – pion separation on the ratio $E_{\mathrm{Calo}}/p_{\mathrm{rec}}$ of the energy deposited in the calorimeter over the reconstructed momentum. Figure 3.6(a) shows this ratio for positrons and hadrons which have been identified by a probability analysis based on the responses of all four PID detectors, insuring low contamination of the samples (see Sect. 5.2). The peak at $E_{\mathrm{Calo}}/p_{\mathrm{rec}} = 1.0$ is produced by positrons, the shaded distribution at lower values corresponds to hadrons. The tail to larger ratios is created by electromagnetic clusters originating from photons radiated off by the positron before or inside the magnet where their momentum is determined. For small bending angles of the positron track the electromagnetic clusters of the positron and the photon overlap, and hence their total energy is taken into account.

In front of the calorimeter the preshower hodoscope H2 is installed which consists of a wall of 42 vertically oriented plastic scintillator paddles behind a lead radiator of 11 mm thickness corresponding to 2 radiation lengths. Each scintillator paddle is read out

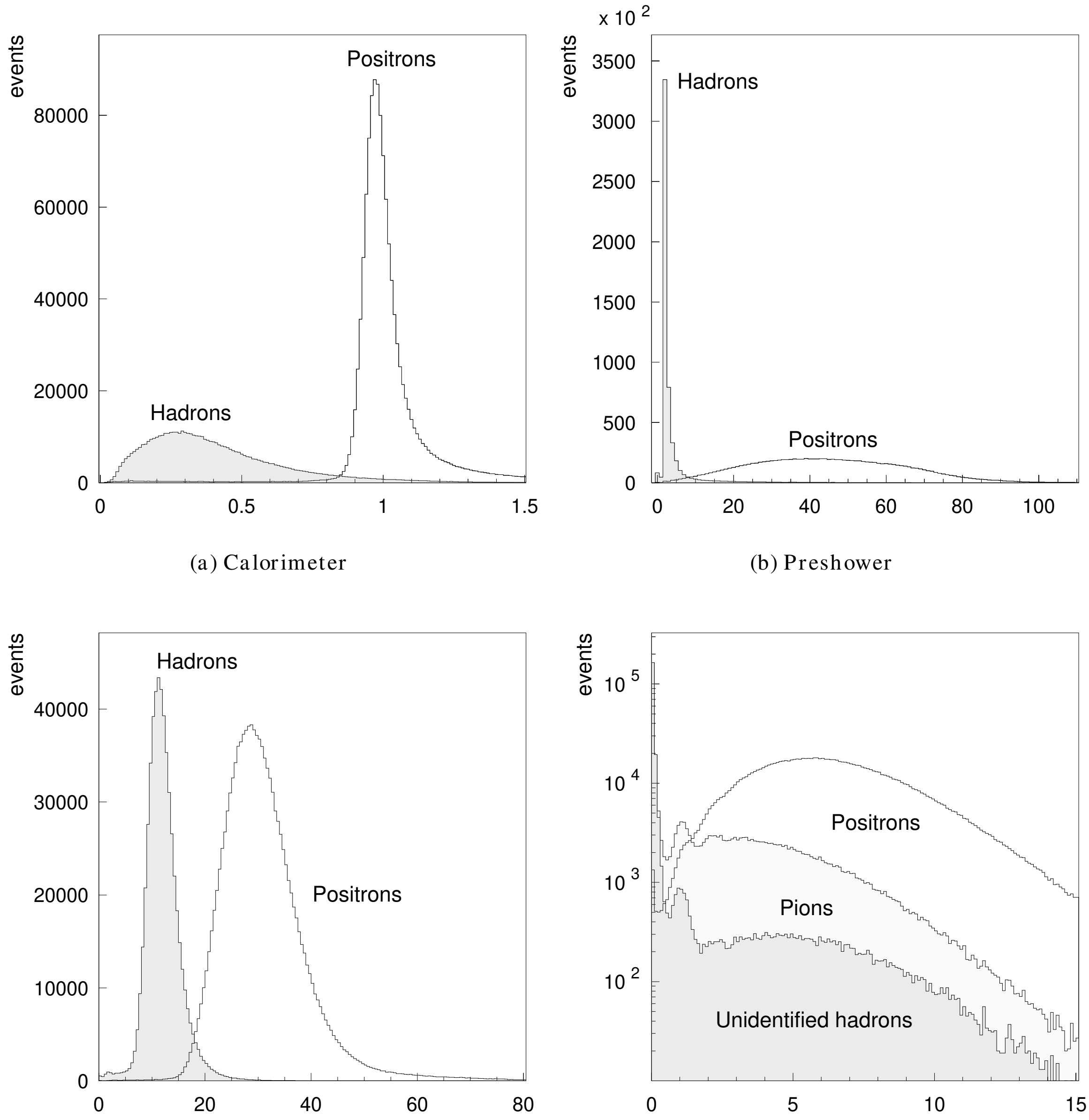

(a) Calorimeter (b) Preshower

(c) TRD (d) Čerenkov

Figure 3.6: The responses of the four different PID detectors for positrons (open distributions) and hadrons (shaded distribution). For the Čerenkov detector, also the response for pions is shown. The characteristics of the individual detector responses are described in the text.

by an individual photo multiplier tube and adjacent paddles are staggered with some overlap between two modules for maximum efficiency. While positrons create an electromagnetic shower in the radiator material and deposit up to 70 MeV energy, pions deposit only about 2 MeV in the radiator. Figure 3.6(b) shows the distributions of the deposited energy for positron and hadron samples in the preshower counter H2.

In front of the preshower hodoscope H2 the Transition Radiation Detector (TRD) is installed as the third PID detector. It also serves to separate pions from positrons.

Transition radiation (TR) occurs when charged particles with a large Lorentz factor γ cross the dielectric boundary between two media with different refractive indices n_i. The TR is mostly emitted in the forward direction in a narrow cone with an opening angle $\theta \propto 1/\gamma$. The energy spectrum of the TR possesses a soft cutoff $E \lesssim \gamma\omega_{\mathrm{p}}$, where ω_{p} denotes the plasma frequency of the medium [Dol 93]. As the intensity of the TR from a single dielectric boundary is very small, a TR detector employs many boundaries, sometimes realised as foil stacks. In the case of the HERMES TRD the radiator is made of polyethylene/polypropylene fibres arranged in plane to form a radiator module of 6.35 mm thickness.

The radiator module is followed by a large MWPC filled with a mixture of 90% Xe and 10% CH_4 gas. Due to its short absorption length for soft X–rays, Xenon is used as the major chamber gas component.

A charged particle traversing a TRD module, which consists of the radiator and the MWPC, deposits energy due to ionisation losses $\mathrm{d}E/\mathrm{d}x$ in the wire chamber. If the Lorentz factor γ of the charged particle is large enough to create a significant intensity of TR, this energy is additionally deposited in the MWPC. For the HERMES TRD the effective threshold for particles to generate a significant amount of TR relates to a Lorentz factor of $\gamma \simeq 500$ [Kai 97a]. This implies that at HERMES kinematics positrons are always above this threshold and generate TR while pions do not. Figure 3.6(c) shows the TRD signal for positrons and hadrons. Shown in this plot is the 'truncated mean' of the responses from the six TRD modules, i.e. the average signal calculated from five modules without taking the module with the largest response into account. This way the Landau tail in the detector responses, originating from δ–electrons, can be significantly reduced and the two particle classes become better separated.

The HERMES TRD consists of six identical modules as described above. The discrimination between positrons and pions is done on a probability based analysis of the signals from all six modules. While positrons on average deposit more energy than pions due to the TR component, the energy distribution is relatively broad and only the combination of multiple TRD modules allows to achieve a pion rejection factor (PRF)[iii] above 300 at a positron identification efficiency of 90% [Kai 97b].

The fourth PID detector at HERMES is a threshold Čerenkov counter which is located in between the drift chamber groups BC1/2 and BC3/4 in each spectrometer half. One module of the Čerenkov counter is equivalent to only 0.35% of a radiation length, so that the placement in between the two sets of drift chambers does not compromise the tracking resolution by multiple scattering. Each module consists of a gas radiator and a system of 20 spherical mirrors and 20 matching photo multiplier tubes mounted on the outside of the aluminium enclosure containing the gas and the mirrors. In 1995 the radiator was pure N_2 gas at atmospheric pressure while during 1996 and 1997 a mixture of 70% N_2 and 30% (by volume) C_4F_{10} was used. Charged particles traversing the radiator with a velocity v greater than the phase velocity of light c_{med} in the radiator emit Čerenkov light which is detected by the photo multiplier tubes. The threshold velocity for the emission of Čerenkov light is given by

$$v \geq c_{\mathrm{med}} = \frac{c_{\mathrm{vac}}}{n_{\mathrm{med}}}\,, \tag{3.1}$$

where c_{vac} is the speed of light in vacuum and n_{med} is the refractive index of the radiator

[iii]The PRF is the ratio of the total number of pions to the number of pions misidentified as positrons at a given positron identification efficiency.

material. The threshold momentum p_{thres} for the emission of Čerenkov radiation can be calculated from

$$p_{\text{thres}} = \beta_t \gamma_t \, m_0 \,, \qquad (3.2)$$

where

$$\beta_t \gamma_t = \sqrt{\frac{1}{n_{\text{med}}^2 - 1}} \,, \qquad (3.3)$$

and m_0 is the particle's rest mass. In Table 3.2 the threshold momenta for the emission of Čerenkov light for pions, kaons and protons are given.

For particle momenta below the threshold for pions the detection of Čerenkov light provides a clear positron identification. For momenta between the Čerenkov thresholds for pions and kaons, this detector is used to identify pions based on the additional hadron identification established by the three remaining PID detectors. In Fig. 3.6(d) the number $N_{\text{p.e.}}$ of generated photo electrons is shown for positrons and hadrons, integrated over all momenta. Hadrons within the momentum window between the thresholds for pions and kaons are identified as pions if at least one photo electron is registered in the Čerenkov detector.

After the running period 1997 the threshold Čerenkov detector was converted into a dual radiator **R**ing **I**maging **Č**erenkov (RICH) counter [Cis 97]. In the RICH detector, the Čerenkov light cones are projected by a mirror system onto a photon detector matrix with sufficiently fine granularity where they appear as rings. The diameter of these rings can be related to the opening angle of the Čerenkov light cone, which allows to determine the particle velocity $\beta = v/c_{\text{vac}}$. Together with the measured particle momentum this allows to identify pions, kaons and protons over almost the full momentum range of these hadrons in the HERMES kinematics.

Table 3.2: Parameters of the threshold Čerenkov detector for the different years of operation. The parameter p_{thres} gives the threshold momentum for the emission of Čerenkov light for the different types of charged particles. The values for p_{thres} were calculated from the refractive indices of the radiator gases [Kai 97a], [Asc 99] using Eqn. (3.2).

	1995	1996/1997
Radiator material	N_2	N_2 (70%) : C_4F_{10} (30%)
Refractive index n	1.000298	1.000629
$p_{\text{thres}}(e)$	20.9 MeV	14.4 MeV
$p_{\text{thres}}(\pi^{\pm})$	5.7 GeV	3.9 GeV
$p_{\text{thres}}(K^{\pm})$	20.2 GeV	13.9 GeV
$p_{\text{thres}}(\text{p})$	38.4 GeV	26.4 GeV

3.3 The Luminosity Monitor

The luminosity monitor serves to measure the luminosity $\mathcal{L}$, which for a fixed target experiment is defined as the product

$$\mathcal{L} = \Phi_{\text{beam}} \cdot N_{\text{targ}} \tag{3.4}$$

of the flux of beam particles Φ_{beam} times the number N_{targ} of target atoms within the cross section of the beam. The measurement of the luminosity employs the processes of elastic scattering $e^+e^- \rightarrow e^+e^-$ of the beam positrons off the shell electrons from the target gas atoms (Bhabha scattering) and pair annihilation $e^+e^- \rightarrow \gamma\gamma$ of beam positrons with the shell electrons of the target gas. The cross sections for both processes are well known and have been calculated in the framework of QED as contributions from weak currents can be neglected at the available centre of mass energy $\sqrt{s} = 168$ MeV. For the HERMES luminosity monitor the cross sections integrated over the acceptance of the device are 1.73 mbarn (Bhabha scattering) and 398 μbarn (pair annihilation), including radiative corrections up to the third order in the electromagnetic coupling constant α [Ben 98]. The integrated cross sections give the factor of proportionality, which relate the measured coincidence rates of the detected final state e^+e^- or $\gamma\gamma$–pairs to the luminosity $\mathcal{L}$.

The luminosity monitor comprises a pair of electromagnetic calorimeters which are mounted on both sides close to the positron beam pipe 7.2 m downstream of the storage cell (see Fig. 3.4). This position has been optimised to match the opening angle of 6.1 mrad in the laboratory system for a e^+e^- pair which is scattered symmetrically, corresponding to a scattering angle of 90° in their centre of mass system. The calorimeters consist of radiation hard Čerenkov active $NaBi(WO_4)_2$ (NBW) crystals arranged in a $3{\times}4$ matrix, resulting in a total size of 66×88 mm^2 for the front face of the calorimeter. Each crystal is read out by an individual photo multiplier tube.

To select Bhabha and photon pair events the trigger for the luminosity measurement requires two coincident signals in both calorimeters corresponding to an energy deposition above 4.5 GeV. Background events typically deposited only a significant amount of energy in one of the two calorimeter blocks. For typical running conditions in the year 1997 the coincidence rate during data taking with a polarised proton target normalised to the beam current was around 1 Hz/mA at a target areal density of $\sim 8 \times 10^{13}$ nucleons/cm^2.

3.4 The Trigger and the Data Acquisition System

The trigger system initiates the full readout of the detector information for an event which is considered to be of physical interest while disregarding background events as efficiently as possible. During the time needed for the readout of the detector, no new triggers can be accepted, leading to a *dead time* of the trigger system. The fractional dead time δ_{Dead} is defined as

$$\delta_{\text{Dead}} = 1 - \frac{N_{\text{accepted}}}{N_{\text{generated}}} = \frac{N_{\text{rejected}}}{N_{\text{generated}}}\,, \tag{3.5}$$

where N_{accepted} is the number of trigger requests, for which the detector could be read out, and $N_{\text{generated}}$ is the total number of readout requests. The difference between these two quantities gives the number N_{rejected} of trigger requests which had to be rejected.

At HERMES, a positron traversing one full detector half including detection in the calorimeter with an energy above a certain threshold is considered a candidate for a DIS event. The decision is based on the coincidence of signals from three fast scintillator detectors (the small hodoscope H0 located upstream of the front chamber FC1, the hodoscope H1 and the preshower detector H2, see Fig. 3.4) and the column–wise sum of calorimeter signals. Specifically, the coincidence of the following conditions to occur in the same half of the detector was required to trigger the acquisition of the detector information:

1. A signal in the hodoscopes H0, H1, and the preshower hodoscope H2 above noise level,
2. a cluster with an energy above 1.4 (3.5) GeV deposited in two adjacent columns of calorimeter blocks.

The energy threshold for the calorimeter was lowered to 1.4 GeV in the beginning of 1997 for data taking with the polarised proton target in order to accept also events from a kinematical region with low x and Q^2 values.

Once a trigger signal is generated, the analogue and timing information from all detector channels is digitised in ADC and TDC modules located in Fastbus crates. The information from the different Fastbus modules is collected by event builder modules and sent over a fast optical link to a cluster of DEC Alpha workstations where the raw detector data is buffered on an array of hard disks. During the breaks in between HERA fills the data on these disks are then replayed and stored permanently on tapes both locally in the experimental hall and in the computing centre on the DESY main site. The HERMES **D**ata **AQ**uisition system (DAQ) is capable of reading out the full detector information at rates up to 500 Hz with fractional dead times below 10%.

Besides the trigger for DIS events numerous other physics triggers (like photo production events, etc.) as well as more technical triggers for calibration issues are implemented at HERMES. The typical trigger rate for the DIS trigger normalised to the beam current is $\sim$2 Hz/mA for data taking with the polarised proton target in 1997.

3.5 Event Reconstruction and Data Handling

The raw detector hit and timing information stored on tape in the EPIO format has to be processed in several steps before the physical track parameters (like momentum, energy deposited in the calorimeter, etc.) and the likelihood information from the PID detectors is available for physics analyses.

The first part in the HERMES offline software chain is the decoder HDC. This program translates the raw data from the EPIO format to entries in an ADAMO [CER 93] data base, using mapping, geometry and calibration information from separate data bases.

The decoded raw detector information is next passed to the track reconstruction code HRC [Wan 96]. The algorithm tries to find partial straight tracks for the front and back detector region separately which are then combined to full tracks representing physical events. The reconstructed track information is again stored in entries to an ADAMO data base.

ADAMO is an entity–relationship data base which allows well structured and portable data storage. All data in the HERMES software chain with the exception of the raw detector information is stored in ADAMO tables. To overcome the limitation of the centralised data base model in ADAMO, the client–server extension DAD (**D**istributed **A**DAMO **D**ata base) [Wan 95] was developed at HERMES. It provides distributed data bases in the ADAMO format and is mainly used to store "slow control" data. The term slow control refers to all information, whose read out is **not** initiated by a physics trigger, like supply voltages, temperatures, pressures, e.g. Slow control data is read out on a time scale of typically one second and is stored directly in DAD tables, in contrast to the "fast" raw detector data.

The reconstructed track information from HRC is synchronised with slow control data and stored in so–called μDSTs[iv], which are then used for physics analysis. The μDSTs contain all physics information from the triggered events at a reduced file size compared to earlier stages in the production chain. This does not only save disk space but also shortens the running times of the analysis codes.

In order to further minimise the file size and analysis CPU time requirements, the μDSTs were filtered into an even smaller data set, called nano–DSTs (nDSTs). The size reduction was accomplished by applying loose cuts on the events, placing only those events into the nano–DSTs which contain at least one lepton candidate track. The major part of events in the μDSTs do not contain lepton tracks, which makes them *a priori* useless to any deep inelastic scattering analysis. The efficiency of this filtering is demonstrated best by comparing the total file size of 6.3 GB (8.7 GB) for the nano–DSTs to the total size of 19.0 GB (36.2 GB) for the μDSTs from the data productions for 1996 (1997) running used in the analysis presented in this thesis.

At HERMES, the data are grouped in three different levels, which allow the unique representation of a physical event. The lowest level is represented by an *event*, which contains all reconstructed tracks in the spectrometer, when a trigger was generated. Events are grouped in *bursts*, which correspond to about ten seconds of data taking. A burst also represents the time scale, on which slow control information is read out. As the top level of this scheme, bursts are grouped in *runs*, which correspond to about ten minutes of data taking. A new run is started automatically, whenever about 450 MB of raw EPIO data have been taken, or manually, at controlled changes of the experimental conditions, like the change of the target from polarised to unpolarised operation, for instance.

The HERMES software scheme is much more complex than outlined here and makes extensive use of the client–server concept, also for the online control of the experiment during data taking. A detailed description of the full software scheme, including the various data flows, can be found in [Fun 98].

[iv]DST is the short term for **D**ata **S**ummary **T**ape, a format introduced at CERN for the storage of event data.

4 Beam Polarisation and Polarimetry at HERA

The measurement of the spin–dependent structure function g_1 and of the spin–dependent quark polarisations Δq in deep inelastic scattering, as described in Chapter 2, requires both a polarised beam and a polarised target. The orientation of the beam spin has to be along the beam axis and the target spin needs to be aligned (anti–) parallel to this direction.

This chapter describes how the beam positrons become longitudinally polarised, the measurement of the degree of polarisation, and the experimental setup of one of the two HERA beam polarimeters, the Longitudinal Polarimeter.

4.1 How to Polarise Positrons

The HERA storage rings have a circumference of 6.3 km and provide an electron/positron beam with a momentum of 27.5 GeV/c and a proton beam with a momentum of 820 GeV/c [i].

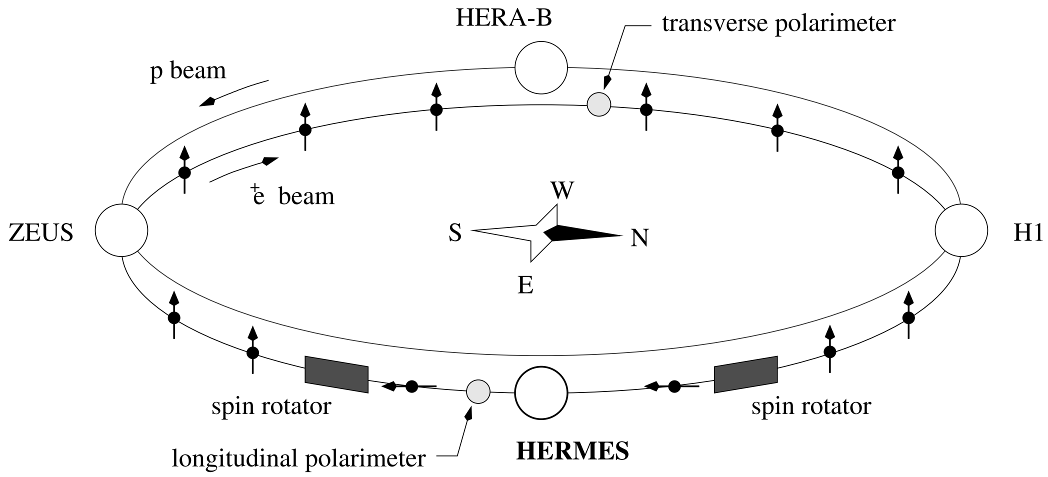

Figure 4.1: Sketch of the HERA positron and proton storage rings with the locations of the four experiments. A pair of spin rotators up– and downstream of the HERMES experiment is used to tilt the positron spin from its transverse orientation elsewhere in the ring to longitudinal and back. Also shown are the locations of the two polarimeters in HERA where the transverse and the longitudinal positron polarisation is measured.

In the vertical magnetic field of the dipole bending magnets in the curved sections of HERA, the spins of the positrons can only be aligned in the transverse direction (see Fig. 4.1). The positron beam is initially unpolarised after injection, i.e. the number of positrons with their spins aligned with the magnetic dipole field ($N^{\uparrow}$) equals the number of positrons aligned in the opposite direction ($N^{\downarrow}$); the polarisation P is defined as:

$$P = \frac{N^{\uparrow} - N^{\downarrow}}{N^{\uparrow} + N^{\downarrow}} \,. \tag{4.1}$$

[i] During the winter break 1997/98 the proton machine was upgraded and is capable of delivering a beam momentum of 920 GeV/c since.

Due to a small asymmetric component in the spin flip probability at the emission of synchrotron radiation photons in the curved sections of the storage ring, the initially unpolarised ensemble of positrons becomes polarised. This is known as the Sokolov–Ternov (ST) mechanism [Sok 64]. The polarisation in the ring increases with a time constant τ_{ST} according to

$$P(t) = P_{\mathrm{ST}} \cdot (1 - e^{-\frac{t}{\tau_{\mathrm{ST}}}}) \,, \tag{4.2}$$

where $P(t)$ is the polarisation at the time t with the assumption that $P(t = 0) = 0$. P_{ST} is the asymptotic maximum polarisation value, which for an ideal, flat machine is universal [Sok 64]:

$$P_{\mathrm{ST}} = \frac{8}{5\sqrt{3}} = 92.4\% \,. \tag{4.3}$$

A synchrotron is called “flat” when no vertically deflecting dipole magnets are present throughout the ring.

The value of τ_{ST} is dependent on machine parameters like the ring radius and the energy of the stored beam:

$$\tau_{\mathrm{ST}} = \left(\frac{5\sqrt{3}}{8} \frac{c \lambdabar_{\mathrm{c}} r_0 \gamma^5}{\rho_{\mathrm{eff}}^3} \right)^{-1} \,, \tag{4.4}$$

where ρ_{eff} is the effective radius of the storage ring, r_0 is the classical electron radius, $\lambdabar_{\mathrm{c}} = 1/m_e$ denotes the reduced positron Compton wavelength, and $\gamma = E/m_e$ is the positron Lorentz factor. At the HERA positron ring the average effective radius is $\rho_{\mathrm{eff}} = 707$ m [HER 93] and $\gamma = 53.9 \cdot 10^3$ for a typical positron energy of $E = 27.56$ GeV, resulting in a value of $\tau_{\mathrm{ST}} = 2194$ s $\simeq 36.5$ min for the build–up time constant.

In a real machine the polarisation mechanism is counteracted by depolarising effects which limit the achievable polarisation to values smaller than P_{ST}. The dominant contribution arises from non–vertical magnetic field components along the positron beam orbit. Due to small magnet misalignments and/or the positron beam running off the design orbit on the central axis in quadrupole magnets the magnetic field is not exactly vertical everywhere in the ring. In addition, the emission of synchrotron radiation excites oscillations of the positrons within one bunch around the design orbit and hence the positrons experience non–vertical magnetic fields. This stochastic motion of the particles leads to a diffusion of the spins within one bunch which ultimately causes depolarisation [Bar 93]. Furthermore, in a collider like HERA, the Coulomb interaction of the positron with the proton bunches may reduce the beam polarisation.

In the positron rest frame the classical spin vector precesses about the direction of the magnetic field vector as described by the Bargmann–Michel–Telegdi equation (see e.g. [Jac 83]). The number of rotations of the spin vector during one turn of the positron in the storage ring is called the spin tune ν and is given by

$$\nu = a\,\gamma = \frac{g-2}{2}\,\gamma \,, \tag{4.5}$$

where $a = 1.1597 \times 10^{-3}$ is the anomalous magnetic moment of the positron. The depolarising effects are strongest near spin orbit resonances when there is an integer relation between the spin tune ν and the beam orbital frequency:

$$\nu = m + m_x Q_x + m_y Q_y + m_s Q_s \,, \tag{4.6}$$

where $Q_{x(y)}$ and the fractional parts of the horizontal (vertical) betatron tunes, Q_s is the synchrotron tune of the machine, and the m_i are small integer numbers [Dür 95]. The nominal HERA positron beam energy is set to a value of $E = 27.56$ GeV, corresponding to a spin tune of $\nu = 62.5$, in order to avoid the depolarising resonances.

The strength of the depolarising effects can be summarised by a depolarising time constant $\tau_{\rm dep}$. In the presence of depolarising effects, the asymptotic maximum polarisation value $P_{\rm max}$ and the build–up time constant τ become modified:

$$P_{\rm max} = P_{\rm ST} \frac{\tau_{\rm dep}}{\tau_{\rm ST} + \tau_{\rm dep}} , \quad (4.7)$$

$$\tau = \tau_{\rm ST} \frac{\tau_{\rm dep}}{\tau_{\rm ST} + \tau_{\rm dep}} , \quad (4.8)$$

where $P_{\rm ST}$ and $\tau_{\rm ST}$ are defined in Eqns. (4.3) and (4.4). In general, depolarising effects lead to a shorter build–up time and a reduced maximum polarisation value.

Taking the ratio of Eqn. (4.8) over Eqn. (4.7) yields the expression

$$\tau = \frac{\tau_{\rm ST}}{P_{\rm ST}} \cdot P_{\rm max} , \quad (4.9)$$

which relates the rise time constant τ to the asymptotic polarisation value $P_{\rm max}$. As the quantities $\tau_{\rm ST}$ and $P_{\rm ST}$ are calculable, this relationship provides a way to determine $P_{\rm max}$. For this purpose, the beam polarisation is destroyed using resonant distortions of the beam orbit by dedicated kicker magnets, matching the condition in Eqn. (4.6). After switching off the distortions, the beam polarisation builds up again with time according to Eqn. (4.2) with $\tau_{\rm ST}$ replaced by τ. A fit of the function

$$P(t) = P_{\rm max} \cdot \left(1 - e^{-\frac{t-t_0}{\tau}}\right) \quad (4.10)$$

to the measured polarisation values with $P_{\rm max}, t_0$, and τ as free parameters allows to determine the polarisation scale $P_{\rm max}$ from the fitted rise time constant τ. Figure 4.2 shows a measurement of a rise time curve together with a fit of the above functional form.

It should be noted that Eqn. (4.7) is strictly valid for a flat machine only. A storage ring like HERA is not an ideal flat machine, in particular because of the spin rotators, which consist of alternating horizontally and vertically deflecting dipole magnets. For a non–flat machine Eqn. (4.7) has to be multiplied by an additional factor $(1+\delta)$ [Der 73]. The size of the correction term δ can be estimated from Monte Carlo simulations which track the beam particles through the magnetic field of the real machine setup for many turns. For HERA with the spin rotators switched on, this correction term is $\delta \lesssim 0.03$ whereas for a configuration with the spin rotators switched off $\delta \lll 1$ is negligible [Bar 97]. The uncertainty in δ is the limiting factor for the precision of a determination of the maximum polarisation $P_{\rm max}$ according to Eqn. (4.9) with a non–flat machine.

In [Bar 94] a method is described to reduce the influence of depolarising effects and hence increase the maximum achievable polarisation $P_{\rm max}$ by means of so–called *harmonic bumps*. This scheme introduces additional vertical closed orbit corrections at strategic locations to compensate for the effect of the spin–orbit distortions in the real, non–perfect machine [Dür 95]. At HERA, a total of eight *harmonic bumps* is available. Empiric optimisations of these helped to achieve up to 70% asymptotic positron polarisation values during the data taking periods 1995 to 1997.

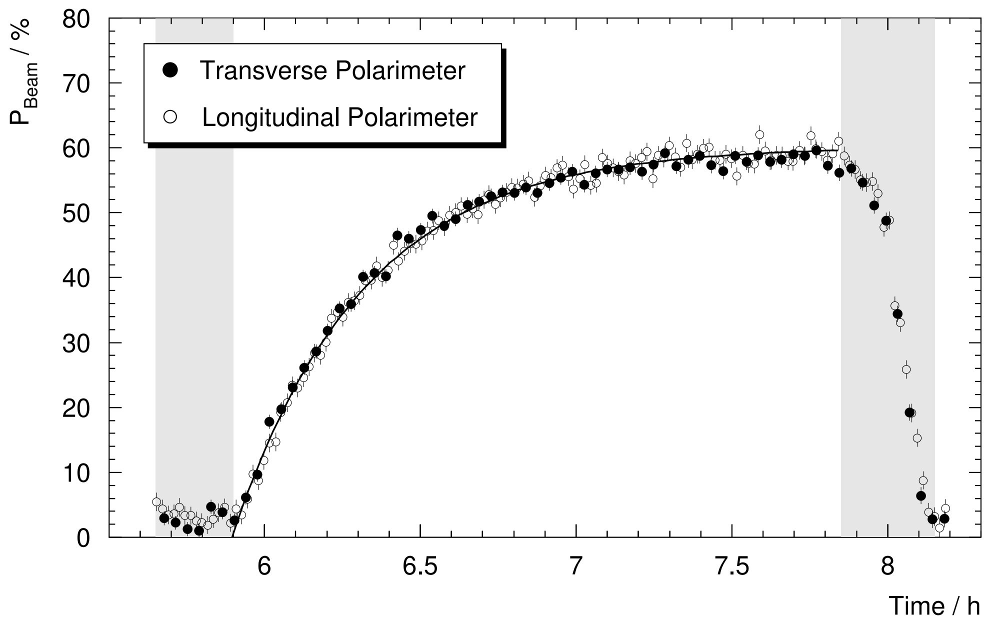

Figure 4.2: Rise time curve of the beam polarisation measured by the Transverse and Longitudinal Polarimeters. The shaded areas indicate the times when the beam polarisation was destroyed on purpose using resonant depolarisation. The asymptotic polarisation value derived from the shown fit of a functional form defined in Eqn. (4.10) is $P_{\max} = (60.2 \pm 0.3)\%$.

4.2 Polarised Compton Scattering

The differential cross section for Compton scattering of polarised photons off polarised positrons in the rest frame of the initial positron is given by:

$$\frac{\mathrm{d}\sigma_{\mathrm{c}}}{\mathrm{d}\Omega}(\vec{S},\vec{P}) \; = \; \Sigma_0 + \Sigma_1(S_1) + \Sigma_2(S_3,\vec{P}) \tag{4.11}$$

with

$$\begin{aligned}
\Sigma_0 &= \frac{r_0^2\,k_f^2}{2\,k_i^2}\left[(1+\cos^2\theta) + ƛ_{\mathrm{c}}\,(|\vec{k}_i| - |\vec{k}_f|)\,(1-\cos\theta)\right] \\
\Sigma_1(S_1) &= \frac{r_0^2\,k_f^2}{2\,k_i^2} S_1(\phi)\sin^2\theta \\
\Sigma_2(S_3,\vec{P}) &= -\frac{r_0^2\,k_f^2}{2\,k_i^2} S_3\,ƛ_{\mathrm{c}}\,(1-\cos\theta)\,(\vec{k}_i\cos\theta + \vec{k}_f)\cdot\vec{P}\,,
\end{aligned}$$

where r_0 is the classical electron radius, $\vec{S} = (S_0, S_1, S_2, S_3)$ is the Stokes vector describing the polarisation of the initial photon, and $\vec{P} = (P_x, P_y, P_z)$ is a Cartesian vector which holds the three components of the positron polarisation. The $\vec{k}_i$ and $\vec{k}_f$ are the wave number vectors of the initial and the scattered photon, respectively, and $ƛ_{\mathrm{c}} = \frac{1}{m_e} = 3.862 \cdot 10^{-13}$ m is the (reduced) Compton wavelength of the positron. The angle θ in Eqn. (4.11) is the scattering angle of the photons in the rest frame of the

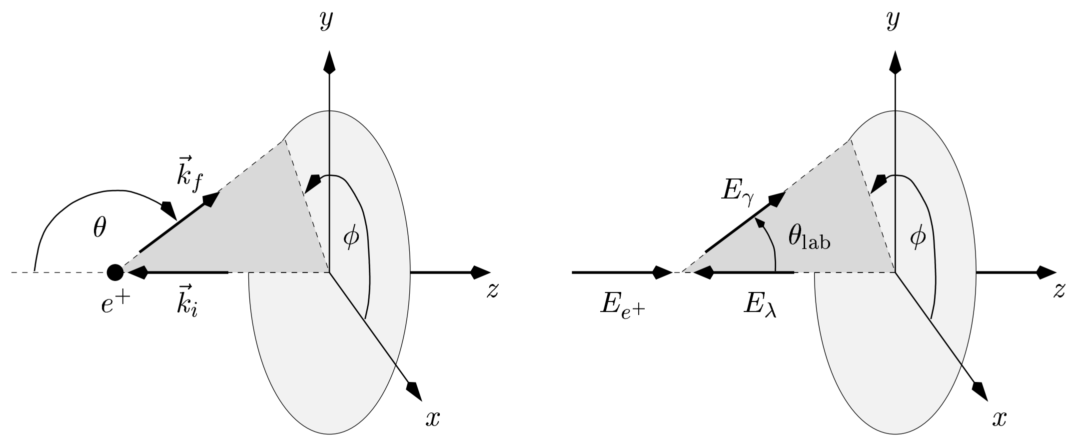

Figure 4.3: Orientation of the coordinate systems to describe the Compton scattering process in the positron rest frame (left) and in the laboratory (right). The final positron is not shown in these figures. For graphical reasons, a left–handed coordinate system has been chosen. The definitions of the scattering angle θ differ between the positron rest frame and the laboratory frame, in order to be consistent with the treatment in [Bar 93].

initial positron and ϕ is the azimuthal angle of the scattered photon with respect to the horizontal x axis (see Fig. 4.3).

The term Σ_0 in Eqn. (4.11) gives the cross section for unpolarised Compton scattering, which is independent of the azimuthal scattering angle ϕ, while the two other terms $\Sigma_1(S_1)$ and $\Sigma_2(S_3, \vec{P})$ are spin dependent contributions. The second term $\Sigma_1(S_1)$ depends on the linear light component of the incident photons and leads to a variation of the Compton cross section with the azimuthal scattering angle ϕ. The dependence of $S_1(\phi)$ on the angle ϕ arises from the fact that S_1 equals the projection of the linear light component $S_{\rm lin}$ along an axis (see Eqn. (B.2)), which is given here by the scattered positron. The third term Σ_2 depends both on the degree of circular polarisation S_3 of the incident photon and the positron polarisation vector $\vec{P}$.

For the special case that the transverse polarisation component of the positron sample is completely along the y axis ($P_x = 0$), the last term Σ_2 in Eqn. (4.11) can be split up in two parts, dependent on the transverse (P_y) and longitudinal (P_z) positron polarisation components, respectively:

$$\frac{{\rm d}\sigma_{\rm c}}{{\rm d}\Omega}(\vec{S}, \vec{P}) \;=\; \Sigma_0 + \Sigma_1(S_1) + \Sigma_{2,y}(S_3, P_y) + \Sigma_{2,z}(S_3, P_z) \tag{4.12}$$

with Σ_0 and $\Sigma_1(S_1)$ as defined in Eqn. (4.11) and

$$\Sigma_{2,y}(S_3, P_y) \;=\; -\frac{r_0^2\, k_f^2}{2\, k_i^2}\, S_3\, ƛ_{\rm c}\, (1 - \cos\theta)\, \sin\phi\, \sin\theta\, |\vec{k}_f| \cdot P_y\,, \tag{4.13}$$

$$\Sigma_{2,z}(S_3, P_z) \;=\; \frac{r_0^2\, k_f^2}{2\, k_i^2}\, S_3\, ƛ_{\rm c}\, (1 - \cos\theta)\, \cos\theta\, (|\vec{k}_i| + |\vec{k}_f|) \cdot P_z\,. \tag{4.14}$$

The measurement of the positron polarisation by Compton scattering employs the spin dependent contributions to the Compton cross section. In general, there is a dependence on the energy of the back scattered Compton photons, which is directly related to the polar scattering angle θ (see Eqn. (A.3) in App. A). For vertical positron polarisation ($P_y \neq 0$) the Compton cross section becomes also dependent on the azimuthal angle ϕ which leads to an asymmetric spatial distribution of the back scattered Compton photons when projected along the vertical y axis. In the case of only longitudinal positron polarisation components ($P_y = 0, P_z \neq 0$) the mean energy of the back scattered photons is shifted to higher or lower energies whereas the spectrum is isotropic in the angle ϕ, provided the linear light component is so small that $S_1 \ll 1$ and can be neglected.

4.3 The Transverse Polarimeter

The Transverse Polarimeter (TPOL) was installed in the HERA West Hall in 1992. The successful operation and the first observation of positron polarisation in an high–energy storage ring with activated spin rotators [Bar 94] by the Transverse Polarimeter were the prerequisites for the approval of the proposed HERMES experiment. The TPOL is described in full detail in [Bar 93].

At the location of the Transverse Polarimeter the spin of the positrons is oriented vertically, transverse to the beam direction ($P_z = 0$, cf. Fig. 4.1). The positron polarisation is determined from measuring a vertical spatial asymmetry of the back scattered Compton photons. An electromagnetic tungsten scintillator sandwich calorimeter which is separated into two halves along the plane of the positron beam allows to measure the energy and vertical position of high energy photons. Switching the helicity of the laser light an asymmetry

$$\Delta y(E_\gamma) = \frac{\langle y(E_\gamma)\rangle^- - \langle y(E_\gamma)\rangle^+}{2} = \Delta S_3 \cdot P_y \cdot \Pi_y(E_\gamma) \tag{4.15}$$

of the mean vertical positions $\langle y(E_\gamma)\rangle^\pm$ of the distributions of Compton photons can be observed. Here, $\Delta S_3 = (S_3^+ - S_3^-)/2$ is the mean magnitude of circular light polarisation, where the signs of S_3 are defined in Sect. B.2. The analysing power $\Pi_y(E_\gamma)$ in Eqn. (4.15) relating the measured spatial asymmetry $\Delta y(E_\gamma)$ to the positron polarisation P_y is derived from the ratio $\Sigma_{2,y}/\Sigma_0$ of the spin dependent over the unpolarised terms in the Compton cross section in Eqn. (4.12).

The absolute calibration of the Transverse Polarimeter is performed using measurements of the rise time of the beam polarisation as described in Sect. 4.1. The TPOL measures the positron polarisation every minute with an absolute statistical error of 1 – 2%, depending on the beam current. The fractional systematic error is dominated by the uncertainty from the rise time calibration and is $\delta P_{\mathrm{TPOL}}/P_{\mathrm{TPOL}} = 4.0\%$ for the year 1995 and 3.4% in 1996/1997.

4.4 The Longitudinal Polarimeter

The Longitudinal Polarimeter (LPOL) was installed in the East Right straight section of the HERA positron ring in 1995/1996. It measures the beam polarisation behind the HERMES interaction point, in between the two spin rotators, where the spin of the positrons is longitudinal (see Fig. 4.1). Like the TPOL, the LPOL employs polarised Compton scattering; also the setup, which is shown in Fig. 4.4, is similar to the TPOL.

Light pulses from a laser are circularly polarised with alternating helicity at each pulse and transmitted over a distance of about 80 m by a laser transport system (see

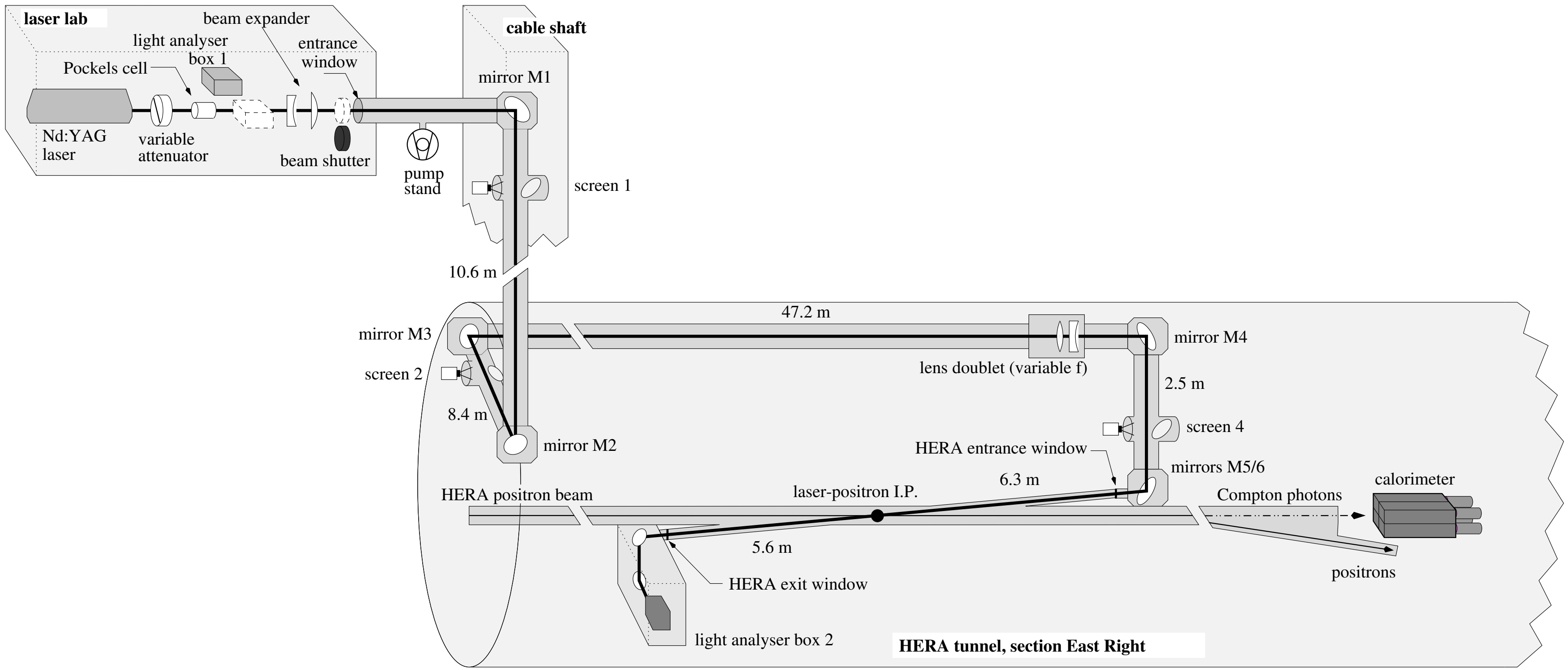

Figure 4.4: Sketch of the installation of the Longitudinal Polarimeter in the HERA East Hall (not to scale). The HERMES target and detector are upstream of the laser–positron interaction point (to the left) and not shown in this figure. Also not shown are screen 3, which is located between mirrors M3 and M4, and the dipole bending magnet (BH90), which separates the HERA positron beam from the Compton photons.

Sect. 4.4.2) to the interaction point (I.P.) with the HERA positron bunches in the HERA tunnel. The Compton scattered photons are travelling almost collinear with the positron bunches until the latter get separated after 38 m by a dipole bending magnet (BH 90), which deflects the positron beam orbit by 2.66 mrad. At a distance of 54 m downstream of the I.P. the Compton photons leave the HERA beam pipe and are detected in a calorimeter (see Sect. 4.4.3). A weak dipole magnet (BH 39) upstream of the I.P. bends the beam orbit by $\phi_{\text{orbit}} = 0.538$ mrad [Hol 00], causing a rotation of the positron spin by $\phi_{\text{spin}} = (\nu+1)\cdot\phi_{\text{orbit}} = 34.2$ mrad. This reduces the measured longitudinal polarisation at the I.P. negligibly by $1 - \cos\phi_{\text{spin}} = 0.06\%$.

In the following sections, the measurement principle, the setup of the laser optical system, the calorimeter, and the data processing scheme are explained in detail, concluding with a section on the performance of the LPOL.

4.4.1 The Measurement Principle of Longitudinal Polarisation

As already discussed earlier, for only longitudinal positron polarisation components ($P_x = P_y = 0, P_z \neq 0$) the term $\Sigma_{2,y}$ in Eqn. (4.12) vanishes and the Compton cross section becomes approximately independent of the azimuthal angle ϕ, provided the linear light component is small ($S_1 \ll 1$). Hence, switching the helicity of the laser light will modify the energy spectrum of the back scattered Compton photons but not their distribution in the angle ϕ. In Fig. A.1 the Compton cross section in dependence of the energy of the scattered photon in the laboratory frame is shown for the unpolarised case and for scattering fully circularly polarised light off fully polarised positrons.

At the location of the Longitudinal Polarimeter a high rate of bremsstrahlung photons from the HERMES gas target and of synchrotron photons from the bending dipole magnet upstream of the LPOL I.P. is incident on the calorimeter. In order to reduce their influence on the measurement, the Longitudinal Polarimeter is operated in the so–called "multi photon" mode where the instantaneous light intensity of pulses from a laser is so high, that during one laser–positron bunch interaction many photons are Compton scattered. This precludes the detection of individual scattered photons for the accumulation of an energy spectrum; in the absence of large backgrounds such a spectrum would allow the extraction of the beam polarisation using a fit of the theoretical shape as given in Eqn. (A.7) in the Appendix. Instead, in the regime of multi photon scattering the total energy ζ deposited in a sufficiently large calorimeter is measured. The energy ζ is the integral over the energy weighted cross section:

$$\zeta(S_3, P_z) := \int_{E_{\min}}^{E_{\max}} \left(\frac{\mathrm{d}\sigma_c(S_3, P_z)}{\mathrm{d}E_\gamma} \right) \cdot E_\gamma \ \mathrm{d}E_\gamma \, . \tag{4.16}$$

Note that the energy E_γ is related to the azimuthal scattering angle θ_{lab} (see Eqn. (A.3)), so that the above expression Eqn. (4.16) is implicitely integrated over the acceptance of the calorimeter. Hence, the lower integration limit $E_{\min}$ is given by the geometrical acceptance and the response function of the calorimeter while the upper integration limit $E_{\max}$ is the energy of the Compton edge. For the kinematics at the Longitudinal Polarimeter given in Appendix A, the Compton edge has an energy of $E_{\max} = 13.67$ GeV. In Fig. 4.5 the integrand of Eqn. (4.16) is shown for the cases $P_z = 0, \pm 1$.

The asymmetry $\mathcal{A}$ in the energy deposited in the calorimeter when scattering laser light with positive (S_3^+) and negative (S_3^-) helicity is proportional to the difference in

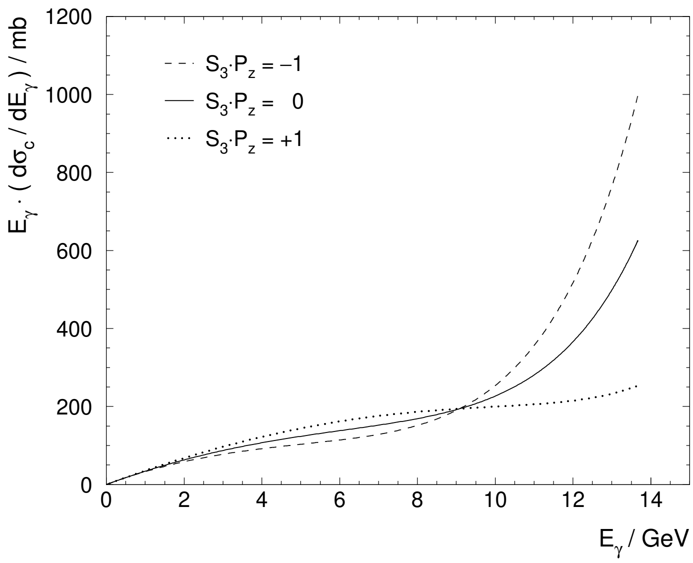

Figure 4.5: The energy weighted differential Compton cross section $E_\gamma \cdot \frac{d\sigma_c}{dE_\gamma}$ in dependence of the energy E_γ of the scattered photon in the laboratory frame. The full line corresponds to the unpolarised case, the dotted and the dashed lines give the cross sections for scattering fully circularly polarised laser light ($S_3 = \pm 1$) off longitudinally polarised positrons ($P_z = +1$).

the light helicity ΔS_3 and the longitudinal positron polarisation P_z:

$$\mathcal{A}(\Delta S_3, P_z) = \frac{\zeta(S_3^+, P_z) - \zeta(S_3^-, P_z)}{\zeta(S_3^+, P_z) + \zeta(S_3^-, P_z)} = \Delta S_3 \cdot P_z \cdot \Pi \,, \tag{4.17}$$

where

$$\Pi = \frac{\zeta(S_3 \cdot P_z = +1) - \zeta(S_3 \cdot P_z = -1)}{\zeta(S_3 \cdot P_z = +1) + \zeta(S_3 \cdot P_z = -1)} \,, \tag{4.18}$$

and ΔS_3 is defined as in the previous Sect. 4.3.

For small values of the lower energy cutoff of the calorimeter $E_{\text{min}} \lesssim 2$ GeV, the analysing power Π in Eqn. (4.18) is only weakly dependent on E_{min}. Assuming a perfectly linear calorimeter, the value is $\Pi = -0.1838$ for a cutoff energy $E_{\text{min}} = 0$ GeV and $\Pi = -0.1853$ for $E_{\text{min}} = 1$ GeV.

4.4.2 The Laser Optical System

In a laser optical laboratory with separate air conditioning and cleaning systems a frequency doubled Nd:YAG laser (Coherent, Infinity 40–100) generates light pulses of 3 ns duration with a wavelength of $\lambda = 532$ nm. The laser is triggered in synchronisation with the HERA positron bunches at a rate of ~ 97 Hz. In Fig. 4.6 the setup of the laser and optical components in the optical laboratory is shown.

After leaving the laser head, the beam is guided by a pair of mirrors through a rotatable half–wave plate and a Glan–Thompson prism. This combination serves as a

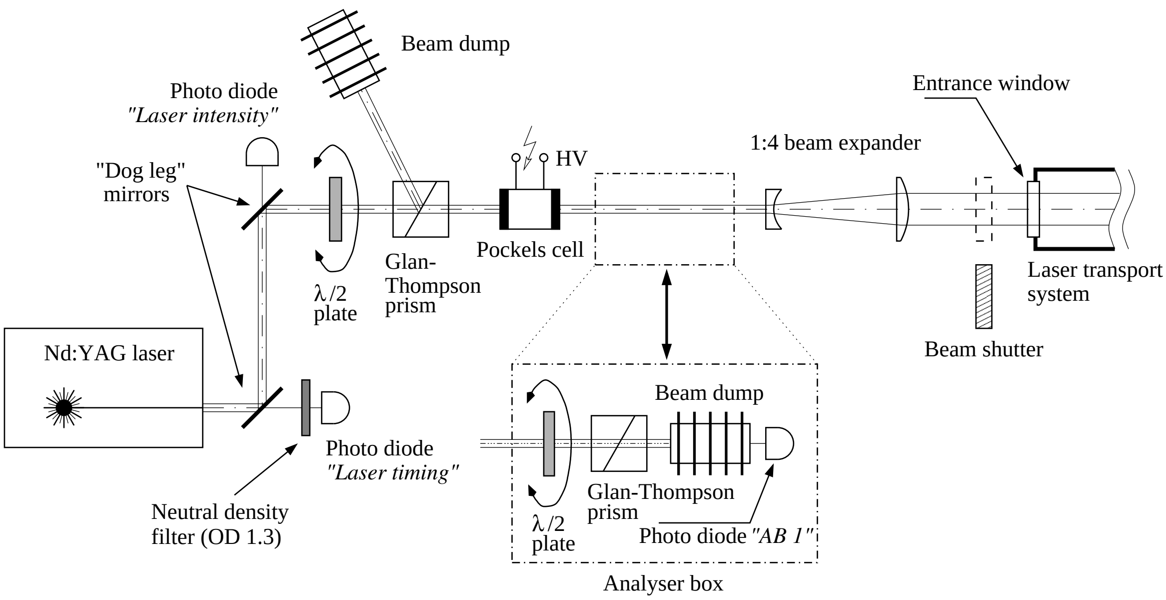

Figure 4.6: Setup of the optical system for the generation and analysis of polarised laser light at the Longitudinal Polarimeter. All elements are located within the enclosure of the laser lab and laser light can only emerge through the steel tube of the laser transport system.

variable attenuator for the laser light which is linear polarised. The half–wave plate rotates the plane of linear polarisation by the angle 2ϕ, where ϕ denotes the angle between the plane of polarisation and the fast axis of the half–wave plate. By turning the retardation plate the orientation of the plane of polarisation of the light incident on the Glan–Thompson prism can also be rotated. The Glan–Thompson prism acts as an analyser and transmits only the component with vertical linear polarisation while deflecting the light component with horizontal polarisation sideways into a beam dump which can withstand the high intensity of the laser pulses. The attenuator enables to run the laser at a constant intermediate energy setting where its pulse–to–pulse energy fluctuations are smallest while controlling the amount of light which is sent through the laser transport system to the interaction point. Additionally, the Glan–Thompson prism ensures a high degree of linear polarisation along a fixed axis which is required for efficient operation of the Pockels cell. Fast photo diodes behind the two so–called “dog leg” mirrors sample the transmitted fraction of laser light. One photo diode is read out by a TDC and monitors the exact timing of the laser pulse with respect to the HERA positron bunch pick–up signal. The second photo diode is connected to an ADC input and measures the intensity of each individual laser pulse. Both informations may be used to correct for fluctuations of the luminosity at the Compton I.P. in the analysis of the calorimeter signals.

The laser beam is circularly polarised using a Pockels cell. The Pockels cell can be regarded as a variable retardation plate where the phase difference between the light components along the two crystalline axes is proportional to the applied (high) voltage. When the voltage across the terminals of the Pockels cell generates a retardation of $\lambda/4$, linear polarised light with the plane of polarisation oriented at an angle of 45° to both crystalline axes becomes circularly polarised. By reversing the sign of the applied voltage the helicity of the circular polarised light is changed. Two high voltage supplies, which can be adjusted independently, provide voltages with positive and negative polarity. A fast high voltage switch which is flipped in between two laser pulses alternately selects one voltage supply so that the laser pulses in turn are left– and right–handed circularly polarised.

In order to measure the degree of polarisation of the laser light, a so–called "analyser box" can be moved into the beam path immediately behind the Pockels cell. The setup and measurement principle of this analyser box is explained in Appendix B. In [Bur 96] a detailed description of the design ideas and the setup of the analyser box can be found. Circular polarisation values of $|S_{\rm circ}| \geq 99.9\%$ for both helicities are obtained at this location.

Before entering the laser transport system, the polarised laser beam is expanded by a factor of four to a diameter of 22 mm[ii]. In front of the entrance window to the evacuated laser transport beam pipe an interlock controlled shutter is mounted. The interlock system is required to prevent light from the class IV laser system to leave the laser laboratory unless safe operating conditions are given.

The laser beam is then transported by means of six remotely controlled mirrors (M1 – M6) over a distance of 78 m to the I.P. with the HERA positron beam (see Fig. 4.4). A lens doublet with adjustable focal width is used to focus the laser beam on the interaction point. In order to preserve the circular polarisation of the light during the transport, special measures have been taken; the coatings of the used mirrors (CVI, Y2-4050-45UNP-37-SPECIAL) were optimised to provide the same reflectivity for s– and p–polarised light with the laser wavelength of $\lambda = 532$ nm incident under an angle of 45°. Furthermore, the mirrors are arranged in a phase compensating setup of three groups with two mirrors each. The reflecting surfaces of the two mirrors in a group are perpendicular to each other so that an s–wave on the first mirror becomes a p–wave on the second mirror and vice versa; this way remaining phase shifts between the two orientations cancel out after the reflection at the second mirror in a pair. Test measurements showed that the degree of circular polarisation is conserved to $(99.8 \pm 0.1)\%$ after the reflection at one pair of mirrors [Bec 97a].

The laser beam is entirely guided in a stainless steel tube which is evacuated to a pressure of 10^{-4} – 10^{-2} mbar. The vacuum avoids laser beam pointing instabilities from air convection flows in the long pipe and aids to keep the optical surfaces dust free. Furthermore, monitoring the pressure in the beam pipe provides a simple check of the integrity of the tubing in order to ensure laser safety.

In every straight section, in between two consecutive mirrors, *screens* are installed, which are also shown in Fig. 4.4. A screen consists of a metal plate with an engraved graticule, and is oriented under an angle of 45° with respect to the laser beam axis. The screen can be driven pneumatically into the nominal path of the laser beam and is monitored by a CCD camera, which is installed outside a vacuum viewport. When the screen is moved into the beam path, a spot becomes visible at the intersection of the metal plate with the laser beam. The screens are mounted not too far from the respective upstream mirrors and allow a coarse centering of the laser beam in the pipe when the beam is first steered through the system. After retracting the screen, images from CCD cameras, which are mounted behind each mirror and monitor the small fraction of transmitted light, allow a fine centering of the beam on the downstream mirror.

[ii] The laser beam does not have a Gaussian intensity profile but a so–called "flat top" profile with an almost constant intensity distribution over a large cross section. Within the quoted diameter 95% of the light intensity are contained [Coh 95].

This system provides an efficient way to feed the laser beam through the long pipe and monitor its position continuously, once the beam has been centered on all mirrors.

After the reflection at the last mirror pair M5/6 the laser beam enters the high vacuum of the HERA positron ring through a fused silica window. The laser beam crosses the positron beam orbit at an angle of 8.7 mrad. At the I.P. with the HERA positron beam the laser beam has a waist with a width of 0.5 – 1 mm. The laser light which is not scattered leaves the HERA beam pipe through a second fused silica window 5.6 m behind the I.P. and its polarisation and intensity are measured in a light analyser box whose setup is similar to the analyser box in the laser laboratory.

Behind the Compton I.P. circular polarisation values of $S_{\mathrm{circ}} = 99.4 - 99.9\%$ can be measured in the analyser box 2, as shown in Fig. B.2 in Appendix B.2. A test measurement confirmed that the polarisation measured in the analyser box does not deviate from the polarisation at the Compton I.P. within the statistical accuracy of the measurement. In this test, the section of the HERA beam pipe around the I.P. was vented to air and the exit window removed, so that there were no optical elements left between the I.P. and the analyser box. The light polarisation was continuously monitored during re–insertion of the exit window and tightening of the gaskets. It was demonstrated that the special gaskets used in this location allowed to achieve a vacuum tight connection without inducing birefringence in the windows due to mechanical stress, even after evacuation of the HERA beam pipe.

4.4.3 The LPOL Calorimeter

The calorimeter at the Longitudinal Polarimeter is very similar to the calorimeters used in the luminosity monitor (see Sect. 3.3). At the location of the calorimeter the positron beam and the centre of the cone of Compton photons nominally are separated by 42 mm, only. This neccesitated a very compact design of the calorimeter and a modification of the HERA positron beam line in order to move the calorimeter as close to the positron beam orbit as possible. The calorimeter consists of four Čerenkov active NBW crystals arranged in a 2×2 matrix. Each crystal is optically isolated from the neighbouring crystals and is $2.2 \times 2.2 \times 20$ cm^3 in size. The crystals are read out individually by photo multipliers (Hamamatsu, R4125Q) coupled by a small air gap to the end faces of each crystal. The individual readout of the four crystals allows for a determination of the centre of the electromagnetic shower induced by the incident Compton photons.

In front of the crystals 12 mm of lead, equivalent to about two radiation lengths, are mounted. The lead serves as preshower for the Compton photons and as shielding against synchrotron radiation. At this location a significant amount of synchrotron radiation photons with energies up to a few keV is incident on the calorimeter, which has to be shielded in order to prevent early radiation damage of the crystals. During the injection and dump procedures of the storage ring, the calorimeter is protected from excessive radiation doses by a shutter block made of Densimet[iii] [Pla 00], which can be driven pneumatically in front of the calorimeter box.

In the multi photon measurement mode (see Sect. 4.2) $10^3 - 10^4$ Compton photons with an average energy around 6.8 GeV hit the calorimeter in one pulse, creating an enormous amount of charged particles in the electromagnetic shower and hence a large number of Čerenkov photons emerging from the crystals. In order to attenuate their

[iii]Densimet is an high density alloy, which consists of more than 90% tungsten plus a balance of nickel and copper. This material has a density of 17.5 g cm^{-3} and a short radiation length.

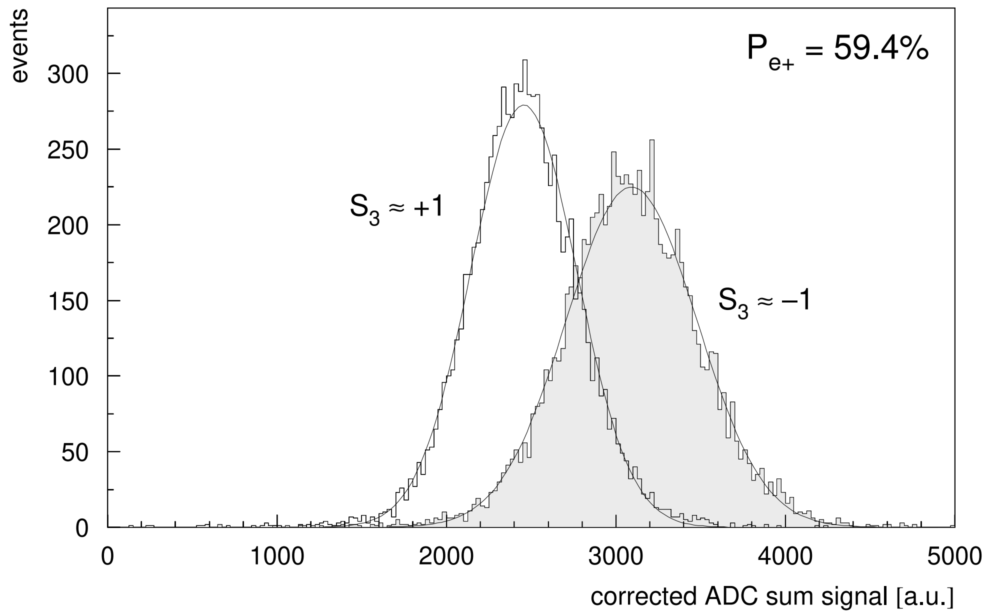

Figure 4.7: Spectra of ADC sum signals taken with the NBW calorimeter at the Longitudinal Polarimeter in the multi photon mode. The two different distributions correspond to Compton scattering of left– ($S_3 \approx -1$, shaded histogram) and right–handed ($S_3 \approx +1$, open histogram) laser light. The data have been corrected for pedestal shifts, the different currents in each bunch and jitter of the relative timing of the laser pulses with respect to the positron bunches [Men 99]. After corrections, the distributions of the sum signals for each helicity can be described well by a fit of a Gaussian distribution, which are also shown in the plot. The beam polarisation derived from this measurement was $P_{e+} = 59.4\%$.

intensity, a thin Nickel foil, which has a grid of tiny holes etched in it to transmit only a small fraction of the light, can be moved in between the crystals and the photo multipliers. During standard data taking this Nickel foil was always inserted. It was only removed for studies with reduced laser intensity to perform measurements in the so–called "single/few photon mode". In Fig. 4.7 spectra of the sum signal of all four photo multipliers, taken in the multi photon mode, are shown. This plot shows two distributions, which correspond to the scattering of laser with left– and right–handed helicity.

The crystals and photo multipliers are housed in a light tight box which is mounted on a remote controlled motorised table. In order to centre the Compton cone on the calorimeter, this table can be moved in the vertical direction. Due to the very close proximity of the calorimeter box to a thin walled section of the positron beam pipe, the horizontal centring of the Compton photons was not performed by moving the calorimeter but by steering the slope of the positron beam at the Compton I.P. using correction coils[iv].

[iv]In 1998 also a horizontal motion of the table was implemented which allowed to move the calorimeter away from the positron beam line. Furthermore the vertical range of travel was extended, so that the shutter in front of the calorimeter became obsolete and was removed. Since then the calorimeter is vertically

The resolution of the calorimeter can be parameterised by $\sigma(E)/E = P_1/\sqrt{E} \oplus P_2$ with $P_1 = (24.5 \pm 0.5)\%$ and $P_2 = (12.3 \pm 0.5)\%$ [Men 99] when the Nickel foil is not inserted between the crystals and the photo multipliers. Furthermore, the energy response of the calorimeter is not exactly linear. The deviation from linearity increases strongly when the Nickel foil is inserted in order to attenuate the Čerenkov light. The consequences of this non–linearity are discussed in Section 4.4.5 below.

4.4.4 Data Processing and Online Control

The Longitudinal Polarimeter is fully integrated into the HERMES DAQ in the sense that all signals are read out and processed in the same way as the responses from the individual detector components (see Sect. 3.4). This scheme has the drawback that the full detector information has to be read out for a measurement of the beam polarisation with the LPOL. In general, knowledge of the beam polarisation as an important and sensitive machine parameter is desired also during periods when no data taking with the HERMES spectrometer is possible, like immediately after injection of the beams or during dedicated periods for studies of the HERA accelerators. Hence, in 1998 the so–called "LPOL runs" were introduced into the HERMES DAQ where only the data from equipment relevant for the Longitudinal Polarimeter is read out and stored on tape.

Nearly all hardware of the Longitudinal Polarimeter can be controlled remotely using the graphical user interface COP (**CO**mpton **P**olarimeter Control) [Bra 96a]. Besides the fundamental control of all hardware (like mirrors, the laser, rotary stages, etc.) the program also provides a so–called "auto pilot" which automates the regular operation of the LPOL to a very high degree. The auto pilot deduces from HERA status messages and readings of the positron beam energy and current the state of the machine operation, which normally follows a cycle injection – tuning – luminosity run (normal data taking) – beam dump. The auto pilot accordingly switches the laser on or off, moves the calorimeter into the Compton cone or parking positions, sets triggers, performs optimisations of the Compton rate by steering the laser beam plus a few additional standard tasks.

The polarisation values are calculated online by a separate program which also provides a graphical history of the measured beam polarisation together with other important parameters for the operation of the LPOL, like beam positions and the relative luminosity at the Compton I.P. The measured polarisation values are stored using the DAD distributed data base model (see Sect. 3.5) which allows easy access by different groups like HERMES and the HERA operators.

4.4.5 Performance of the Longitudinal Polarimeter

The Longitudinal Polarimeter became operational in the beginning of the 1996 data taking period. Initially its availability was strongly limited by mirrors which did not meet their specifications for the laser damage threshold and by mechanical problems of the mounts for mirrors M3 and M4 under vacuum operation. After replacement of the mirrors with parts from a different manufacturer (CVI, Albuquerque) and exchange of the affected mirror boxes with the same model as for the mirrors M1 and M2 (OWIS, Staufen) the laser transport system worked without interruption since then, providing a stable laser beam with very high degrees of circular light polarisation at the I.P.

---

moved out of the plane of the positron machine in between fills for protection.

However, the values for the beam polarisation calculated from the measured energy asymmetry using Eqn. (4.17) were on average 25% above the values measured by the TPOL at the same time. For the calculation of the beam polarisation an analysing power of $\Pi = -0.1838$ was assumed, corresponding to a lower energy cut off of $E_{\text{min}} = 0$ GeV (see Eqn. (4.18)). Despite considerable efforts the explanation of this excess asymmetry was not found until the year 1999. Longitudinal leakage of charged particles from the electromagnetic shower in the NBW crystals into the photo multipliers seems to be the fundamental reason for a non–linear energy response of the calorimeter. This requires a modification of the integrand in Eqn. (4.16) and leads to a value for the analysing power which is significantly larger than the numbers calculated in Sect. 4.4.1 [Men 99].

Due to the remaining problem with the correct determination of the analysing power in the years 1996 to 1998, the LPOL was calibrated using the rise time method as described in Sect. 4.1. Detailed systematic studies [Bec 97b] performed during these years showed that, apart from the incorrectly determined value for the analysing power, the LPOL worked very stable and is insensitive against variations of the beam positions and the total energy deposited in the calorimeter. In Fig. 4.2 a measurement of the rise time of the beam polarisation taken by both polarimeters is shown. The polarisation values measured by the LPOL have been normalised to the measurement of the TPOL in this figure. Apart from the scale uncertainty of the LPOL, the measurements of the two polarimeters do not deviate systematically from each other. The absolute statistical error of the beam polarisation with the Longitudinal Polarimeter is $\sim$1% per minute measurement, the fractional systematical error in 1997 was $\delta P_{\text{LPOL}}/P_{\text{LPOL}} = 4.0\%$, mainly arising from the systematic uncertainty of the scale calibration of the Transverse Polarimeter.

5 Extraction of Semi Inclusive Asymmetries

5.1 Formation of the Asymmetries

The longitudinal double spin asymmetry $A_{\|}(x,Q^2)$ in the laboratory system is defined in Eqn. (2.27) as the difference of the cross sections for anti–parallel and parallel alignments of the beam and target spins, normalised to the sum of these two cross sections. The unpolarised cross section $\overline{\sigma} = (\sigma^{\rightleftarrows} + \sigma^{\rightrightarrows})/2$ equals the average of the polarised cross sections. Using this, the polarised cross sections can be rewritten as

$$\sigma^{\rightleftarrows\,(\rightrightarrows)}(x,Q^2) \;=\; \overline{\sigma}(x,Q^2)\left[1 \overset{+}{_{(-)}} A_{\|}(x,Q^2)\right] . \tag{5.1}$$

The measured experimental asymmetry $A_{\|}^{\mathrm{exp}}(x,Q^2)$ is proportional to the asymmetry $A_{\|}(x,Q^2)$:

$$A_{\|}^{\mathrm{exp}}(x,Q^2) \;=\; f \cdot P_{\mathrm{B}} \cdot P_{\mathrm{T}} \cdot A_{\|}(x,Q^2) , \tag{5.2}$$

where f is the target dilution factor and P_{B} and P_{T} denote the beam and target polarisations, respectively. The target dilution factor f represents the fraction of nucleons in the target which are polarised. For the polarised proton target at HERMES $f = 1$, which is unique compared to all other previous or existing experiments on polarised DIS. Other experiments (SMC [Ada 97], E143 [Abe 98], etc.) use polarised solid state targets with dilution factors $f \approx 0.04 - 0.2$, thereby reducing the size of their measured experimental asymmetries significantly. As the present analysis only deals with data taken on a polarised proton target, f is neglected from here on.

The total number of events measured per spin state, $N^{\rightleftarrows\,(\rightrightarrows)}(x,Q^2)$, is related to the unpolarised cross section $\overline{\sigma}(x,Q^2)$ and the asymmetry $A_{\|}(x,Q^2)$ by

$$\begin{aligned} N^{\rightleftarrows\,(\rightrightarrows)}(x,Q^2) \;&=\; \overline{\sigma}(x,Q^2)\int_{\rightleftarrows\,(\rightrightarrows)} \Gamma(t,x,Q^2)\cdot\mathcal{E}(t,x,Q^2)\cdot\mathcal{L}(t)\;\left[1 \overset{+}{_{(-)}} P_{\mathrm{B}}(t)\,P_{\mathrm{T}}(t)\,A_{\|}(x,Q^2)\right]\mathrm{d}t \\ &\simeq\; \overline{\sigma}(x,Q^2)\cdot\Gamma(x,Q^2)\cdot\mathcal{E}_{\mathrm{rec}}(x,Q^2)\int_{\rightleftarrows\,(\rightrightarrows)} \mathcal{E}_{\mathrm{DAQ}}(t)\,\mathcal{L}(t)\;\left[1 \overset{+}{_{(-)}} P_{\mathrm{B}}(t)\,P_{\mathrm{T}}(t)\,A_{\|}(x,Q^2)\right]\mathrm{d}t , \end{aligned} \tag{5.3}$$

where the integration is performed over time periods with anti–parallel (parallel) spin states. $\mathcal{L}$ denotes the luminosity delivered per spin state and the beam and target polarisations account for the dilution of the experimental asymmetry $A_{\|}^{\mathrm{exp}}$ as given in Eqn. (5.2).

$\Gamma(t,x,Q^2) \simeq \Gamma(x,Q^2)$ in Eqn. (5.3) represents the geometrical acceptance function, which is independent of the relative orientation of the beam and target spins. Furthermore, it is assumed to be nearly independent of the time t. This assumption is justified by the fact that the experimental setup is essentially left unchanged during one year of data taking. The quantity $\mathcal{E}(t,x,Q^2)$ in Eqn. (5.3) is the detection efficiency, which is the product of the reconstruction efficiency $\mathcal{E}_{\mathrm{rec}}(x,Q^2)$, which may vary over the geometrical acceptance of the spectrometer, and the trigger efficiency $\mathcal{E}_{\mathrm{DAQ}}(t)$ of the data acquisition system. The trigger efficiency $\mathcal{E}_{\mathrm{DAQ}}(t)$ may vary on the time scale of a burst and is related to the fractional dead time δ_{Dead}, defined in Eqn. (3.5), by $\mathcal{E}_{\mathrm{DAQ}}(t) = 1 - \delta_{\mathrm{Dead}}$. Time dependent variations of the reconstruction efficiency $\mathcal{E}_{\mathrm{rec}}$ are small and happen on a time scale which is much longer than the duration of one target spin cycle. In [Lac 98] the effect of these small variations on the extracted inclusive proton asymmetry was investigated and found to be negligible. The trigger efficiency $\mathcal{E}_{\mathrm{DAQ}}$ is totally uncorrelated to the kinematics of the scattering process and hence is independent of x and Q^2. Rewriting the integrals over the luminosity for a given burst i as

$$\ell_i^{\rightleftarrows(\rightrightarrows)} := \int\limits_{\rightleftarrows(\rightrightarrows)_i} \mathcal{E}_{\mathrm{DAQ}}(t)\,\mathcal{L}(t)\,\mathrm{d}t\,, \tag{5.4}$$

$$\ell_{p_i}^{\rightleftarrows(\rightrightarrows)} := \int\limits_{\rightleftarrows(\rightrightarrows)_i} \mathcal{E}_{\mathrm{DAQ}}(t)\,\mathcal{L}(t)\,P_{\mathrm{B}}(t)\,P_{\mathrm{T}}(t)\,\mathrm{d}t\,, \tag{5.5}$$

the number of events $n_i^{\rightleftarrows(\rightrightarrows)}(x,Q^2)$ in this burst can be expressed as

$$n_i^{\rightleftarrows(\rightrightarrows)}(x,Q^2) = \overline{\sigma}(x,Q^2)\,\Gamma(x,Q^2)\,\mathcal{E}_{\mathrm{rec}}(x,Q^2)\,\left(\ell_i^{\rightleftarrows(\rightrightarrows)} \underset{(-)}{+} \ell_{p_i}^{\rightleftarrows(\rightrightarrows)} A_{\parallel}(x,Q^2)\right)\,. \tag{5.6}$$

When summing over all bursts and using the following definitions

$$N^{\rightleftarrows(\rightrightarrows)} := \sum_i n_i^{\rightleftarrows(\rightrightarrows)}\,, \tag{5.7}$$

$$L^{\rightleftarrows(\rightrightarrows)} := \sum_i \ell_i^{\rightleftarrows(\rightrightarrows)}\,, \tag{5.8}$$

$$L_p^{\rightleftarrows(\rightrightarrows)} := \sum_i \ell_{p_i}^{\rightleftarrows(\rightrightarrows)}\,, \tag{5.9}$$

the time averaged asymmetry $A_{\parallel}$ can be related to the total event numbers $N^{\rightleftarrows(\rightrightarrows)}$ in each spin state by

$$A_{\parallel} = \frac{N^{\rightleftarrows}L^{\rightrightarrows} - N^{\rightrightarrows}L^{\rightleftarrows}}{N^{\rightleftarrows}L_p^{\rightrightarrows} + N^{\rightrightarrows}L_p^{\rightleftarrows}}\,, \tag{5.10}$$

where the unpolarised cross section $\overline{\sigma}(x,Q^2)$ and the efficiences $\Gamma(x,Q^2)$ and $\mathcal{E}_{\mathrm{rec}}(x,Q^2)$ cancel out. The explicit dependence of $A_{\parallel}$ and $N^{\rightleftarrows(\rightrightarrows)}$ on the kinematic quantities x and Q^2 has been omitted in these expressions.

The virtual photon asymmetry A_1 is then calculated according to Eqn. (2.37) as

$$A_1 = \frac{1}{(1+\eta\gamma)} \cdot \frac{N^{\rightleftarrows}L^{\rightrightarrows} - N^{\rightrightarrows}L^{\rightleftarrows}}{N^{\rightleftarrows}L_p^{\rightrightarrows}D^{\rightrightarrows} + N^{\rightrightarrows}L_p^{\rightleftarrows}D^{\rightleftarrows}}\,, \tag{5.11}$$

where the kinematic factors, η, γ, and D, are defined in Sect. 2.2 and 2.3. To account for slightly different values for the depolarisation factor D in the different spin states due to binning effects, D is evaluated for each target spin state.

The statistical uncertainty δA_1 on the asymmetry A_1 is obtained from the statistical uncertainties $\delta N = \sqrt{N}$ on the event numbers as

$$\begin{aligned} \delta A_1 &= \sqrt{\left(\frac{\partial A_1}{\partial N^{\rightrightarrows}}\,\delta N^{\rightrightarrows}\right)^2 + \left(\frac{\partial A_1}{\partial N^{\rightleftarrows}}\,\delta N^{\rightleftarrows}\right)^2} \\ &= \frac{1}{(1+\eta\gamma)} \cdot \frac{L^{\rightleftarrows}L_p^{\rightrightarrows}D^{\rightrightarrows} + L^{\rightrightarrows}L_p^{\rightleftarrows}D^{\rightleftarrows}}{\left(N^{\rightleftarrows}L_p^{\rightrightarrows}D^{\rightrightarrows} + N^{\rightrightarrows}L_p^{\rightleftarrows}D^{\rightleftarrows}\right)^2}\,\sqrt{\left(N^{\rightrightarrows}\right)^2 N^{\rightleftarrows} + \left(N^{\rightleftarrows}\right)^2 N^{\rightrightarrows}}\,. \end{aligned} \tag{5.12}$$

This expression is valid under the assumption of a Poisson distribution for the number of scattering events and for experimental asymmetries which are not too close to one.

The semi inclusive asymmetries A_1^h are extracted in complete analogy to the procedure for the inclusive asymmetry A_1. In case of the semi inclusive asymmetries, the event numbers in the above expressions have to be substituted by $N_h^{\rightleftarrows(\rightrightarrows)}$, which denote the number of events with a hadron of type h in coincidence with the positron. More specifically, if more than one hadron passes the selection cuts explained in Sect. 5.4.2, the event is counted multiply, once for each hadron passing the cuts.

Table 5.1: Definition of the binning in x. The first column gives the ordinal number of each bin, with the limits defined in the second column. In the third column the mean value $\langle x\rangle$ for the inclusive proton asymmetry $A_{1,\mathrm{p}}$ is given.

Bin number	Range in x	$\langle x\rangle$
1	0.023 ... 0.040	0.033
2	0.040 ... 0.055	0.047
3	0.055 ... 0.075	0.065
4	0.075 ... 0.100	0.087
5	0.100 ... 0.140	0.119
6	0.140 ... 0.200	0.168
7	0.200 ... 0.300	0.245
8	0.300 ... 0.400	0.342
9	0.400 ... 0.600	0.466

In this analysis the events are extracted as a function of x. The binning in x consists of nine bins with the limits given in Tab. 5.1. The binning was chosen to approximately yield the same number of events in each bin. Within one bin, the asymmetries are evaluated at the mean value of x, and integrated over the range in Q^2 (and in z, in case of the semi inclusive asymmetries) of all events in this bin. The mean values of x in each bin for the inclusive proton asymmetry are also given in Tab. 5.1. In Appendix D the mean values of x, Q^2, and z in every bin are tabulated for the inclusive and semi inclusive hadron asymmetries.

5.2 Particle Identification

The particle identification (PID) is based on the combined responses of all four PID detectors (see Sect. 3.2.3) to achieve minimum contamination at high detection efficiencies. The individual detector responses are converted into *conditional probabilities* $\mathcal{L}_D^i(\xi)$, which yield the probability that a given particle of type i generates a response ξ in the detector D. In order to derive the probability distributions $\mathcal{L}_D^i(\xi)$ for one detector D, clean samples of particle type i are selected from the data by very restrictive cuts on the responses of the three remaining PID detectors. Particle identification by these "hard" cuts on the individual detector signals has the disadvantage of low detection efficiencies. Hence this procedure is only applied for the determination of the conditional probabilities in a first step.

The relevant quantity for the particle identification is the probability $\mathcal{P}_D^i(\xi)$ that a given signal ξ in the detector D was caused by a particle of type i. This probability is related to the conditional probabilities $\mathcal{L}^i_D(\xi)$ by the incident particle fluxes Φ^i:

$$\mathcal{P}^i_D(\xi) \;=\; \frac{\Phi^i \mathcal{L}^i_D(\xi)}{\sum_j \Phi^j \mathcal{L}^j_D(\xi)}\,, \tag{5.13}$$

where the index j loops over all particle types to be distinguished.

In order to separate leptons (ℓ) from hadrons (h), for each detector D the quantity PID_D is defined as:

$$\mathrm{PID}_D \;:=\; \log_{10} \frac{\mathcal{L}^\ell_D}{\mathcal{L}^h_D}\,. \tag{5.14}$$

At HERMES, the responses of the three PID detectors Čerenkov counter, preshower detector and calorimeter are combined into the quantity "PID_3":

$$\mathrm{PID}_3 \;:=\; \log_{10} \frac{\mathcal{L}^\ell_{\mathrm{Cer}}\,\mathcal{L}^\ell_{\mathrm{Pre}}\,\mathcal{L}^\ell_{\mathrm{Cal}}}{\mathcal{L}^h_{\mathrm{Cer}}\,\mathcal{L}^h_{\mathrm{Pre}}\,\mathcal{L}^h_{\mathrm{Cal}}}\,. \tag{5.15}$$

In the analysis of the 1996/1997 proton data the quantity "PID_5" is formed from the individual responses of the six TRD modules:

$$\mathrm{PID}_5 \;:=\; \log_{10} \frac{\prod_{m=1}^{6} \mathcal{L}^\ell_{\mathrm{TRD}_m}}{\prod_{m=1}^{6} \mathcal{L}^h_{\mathrm{TRD}_m}}\,. \tag{5.16}$$

The likelihood information from all four PID detectors is combined into the quantity PID, which is defined as:

$$\mathrm{PID} \;:=\; \mathrm{PID}_3 + \mathrm{PID}_5 - \log_{10}\Phi \;=\; \log_{10}\frac{\mathcal{P}^\ell}{\mathcal{P}^h}\,, \tag{5.17}$$

where $\Phi := \Phi^h/\Phi^\ell$ is the (hadron) flux factor. The particle fluxes $\Phi^i = \Phi^i(p,\theta)$ are dependent on the momentum p and scattering angle θ of the particle. Due to the dominance of positrons over electrons in the data, the flux factors are quite different for the two charges. Over the kinematical range of the DIS event sample they cover a range of $\log_{10}\Phi_- = -0.8\ldots+2.2$ and $\log_{10}\Phi_+ = -2.4\ldots+1.7$ [Gär 00] for negative and positive particles, respectively. By the inclusion of the flux factor in the above definition, the quantity PID can directly be interpreted as the logarithm of the probability ratio that a given particle is a lepton or a hadron.

In this analysis, the particle identification into leptons and hadrons is based on the following conditions:

$$\mathrm{PID}_3 + \mathrm{PID}_5 - \log_{10}\Phi > 2 \quad \Leftrightarrow \quad \text{lepton}, \tag{5.18}$$

$$\mathrm{PID}_3 + \mathrm{PID}_5 - \log_{10}\Phi < 0 \quad \Leftrightarrow \quad \text{hadron}. \tag{5.19}$$

In addition, identified hadrons with a momentum above the Čerenkov threshold for pions and below the threshold for kaons (see Tab. 3.2) were identified as pions if a signal of $N_{\mathrm{p.e.}} \geq 0.5$ generated photo electrons was registered in the Čerenkov counter.

In Fig. 5.1 the one dimensional distribution of the quantity PID used in the particle identification is shown. The cut efficiencies and the contaminations of the lepton sample by misidentified hadrons and vice versa was determined by fitting the sum of two Gaussian distributions to the tails of the lepton and hadron distributions in the region around the valley in between them. For the cuts given in Eqns. (5.18) and (5.19) the lepton identification efficiency is 0.97 with a hadron contamination of 1.1×10^{-4} averaged over the kinematical range; for positive hadrons the averaged efficiency is 0.99 with a positron contamination of 5.7×10^{-3} [Gär 00].

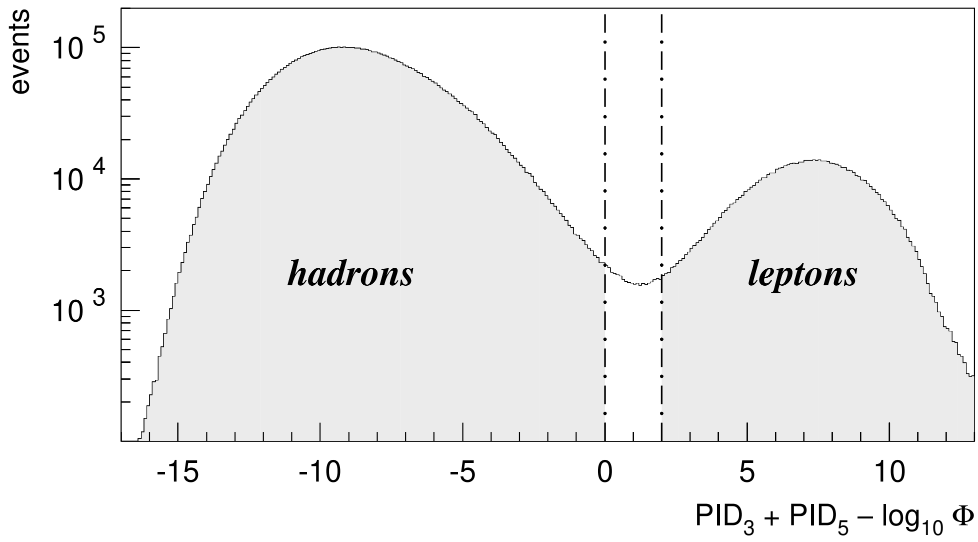

Figure 5.1: One dimensional distribution of the combined information from all PID detectors. The dotted–dashed vertical lines correspond to the cuts used for the identification of leptons (right line) and hadrons (left line).

5.3 Alignment Corrections

For the reconstruction of the particle tracks from the individual detector hit information, an alignment of the tracking chambers has to be performed. This alignment procedure consists of two successive steps: an *internal* alignment of the individual tracking chamber planes with respect to each other, followed by an *external* alignment of the entire set of tracking chambers within each half of the spectrometer with respect to the reference frame of the spectrometer. The positions of the tracking devices with respect to this reference frame are stored in a geometry data base.

This geometry data base is used in the track reconstruction by the HRC program. Offsets or tilts of one spectrometer half with respect to the information in the geometry data base lead to a change in the geometrical acceptance and/or the reconstructed scattering angle θ of a track. A systematic shift in the scattering angle θ influences directly the reconstructed kinematical quantities $Q^2 = 4EE' \sin^2(\theta/2)$ and $x = Q^2/(2M\nu)$.

By comparing the vertex positions of DIS positron tracks from the full Monte Carlo simulation of the HERMES detector (HMC) with data, a significant vertical offset of the bottom half of the spectrometer by $-1.20 \pm 0.24_{\mathrm{stat.}} \pm 0.10_{\mathrm{sys.}}$ mm was observed [Böt 99]. This offset manifests itself clearly in the distribution of the longitudinal vertex positions, which is shown in the open histogram in Fig. 5.2. The distribution is not symmetrically around the centre of the storage cell, where the target gas atoms are injected.

To compensate for this external alignment offset, all tracks in the bottom half of the spectrometer were corrected using an algorithm which is given in [Böt 99]. This algorithm takes into account the position and the slope of the HERA positron beam at the interaction point, which also determine the longitudinal position of the scattering vertex. After applying this correction, the distribution of the scattering vertices is symmetrical around the centre of the storage cell, as shown in the shaded histogram in

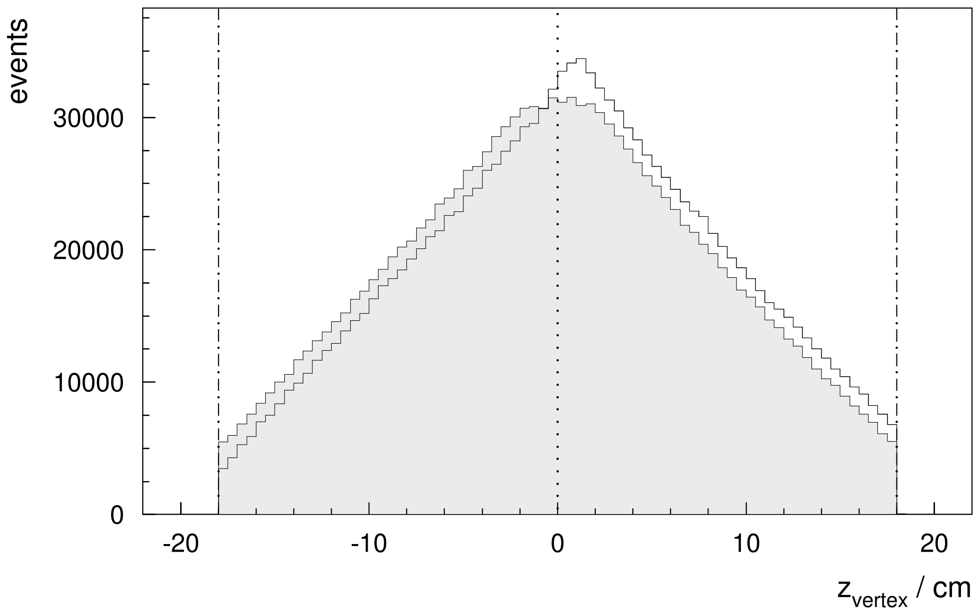

Figure 5.2: Distribution of the longitudinal vertex position of DIS lepton tracks with (shaded histogram) and without (open histogram) alignment corrections. The dotted vertical line at $z_{\text{vertex}} = 0$ cm marks the centre of the storage cell where the target atoms are injected. The dotted–dashed lines at $z_{\text{vertex}} = \pm 18$ cm indicate the cuts used in the analysis.

Fig. 5.2. The alignment correction was applied to data from both years 1996 and 1997, as the spectrometer setup was unchanged between these two data taking periods.

5.4 Event Selection

For the analysis of double spin asymmetries in deep inelastic scattering, a suitable subset of all events recorded with the HERMES detector has to be isolated. The selection process can be subdivided into two classes, which will be explained in the following two subsections.

5.4.1 Data Quality Cuts

The data quality cuts identify data taken on a polarised proton target when all required detector components were fully operational. In order to minimise the losses of data they are carried out on the shortest time scale during which the relevant information is read out or can change.

At HERMES, controlled changes of the target type occur only in between *runs*; quantities like high voltages for the tracking chambers, scaler registers, gas pressures, etc. are read out once every burst. In Table 5.2 all data selection criteria are listed in the order they are applied to the data. With the exception of the requirements of a polarised proton target and the target operation in the so–called "RHX" mode, which are applied on a run basis, all other cuts are applied for each individual burst.

The cuts on the beam and target parameters discard data with low statistical weight

Table 5.2: List of burst selection cuts used in this analysis. The "g_1 Data Quality" criterium is explained in the text.

Quantity	Requirement
Target type	Polarised proton target
"g_1 Data Quality"	Top and bottom spectrometer half fully operational
Target operation mode	"RHX" mode
Target spin state	Stable parallel or anti–parallel
Dead time correction factor	$0.5 \leq \eta_{\text{Dead}} \leq 1.0$
Fitted luminosity detector rate	$5\ \text{Hz} \leq f^{\text{fit}}_{\text{Lumi}} \leq 60\ \text{Hz}$
Averaged target gas atomic fraction	$0.7 \leq \langle\alpha_{\text{TGA}}\rangle \leq 1.0$
Beam polarisation	$0.3 \leq \lvert P_{\text{Beam}}\rvert \leq 0.8$
Target polarisation	$0.7 \leq \lvert P_{\text{Target}}\rvert$

due to low polarisation values, or from periods with low luminosities. The upper cuts on these quantities are introduced to isolate data when glitches of the measuring devices caused the generation of unphysical values.

During the 1996 data taking period the target was sometimes operated in a special mode to perform measurements of Bhabha asymmetries simultaneously with the measurements of deep inelastic double spin asymmetries. In this special operation mode not only the nuclear polarisation of the target atoms was flipped, but also the spin of the shell electron, causing an asymmetry in the rate measured by the luminosity monitor. As the variations in the luminosity rate still persisted after smoothing of the measured rates and introduced false asymmetries in the DIS data, periods when the target was operated in the Bhabha mode were discarded from the analysis.

In the analysis performed for the extraction of the spin structure function g_1^{p} [Air 98] from an inclusive asymmetry measurement, a detailed check of the spectrometer performance for every burst was performed [Gut 99a, Has 99]. Separately for each detector half, stable tracking and particle identification efficiencies were tagged by monitoring the supply high voltages on the chamber planes and on the PID detectors. For each burst in every run, this information is stored in a list, supplemented by entries from the main logbook of the experiment, where periods of test measurements or known failures of essential equipment are recorded. For the analysis of semi inclusive events presented here, a data sample was selected based on this list, requiring that both halves of the spectrometer were fully operational. This requirement is called "g_1 Data Quality" in Table 5.2.

5.4.2 Kinematic Cuts

Once a data sample has been established by the data quality cuts, events originating from deep inelastic scattering processes have to be identified out of all recorded events. The trigger requirements as described in Sect. 3.4 already enhance DIS events over other competing processes. In order to further increase the purity of the sample of

DIS events and to discard tracks from the edges of the acceptance, cuts on geometrical and kinematic track quantities are applied as listed in Table 5.3. They will be briefly discussed in the following paragraphs.

Table 5.3: List of event selection cuts for the analysis of inclusive and semi inclusive asymmetries. The cuts are applied in the order they are listed.

<table>
<tr><th>Quantity</th><th>Inclusive asymmetry</th><th>Semi inclusive asymmetries</th></tr>
<tr><td rowspan="2">Vertex position</td><td colspan="2">$-18\ \mathrm{cm} \leq z_{\mathrm{vertex}} \leq +18\ \mathrm{cm}$</td></tr>
<tr><td colspan="2">$d_{\mathrm{vertex}} \leq 0.75\ \mathrm{cm}$</td></tr>
<tr><td rowspan="2">Scattering angle</td><td colspan="2">$|\theta_{\mathrm{hor.}}| \leq 170\ \mathrm{mrad}$</td></tr>
<tr><td colspan="2">$40\ \mathrm{mrad} \leq |\theta_{\mathrm{vert.}}| \leq 140\ \mathrm{mrad}$</td></tr>
<tr><td rowspan="2">Calorimeter cluster position</td><td colspan="2">$|x_{\mathrm{Calo}}| \leq 175\ \mathrm{cm}$</td></tr>
<tr><td colspan="2">$30\ \mathrm{cm} \leq |y_{\mathrm{Calo}}| \leq 100\ \mathrm{cm}$</td></tr>
<tr><td>Track momentum</td><td colspan="2">$p \geq 0.5\ \mathrm{GeV}$</td></tr>
<tr><td>Calorimeter cluster energy</td><td colspan="2">$E_{\mathrm{Calo}} \geq 1.4\ \mathrm{GeV}$</td></tr>
<tr><td>DIS scale variable</td><td colspan="2">$Q^2 \geq 1.0\ \mathrm{GeV}^2$</td></tr>
<tr><td>Fractional energy transfer</td><td colspan="2">$y \leq 0.85$</td></tr>
<tr><td>Invariant mass</td><td>$W^2 \geq 4.0\ \mathrm{GeV}^2$</td><td>$W^2 \geq 10.0\ \mathrm{GeV}^2$</td></tr>
<tr><td>Hadron energy fraction</td><td></td><td>$z \geq 0.2$</td></tr>
<tr><td>Feynman variable</td><td></td><td>$x_{\mathrm{F}} \geq 0.1$</td></tr>
</table>

In each event only those tracks are regarded for the analysis, which originate within the volume of the target cell and are scattered into the geometrical acceptance of the spectrometer, which is given by the opening in the spectrometer magnet. Furthermore, in order to ensure that an electromagnetic shower created in the calorimeter is mostly contained within the calorimeter glass blocks, the centre of a cluster must not be too close to the edges of the calorimeter wall. Tracks with very low momenta are not included in the analysis.

After these cuts, the scattered positron from the DIS process is identified among all remaining lepton tracks in the event. The energy of the cluster assiociated with a lepton track is required to match the trigger condition. A cut on the negative four–momentum transfer squared of $Q^2 \geq 1.0\ \mathrm{GeV}^2$ sets the scale for the deep inelastic scattering process. The invariant mass of the hadronic final state is required to be above the highest resonant nucleon state, $W \geq 2$ GeV. An upper limit on the fractional lepton energy transfer of $y \leq 0.85$ eliminates events where radiative corrections and the associated uncertainties become too large.

For semi inclusive events, where a hadron is detected in coincidence with the scattered lepton, a higher cut on the invariant mass of the final hadronic state is applied. In the analysis of semi inclusive events, using the so–called method of *flavour tagging*, one tries to deduce the flavour of the struck quark from the type of the observed hadron, as explained in Sect. 2.7. Hadrons from the current fragmentation region are preferably selected by the cuts on the hadron energy fraction $z \geq 0.2$ and on the Feynman variable

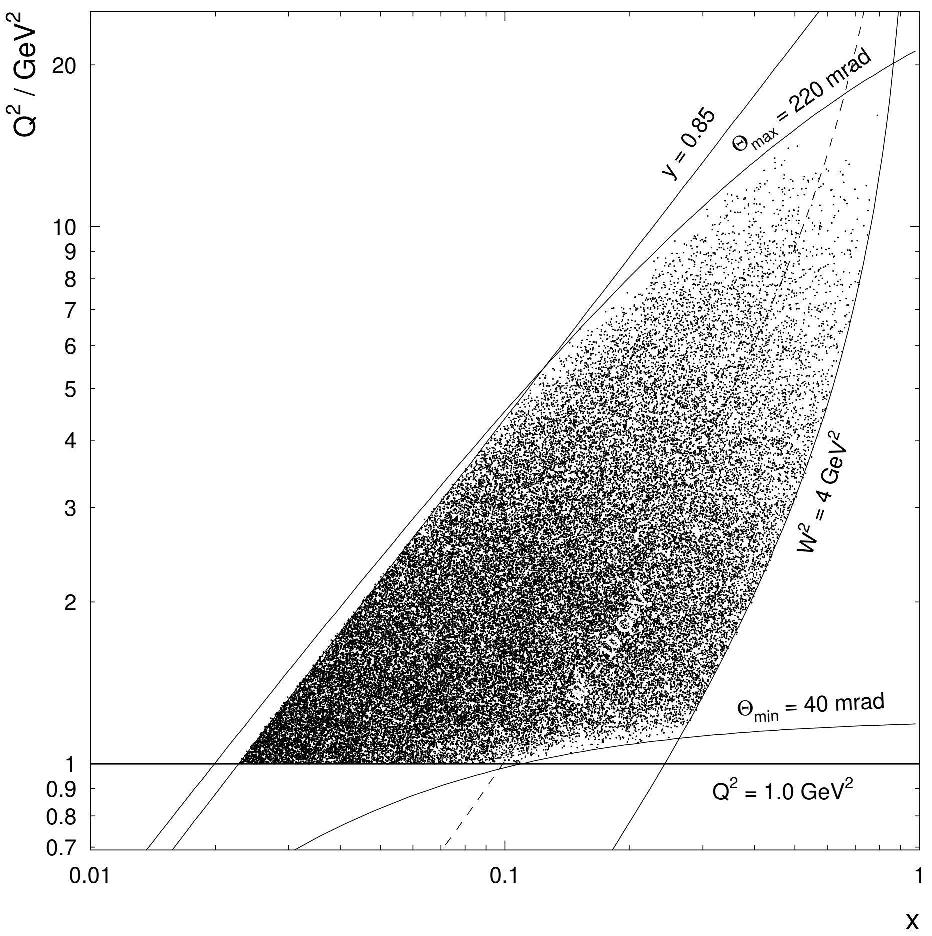

Figure 5.3: Distribution of events in the kinematic x–Q^2 plane. The lines indicate the cuts applied to the data. The cut $W^2 \geq 10$ GeV^2 specified by the dashed line is only applied in the analysis of semi inclusive DIS events.

$x_\mathrm{F} \geq 0.1$. The correlation between the selected hadrons and the struck quark can be increased by requiring a higher invariant mass of the final hadronic state. Monte Carlo studies [Ihs 96] revealed that the given cut of $W^2 \geq 10.0$ GeV^2 provides an optimum between increasing hadron–quark correlation and decreasing statistics for larger values of W^2.

The distribution of events selected for the analysis of inclusive and semi inclusive asymmetries in the kinematical x–Q^2 plane is shown in Fig. 5.3. The total numbers of leptons and hadrons in the analysis data samples after all cuts are listed in Tab. 5.4, separately for the 1996 and 1997 data taking periods. In Appendix D the particle numbers for inclusive and semi inclusive events are tabulated for each x bin.

5.5 Determination of the Target Polarisation

In contrast to the beam polarisation, for instance, a calibrated and corrected value of the target polarisation is not readily available in the HERMES data production. During the first year of operation (1996) of the polarised hydrogen target, diagnostics were

Table 5.4: Total numbers of particles in the analysis samples on the polarised proton target after all cuts for the different data taking periods. For comparison, the numbers for the ^{3}He data sample from [Tip 99] are given as well. The number of DIS positrons is given after the correction for charge symmetric background processes (see Sect. 5.6.1).

Particle type	Asymmetry data sample		
	1995 (^{3}He)	1996 (p)	1997 (p)
e^+ (DIS)	2099733	601493	1335031
e^-	21784	6140	13483
h^+	269958	81617	174955
h^-	169666	47088	100539
π^+	15657	34268	75635
π^-	10848	23920	52675

limited and the operation parameters were not optimal as compared to the following year. As a consequence, different schemes for the calculation of the target polarisation were chosen in both years, which will be explained in this section.

The effective nuclear target polarisation value which is entering into the asymmetry calculation in Eqn. (5.11) is not identical to the polarisation values measured by the BRP (see Sect. 3.1.3) for two reasons: first, by design, the BRP can only measure the polarisation of hydrogen atoms but not of hydrogen molecules, which partly originate from the recombination of polarised hydrogen atoms. Secondly, the BRP (and TGA) take a sample of the target gas atoms from the centre of the storage cell. Target atoms within the storage cell, which take part in the DIS process, on average have a different "history" in terms of wall collisions as compared to the atoms analysed in the BRP and TGA. As depolarisation and recombination of the target atoms predominantly occur during wall collisions, the measured polarisation values have to be corrected to obtain the effective polarisation of the target atoms.

For the 1997 data taking period the effective nuclear target polarisation $P_{\rm T}$ was determined as follows:

$$P_{\rm T}^{1997} = P_{\rm BRP} \cdot \alpha_0 \cdot [\alpha_R + (1-\alpha_R) \cdot \beta] \tag{5.20}$$

with

$$\alpha_R = C_\alpha \cdot \alpha_{\rm TGA} , \tag{5.21}$$

where $P_{\rm BRP}$ and $\alpha_{\rm TGA}$ denote the calibrated values for the nuclear polarisation and the degree of dissociation measured by the BRP and the TGA, respectively. The value α_0 in Eqn. (5.20) is the degree of dissociation of hydrogen within the ABS, i.e. before injection into the storage cell. In contrast, $(1-\alpha_R)$ is the fraction of hydrogen molecules in the target cell originating from the recombination of atomic hydrogen atoms. These molecules may retain the nuclear polarisation of the constituent atoms to a certain degree, which is the quantity β in Eqn. (5.20). The value of β is not accessible in a direct measurement and the uncertainty on this quantity contributes a large fraction of the total systematic uncertainty on the target polarisation. By measuring how the inclusive experimental asymmetry $A_{\|}$ varies with changing the atomic fraction α_R, a constraint on the molecular polarisation of $0.2 \leq \beta \leq 1.0$ has been derived [Kol 98].

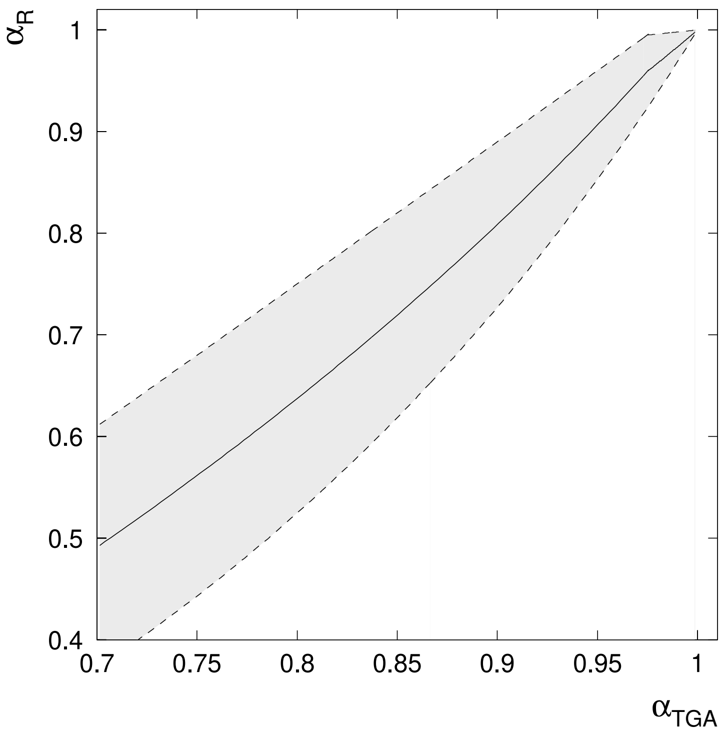

Figure 5.4: The effective degree of dissociation after recombination, α_R, in dependence of the measured value α_{TGA} in the TGA. The full line is calculated using the best value for the sampling correction C_α (see Eqn. (5.22)), the dashed lines indicate the upper and lower limits on this quantity, respectively.

The sampling correction C_α in Eqn. (5.21), which relates the measured value to the effective degree of dissociation, is obtained from Monte Carlo simulations of the ballistic flow of the atoms inside the storage cell [Bau 98, Hen 99]. As mentioned earlier, the properties of the surfaces encountered by the target atoms strongly influence depolarisation and recombination and hence the sampling correction factor C_α. Furthermore, local variations of the surface quality in the storage cell may occur due to damage after losses of the HERA positron beam near the target, deeming a detailed modelling of the surface parameters in such simulations impossible. Hence, in order to get a realistic estimate of the sampling corrections in practice, two extreme, unlikely configurations of the storage cell surface quality were assumed. The resulting expression for the sampling correction is the mean of the two limiting parametrisations:

$$C_\alpha = \frac{C_\alpha^{\mathrm{min}} + C_\alpha^{\mathrm{max}}}{2}, \tag{5.22}$$

where the expressions for C_α^{min} and C_α^{max} are given in [Hen 00].

In Fig. 5.4 the corrected value for α_R as a function of the measured value α_{TGA} is shown. The shaded band in this plot indicates the uncertainty in the sampling correction which is limited by the two extreme parametrisations, entering in the systematic uncertainty of the target polarisation.

In order to reduce statistical fluctuations, the measured value α_{TGA} has been averaged over time intervals of 10 min. duration. Changes of the atomic fraction occur on much longer time scales, except for incidents, when a loss of the positron beam in the near vicinity of the storage cell leads to drastic changes of the surface properties. Such periods have been excluded from the analysis.

As already noted, different parameters of operation in 1996 led to an increased fraction $1 - \langle\alpha_{\mathrm{TGA}}\rangle = 12\%$ of recombined atoms, as opposed to a value of 3.1% for the same quantity in 1997. Due to the large uncertainty in the polarisation β of molecules originating from recombination and the larger sampling corrections, the calculation of the target polarisation with the above scheme would have caused an unacceptably large systematic uncertainty. Therefore the target polarisation for 1996 data was calculated differently, according to:

$$P_{\mathrm{T}}^{1996} = P_{\mathrm{BRP}} \cdot \alpha_0 \cdot \eta_{\mathrm{norm}} \, . \tag{5.23}$$

The global correction term η_{norm} was determined from scaling the inclusive asymmetry $A_1 \simeq g_1/F_1$ from 1996 data to the result from 1997 data, which was evaluated using the complete target calculation scheme laid out above. From this a value of $\eta_{\mathrm{norm}} = 0.929 \pm 0.042$ was derived, where the uncertainty of ± 0.042 arises from the statistical uncertainties of the asymmetries from both years. This procedure is justified by the fact that the physical processes which determine the poorly known molecular polarisation of the recombined hydrogen atoms are universal for both years of operation.

Averaged over both spin states, the corrected mean target polarisation values in 1996 (1997) were 79.6% (87.5%). The fractional systematic uncertainty on the target polarisation $\delta P_{\mathrm{T}}/P_{\mathrm{T}}$ in 1996 (1997) is 6.3% (4.4%), where the value for 1996 is the quadratic sum of the systematic uncertainty for 1997 and the relative uncertainty of the scaling factor η_{norm}.

In case of the determination of the target polarisation values, as an exception, not all quantities were taken from the official μDST production (release 97b2). The values for α_0 and α_{TGA} stored in the official μDST data set are corrupt and were superseded by a separate external data set [Kol 00]. As a consequence, the values for the average target polarisation and for the systematic error given above differ slightly from the values published in [Air 98, Ack 99c].

5.6 Corrections to the Measured Asymmetry

5.6.1 Background Corrections

The sample of DIS events selected by the kinematic cuts described in Sect. 5.4 was corrected for misidentified positrons from charge symmetric background processes, such as e^-e^+ pair production. Photo production is a potentially large source for charge symmetric background to the DIS process, especially in the regime of small values of Bjørken–x.

Neutral pions, generated mainly in photo production processes, may decay via $\pi^0 \to \gamma\gamma$ with the subsequent conversion of one or both photons into an electron–positron pair $\gamma \to e^-e^+$ within the acceptance of the spectrometer. The beam positron, however, will be scattered under small angles in photo production processes and may escape detection in the spectrometer. Similarly, high energy bremsstrahlung photons may convert into an e^-e^+ pair. In both cases, the positron from these processes might be misidentified as the scattered beam positron from the DIS process.

On the other hand, both processes also are the dominating sources for detected electrons, which are passing the kinematic cuts for the lepton from the DIS process. Hence, they are considered a tag on the above background processes and are used for correcting the sample of identified DIS leptons under the assumption of equal detection efficiencies for both charges. Whenever the leading[i] lepton, which passes all kinematic DIS cuts, is an electron, it is subtracted from the sample of DIS positrons with the reconstructed kinematics. Additionally, in case of a semi inclusive event, the coincident hadrons are also subtracted from the corresponding hadron samples.

The charge symmetric background is largest at small values of x with up to 16% of the leptons not originating from deep inelastic scattering (corresponding to 8% electrons in the sample), while it quickly falls off at higher values of x. In Fig. 5.5 the fraction of corrected background events is shown versus Bjørken–x.

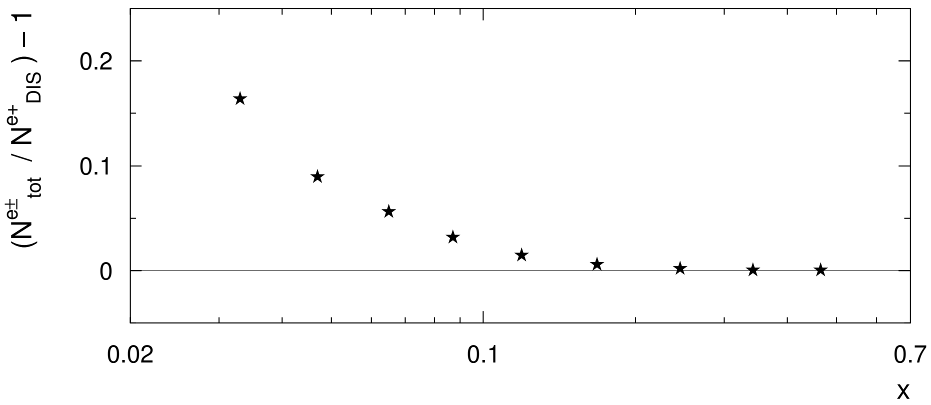

Figure 5.5: Fraction of events which have been subtracted from the DIS sample as originating from charge symmetric background processes.

As mentioned earlier in Sect. 5.2, the contamination of the electron/positron sample by misidentified hadrons and vice versa is negligible and hence has not been corrected for. The same is true for the contributions to the positron sample from other processes than described above, which are not related to the nucleon spin structure. In particular the diffractive production of ρ mesons with the subsequent decay into pions has been estimated to be negligible [Tal 98, Ihs 98].

5.6.2 Smearing Corrections

Apparatus effects in general lead to a systematic deviation of the reconstructed, measured asymmetry from the underlying, real asymmetry. There are several mechanisms contributing to this systematic deviation called smearing.

In the track reconstruction the particles' trajectories are assumed to be straight lines outside the field of the spectrometer magnet. Multiple scattering of the particles on their path through the detector, however, alters their direction slightly and induces

[i]The *leading* particle is the particle with the largest energy within the respective class of particles in this event.

kinks in the tracks. Furthermore, imperfect calibrations of the tracking devices, as well as the reconstruction algorithm itself can introduce a systematic deviation of the measured kinematic quantities from the real values. These processes are called kinematic smearing.

Another source of smearing arises from the limited acceptance of the spectrometer, which leads to a kinematical bias of the detected event sample. The proton asymmetry A_1 is strongly dependent on the kinematic variable x. Due to this dependence, events within one x–bin have different weights, leading to a systematic shift of the central value in this bin.

The above effects can be estimated and corrected for using a realistic Monte Carlo simulation of both the DIS process and the detection in the spectrometer. This was done by generating a large sample of polarised DIS events with the PEPSI event generator [Man 92]. The generated events were then propagated through a realistic representation of the HERMES spectrometer in the HMC program [HMC 96]. Both from the initially generated sample, and from the events which were tracked through HMC, the physics asymmetries A_1^{perfect} and A_1^{HMC} were formed, respectively. The size of the combined smearing effects is then given as

$$\eta_{\text{smear}} = \frac{A_1^{\text{perfect}}}{A_1^{\text{HMC}}} . \tag{5.24}$$

Using this factor, the measured asymmetry A_1^{raw} is corrected for smearing effects by

$$A_1^{\text{corr}} = A_1^{\text{raw}} \cdot \eta_{\text{smear}} . \tag{5.25}$$

In Tab. 5.5 the smearing correction terms $\eta_{\text{smear}}^{(h\pm)}$ for inclusive and semi inclusive proton asymmetries in each x–bin are listed [Gut 99b]. The semi inclusive smearing corrections for pion asymmetries have not been calculated separately and they are assumed to be identical to the corrections for the semi inclusive hadron asymmetries. The statistical uncertainties in the smearing corrections are determined by the number of generated Monte Carlo events.

Table 5.5: Smearing corrections $\eta_{\text{smear}}^{(h\pm)}$ for the inclusive and semi inclusive proton asymmetries [Gut 99b].

$\langle x \rangle$	$\eta_{\text{smear}} \pm$ stat.	$\eta_{\text{smear}}^{h^+} \pm$ stat.	$\eta_{\text{smear}}^{h^-} \pm$ stat.
0.033	0.946 ± 0.009	0.913 ± 0.011	0.981 ± 0.027
0.047	0.975 ± 0.009	0.931 ± 0.011	0.967 ± 0.025
0.065	0.967 ± 0.009	0.930 ± 0.010	0.944 ± 0.022
0.087	0.955 ± 0.009	0.925 ± 0.009	0.930 ± 0.018
0.119	0.937 ± 0.009	0.929 ± 0.007	0.931 ± 0.011
0.168	0.931 ± 0.008	0.960 ± 0.005	0.961 ± 0.007
0.245	0.934 ± 0.007	0.996 ± 0.004	1.000 ± 0.005
0.342	0.966 ± 0.008	1.019 ± 0.004	1.019 ± 0.005
0.466	0.989 ± 0.006	1.026 ± 0.004	1.023 ± 0.005

The smearing corrections were calculated for the so–called STD (standard) tracking method, which includes the hit information from the micro strip vertex chambers

(VCs), and was used in 1997. In the 1996 data taking period, these chambers were not available and the event reconstruction was performed in the so–called NOVC method. The differences in the smearing corrections between the STD and NOVC method are below 0.5% and hence the same set of corrections is used for both years.

For completeness it is noted that, in case of the ^{3}He asymmetries smearing corrections are negligibly small [Fer 97]. This reflects the fact that the ^{3}He asymmetries are both very small in magnitude and almost constant over the measured range in x (see Fig. 5.14).

5.6.3 Radiative Corrections

The deep inelastic scattering process thus far has been discussed in the approximation of the Born tree graph in QED (one–photon approximation) as depicted in Fig. 2.1. The measured DIS cross section, however, also includes contributions from higher order processes, which have to be corrected for in order to validate the discussion based on the Born level asymmetries. In Fig. 5.6 the Feynman diagrams for the dominant higher order QED processes, which contribute to the DIS cross section, are shown. At HERMES, electroweak corrections are negligible as the maximum value for Q^2 is much smaller than the mass of the Z^0 boson.

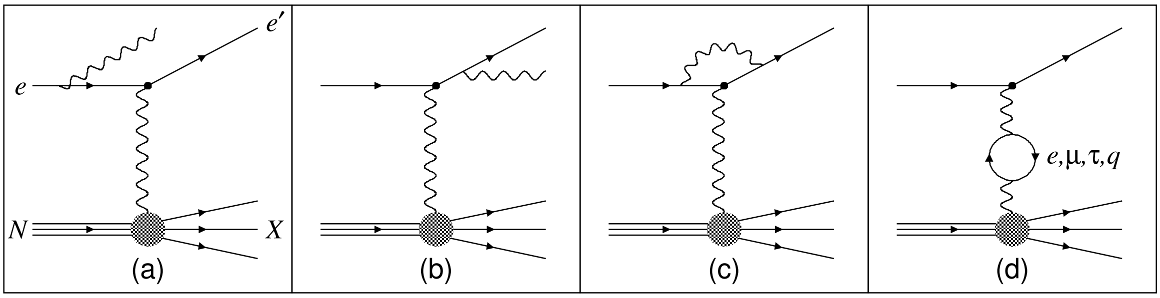

Figure 5.6: Higher order Feynman diagrams for the deep inelastic lepton–nucleon scattering process: initial (a) and final (b) state bremsstrahlung, vertex corrections (c), and vacuum polarisation (d).

In [Aku 94] the formalism to calculate the radiative corrections to spin–dependent cross sections is presented, which is implemented in the program POLRAD 2.0 [Aku 97]. The tree level Born asymmetry $A_1^{\rm Born}$ is obtained from the measured asymmetry $A_1^{\rm meas}$ by

$$A_1^{\rm Born} = A_1^{\rm meas} - \Delta A_1^{\rm RC} \,, \tag{5.26}$$

where $\Delta A_1^{\rm RC}$ accounts for contributions from higher order radiative processes as depicted in Fig. 5.6. In Tab. 5.6 the calculated values for the correction term $\Delta A_1^{\rm RC}$ are listed for the 1996 and 1997 inclusive proton asymmetries. For comparison, the radiative corrections for the inclusive ^{3}He asymmetries are tabulated as well. They are significantly larger than the values for the proton asymmetries because of large contributions from the tails of the elastic scattering process off the ^{3}He nucleus.

The polarised part of the radiative corrections depends on the polarised structure function g_1, which in turn is related to the measured asymmetry $A_1 \simeq g_1/F_1$. Hence, an iterative procedure is implemented in the code POLRAD, starting from a fit to the measured asymmetry A_1^{meas}. Like the measured asymmetries for the years 1996 and 1997 (see Fig. 5.8), the calculated values for the radiative correction term on the proton asymmetries also differ slightly for the two different data sets. The systematic errors quoted in Tab. 5.6 arise from uncertainties in the parametrisations of the structure functions and of the elastic and quasi–elastic form factors.

Table 5.6: Radiative corrections ΔA_1^{RC} to the inclusive ^{3}He [Tip 99] and proton [Aku 99] asymmetries A_1 with the associated systematic uncertainties.

$\langle x \rangle$	$\Delta A_1^{\mathrm{RC}} \pm$ sys.		
	Helium-3	**Proton (1996)**	**Proton (1997)**
0.033	0.0571 ± 0.0029	−0.00121 ± 0.00006	−0.00121 ± 0.00006
0.047	0.0494 ± 0.0013	−0.00119 ± 0.00004	−0.00119 ± 0.00004
0.065	0.0474 ± 0.0006	−0.00117 ± 0.00003	−0.00117 ± 0.00003
0.087	0.0439 ± 0.0002	−0.00097 ± 0.00004	−0.00097 ± 0.00004
0.119	0.0423 ± 0.0006	−0.00049 ± 0.00003	−0.00049 ± 0.00003
0.168	0.0404 ± 0.0010	0.00037 ± 0.00002	0.00037 ± 0.00002
0.245	0.0389 ± 0.0014	0.00123 ± 0.00010	0.00131 ± 0.00010
0.342	0.0399 ± 0.0018	0.00201 ± 0.00006	0.00205 ± 0.00006
0.466	0.0384 ± 0.0020	0.00210 ± 0.00013	0.00223 ± 0.00013

Radiative corrections were only applied to inclusive asymmetries as the correction terms for semi inclusive asymmetries are significantly smaller and can be neglected [Aku 94].

5.7 Systematic Studies

The measurement of cross section asymmetries requires stable operation and detection efficiencies of the spectrometer on a time scale which is sufficiently long compared to the intervals during which the target spin orientation is reversed. To identify, and ideally remove potential sources of systematic influences on the measured asymmetries, a number of systematic checks was performed on different time scales. Limited by various natural time intervals, the entire data set of DIS events taken on a polarised proton target was divided into subsets with increasing granularity.

The most coarse division of the data set is given by the years of data taking (1996 and 1997). In the beginning of the 1997 data taking period the orientation of the beam spin was reversed as compared with the setup in 1996. During the 1997 data taking period the beam spin orientation was reversed twice, leading to a total of four distinct periods which are sketched in Fig. 5.7. The data from 1996 and the second period in 1997 were taken with the same beam spin helicity and combined in the “1996 beam spin” set. The data from the remaining periods in 1997 are combined in the “1997 beam spin” data set. The total numbers of DIS events taken in these periods are summarised in Table 5.7. Systematic checks were further carried out on shorter subdivisions of the data set into fills of the storage ring, and runs and bursts, corresponding to time intervals of typically 10 minutes and 10 seconds, respectively.

In Fig. 5.8 the inclusive and semi inclusive asymmetries $A_1^{(h^\pm/\pi^\pm)}(x)$ on the proton target are shown for the two different years 1996 and 1997. Also shown in this figure

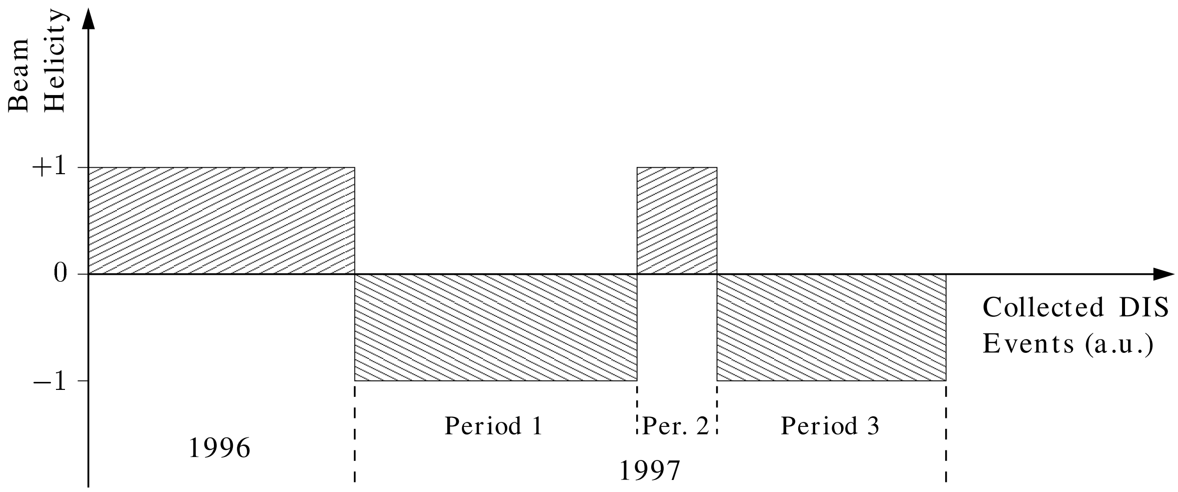

Figure 5.7: Amount of collected DIS events during periods with different beam spin helicities. The area of the hatched boxes is proportional to the number of collected DIS events in each period, after all cuts.

Table 5.7: Numbers of collected DIS events on the polarised proton target during different data taking periods.

Data taking period	DIS events	Fractional contribution
1996	601493	0.311
1997, Period 1	636912	0.329
1997, Period 2	178286	0.092
1997, Period 3	519833	0.268
"1996 beam spin"	779779	0.403
"1997 beam spin"	1156745	0.597
Total	1936524	1.000

is the difference between the two data sets in units of their combined statistical uncertainty. From these differences a reduced χ^2 was calculated to quantify the statistical compatibility of the two asymmetry sets. For the inclusive asymmetries one obtains a value of $\chi^2/\text{ndf} = 1.18$, while for the positive (negative) semi inclusive hadron asymmetries this quantity is $\chi^2/\text{ndf} = 0.37$ (1.85), respectively. While the reduced χ^2 appears to be too small for the positive hadron asymmetries, the negative hadron asymmetries deviate significantly for the two years. When the asymmetries are calculated from the data sets which are combined according to the beam spin orientation, the value of χ^2/ndf becomes 1.46/0.40/1.99 for the inclusive/semi inclusive positive hadron/semi inclusive negative hadron asymmetries, respectively. This change could potentially be explained by an unknown physical process, which is related to the orientation of the beam spin. As the bulk of the 1997 data is taken with an orientation of the beam spin

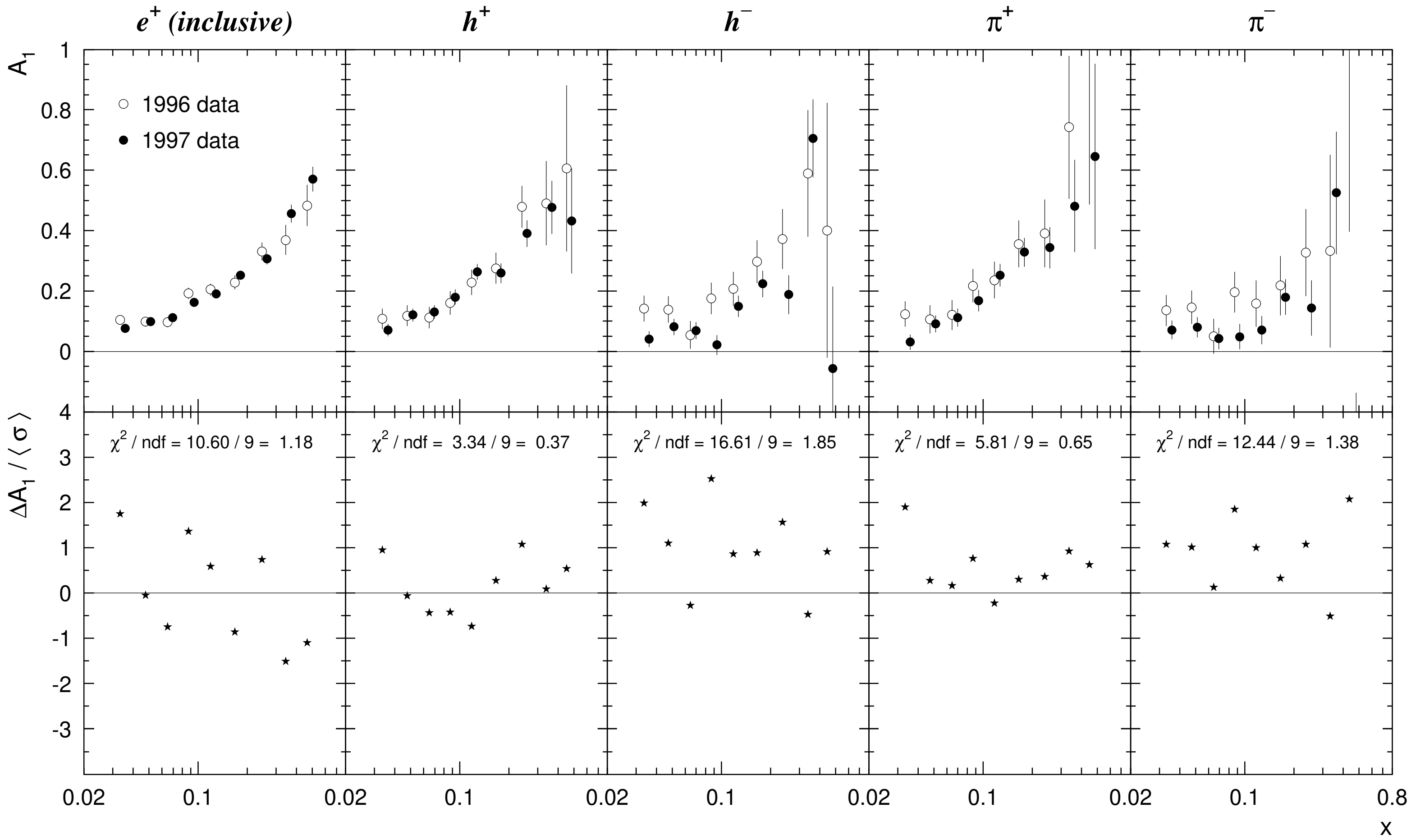

Figure 5.8: Comparison of the proton asymmetries $A_1 \simeq g_1/F_1$ from 1996 and 1997. In the upper row the two data sets for the inclusive and each of the four semi inclusive asymmetries is shown. The error bars in these panels correspond to the statistical uncertainty of each data point. In the lower row the differences $\Delta A_1(x_i) \equiv [A_1(x_i)]_{(1996)} - [A_1(x_i)]_{(1997)}$ of the two asymmetry sets in units of their combined statistical uncertainty $\langle\sigma\rangle_i \equiv \sqrt{\sigma^2_{(1996)}(x_i) + \sigma^2_{(1997)}(x_i)}$ per x–bin is shown. Also shown are the values for the reduced $\chi^2 \equiv \sum_{i\,\in\,\text{bins}}(\Delta A_1(x_i)/\langle\sigma\rangle_i)^2$ comparing the two data sets. The data points for the 1997 asymmetries are shifted slightly horizontally.

which is opposite to 1996, such an effect might show up in the comparison of the two years, as well.

As a consequence of this observation extensive systematic studies were performed in order to identify a reason for the different behaviour of positive and negative semi inclusive hadron asymmetries. The tests comprised comparisons of the particle yields between the different data taking periods, the time dependencies of the asymmetries, the stability of the results against the variation of the kinematic hadron cuts, checks of quality parameters in the track reconstruction code HRC, and variations of the PID cuts. Furthermore, possible correlations of the semi inclusive asymmetries with beam parameters, as positions and slopes, with the rate of triggers caused by protons originating from the HERA–p storage ring and travelling backwards through the spectrometer, as well as asymmetries versus different parameters, like the horizontal and vertical scattering angles, and the particle momenta, have been investigated. All studies are documented in detail in [Bai 99].

As a result, systematic differences, for instance in the particle yields between the two years, could be established. Yet, no clear systematic effect of the apparatus was identified, which could explain the observed difference in the semi inclusive asymmetries. Likewise, a potential physical effect related to the orientation of the beam spin, could neither be established, nor rejected.

However, it should be noted that, summed over the inclusive and the semi inclusive charged hadron asymmetries, the value of $\chi^2/\mathrm{ndf} = 30.6/27 = 1.13$ for the comparison of data from 1996 and 1997, close to the expectation for two data sets with only statistical fluctuations. Hence it was decided to combine the data from the two different years. Furthermore, this treatment is also a good approximation in case of an underlying unknown physical process, which is related to the orientation of the beam spin. If such a hypothetical process existed, it had to be small in comparison to the measured semi inclusive asymmetries, as can be deduced from the moderate change of the discrepancy between the two data sets when comparing data from 1996 to 1997 or from the two periods with different beam helicity. Furthermore, the fractions of DIS events taken during the periods with opposite beam spin orientation, differ by only $\sim$20%, as can be seen in Tab. 5.7. The combination of the two data sets would effectively average over a beam helicity dependent contribution to the measured asymmetries. Since 1998 the orientation of the beam spin is being reversed more frequently in time intervals of 4 to 8 weeks, in order to establish or reject such a dependence with better systematical accuracy in future analyses.

5.8 Systematic Uncertainties

The extracted asymmetries $A_1^{(h^\pm/\pi^\pm)}$ are subject to several systematic uncertainties, which can be divided into two classes. One class contains experimental uncertainties, like in the beam and target polarisation measurements and in the smearing corrections. The other group of uncertainties comprises contributions from external quantities, like the measurements of the cross section ratio $R = \sigma_L/\sigma_T$ and the spin structure function g_2, or the parametrisations of form factors used in the computation of the radiative corrections.

The individual contributions to the systematic uncertainty on the inclusive and semi inclusive proton asymmetries will be discussed in the following subsections. Unless otherwise noted, all results refer to both inclusive and semi inclusive asymmetries. For the ^{3}He asymmetries from 1995 data an additional source, arising from non–statistical behaviour of data subsamples ("yield fluctuations"), contributes substantially to the systematic uncertainty. In [Ako 97, Tal 98] details and the size of this additional contribution are given.

5.8.1 Beam Polarisation

During the 1996 and 1997 data taking periods, the default device for the measurement of the beam polarisation was the Transverse Polarimeter. In periods when the TPOL did not deliver a valid measurement, data from the LPOL was used, when available. The absolute calibration of both devices was performed by measurements of the rise time of polarisation, as described in Sect. 4.1. The fractional systematic uncertainty from this calibration was determined as $[\delta P_{\mathrm{B}}/P_{\mathrm{B}}]_{\mathrm{rise}} = 3.3\%$ [Tip 99], which is fully correlated between measurements of different years (including the 1995 data taking period). Additional systematic uncertainties arise from corrections, which have to be applied to the measured raw polarisation. For the years 1996 and 1997 they contribute $[\delta P_{\mathrm{B}}/P_{\mathrm{B}}]_{\mathrm{point}} = 0.9\%$ [Tip 99], uncorrelated between the different years of operation. These two contributions were added in quadrature to obtain the total fractional uncertainty on the beam polarisation measurement of $\delta P_{\mathrm{B}}/P_{\mathrm{B}} = 3.4\%$. The systematic uncertainty on the asymmetry A_1 from this contribution is given by

$$[\delta A_1]_{P_{\mathrm{B}}} = \sqrt{\left(\frac{\partial A_1}{\partial P_{\mathrm{B}}}\right)^2 (\delta P_{\mathrm{B}})^2} = \left| A_1 \cdot \frac{\delta P_{\mathrm{B}}}{P_{\mathrm{B}}} \right| . \tag{5.27}$$

5.8.2 Target Polarisation

The systematic uncertainties in the measurement of the target polarisation are detailed in Section 5.5 above. The relative uncertainty from the 1997 data $[\delta P_{\mathrm{T}}/P_{\mathrm{T}}]_{1997} = 4.4\%$ is fully correlated between both years. For the 1996 data the fractional uncertainty arising from the scaling factor $[\delta P_{\mathrm{T}}/P_{\mathrm{T}}]_{\mathrm{norm}} = 4.5\%$ was added in quadrature, resulting in a fractional uncertainty of $\delta P_{\mathrm{T}}/P_{\mathrm{T}} = 6.3\%\,(4.4\%)$ for the year 1996 (1997). Similarly to the contribution from the beam polarisation measurement, the resulting systematic uncertainty in the asymmetry A_1 is

$$[\delta A_1]_{P_{\mathrm{T}}} = \left| A_1 \cdot \frac{\delta P_{\mathrm{T}}}{P_{\mathrm{T}}} \right| . \tag{5.28}$$

5.8.3 Smearing Corrections

The systematic uncertainty of the smearing corrections η_{smear} was taken to be their statistical uncertainty $\delta\eta_{\mathrm{smear}}$. The smearing corrections are assumed to be fully correlated between the two years. For semi inclusive pion asymmetries the smearing corrections and their uncertainties are approximated by the corresponding quantities for the hadron asymmetries. The resulting uncertainty on the asymmetry is

$$[\delta A_1]_{\eta_{\mathrm{smear}}} = |A_1 \cdot \delta\eta_{\mathrm{smear}}| . \tag{5.29}$$

5.8.4 Cross Section Ratio R

For the cross section ratio $R(x, Q^2) = \sigma_L/\sigma_T$, which enters in the depolarisation factor $D(x, Q^2)$ of the virtual photon, the parametrisation given in [Abe 99] was used. This parametrisation is a fit to the world data available on this ratio, shown as the full line in Fig. 5.9. Especially in the kinematic region of the HERMES data, measurements from many different experiments constrain this fit tightly. The associated uncertainty on the parametrisation given in [Abe 99] is used as the systematic uncertainty $\delta R(x, Q^2)$.

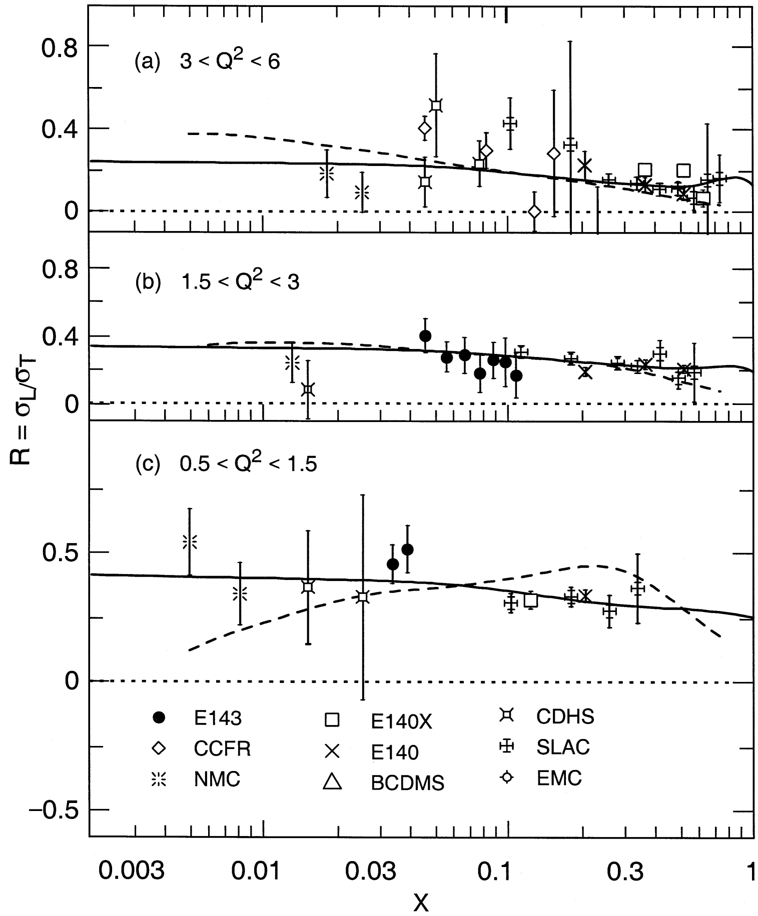

Figure 5.9: The cross section ratio $R = \sigma_L/\sigma_T$ as a function of x in three different ranges of Q^2: (a) $3 < Q^2/\mathrm{GeV}^2 < 6$, (b) $1.5 < Q^2/\mathrm{GeV}^2 < 3$, and (c) $0.5 < Q^2/\mathrm{GeV}^2 < 1.5$ [Abe 99]. Shown are measurements from different experiments together with a parametrisation of $R(x, Q^2)$ given by the full line. The dashed line is the prediction of a NNLO pQCD calculation.

Using $A_1 = A_\parallel/[D(1 + \eta\gamma)]$ together with Eqn. (2.34) one obtains

$$[\delta A_1]_R = \left| A_1 \cdot \frac{\varepsilon}{1 + \varepsilon R} \cdot \delta R(x, Q^2) \right| . \tag{5.30}$$

This uncertainty is fully correlated between the years 1996 and 1997.

5.8.5 Spin Structure Function g_2

In the derivation of Eqn. (2.37) the assumption $g_2^{(h)}(x) = 0$ was used, which leads to $A_1^{(h)} = g_1^{(h)}/F_1^{(h)}$. For a non–vanishing spin structure function $g_2^{(h)}(x)$ this relation breaks up and the resulting expressions become

$$A_1^{(h)} = \frac{A_{\parallel}^{(h)}}{D(1+\eta\gamma)} - \frac{\eta\gamma(1+\gamma^2)}{1+\eta\gamma}\frac{g_2^{(h)}}{F_1^{(h)}}, \tag{5.31}$$

$$\frac{g_1^{(h)}}{F_1^{(h)}} = \frac{A_{\parallel}^{(h)}}{D(1+\eta\gamma)} + \frac{\gamma(\gamma-\eta)}{1+\eta\gamma}\frac{g_2^{(h)}}{F_1^{(h)}}. \tag{5.32}$$

The spin structure function $g_2(x)$ has been measured for the proton [Ada 94, Abe 98, Ant 99a] and for the neutron [Abe 97b] in a range of x and Q^2 similar to the HERMES experiment. In Fig. 5.10 the measurements of the SLAC experiments E143 [Abe 98] and E155 [Ant 99a] for $x \cdot g_2^{\mathrm{p}}(x)$ are shown. The data points cover a range in Q^2 of $1.3 \leq Q^2/\mathrm{GeV}^2 \leq 10$ ($1.0 \leq Q^2/\mathrm{GeV}^2 \leq 30$) for the E143 (E155) experiment. For values of $x \lesssim 0.3$ the results are compatible with the simple QPM expectation $g_2(x) \equiv 0$ within the experimental uncertainties. In [Ant 99a] it has been shown that the data seem to be sufficiently described by the twist–2 Wandzura–Wilczek term $g_2^{\mathrm{WW}}(x,Q^2) = -g_1(x,Q^2) + \int_x^1 \mathrm{d}x' g_1(x',Q^2)/x'$ [Wan 77], without requiring higher twist contributions.

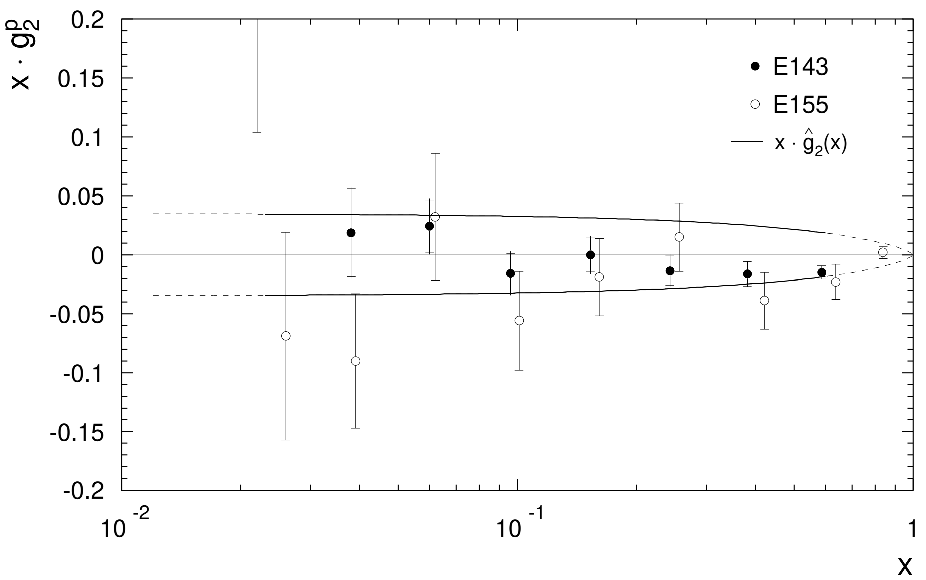

Figure 5.10: Measurements of the spin structure function $x \cdot g_2^{\mathrm{p}}(x)$ by the SLAC experiments E143 [Abe 98] and E155 [Ant 99a]. The two lines drawn symmetrically around $x \cdot g_2(x) = 0$ show the parametrisation $x \cdot \hat{g}_2(x)$ used to estimate the uncertainty on $g_2(x)$.

In order to estimate the systematic uncertainty on the asymmetry A_1 and the structure function ratio g_1/F_1 due to the assumption $g_2(x) = 0$, a simple limiting parametrisation $\hat{g}_2(x) = \pm 0.035 \cdot x^{-1} \cdot (1-x)^{0.7}$ was chosen. The lines around $x \cdot g_2(x) = 0$ in Fig. 5.10 represent an upper and lower limit on the size of the structure function

$g_2(x)$, motivated by the available measurements. The full lines indicate the range in x of the HERMES data, continued by the dashed lines outside the kinematical range of HERMES. For $x \to 1$ the chosen parametrisation $\hat{g}_2(x)$ follows the behaviour of the Wandzura–Wilczek term $g_2^{\mathrm{WW}}(x)$, which approaches zero in this limit.

Using this parametrisation, the systematic uncertainty on the asymmetry A_1 (5.31) becomes

$$[\delta A_1]_{g_2} = \left|\frac{\eta\gamma(1+\gamma^2)}{1+\eta\gamma}\cdot\frac{\hat{g}_2(x)}{F_1(x)}\right| , \tag{5.33}$$

where the unpolarised structure function $F_1(x)$ is evaluated using a parametrisation of $F_2^{\mathrm{p}}(x)$ [Arn 95] according to Eqn. (2.17). As no measurements exist for $g_2^h(x)$, the assumption $\hat{g}_2^h(x) = \hat{g}_2(x)$ was used in the determination of the systematic uncertainties on semi inclusive hadron asymmetries.

For the extraction of polarised quark distributions presented in Chapter 6 the structure function ratio $g_1(x)/F_1(x)$ enters in Eqn. (6.1) instead of the photon nucleon asymmetry A_1. Due to the different kinematic coefficients of the contributions from $g_2(x)$ in Eqns. (5.31) and (5.32), the systematic uncertainty on the structure function ratio writes

$$\left[\delta\left(\frac{g_1}{F_1}\right)\right]_{g_2} = \left|\frac{\gamma(\gamma-\eta)}{1+\eta\gamma}\cdot\frac{\hat{g}_2(x)}{F_1(x)}\right| . \tag{5.34}$$

It is noted that in the kinematical range of HERMES the leading term in this expression varies over a range $\gamma(\gamma-\eta) = 0.002\ldots0.021$, which is much smaller than the corresponding expression $\eta\gamma(1+\gamma^2) = 0.001\ldots0.167$ in case of the uncertainty on the asymmetry A_1. The systematic uncertainty arising from $g_2(x)$ is fully correlated within both years.

5.8.6 Radiative Corrections

The systematic uncertainties related to the radiative correction were already discussed in Sect. 5.6.3. The contribution to the systematic uncertainty in the asymmetry is given by the systematic uncertainty on the radiative corrections:

$$[\delta A_1]_{\eta_{\mathrm{RC}}} = \left|\delta\left(\Delta A_1^{\mathrm{RC}}\right)\right| . \tag{5.35}$$

Note that the radiative corrections are only applied to the inclusive asymmetries. Furthermore, they contribute least among all sources of systematic uncertainties.

5.8.7 Combined Systematic Uncertainty

The systematic uncertainties arising from all contributions i, which were discussed in the previous sections, were added in quadrature to give the total systematic uncertainty in every x–bin j:

$$\delta A_1^{\mathrm{tot}}(x_j) = \sqrt{\sum_i \left([\delta A_1(x_j)]_i\right)^2} . \tag{5.36}$$

In Fig. 5.11 the decomposition of the relative contributions $[\delta A_1]_i$ as a function of x is shown for the inclusive proton asymmetry A_1^{p}, separately for the years 1996 and 1997.

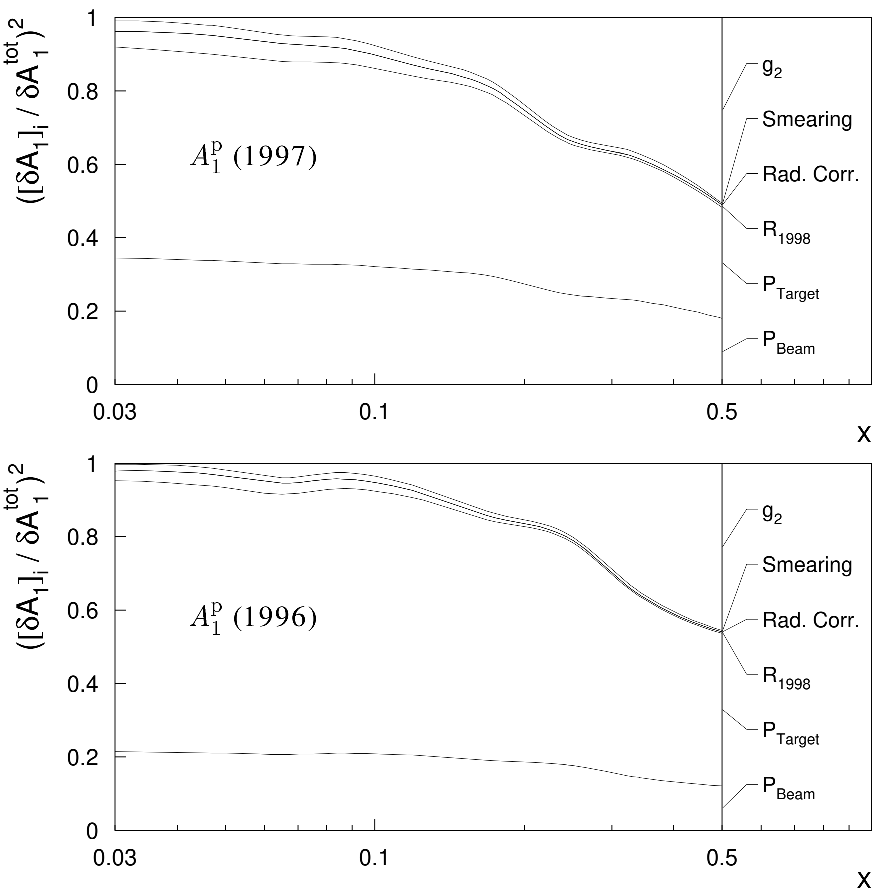

Figure 5.11: Decomposition of the relative systematic uncertainty contributions to the inclusive proton asymmetries A_1^{p} in dependence of x, separately for the years 1996 and 1997. In these diagrams the fractional systematic uncertainties $([\delta A_1]_i/\delta A_1^{\mathrm{tot}})^2$ are shown. Here, $[\delta A_1]_i$ denotes the systematic uncertainty in A_1 arising from the contribution i, and $\delta A_1^{\mathrm{tot}}$ is the total systematic uncertainty. The values of $([\delta A_1]_i/\delta A_1^{\mathrm{tot}})^2$ were calculated at the central value in each x–bin and connected by smooth lines.

In both years, over almost the entire kinematical range the dominating source is the uncertainty on the target polarisation. The contribution from the uncertainty on the spin structure function $g_2(x)$ is strongly dependent on the kinematics and becomes the largest term in Eqn. (5.36) in the highest x–bin. Another sizeable contribution arises from the uncertainty of the beam polarisation measurement. Due to the larger uncertainty in the target polarisation, however, this contribution has less weight in 1996. The three remaining contributions to the total systematic uncertainty are comparatively small and can even be neglected at higher values of x. In Tables D.8 and D.9 the numerical values of the individual contributions and the total systematic uncertainties are listed for the inclusive and the semi inclusive hadron asymmetries.

Similarly to Fig. 5.11, Fig. 5.12 shows the decomposition of the systematic uncertainty on the proton structure function ratio $g_1^{\mathrm{p}}/F_1^{\mathrm{p}}$. As already explained earlier, due to different kinematical weighting, the contribution from the uncertainty in the spin structure function $g_2(x)$ is much smaller than in the case of the asymmetry A_1. For

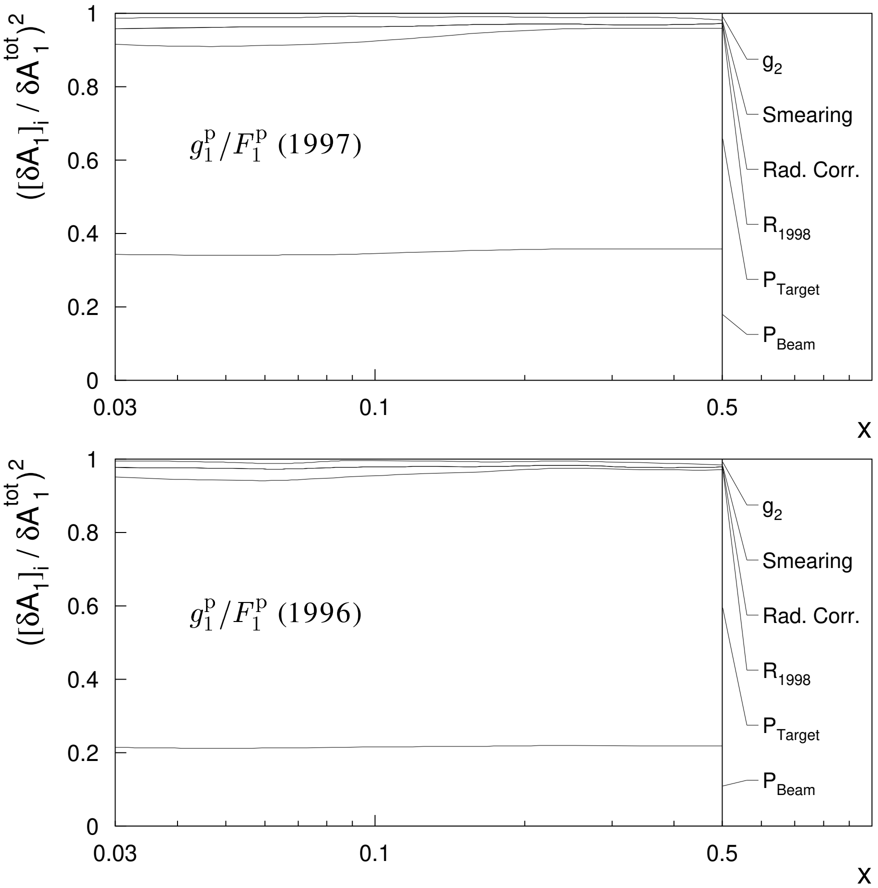

Figure 5.12: Decomposition of the relative systematic uncertainty contributions to the proton structure function ratio $g_1^{\rm p}/F_1^{\rm p}$, separately for 1996 and 1997. The quantities $([\delta A_1]_i/\delta A_1^{\rm tot})^2$ are defined similarly to Fig. 5.11.

the structure function ratio, the decomposition of the systematic uncertainty becomes nearly independent of x and the dominating contributions arise from the target polarisation measurement, followed by the measurement of the beam polarisation.

5.9 Results

In Figure 5.13 the extracted inclusive and semi inclusive virtual photon–nucleon asymmetries $A_1^{(h)}(x)$ on a polarised proton target are shown. The different systematic uncertainties for the data from 1996 and 1997 were combined, weighted by the number of events in each data set. Despite a slightly different normalisation, the inclusive asymmetry $A_{1,\rm p}$ agrees with results on $g_1^{\rm p}/F_1^{\rm p}$ from the SLAC experiment E143 [Abe 98] within the total experimental uncertainties. The data from E143 were taken over a range in Q^2 of $Q^2/\mathrm{GeV}^2 = 1.3 - 9.5$, which is similar to the range at HERMES of $Q^2/\mathrm{GeV}^2 = 1.2 - 5.2$.

The semi inclusive charged hadron asymmetries are compared with results from the SMC experiment [Ade 98a], taken at an average value of $\langle Q^2 \rangle \approx 10\ \mathrm{GeV}^2$, which is significantly larger than the average value of $\langle Q^2 \rangle_{\rm semi} = 2.4\ \mathrm{GeV}^2$ for semi inclusive

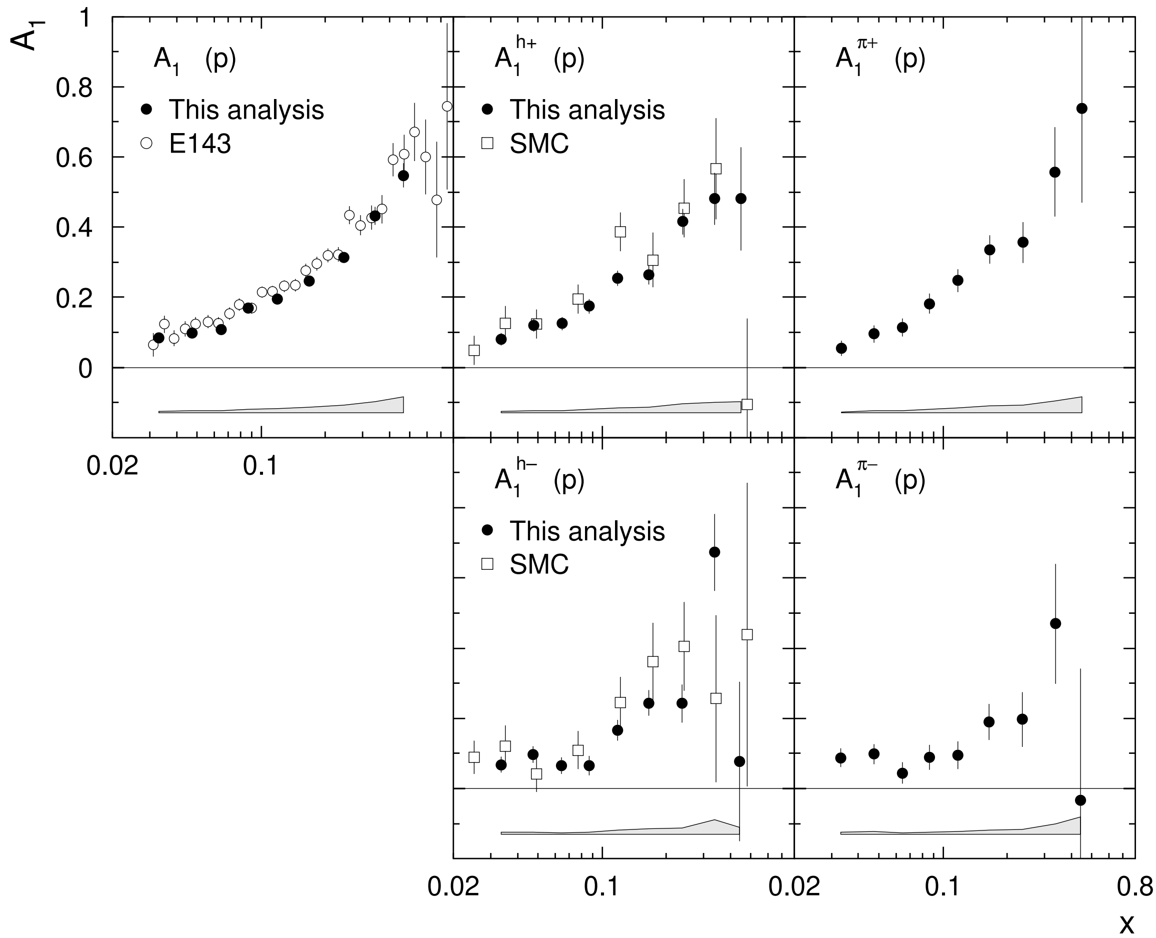

Figure 5.13: The inclusive and semi inclusive charged hadron asymmetries on a polarised proton target as a function of x. For each point the error bars represent the statistical uncertainties; the shaded bands give the systematic uncertainty for the HERMES data. The inclusive asymmetry is compared to SLAC results from the experiment E143 [Abe 98] for g_1/F_1 (open circles). The semi inclusive hadron asymmetries are compared to data from SMC [Ade 98a] (open squares).

events at HERMES. It should be noted that the SMC results have been derived under the (more simple) assumption $A_{2,\mathrm{p}}(x) = 0$ instead of the approximation $g_2^{\mathrm{p}}(x) = 0$ used in this analysis. The agreement between the two experiments is good, despite the large difference in the average values of Q^2. By the inclusion of the HERMES results, the precision of the world data on the charged semi inclusive hadron asymmetries on the proton improves significantly. The semi inclusive charged pion asymmetries on the proton have not been measured by any other experiment previously.

The asymmetries A_1 on the proton are all positive and increase strongly for large values of x. Due to the dominance of up quarks this is already an indication for a large positive polarisation of the valence up quarks in the proton. The semi inclusive negative hadron and pion asymmetries tend to be smaller than the corresponding positive hadron asymmetries, which can be interpreted in terms of a much smaller or even negative polarisation of the down quarks. Negatively charged hadrons in coincidence with a DIS positron are created predominantly in the fragmentation process when a down quark has been struck in the DIS process, instead of an up quark.

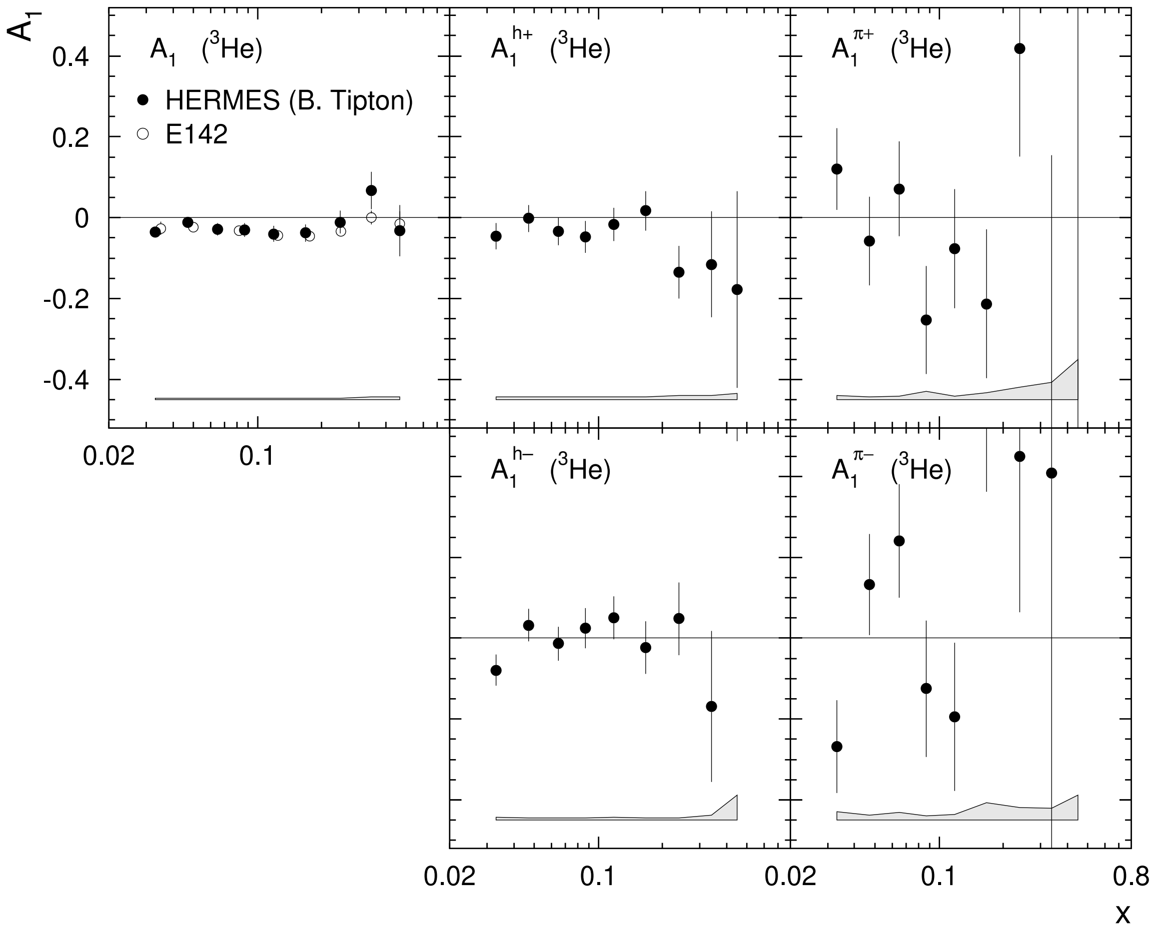

Figure 5.14: The inclusive and semi inclusive charged hadron asymmetries on a polarised ^{3}He target [Tip 99] as a function of x. For each point the error bars represent the statistical uncertainties. The shaded bands give the systematic uncertainty for the HERMES data. For the inclusive asymmetry the HERMES results are compared to data from the SLAC experiment E142 [Ant 96] for g_1/F_1 (open circles).

In Figure 5.14 the HERMES results on the inclusive and semi inclusive hadron asymmetries on a ^{3}He target [Tip 99] are shown; the values are listed in Tab. D.7. The inclusive asymmetry $A_{1,^3\mathrm{He}}$ agrees well with results from the SLAC experiment E142 [Ant 96]. The semi inclusive asymmetries for charged hadrons and identified pions have not been measured by any other experiment. The inclusive and semi inclusive hadron asymmetries on the ^{3}He target will be used together with the corresponding proton asymmetries for the extraction of the polarised quark distributions as described in Chapter 6.

The asymmetries on the helium target are very small and slightly negative. Their dependence on x is very weak in the measured range. The wave function of the ^{3}He nucleus is dominated by the state with the two proton spins paired to spin zero, so that most of the observed asymmetry arises from scattering off the neutron. Since the inclusive asymmetry A_1 is related to the polarised and unpolarised quark distributions by $A_1(x,Q^2) = \sum_f e_f^2 \Delta q_f(x,Q^2) / \sum_{f'} e_{f'}^2 q_{f'}(x,Q^2)$, the observed very small asymmetry on the ^{3}He target together with the large positive asymmetry on the proton target is a hint for a negative polarisation of the down quarks to compensate the above mentioned positive polarisation of the up quarks.

6 Extraction of Polarised Quark Distributions

As laid out in Chapters 2 and 5, the measured semi inclusive photon–nucleon asymmetries $A_1^h(x)$ provide insight into the spin structure of the nucleon. In this chapter a formalism is introduced to relate the measured asymmetries to the polarised parton densities in the nucleon. Using the results presented in the previous chapter, polarised up, down, and sea quark distributions are extracted and compared with an existing measurement and parametrisations of these quantities.

6.1 The Purity Formalism

Recalling Eqn. (2.86), the semi inclusive virtual photon–nucleon asymmetries $A_1^h(x,Q^2)$ can be related to the polarised and unpolarised PDFs on the nucleon:

$$A_1^h(x,Q^2) \overset{g_2^h=0}{\simeq} \frac{g_1^h(x,Q^2)}{F_1^h(x,Q^2)} = \frac{1+R(x,Q^2)}{1+\gamma^2} \cdot \frac{\sum_f e_f^2\, \Delta q_f(x,Q^2) \int_{z_{\min}}^1 \mathrm{d}z\, D_f^h(Q^2,z)}{\sum_f e_f^2\, \widetilde{q}_f(x,Q^2) \int_{z_{\min}}^1 \mathrm{d}z\, D_f^h(Q^2,z)} . \tag{6.1}$$

In contrast to Eqn. (2.86), an additional factor $(1+R)/(1+\gamma^2)$, and modified unpolarised PDFs $\widetilde{q}_f$ occur in this relation. While Eqn. (2.86) is valid in leading order QCD, the above equation (6.1) is rephrased using quantities, which are derived from measurements. The origin of this difference will be illuminated in the following two paragraphs.

In the analysis presented here, two different parametrisations for the unpolarised quark distributions are used: *CTEQ4LQ* (low Q^2, NLO) [Lai 97], and alternatively *GRV* (LO) [Glü 95]. Technically, the LO parametrisations are obtained by fits of the expression

$$F_2(x,Q^2) = \sum_f x\, e_f^2\, \widetilde{q}_f(x,Q^2) \tag{6.2}$$

to world data on $F_2(x,Q^2)$. The values for the unpolarised structure function $F_2(x,Q^2)$ were in turn extracted from measurements of cross sections, using non–zero values for the cross section ratio $R=\sigma_L/\sigma_T$ and $\gamma^2 = Q^2/\nu^2$.

Owing to Eqns. (2.17) and (6.2), the parton distributions $\widetilde{q}_f(x,Q^2)$ obtained from the global fits to world data can be related to the structure function $F_1(x,Q^2)$:

$$F_1(x,Q^2) = \frac{1+\gamma^2}{1+R(x,Q^2)}\, \frac{1}{2} \sum_f e_f^2\, \widetilde{q}_f(x,Q^2) , \tag{6.3}$$

thus explaining the additional factor in Eqn. (6.1). For simplicity, the unpolarised PDFs from the above mentioned parametrisations will again be labelled $q_f(x,Q^2)$ hereafter.

In this analysis, the asymmetries $A_1^{(h)}(x,Q^2)$ are evaluated in x–bins and integrated over the corresponding range in Q^2 (and in z, in case of the semi inclusive asymmetries). This leads to a further modification of Eqn. (6.1):

$$\begin{aligned} A_1^h(x_i) &\overset{g_2=0}{\simeq} \underbrace{\frac{1+R(x_i,Q_i^2)}{1+\gamma_i^2}}_{=\mathcal{C}_i} \cdot \frac{\sum_f e_f^2 \int_{1.0}^{\infty} \mathrm{d}Q^2\, \Delta q_f(x_i,Q^2) \int_{0.2}^1 \mathrm{d}z\, D_f^h(Q^2,z)\, \mathcal{A}(x_i,Q^2,z)}{\sum_f e_f^2 \int_{1.0}^{\infty} \mathrm{d}Q^2\, q_f(x_i,Q^2) \int_{0.2}^1 \mathrm{d}z\, D_f^h(Q^2,z)\, \mathcal{A}(x_i,Q^2,z)} \\ &= \mathcal{C}_i \cdot \frac{\sum_f e_f^2\, \Delta q_f(x_i,Q_i^2)\, \mathcal{D}_f^h(x_i,Q_i^2,z_i)}{\sum_f e_f^2\, q_f(x_i,Q_i^2)\, \mathcal{D}_f^h(x_i,Q_i^2,z_i)} , \end{aligned} \tag{6.4}$$

where $\mathcal{A}(x, Q^2, z)$ is the acceptance function of the spectrometer for events with the kinematics (x, Q^2, z). The kinematic quantities with the subscript i in Eqn. (6.4) denote the respective mean values of all events in bin number i. The acceptance function can be multiplied with the fragmentation functions to form *effective* fragmentation functions $\mathcal{D}_f^h(x, Q^2, z)$, which give the probability that a quark of flavour f, probed in a semi inclusive scattering process with the kinematics (x, Q^2), fragments into a hadron h with fractional energy z within the acceptance of the spectrometer. Furthermore, Eqn. (6.4) can be generalised to describe inclusive scattering processes as well. In this case, the fragmentation function becomes $D_f(z, Q^2) \equiv 1$, independent of the kinematics, and the effective fragmentation function merely reproduces the acceptance function of the spectrometer, $\mathcal{D}_f(x, Q^2) = \mathcal{A}(x, Q^2)$.

As the key approach of this analysis, one introduces the *purities* [Nic 98], which are unpolarised quantities and defined by

$$P_f^h(x_i) \;:=\; \frac{e_f^2\, q_f(x_i, Q_i^2)\, \mathcal{D}_f^h(x_i, Q_i^2, z_i)}{\sum_{f'} e_{f'}^2\, q_{f'}(x_i, Q_i^2)\, \mathcal{D}_{f'}^h(x_i, Q_i^2, z_i)}\,. \tag{6.5}$$

Note that the purities only depend on a single free parameter x_i in this definition, as the mean values Q_i^2 and z_i are fixed within one x–bin i. Obviously, the purities add up to one in each bin: $\sum_f P_f^h(x_i) \;=\; 1$.

The purities may be physically interpreted as the probability that an event of type h originated from scattering off a quark of flavour f in the nucleon. As already mentioned, the purities can also be generalised to inclusive scattering processes. These *inclusive* purities are labelled $P_f^{e^+}(x_i)$. Under the assumption that the acceptance function of the spectrometer only depends on the kinematics of the scattering process, but not on the flavour of the struck quark, the effective fragmentation functions in Eqn. (6.5) cancel out for the inclusive purities:

$$P_f^{e^+}(x_i) \;=\; \frac{e_f^2\, q_f(x_i, Q_i^2)}{\sum_{f'} e_{f'}^2\, q_{f'}(x_i, Q_i^2)}\,. \tag{6.6}$$

Using the definition of purities in Eqn. (6.5), the above Eqn. (6.4) can be rewritten as

$$A_1^h(x_i) \;=\; \mathcal{C}_i \cdot \sum_f P_f^h(x_i) \cdot \frac{\Delta q_f(x_i, Q_i^2)}{q_f(x_i, Q_i^2)} \;\simeq\; \mathcal{C}_i \cdot \sum_f P_f^h(x_i) \cdot \frac{\Delta q_f}{q_f}(x_i)\,. \tag{6.7}$$

In this expression we assume that the ratio of the polarised to the unpolarised PDFs is approximately independent of Q^2. This assumption was justified in Sect. 2.5, given the limited range of Q^2 within one x–bin. Equation (6.7) is the central expression used in this analysis to relate the quark polarisations $\Delta q/q$ to the measured asymmetries $A_1^{(h)}$.

Under the assumption of factorisation (see Sect. 2.7.1), the purities provide a simple way to separate the polarised quark distributions from other quantities, which are related to unpolarised physics and the detector geometry. Compared to the polarised PDFs, the input parameters for the purities are known with good precision from a large number of DIS experiments on unpolarised targets, augmented by data on fragmentation functions from e^+e^-–colliders. The generation of purities will be explained in detail in Sect. 6.2.

Obviously, in order to determine the quark polarisations for more than one flavour, also more than one measured asymmetry is needed. For a set of m asymmetries and

n different quark polarisations to be extracted, Eqn. (6.7) turns into a system of linear equations. Using the definitions

$$\vec{A}(x_i) = \begin{pmatrix} A_1^{h_1}(x_i) \\ \vdots \\ A_1^{h_m}(x_i) \end{pmatrix}, \quad \vec{Q}(x_i) = \begin{pmatrix} \frac{\Delta q_1}{q_1}(x_i) \\ \vdots \\ \frac{\Delta q_n}{q_n}(x_i) \end{pmatrix}, \quad \mathbf{P}(x_i) = \begin{pmatrix} P_{q_1}^{h_1}(x_i) & \cdots & P_{q_n}^{h_1}(x_i) \\ \vdots & \ddots & \vdots \\ P_{q_1}^{h_m}(x_i) & \cdots & P_{q_n}^{h_m}(x_i) \end{pmatrix}, \tag{6.8}$$

the central purity Equation (6.7) may be recast in matrix form:

$$\vec{A} = \mathcal{C}_i \cdot \mathbf{P}\,\vec{Q}\,. \tag{6.9}$$

This system of linear equations is typically overdetermined, as the number of asymmetries is larger than the number of different quark polarisations to be extracted. Ideally, from m different asymmetries one could determine as many different quark polarisations $n = m$. In the present analysis, the vector $\vec{A}$ contains nine different asymmetries, $\vec{A} = (A^{e+}_{^3\mathrm{He}}, A^{h^+}_{^3\mathrm{He}}, A^{h^-}_{^3\mathrm{He}}, A^{e+}_{\mathrm{p},96}, A^{h^+}_{\mathrm{p},96}, A^{h^-}_{\mathrm{p},96}, A^{e+}_{\mathrm{p},97}, A^{h^+}_{\mathrm{p},97}, A^{h^-}_{\mathrm{p},97})$, where the A^h_j are short notations for the virtual photon asymmetry A^h_1 of type h, taken on a target j. The proton asymmetries from the two different years of data taking are treated separately, because of their different systematic uncertainties. Many of the elements in this asymmetry vector are correlated. For instance, the corresponding asymmetries on the proton target are systematically correlated due to the same underlying physics. The inclusive and the semi inclusive asymmetries on one target are correlated statistically, as the semi inclusive events represent a subsample of the inclusive events. These correlations imply that the number of independent asymmetries m' is smaller than the number of elements in $\vec{A}$. Consequently, at most m' independent quark polarisations can be extracted from this system of linear equations. Attempts to extract four different quark polarisations $\Delta u/u, \Delta d/d, \Delta q_\mathrm{s}/q_\mathrm{s}, (\Delta s + \Delta\overline{s})/(s+\overline{s})$ from this set of asymmetries, where $q_\mathrm{s} = \overline{u}, \overline{d}$ denotes the light sea quark flavours, have not resulted in statistically decisive results for the strange quark polarisation [Tip 98]. Hence, in this analysis only three different quark polarisations will be extracted from the given set of asymmetries. As we regard six different quark flavours $f = u, \overline{u}, d, \overline{d}, s, \overline{s}$ in this context, some of these have to be combined, employing symmetry assumptions. This topic will be taken up again in Sect. 6.4.

A solution vector $\vec{Q}$ for Eqn. (6.9) also minimises the expression

$$\chi^2 = \left(\vec{A} - \mathcal{C}_i \cdot \mathbf{P}\,\vec{Q}\right)^{\mathrm{T}} \mathcal{V}_A^{-1} \left(\vec{A} - \mathcal{C}_i \cdot \mathbf{P}\,\vec{Q}\right), \tag{6.10}$$

where $\mathcal{V}_A$ denotes the covariance matrix of the set of asymmetries. This covariance matrix takes into account the correlations between the different elements in the asymmetry vector. The elements $(\mathcal{V}_A)_{jk}$ of this matrix contain the product of the uncertainties of the asymmetries of types j, k and the correlation coefficient ρ_{jk} between these two asymmetries,

$$(\mathcal{V}_A)_{jk} = \rho_{jk}\, \delta A_1^{h_j}\, \delta A_1^{h_k}\,. \tag{6.11}$$

The correlation coefficient between two identical elements in the asymmetry vector is unity, so that the diagonal elements of the covariance matrix contain the squares of the total uncertainties of the asymmetry of type j:

$$(\mathcal{V}_A)_{jj} \;=\; \left[\delta A_1^{h_j}\right]^2 . \tag{6.12}$$

The covariance matrix $\mathcal{V}_A$ may be split in two parts

$$\mathcal{V}_A \;=\; \mathcal{V}_A^{\text{stat}} + \mathcal{V}_A^{\text{sys}} , \tag{6.13}$$

which contain the statistical and the systematic correlations, respectively. The systematic covariance matrix $\mathcal{V}_A^{\text{sys}}$ will be treated in more detail in Sect. 6.5.3 at the calculation of the systematic uncertainties.

As shown in [Pre 97], the statistical correlation coefficients ρ_{jk} can be related to the averaged particle multiplicities for each event type, $\langle n^{h_j}\rangle$:

$$\rho_{jk} \;\equiv\; \mathrm{Cor}(A_1^{h_j}, A_1^{h_k}) \;=\; \frac{\langle n^{h_j}\, n^{h_k}\rangle}{\sqrt{\langle (n^{h_j})^2\rangle\,\langle (n^{h_k})^2\rangle}} . \tag{6.14}$$

Note that by definition $n^{e^+} \equiv 1$, and that the statistical correlation between asymmetries from two different years vanishes. Furthermore, the above expression is only valid when the asymmetries are not too close to one, and when the distributions of events fulfil the requirements for the applicability of a Poisson distribution. Both conditions are met at HERMES. The measured experimental asymmetries $A_{\|}^{\text{exp}}$ are $\lesssim 0.15$ in almost every kinematical bin, and the probability p for a detected deep inelastic scattering event per positron–target nucleon approach is almost zero. The elements of the statistical covariance matrix $\mathcal{V}_A^{\text{stat}}$ were calculated from the particle multiplicities, according to Eqns. (6.11) and (6.14). In Tables D.10 and D.11 the correlation coefficients for the proton and ^{3}He asymmetries are listed.

The covariance matrix $\mathcal{V}_Q$ for the quark polarisations is related to the covariance matrix $\mathcal{V}_A$ for the asymmetries by

$$\mathcal{V}_Q \;=\; \mathcal{C}_i^{-1}\,\left(\mathbf{P}^{\mathrm{T}}\,\mathcal{V}_A^{-1}\,\mathbf{P}\right)^{-1} . \tag{6.15}$$

Like for the covariance matrix of the asymmetries, the diagonal elements of the quark covariance matrix contain the squared uncertainties of the quark polarisations:

$$\delta\frac{\Delta q_j}{q_j} \;=\; \sqrt{(\mathcal{V}_Q)_{jj}} . \tag{6.16}$$

This expression gives the recipe for the determination of the uncertainties on the extracted quark polarisations.

Technically, the solution of Eqn. (6.10) is obtained by employing the **S**ingular **V**alue **D**ecomposition (SVD) method [Pre 92, Fun 98]. SVD is a numerically very stable algorithm for the solution of systems of linear equations, which show *singular* values. A set of equations is called singular, in case it is degenerate, that is if one or more equations are linear combinations of the other equations. As laid out above, the elements of the asymmetry vector are highly correlated, corresponding to an almost degeneracy of the system of equations. To avoid numerical instabilities, an implementation of the SVD algorithm is used in this analysis. A detailed description of the algorithm and its implementation can be found in [Fun 98].

6.2 Generation of Purities

The purities only depend on unpolarised physics quantities and on the acceptance function of the detector. A Monte Carlo method is used for the generation of the purities from the parameters in Eqn. (6.5). This section details the process of the generation of purities, as depicted schematically in Fig. 6.1.

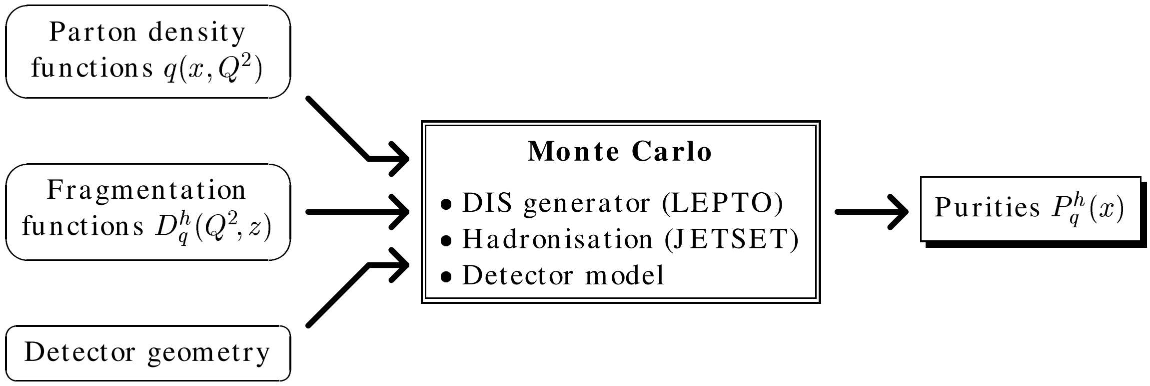

Figure 6.1: A schematic diagram of the generation of purities.

In a first step, DIS events are generated on the parton level with the LEPTO Monte Carlo program [Ing 97]. In this analysis, by default the CTEQ4LQ parametrisation of unpolarised PDFs was used as input for the event generation. This particular parametrisation was chosen because of its low initial evolution scale of $Q_0^2 = 0.5\,\mathrm{GeV}^2$ [Lai 97]. Alternatively, the LO GRV set is used to estimate the systematic uncertainty arising from the choice of unpolarised PDFs. The kinematic cuts used for the generation of events match those used in the analysis of the semi inclusive asymmetries, as given in Sect. 5.4.2

Table 6.1: Settings of the JETSET parameters for the different fragmentation models used in this analysis. An entry "–" in the table means that the default value for this parameter was left unchanged. The same applies for all other JETSET parameters, which are not listed in this table. A detailed description of the physical meaning of the listed parameters can be found in [Sjö 94] and [Ruh 99].

Parameter name in JETSET	Default value	Model		
		SF1	SF2	IF
PARJ(1)	0.10	–	0.01	–
PARJ(14)	0.00	–	–	0.23
PARJ(21) [GeV]	0.36	0.34	0.40	0.31
PARJ(41)	0.30	0.82	0.15	1.38
PARJ(42) [GeV^{-2}]	0.58	0.24	0.35	1.16
MSTJ(1)	1	–	–	2
MSTJ(2)	3	–	–	1
MSTJ(3)	0	–	–	1
MSTJ(42)	2	–	–	1

Next, the hadronisation of the generated partons is simulated in the JETSET Monte Carlo package [Sjö 94], which is based on the LUND string model. As explained in Sect. 2.8.2, this model contains several parameters, which have been tuned in a specific procedure for an optimum description of the hadron multiplicity spectra measured at HERMES [Gei 98, Tal 98]. This standard setting is called "SF1" and the corresponding parameters are listed in Table 6.1. For an estimate of the systematic uncertainty due to the description of the hadronisation process by this Monte Carlo, purities were alternatively generated with a second set of parameters (SF2), which were tuned to multiplicities of identified pion only instead of all hadrons. Purities were also generated using the Independent Fragmentation model (IF) with a tuned set of parameters for an optimum description of measured hadron spectra [Ruh 99]. The parameters for the models SF2 and IF are given in Tab. 6.1 as well.

To model the acceptance of the HERMES detector, the Monte Carlo package HMC [HMC 96] exists. However, this very detailed simulation requires a lot of CPU time. In order to facilitate the generation of samples for different choices of the unpolarised PDFs and different fragmentation models with sufficient statistics, a more simple approach was chosen here. The geometrical acceptance of the spectrometer was modelled with the same cuts on the scattering angle as in the analysis of the data. This *box acceptance* model was augmented by a look–up table, which parameterises the bending of the charged particles' tracks in the field of the spectrometer magnet, depending on the position and momentum of the track. This look–up table was calculated once from tracking many particle trajectories with different starting positions and angles. In this simulation, a measurement of the field of the spectrometer magnet on a fine grid in three dimensions is employed [Wan 96]. Behind the magnet, the particle tracks were again approximated by straight lines, neglecting multiple scattering in the backward detectors. The generated tracks were furthermore subject to all event selection cuts applied to the data, as listed in Tab. 5.3.

For a proton and a neutron target, purities were generated from samples of 20 million DIS events on each target. Due to the high statistics of the generated samples, the statistical uncertainty on the purities can be neglected when compared to the data. As already noted earlier, sets of purities with the same statistics were also generated for two different choices of the fragmentation model, and for a different parametrisation of the unpolarised PDFs. In Fig. 6.2 the purities for the proton and the neutron are shown, obtained from the CTEQ4LQ parton distribution and the tuned LUND string fragmentation model SF1. On both targets, the purities for up quarks are dominating in almost the entire kinematical range, except for the negative hadrons on the neutron target in the highest x–bins. This dominance arises from the charge weighting factor in Eqn. (6.5), which enhances the up quarks by a factor of four over the other flavours. For technical reasons, the *inclusive* purities were calculated from the unpolarised PDFs according to Eqn. (6.6), instead of deriving them from the Monte Carlo method as described above.

6.3 Modelling of ^{3}He Asymmetries

The parton distributions of interest are defined on the proton. The corresponding quantities on the neutron are easily obtained by an isospin rotation $u \leftrightarrow d$, and $\overline{u} \leftrightarrow \overline{d}$. Consequently, also the purities are defined on the nucleon targets. Experimentally however, a polarised free neutron target is not available, so that nuclear targets with

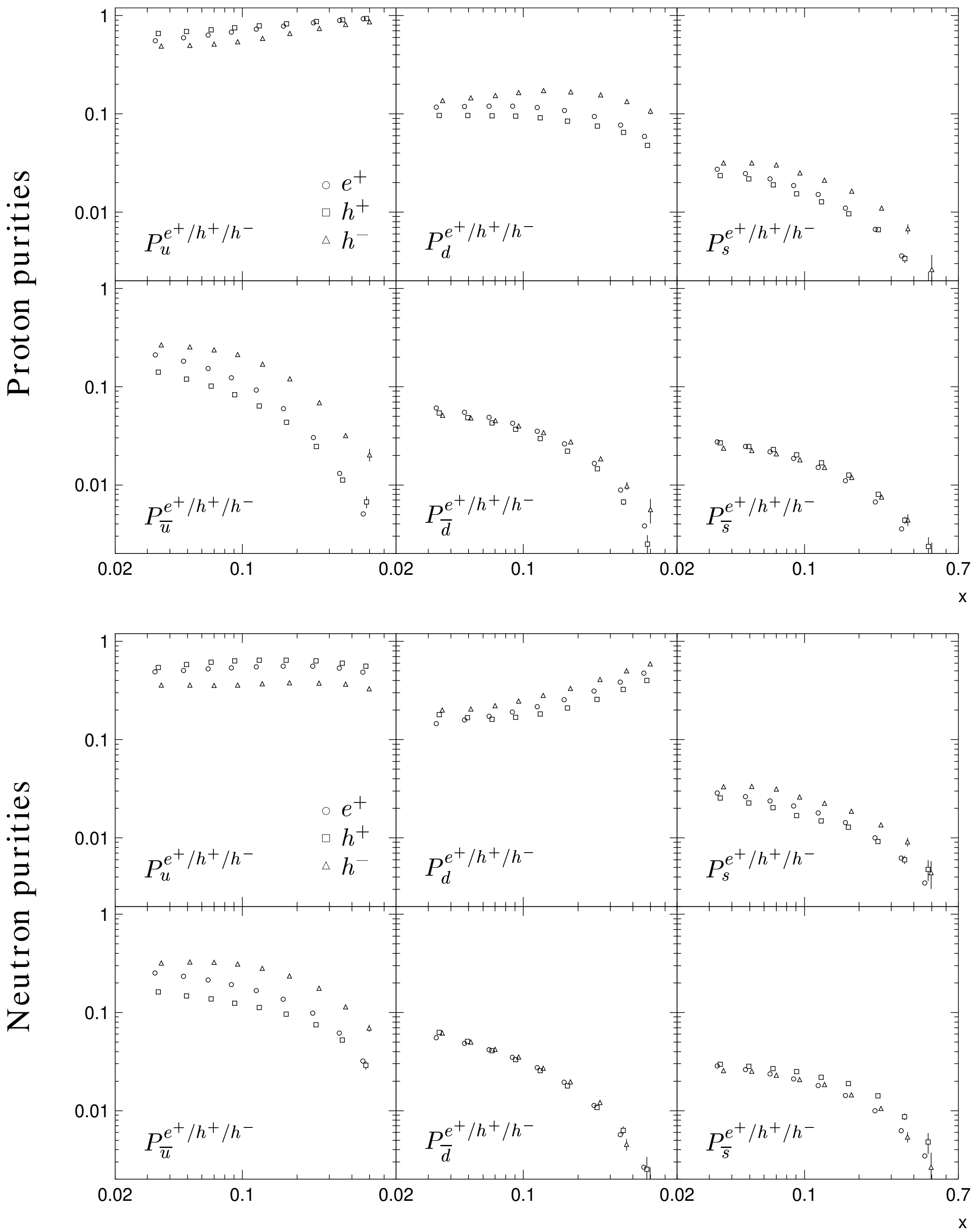

Figure 6.2: Purities on a proton (upper block) and on a neutron target (lower block), generated from the CTEQ4 low Q^2 [Lai 97] PDFs and the tuned LUND string fragmentation model (SF1). In each panel, for a given quark flavour q the purities for positive (h^+) and negative (h^-) hadrons are shown together with the pseudo–purities (e^+) for inclusive events.

an unpaired neutron (d,^{3}He) are employed instead.

In the case of ^{3}He, the two protons couple to spin zero in the ground state, so that the nuclear spin is completely due to the spin of the neutron. The complete wave function of the ^{3}He nucleus also contains admixtures with higher orbital angular momenta, where the proton spins are not paired to zero any longer. These admixtures lead to a dilution of the neutron's contribution to the nuclear spin. The effective polarisations of the protons and the neutron in the ^{3}He nucleus are $p^{\mathrm{p}}_{^3\mathrm{He}} = -0.028 \pm 0.004$, and $p^{\mathrm{n}}_{^3\mathrm{He}} = 0.86 \pm 0.02$, respectively [Att 93]. In order to relate the asymmetries measured on ^{3}He and proton targets to the parton distributions defined on the nucleon, it is necessary to model the ^{3}He asymmetry in terms of asymmetries on the constituent nucleons. Note that this modelling may not simply be performed by generating purities on a ^{3}He target, as the resulting quark polarisations would give the average quark polarisations in a ^{3}He nucleus, instead of a nucleon. These results might of course be transformed into the effective quark polarisations on the nucleon, using a model of the ^{3}He nucleus. Yet this procedure would suffer from the disadvantage, that the model for the ^{3}He nucleus had to be applied twice: once at the generation of the purities and once for the transformation of the resulting quark polarisations.

Here a different ansatz [Fun 98, Tip 99] is pursued, where it is assumed that the nuclear structure functions are the incoherent superpositions of proton and neutron structure functions. This ansatz neglects coherent nuclear effects, like the EMC effect on inclusive structure functions, or nuclear effects on the hadronisation process [Ack 99b] in semi inclusive structure functions. As we only consider the light ^{3}He nucleus here, these effects are negligible compared to other sources of systematic uncertainties. Under these premises, the asymmetry measured on a ^{3}He target can be expressed in terms of the proton and neutron asymmetries:

$$A^h_{1,^3\mathrm{He}} = f^h_{\mathrm{p}}\, p^{\mathrm{p}}_{^3\mathrm{He}}\, A^h_{1,\mathrm{p}} + f^h_{\mathrm{n}}\, p^{\mathrm{n}}_{^3\mathrm{He}}\, A^h_{1,\mathrm{n}} \,. \tag{6.17}$$

The dilution factors $f^h_{\mathrm{p(n)}}$ give the probability that the scattering took place on one of the two protons (on the neutron). Obviously, they add up to one, $f^h_{\mathrm{p}} + f^h_{\mathrm{n}} = 1$. The dilution factor for the proton may be expressed as

$$f^h_{\mathrm{p}} = \frac{2\,\sigma^h_{\mathrm{p}}}{\sigma^h_{^3\mathrm{He}}} = \frac{2\,n^h_{\mathrm{p}}}{n^h_{^3\mathrm{He}}} \cdot \frac{\sigma_{\mathrm{p}}}{\sigma_{^3\mathrm{He}}} = \frac{2\,n^h_{\mathrm{p}}}{n^h_{^3\mathrm{He}}} \cdot \left(\frac{F^{\mathrm{p}}_2}{2F^{\mathrm{d}}_2 + F^{\mathrm{p}}_2}\right) \,. \tag{6.18}$$

In this expression, $\sigma^h_{\mathrm{p},^3\mathrm{He}}$ denote the integrated cross sections for events of the class h on a proton and on a ^{3}He target, while $\sigma_{\mathrm{p},^3\mathrm{He}}$ are the inclusive cross sections, respectively. The $n^h_{p,^3\mathrm{He}}$ are the multiplicities for a particle type h on the respective target. For brevity, the explicit dependence of the cross sections and the multiplicities on the kinematics (x, Q^2) has been omitted in the above expressions.

Using Eqn. (6.17), the asymmetry on the neutron can be distilled from the measured asymmetry on ^{3}He by subtraction of the proton contributions:

$$A^h_{1,\mathrm{n}} = \frac{1}{p^{\mathrm{n}}_{^3\mathrm{He}}(1 - f^h_{\mathrm{p}})} \cdot \left(A^h_{1,^3\mathrm{He}} - f^h_{\mathrm{p}}\, p^{\mathrm{p}}_{^3\mathrm{He}}\, A^h_{1,\mathrm{p}}\right) \,. \tag{6.19}$$

This analysis uses to above model to relate the purities and quark polarisations defined on the nucleons to the asymmetries measured on ^{3}He and proton targets. For this, the elements of the vector $\vec{A}$ and the rows of the purity matrix $\mathbf{P}$ in Eqn. (6.9) are ordered according to the targets they are referring to. The recipe in Eqn. (6.17) to model the ^{3}He asymmetry from the nucleon contributions may then easily be implemented using a new matrix:

$$\begin{pmatrix} \vec{A}_{\mathrm{p}} \\ \vec{A}_{^3\mathrm{He}} \end{pmatrix} = \mathcal{C}_i \cdot \mathbf{N} \cdot \begin{pmatrix} \mathbf{P}_{\mathrm{p}} \\ \mathbf{P}_{\mathrm{n}} \end{pmatrix} \cdot \vec{Q} \,, \tag{6.20}$$

where the nuclear mixing matrix $\mathbf{N}$ is defined as

$$\mathbf{N} := \begin{pmatrix} 1 & & & & & \\ & \ddots & & & 0 & \\ & & 1 & & & \\ a_{h_1} & & & b_{h_1} & & \\ & \ddots & & & \ddots & \\ & & a_{h_m} & & & b_{h_m} \end{pmatrix} , \tag{6.21}$$

with

$$a_{h_j} = f_{\mathrm{p}}^{h_j} \cdot p_{^3\mathrm{He}}^{\mathrm{p}} \,, \qquad b_{h_j} = (1 - f_{\mathrm{p}}^{h_j}) \cdot p_{^3\mathrm{He}}^{\mathrm{n}} \,. \tag{6.22}$$

For a more detailed review of this method, see [Fun 98]. A limitation arises from the requirement that the corresponding proton asymmetries must be known for all used asymmetries taken on the nuclear target. Since the year 1998, DIS asymmetries are being measured on a polarised deuterium target at HERMES, which also requires a similar modelling as for the ^{3}He target. Coincident with the beginning of data taking on polarised deuterium, the threshold Čerenkov counter has been replaced by a RICH detector, which provides the possibility to identify pions, kaons, and protons over a wide kinematic range. However, no corresponding semi inclusive kaon and proton asymmetries on a proton target are available, and the model presented here can not be applied for the analysis of these semi inclusive asymmetries.

6.4 Modelling of the Sea and the Separation of Quark Flavours

The measured set of asymmetries is not sufficient to determine the polarised quark distributions individually for all flavours $f = u, \overline{u}, d, \overline{d}, s, \overline{s}$ with statistically significant precision. As a consequence of the dominance of the purities for the u and d quarks, this applies in particular for the contributions from the sea flavours $\overline{u}, \overline{d}, s$, and $\overline{s}$. Using symmetry assumptions on the individual polarised sea quark distributions, in the following paragraphs different models will be presented for the construction of a common polarised sea quark distribution $\Delta q_{\mathrm{s}}(x)$.

The most simple model uses the trivial assumption of an unpolarised sea $\Delta\overline{u}(x) = \Delta\overline{d}(x) = \Delta s(x) = \Delta\overline{s}(x) \equiv 0$. While this model allows the statistically most precise determination of the polarisation of the up and down quarks, fixing the sea polarisation to zero in advance is not motivated by the discussion in Sect. 2.6.2, where is was argued that the strange sea quarks might indeed contribute significantly to the spin of the nucleon. For this reason, the model of an unpolarised sea is not considered here.

The next simpler model is based on the ansatz of $SU(3)_f$ symmetry for the polarised sea quark distributions:

$$\Delta q_{\mathrm{s}} \equiv \Delta u_{\mathrm{s}} = \Delta d_{\mathrm{s}} = \Delta s = \Delta\overline{u} = \Delta\overline{d} = \Delta\overline{s} \neq 0 \,. \tag{6.23}$$

This assumption is employed in various parametrisations of polarised quark distributions (e.g. [Geh 96a, Flo 98]). For the extraction of the average sea polarisation, the purity P^h_{sea} is given by

$$P^h_{\text{sea}}\,\frac{\Delta q_{\text{s}}}{q_{\text{s}}} \;=\; \left(P^h_{\overline{u}}\,\frac{1}{\overline{u}} + P^h_{\overline{d}}\,\frac{1}{\overline{d}} + P^h_{s}\,\frac{1}{s} + P^h_{\overline{s}}\,\frac{1}{\overline{s}}\right)\Delta q_{\text{s}}\,. \tag{6.24}$$

However, for the *unpolarised* sea quark distributions the $SU(3)_f$ symmetry is broken [Haw 98, Pen 98, Ack 98b], so that there is no strong reason for Eqn. (6.23) to be strict. Furthermore, the unpolarised strange sea quark density $s(x)$ is significantly smaller than $\overline{u}(x)$ and $\overline{d}(x)$, which may lead to a result violating the positivity limit $|\Delta s/s| \leq \mathcal{C}_i^{-1}$ in the $SU(3)_f$ symmetric sea model, where the factor $\mathcal{C}_i$ is defined in Eqn. (6.4).

This problem is absent in a sea model, which assumes that the sea quark *polarisation* is symmetric instead of the polarised quark *distributions*:

$$\frac{\Delta q_{\text{s}}}{q_{\text{s}}} \;\equiv\; \frac{\Delta u_{\text{s}}}{u_{\text{s}}} \;=\; \frac{\Delta\overline{u}}{\overline{u}} \;=\; \frac{\Delta d_{\text{s}}}{d_{\text{s}}} \;=\; \frac{\Delta\overline{d}}{\overline{d}} \;=\; \frac{\Delta s}{s} \;=\; \frac{\Delta\overline{s}}{\overline{s}}\,. \tag{6.25}$$

The corresponding purity for the average sea polarisation is simply obtained from

$$P^h_{\text{sea}}\,\frac{\Delta q_{\text{s}}}{q_{\text{s}}} \;=\; \left(P^h_{\overline{u}} + P^h_{\overline{d}} + P^h_{s} + P^h_{\overline{s}}\right)\frac{\Delta q_{\text{s}}}{q_{\text{s}}}\,. \tag{6.26}$$

The model in Eqn. (6.25) of a flavour symmetric sea arises naturally in a simple scenario, where the sea consists of an equilibrium of $q\overline{q}$ pairs from the continuous production and annihilation in a helicity–conserving process.

There are other models existing, like a chiral quark–soliton model [Dre 99], which predict a sizeable positive difference $\Delta\overline{u}(x) - \Delta\overline{d}(x) > 0$. Together with the results [Haw 98, Pen 98, Ack 98b] on the flavour asymmetry of the unpolarised sea, which has the opposite sign $\overline{u}(x) - \overline{d}(x) < 0$, this implies that up and down sea–flavours have opposite polarisations in this model.

In view of the rather ambiguous theoretical model predictions, the assumption given in Eqn. (6.25) was used in all extractions of polarised parton density functions, unless noted otherwise. As will be shown in Sect. 6.5, the sensitivity of the extracted quark polarisations on the chosen sea model is small. Besides the already mentioned low sensitivity from the magnitude of the purities for the sea quarks, this is also a hint that the absolute values of the polarised sea parton densities should be small, so that the positivity limit is not significantly violated in a $SU(3)_f$ flavour symmetric model (see Eqn. (6.23)).

In addition to the sea models, several options for the treatment of the valence quarks, or the up and down flavours are available. In this work, two different combinations of quark flavours have been studied. In the *flavour decomposition*, the quark polarisations are extracted for sets of quarks and anti–quarks of the same flavour:

$$\frac{\Delta u + \Delta\overline{u}}{u + \overline{u}}\,, \qquad \frac{\Delta d + \Delta\overline{d}}{d + \overline{d}}\,, \qquad \frac{\Delta s + \Delta\overline{s}}{s + \overline{s}}\,. \tag{6.27}$$

Due to the assumption in Eqn. (6.25) the polarisation of the strange quark flavours equals the average polarisation of the sea quarks, $(\Delta s + \Delta\overline{s})/(s + \overline{s}) \equiv \Delta q_{\text{s}}/q_{\text{s}}$. Again note that the polarisation of the average sea is dominated by the polarisation of the up flavour in the sea because of its abundance and the charge weighting factor in the cross section. This dominance of the up flavour is also reflected by the magnitudes of the corresponding purities for the sea flavours (cf. Fig. 6.2). To express the fact that the third quark polarisation in Eqn. (6.27) is not an independent determination of the *strange* sea polarisation, this quantity will be labelled $\Delta q_{\mathrm{s}}/q_{\mathrm{s}}$ hereafter. The purity coefficients for the three quark polarisations in Eqn. (6.27) are obtained by rearranging the terms in Eqn. (6.7), as given in App. C.

In the *valence decomposition* the quark polarisations are separated into contributions from valence and from sea quarks:

$$\frac{\Delta u_{\mathrm{v}}}{u_{\mathrm{v}}}, \quad \frac{\Delta d_{\mathrm{v}}}{d_{\mathrm{v}}}, \quad \frac{\Delta q_{\mathrm{s}}}{q_{\mathrm{s}}}, \tag{6.28}$$

where Eqn. (6.25) is used to express the polarisation of the sea flavours. The purity coefficients for this combination are also given in App. C and are obtained in analogy to the flavour separation from rearranging the terms in Eqn. (6.7). In the following section results for the flavour and for the valence decompositions are presented.

6.5 Results on Polarised Quark Distributions

All the results on polarised quark distributions presented in this section were derived by solving Eqn. (6.20), using the set of inclusive and semi inclusive hadron asymmetries listed in Sect. 6.1. A check of the purity extraction mechanism has been performed in [Tip 99], for which the polarised PDFs used as input for the Monte Carlo generation of asymmetries were retrieved by solving the purity equation.

6.5.1 The Flavour Decomposition

The flavour decomposition of the quark polarisations is obtained by solving Eqn. (6.20) for the quark polarisations defined in Eqn. (6.27). Due to the smallness of the unpolarised sea quark densities for $x \gtrsim 0.3$ the statistical uncertainty of the extracted sea polarisation $\Delta q_{\mathrm{s}}/q_{\mathrm{s}}$ exceeds the positivity limit $|\Delta q_{\mathrm{s}}/q_{\mathrm{s}}| \leq \mathcal{C}_i^{-1}$. Therefore the sea polarisation was set to zero and only the remaining up and down flavour polarisations were extracted in this kinematic region. The resulting effect on the polarisations of the non–sea flavours is included in their systematic uncertainties, which will be treated in Sect. 6.5.3.

Figure 6.3 shows the resulting quark polarisations, the numerical values are listed in Tab. E.1. The polarisation of the up flavour is positive everywhere in the measured kinematic range and increases with x. The polarisation of the down flavour features a similar behaviour with an opposite sign and a slightly reduced magnitude of the polarisation. In contrast, the sea polarisation is consistent with zero over the measured x–range. Table E.2 shows the correlations among the quark polarisations $(\Delta u + \Delta\overline{u})/(u + \overline{u})$, $(\Delta d + \Delta\overline{d})/(d + \overline{d})$, and $\Delta q_{\mathrm{s}}/q_{\mathrm{s}}$ together with the reduced χ^2 of the fit in each bin (see Eqn. (6.10)). The correlation coefficients between the up and down flavours are largest in size and have an average value of -0.65, which means that these two polarisations are strongly anti–correlated. The anti–correlation between the down and the sea flavour polarisations is much more pronounced than between the up and the sea flavours. This is explained by the dominance of the sea up flavours in the $\Delta q_{\mathrm{s}}/q_{\mathrm{s}}$ polarisation over the other sea flavours, thus almost compensating the observed anti–correlation between the other quark polarisations.

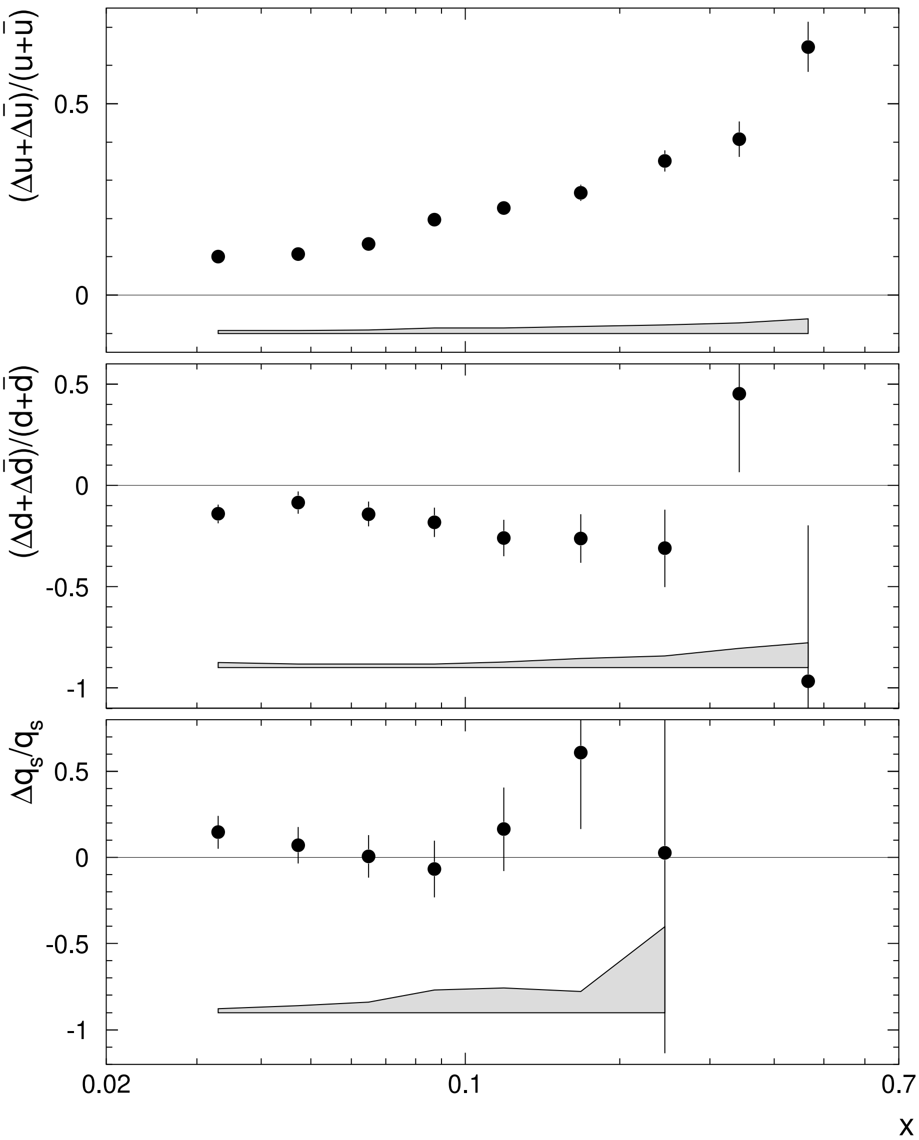

Figure 6.3: The extracted quark polarisations in the flavour decomposition. The error bars give the statistical uncertainties, while the shaded bands indicate the size of the systematic uncertainties.

The systematic uncertainty of the extracted quark polarisation values is given by the shaded bands in Fig. 6.3. Besides the already mentioned contribution from neglecting the sea for $x > 0.3$, the systematic uncertainty includes the contributions from the input asymmetries and the purities. The determination of the systematic uncertainties on the quark polarisations will be addressed in more detail in Sect. 6.5.3.

In order to judge the sensitivity of the resulting quark polarisations on the sea model, the extraction was repeated with the assumption in Eqn. (6.23) for the polarised sea quark distribution instead of Eqn. (6.25). In order to allow a direct comparison of the two results, for the sea polarisation the quantity $\Delta\overline{u}/\overline{u}$ was extracted, which is the dominating contribution to $\Delta q_s/q_s$. Technically, this was achieved by redefining the unpolarised sea quark distribution given in Eqn. (C.9) by $q_s = \overline{u}$, which does not change

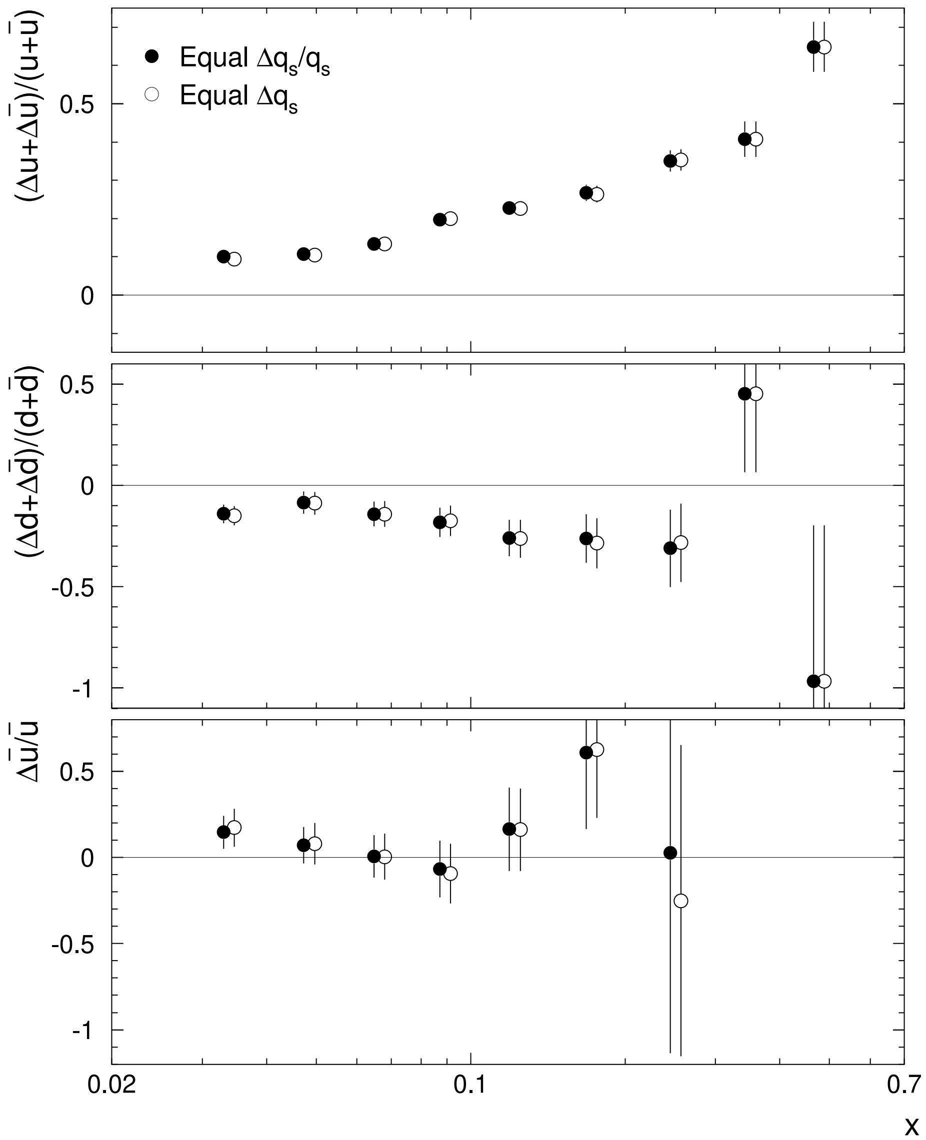

Figure 6.4: Extraction of the quark polarisations in the flavour decomposition for two different symmetry assumptions on the sea polarisation. The solid points were obtained using the model of a polarisation symmetric sea. They are identical to the results shown in Fig. 6.3. The open points give the results for a $SU(3)_f$ symmetric sea. Only statistical uncertainties are shown in this figure.

the extracted polarisation values (see Eqn. (C.10)). Figure 6.4 shows that the resulting changes in the extracted quark polarisations are small and on the order of 1% in most x–bins. This reflects once more the low sensitivity of the measured set of asymmetries on the sea polarisation and is a hint for polarised quark densities $\Delta q_s(x)$ which are small in size so that the positivity limit is not significantly violated in the model of an $SU(3)_f$ symmetric sea (cf. Eqn. (6.23)).

Polarised quark distributions $\Delta q(x, Q_0^2)$ at a scale Q_0^2 are obtained from the extracted quark polarisations $[\Delta q/q](x)$ by multiplication with the unpolarised quark distribution

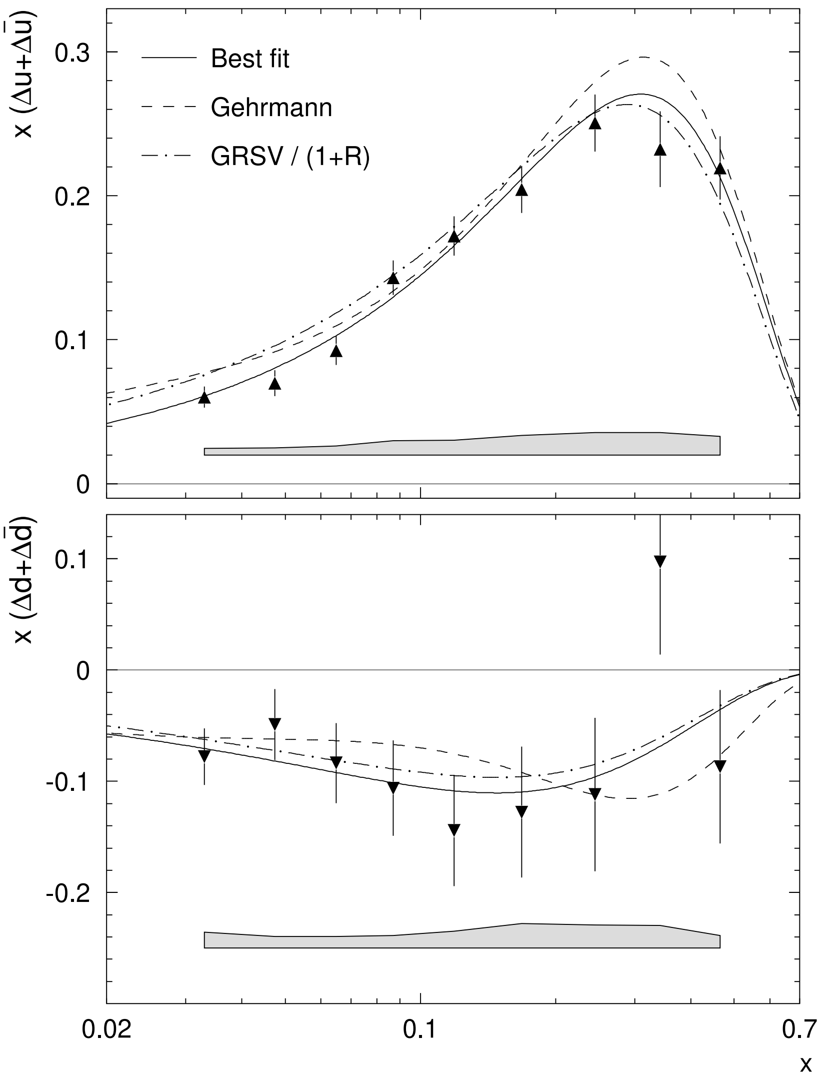

Figure 6.5: The polarised quark distributions $x\,(\Delta u + \Delta\overline{u})$ and $x\,(\Delta d + \Delta\overline{d})$ as a function of x at a scale of $Q^2 = 2.5\,\mathrm{GeV}^2$. The results are compared with the LO parametrisations by Gehrmann and Stirling [Geh 96a] and by Glück *et al.* (GRSV) [Glü 96]. The full line is the result of a best fit and is used in Sect. 6.5.4 for the extrapolation of the extracted polarised quark distributions to values above the measured range in x. For consistency reasons the GRSV parametrisation had to be divided by a factor $(1 + R)$ as explained in the text. The error bars give the statistical uncertainty and the shaded bands denote the systematic uncertainty of the extracted polarised quark distributions.

$q(x, Q_0^2)$. As already discussed in Sect. 2.2.2 this procedure exploits the approximate independence of the quark polarisations from Q^2, and is only valid in the limited range of Q^2 covered by the data. The unpolarised quark distributions are again taken from the CTEQ4LQ parametrisation and the polarised quark distributions have been determined for a fixed scale of $Q_0^2 = 2.5\mathrm{GeV}^2$. Figure 6.5 shows the polarised parton densities $x[\Delta u(x) + \Delta\overline{u}(x)]$ and $x[\Delta d(x) + \Delta\overline{d}(x)]$ obtained in the flavour decomposition. For the ease of presentation, the parton densities have been multiplied by x.

Also shown in Fig. 6.5 are two different LO parametrisations of the polarised quark distributions from Gehrmann and Stirling (GS, LO Gluon Set A, [Geh 96a]) and Glück *et al.* (GRSV, LO Standard Scenario, [Glü 96]). The Gehrmann–Stirling parametrisation is based on inclusive asymmetry measurements on polarised proton, deuterium and ^{3}He targets in the E130 [Bau 83], EMC, SMC and the E142 experiments. The GRSV parametrisation uses the same set of input data plus inclusive asymmetry measurements on a proton and a deuterium target from the E143 experiment. Both parametrisations assume $SU(3)$ symmetry together with the results for hyperon decay constants to obtain constraints on the individual flavours as outlined in Sect. 2.6. As a subtle difference between these two parametrisations, the GRSV parametrisation is based on fits of world data on the asymmetry A_1, while the Gehrmann–Stirling group uses world data on the polarised structure function g_1 as input for the fit procedure. The fits on A_1 assume the cross section ratio R equals zero, while the experimental extractions of g_1 have been corrected for the measured non–zero values of R. To be consistent with the treatment in this analysis (see Sect. 6.1), the GRSV parametrisations have been divided by a factor of $(1 + R)$.

In addition to the parametrisations of the polarised quark distributions, Fig. 6.5 also shows a direct fit to the extracted quark distributions, which uses the functional form of the GRSV parametrisation:

$$\Delta u(x) + \Delta\overline{u}(x) = N_u \cdot x^{\alpha_u} \cdot [u(x) + \overline{u}(x)] \ , \tag{6.29}$$

$$\Delta d(x) + \Delta\overline{d}(x) = N_d \cdot x^{\alpha_d} \cdot \left[d(x) + \overline{d}(x)\right] \ , \tag{6.30}$$

$$\Delta q_{\mathrm{s}}(x) = N_{q_{\mathrm{s}}} \cdot x^{\alpha_{q_{\mathrm{s}}}} \cdot (1-x)^{\beta_{q_{\mathrm{s}}}} \cdot q_{\mathrm{s}}(x) \ , \tag{6.31}$$

where the N_q, α_q and $\beta_{q_{\mathrm{s}}}$ are free fit parameters. The unpolarised quark distributions are obtained from the CTEQ4LQ parametrisation at the mean scale Q_i^2 in each x–bin i. The resulting fit parameters for the "best fits" shown in Fig. 6.5 are listed in Tab. 6.2. This fit is used for the extrapolation of the extracted quark distributions outside the measured x–range in Sect. 6.5.4.

Table 6.2: Parameters for a fit of the x–dependence of the extracted polarised quark distributions in the flavour decomposition.

Quark distribution	N_q	α_q	β_q	χ^2/ndf
$\Delta u + \Delta\overline{u}$	0.92 ± 0.10	0.68 ± 0.05	—	0.68/7
$\Delta d + \Delta\overline{d}$	−0.46 ± 0.22	0.40 ± 0.18	—	0.87/7
Δq_{s}	0.002 ± 0.016	−1.5 ± 1.5	21 ± 130	0.64/4

The extracted polarised up flavour distribution $x\,[\Delta u(x) + \Delta\overline{u}(x)]$ is in better agreement with the GRSV parametrisation, after correction by $1/(1 + R)$, than with the GS parametrisation. Both the GS and the GRSV parametrisations give somewhat larger polarised quark densities at low values of x, yet they are compatible with the data within the uncertainties. For the polarised down flavour distribution $x\,[\Delta d(x) + \Delta\overline{d}(x)]$ the statistical precision of the extracted values is too low to discriminate between the different parametrisations or the best functional fit.

6.5.2 The Valence Decomposition

For the valence decomposition the individual quark flavours are grouped into valence and sea contributions as discussed in Sect. 6.4. Consequently, also the purities are different combinations of the individual terms in Eqn. (6.7) than in the case of the flavour decomposition discussed in the previous section. Apart from this difference, all other features of the extraction procedure are identical to the case of the flavour decomposition.

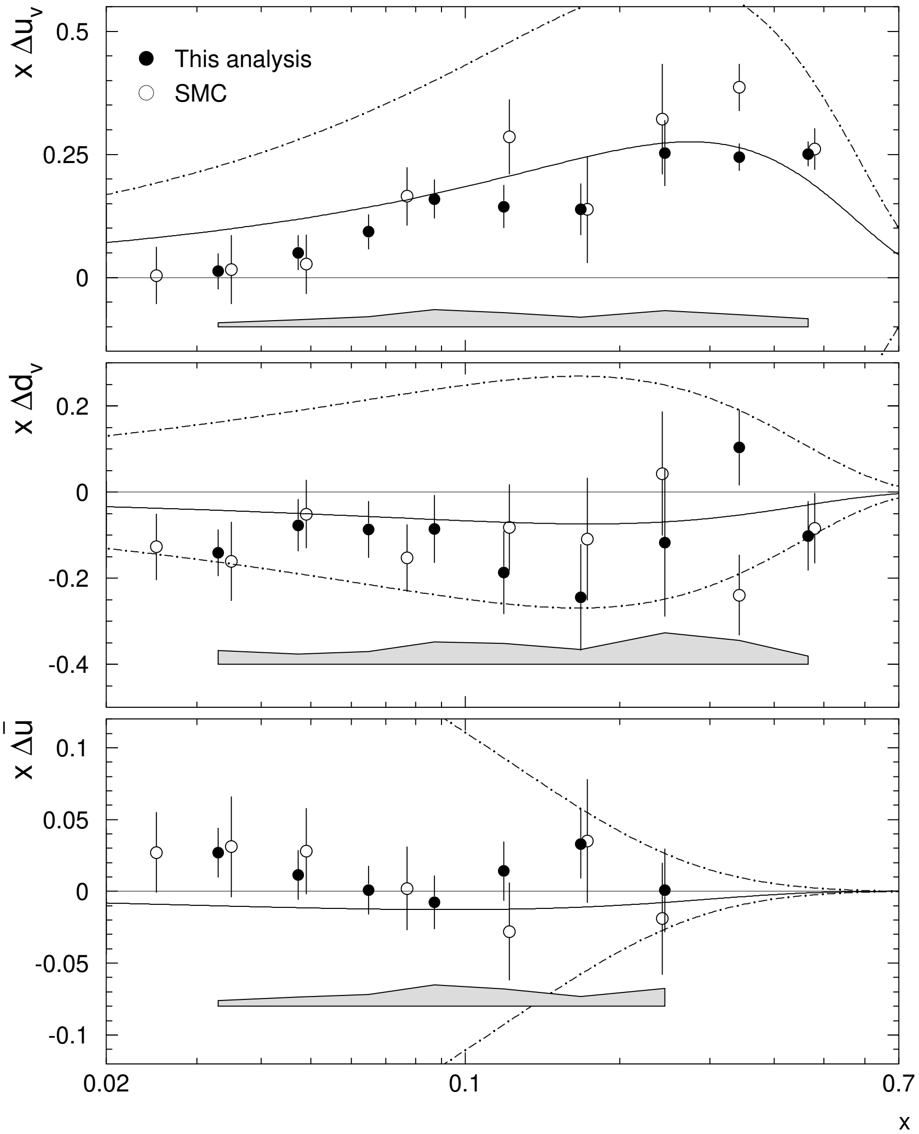

Figure 6.6: The extracted valence and sea quark distributions $x\,\Delta u_{\rm v}$, $x\,\Delta d_{\rm v}$, and $x\,\Delta\overline{u}$ at a common scale of $Q^2 = 2.5\,{\rm GeV}^2$. The results are compared to data from SMC [Ade 98a], which have been evolved to the same scale. The error bars give the statistical uncertainties and the shaded band indicates the systematic uncertainty for the HERMES data. The solid lines are obtained from the GRSV parametrisation, which has been divided by $(1+R)$. Furthermore the positivity limits on the quark distributions are given by the dotted–dashed lines in each panel.

Figure 6.6 shows the polarised valence quark distributions $x\,\Delta u_{\rm v}$ and $x\,\Delta d_{\rm v}$, and the polarised sea quark distribution $x\,\Delta\overline{u}$. The polarised quark distributions were obtained from the extracted quark polarisations at a scale of $Q^2 = 2.5\,\mathrm{GeV}^2$ as described in the previous section. The numerical values of the extracted quark polarisations and the correlation coefficients between the individual polarisations are listed in Tables E.4 and E.5. The values for the reduced χ^2 of the fit, which are also contained in the second table, are identical to the values for the flavour decomposition because the different combination of the individual terms in Eqn. (6.7) does not change the goodness of the fit.

For comparison, the results from the SMC experiment [Ade 98a] are also shown in Fig. 6.6. The SMC data points have been evolved to the same value of Q^2 using the approximate independence from Q^2 of the quark polarisations. The evolved SMC data points are in good agreement with the quark densities extracted from HERMES data which provide an improved precision over the SMC results, in particular for the $\Delta u_{\rm v}(x)$ distribution. The polarised quark distribution for the valence up quarks is significantly positive, whereas the polarised distribution of the valence down quarks is negative in the measured range. The polarised sea distribution, which was assumed to be $SU(3)_f$ symmetric in this extraction, is consistent with zero over the measured x–range. In Fig. 6.6 the polarised sea up quark distribution is shown, as this quantity shows the largest sensitivity on the used set of input asymmetries.

The dotted–dashed lines in Fig. 6.6 give the positivity limits on the extracted polarised quark distributions. They are determined by the unpolarised parton distributions according to

$$\left|\frac{\Delta q(x)}{q(x)}\right| \leq \mathcal{C}_i^{-1} \quad \Leftrightarrow \quad |\Delta q(x)| \leq \frac{1+\gamma^2}{1+R} \cdot |q(x)| \ , \tag{6.32}$$

where the $q(x)$ have been obtained from the CTEQ4LQ parametrisation. The solid lines in Fig. 6.6 show the predictions of the GRSV parametrisation, which has been divided by $(1+R)$ to be consistent with the chosen scheme for the polarised parton distributions. The extracted polarised quark distributions are within the positivity limits and consistent with the GRSV parametrisation. For the sea flavour the GRSV parametrisation gives a negative polarised distribution, whereas the data seem to favour a slightly positive distribution. For large values of $x \gtrsim 0.4$, the polarised valence quark distributions approach the positivity limits. In the measured kinematical range the total spin of the valence up quarks is aligned with the proton spin, whereas the spin of the valence down quark is oriented in the opposite direction.

6.5.3 Systematic Uncertainties

The statistical and systematic uncertainties of the extracted quark polarisations can be obtained from the covariance matrix of the measured asymmetries using Eqns. (6.15) and (6.16). For this, the covariance matrix $\mathcal{V}_Q$ is calculated twice: once using the statistical covariance matrix only and once using the total covariance matrix, including the systematic covariances [Tip 99]. The systematic covariance matrix is the difference

$$\mathcal{V}_Q^{\rm sys} = \mathcal{V}_Q^{\rm tot} - \mathcal{V}_Q^{\rm stat} \ . \tag{6.33}$$

The individual sources of the systematic uncertainty on the input asymmetries were already treated in the previous chapter. Below, the contributions to the covariance matrix $\mathcal{V}_A^{\mathrm{sys}}$ will be given briefly, for a detailled discussion and the numerical values of the individual contributions see Sect. 5.8. For brevity, $(\mathcal{V}_A^i)_{jk}$ denotes the element j,k of the systematic covariance matrix $\mathcal{V}_A^{\mathrm{sys},i}$ on the asymmetries, related to the source i for the systematic uncertainty. The indices j,k refer to the elements of the asymmetry input data set and span a range of $j,k = 1,\ldots,9$ in this analysis.

Beam Polarisation

The contributions to the systematic covariance matrix from the uncertainty in the measurement of the beam polarisation are

$$(\mathcal{V}_A^{P_\mathrm{B}})_{jk} = \left[\left(\frac{\delta P_\mathrm{B}}{P_\mathrm{B}}\right)_{\mathrm{rise}} + \rho_{jk}^{P_\mathrm{B}} \left(\frac{\delta P_\mathrm{B}}{P_\mathrm{B}}\right)_{\mathrm{point},j} \left(\frac{\delta P_\mathrm{B}}{P_\mathrm{B}}\right)_{\mathrm{point},k}\right] A_j\, A_k\,. \tag{6.34}$$

The correlation coefficient $\rho_{jk}^{P_\mathrm{B}}$ equals one for asymmetries j and k from the same year of data taking, and is zero otherwise. The uncertainty $(\delta P_\mathrm{B}/P_\mathrm{B})_{\mathrm{rise}}$ from the rise–time calibration of the Transverse Polarimeter is fully correlated among all measured asymmetries.

Target Polarisation

The fractional systematic uncertainty from the measurement of the target polarisation to the systematic covariance matrix writes as

$$(\mathcal{V}_A^{P_\mathrm{T}})_{jk} = \rho_{jk}^{P_\mathrm{T}} \left(\frac{\delta P_\mathrm{T}}{P_\mathrm{T}}\right)_j \left(\frac{\delta P_\mathrm{T}}{P_\mathrm{T}}\right)_k A_j\, A_k\,. \tag{6.35}$$

The correlation coefficient $\rho_{jk}^{P_\mathrm{T}}$ is one for asymmetries j and k taken on the same target and vanishes otherwise. The relative uncertainty on the polarisation of the ^{3}He target in 1995 is $\delta P_\mathrm{T}/P_\mathrm{T} = 5\%$; the values for the polarised proton target are given in Sect. 5.8.2.

Yield Fluctuations

For the 1995 data set an additional source of systematic uncertainties due to non–statistical fluctuations of the normalised particle multiplicities was taken into account. These *yield fluctuations* only affect the ^{3}He asymmetries. The corresponding entries in the systematic covariance matrix are given by:

$$(\mathcal{V}_A^{\mathrm{Yield}})_{jk} = [\delta A_j]_{\mathrm{Yield}}\, [\delta A_k]_{\mathrm{Yield}}\,, \tag{6.36}$$

where the values of $[\delta A_j]^{\mathrm{Yield}}$ for asymmetries from the 1995 data set are [Ako 97, Tal 98]:

$$[\delta A_1\ ]_{\mathrm{Yield}} = 0.00256\,, \tag{6.37}$$

$$[\delta A_1^{h^+}]_{\mathrm{Yield}} = 0.00575\,, \tag{6.38}$$

$$[\delta A_1^{h^-}]_{\mathrm{Yield}} = 0.00547\,. \tag{6.39}$$

For asymmetries on the polarised proton target the $[\delta A_j]_{\mathrm{Yield}}$ are zero.

Cross Section Ratio R

Besides the contribution to the depolarisation factor $D(x, Q^2)$ of the virtual photon, the cross section ratio $R = \sigma_{\mathrm{L}}/\sigma_{\mathrm{T}}$ also appears in the correction factor $\mathcal{C}_i$ introduced in Eqn. (6.4). Together with Eqn. (5.30) this additional contribution yields the following expression for the systematic uncertainty from the cross section ratio R:

$$(\mathcal{V}_A^R)_{jk} \;=\; \left[\frac{1-\varepsilon}{(1+R)(1+\varepsilon\, R)}\,\delta R(x,Q^2)\right]^2 A_j\, A_k\;, \tag{6.40}$$

where the uncertainty $\delta R(x, Q^2)$ and the value of $R(x, Q^2)$ are taken from [Abe 99].

Spin Structure Function g_2

The systematic uncertainty $\delta\,(g_1/F_1)_{g_2}$ on the structure function ratio g_1/F_1 from the assumption of a vanishing polarised structure function $g_2(x) \equiv 0$ has been given in Eqn. (5.34). Its contribution to the systematic covariance matrix is

$$(\mathcal{V}_A^{g_2})_{jk} \;=\; \rho_{jk}^{g_2}\;\delta\left(\frac{g_1}{F_1}\right)_{g_2,j}\;\delta\left(\frac{g_1}{F_1}\right)_{g_2,k}\;. \tag{6.41}$$

The correlation coefficient $\rho_{jk}^{g_2}$ is one for asymmetries j and k taken on the same target and zero otherwise. Note that this source contributes differently to the systematic uncertainty on the virtual photon asymmetry A_1, as given in Eqn. (5.33).

Smearing Corrections

Smearing corrections were applied to the proton asymmetries only. Their systematic uncertainty $\delta\eta^j_{\mathrm{smear}}$ was discussed in Sect. 5.8.3 and their contribution to the systematic covariance matrix is

$$(\mathcal{V}_A^{\mathrm{smear}})_{jk} \;=\; \rho_{jk}^{\mathrm{smear}}\;\;\delta\eta^j_{\mathrm{smear}}\,A_j\;\;\delta\eta^k_{\mathrm{smear}}\,A_k\;, \tag{6.42}$$

where the correlation coefficient $\rho_{jk}^{\mathrm{smear}}$ is one for asymmetries j and k taken on the proton target and zero otherwise.

Radiative Corrections

Radiative corrections have only been applied to the inclusive asymmetries. Their systematic uncertainties $\delta(\Delta A_j^{\mathrm{RC}})$ are given in Tab. 5.6 for the ^{3}He and for the proton data. The contribution to the systematic covariance matrix writes as

$$(\mathcal{V}_A^{\mathrm{RC}})_{jk} \;=\; \rho_{jk}^{\mathrm{RC}}\;\;\delta(\Delta A_j^{\mathrm{RC}})\;\delta(\Delta A_k^{\mathrm{RC}})\;. \tag{6.43}$$

The correlation coefficient ρ_{jk}^{RC} is one for inclusive asymmetries $j = k$ taken on the same target in the same year and zero otherwise.

Besides from the above mentioned sources of systematic uncertainties, which are related to the input asymmetries, three more contributions were regarded in the extraction of the quark polarisations. They will be discussed in the following paragraphs.

The Systematic Uncertainty from the Unpolarised PDFs

By default, the unpolarised quark distributions from the CTEQ4LQ parametrisation have been used as input for the generation of the purities and for the calculation of the polarised quark distributions $\Delta q_f(x)$ from the extracted quark polarisations. To determine the systematic uncertainty associated with the choice of the unpolarised PDFs, the extraction of the polarised quark distributions was repeated with the CTEQ4LQ parametrisation replaced by the LO GRV parametrisation ("standard scenario", [Glü 95]). This included the generation of a different set of purities from the GRV parametrisation. The contribution to the systematic uncertainty is half of the difference between the results obtained with the two different parametrisations of the unpolarised PDFs.

The Systematic Uncertainty from the Fragmentation Model

As a second important input parameter for the generation of purities, the uncertainty on the knowledge of the fragmentation functions contributes to the systematic uncertainty of the extracted quark polarisations. For the different settings of parameters given in Tab. 6.1, purities were generated in the LUND string fragmentation model, "SF1" and "SF2", and in the Independent fragmentation model "IF" (see Sect. 6.2) . The maximum difference of the extracted quark polarisations in each bin with the different sets of purities was taken as the systematic uncertainty arising from the fragmentation model. The systematic uncertainty on the purities from the used detector model was assumed to be negligible.

The Unpolarised Sea Model Uncertainty

In the extraction of the quark polarisations the polarisation of the sea flavour was artificially set to zero for values of $x > 0.3$, because the number density of sea quarks has almost vanished in this kinematic region. The systematic influence on the polarisation of the two remaining flavours was determined by setting the sea polarisation to the upper and lower positivity limits $\pm \mathcal{C}_i^{-1}$ given by the unpolarised quark distributions. This corresponds to modifying the input asymmetries for $x > 0.3$ as

$$\left(A^h\right)' = A^h \pm P^h_{\text{sea}} \frac{1+\gamma^2}{1+R} , \tag{6.44}$$

where the definitions of the sea purity are given in App. C. Quark polarisations were extracted with modified input asymmetries $(A^h)'$ and the maximum difference to the results obtained from the unmodified input asymmetries was taken as the systematic uncertainty arising from the unpolarised sea model for the highest x–bins.

The total systematic covariance matrix $\mathcal{V}_A^{\text{sys}}$ contains the sum of all contributions mentioned above. The individual contributions σ_i to the total systematic error are obtained from

$$\sigma_i = \sqrt{(\sigma^{\text{sys}}_{\text{tot}})^2 - (\sigma^{\text{sys}}_i)^2} , \tag{6.45}$$

where σ_i^{sys} denotes the systematic error resulting from an extraction of the quark polarisations with a systematic covariance matrix $\mathcal{V}_i^{\text{sys}}$ for which the source i has *not* been

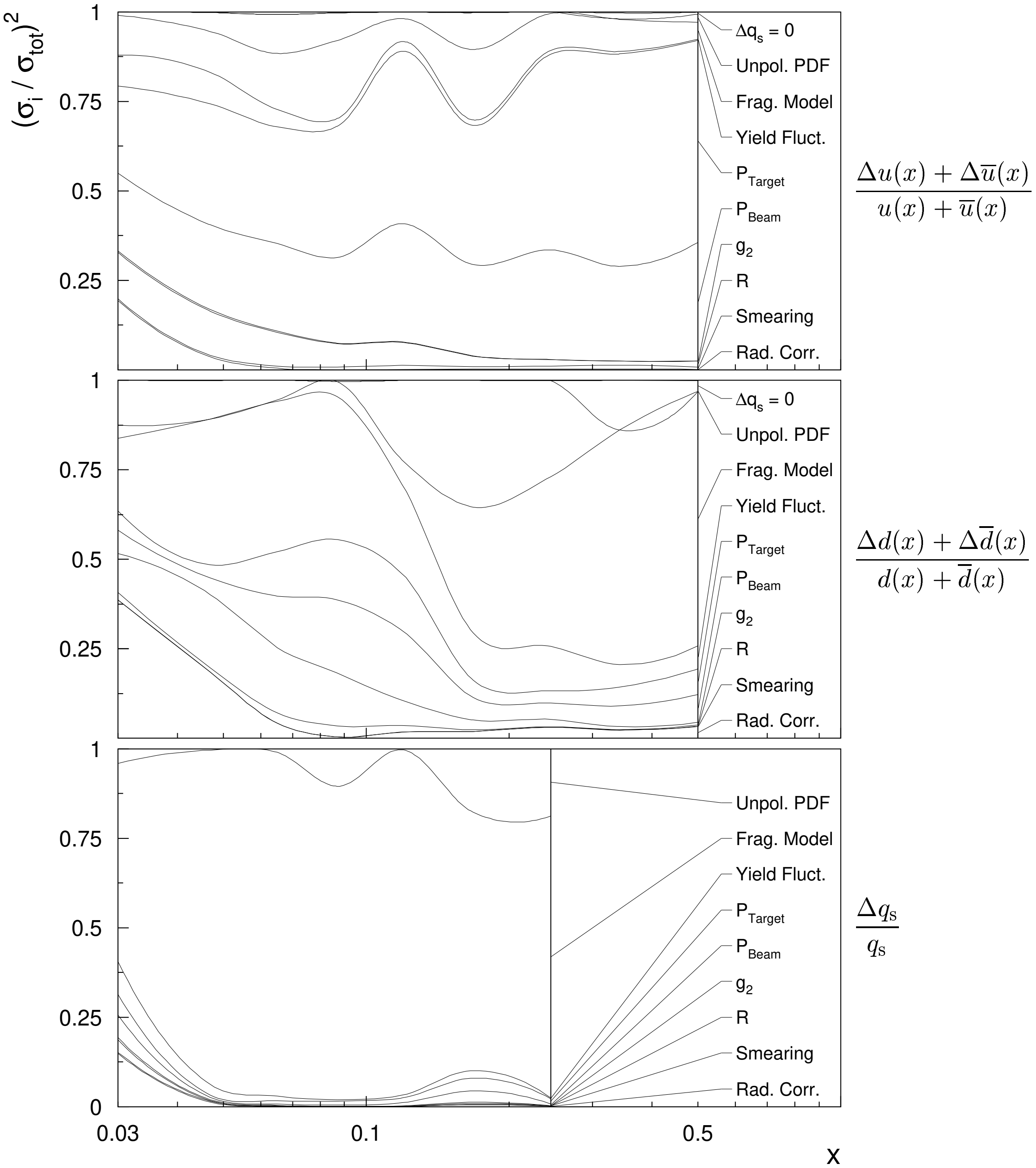

Figure 6.7: The relative contributions $(\sigma_i/\sigma_{\rm tot}^{\rm sys})^2$ to the systematic uncertainty of the quark polarisations in the flavour decomposition. The graphical representation of the relative contributions is identical to Fig. 5.11.

taken into account. The sum over the squares of all systematic error contributions σ_i gives the square of the total systematic uncertainty: $\sum_i(\sigma_i)^2 = (\sigma_{\rm tot}^{\rm sys})^2$.

Table E.3 lists the individual contributions σ_i to the systematic uncertainties on the quark polarisations in the flavour decomposition, the corresponding values for the valence decomposition are listed in Tab. E.6. The relative contributions $(\sigma_i/\sigma_{\rm tot}^{\rm sys})^2$ to the total systematic uncertainties on the quark polarisations in the flavour decomposition are shown in Fig. 6.7. For the polarisation of the up flavours, the systematic uncertainties in the target and beam polarisations are the dominating sources and contribute between 50% and 90% of the total systematic uncertainty. For the down flavours at low values of x the most important contributions to the total systematic uncertainty arise from the yield fluctuations and from the cross section ratio R, whereas in the highest x–bin the uncertainty due to the fragmentation model is dominating with about 70% relative contribution. For the polarisation of the sea flavours, the largest systematic uncertainty over the entire range in x can be attributed to the uncertainty in the fragmentation functions. For $x > 0.08$ also the uncertainty on the unpolarised PDFs contributes sizeably.

For the valence decomposition, the uncertainty related to the fragmentation model plays are more important role also for the $u_{\rm v}$ and $d_{\rm v}$ polarisations (see Tab. E.6), because the polarisation of the sea quarks enters in the determination of the valence quark polarisations.

6.5.4 The Determination of Moments

The n–th moment $\Delta^{(n)} q_f(Q_0^2)$ of a polarised quark distribution $\Delta q_f(x, Q_0^2)$ is defined as

$$\Delta^{(n)} q_f(Q_0^2) \;:=\; \int_0^1 x^{n-1}\, \Delta q_f(x, Q_0^2)\, \mathrm{d}x\,. \tag{6.46}$$

In this work, first and second moments of the extracted polarised quark distributions have been determined at a fixed scale of $Q_0^2 = 2.5\,\mathrm{GeV}^2$. As for any experiment, the measured region in x does not cover the full range $0 < x < 1$. This necessitates an extrapolation of the distributions outside the measured x–range, and the integral in Eqn. (6.46) is split up into three contributions from the measured range $0.023 \le x \le 0.6$, and from the low ($x < 0.023$) and high ($x > 0.6$) ranges in x.

In the measured range, the integral $\Delta^{(n)}_{(\mathrm{meas})}\, q_f(Q_0^2)$ is obtained from

$$\begin{aligned} \Delta^{(n)}_{(\mathrm{meas})}\, q_f(Q_0^2) \;&=\; \int_{0.023}^{0.6} x^{n-1}\, \Delta q_f(x, Q_0^2)\, \mathrm{d}x \\ &=\; \sum_i \left[\frac{\Delta q_f}{q_f}(x_i) \int_{\xi_i}^{\xi_{i+1}} x^{n-1}\, q_f(x, Q_0^2)\, \mathrm{d}x \right]\,, \end{aligned} \tag{6.47}$$

where the sum is performed over all x–bins i with the limits $[\xi_i, \xi_{i+1}]$. In this approach, one assumes that the quark polarisations $\Delta q_f / q_f$ are constant within one x–bin and independent of Q^2. The unpolarised quark distributions are taken from the CTEQ4LQ parametrisation. To obtain the statistical (systematic) uncertainty of the integral in the measured region, the statistical (systematic) uncertainties in each bin were added in quadrature (linearly).

The extrapolation in the low range of x depends heavily on theoretical models and no clear prediction for the low–x extrapolation of the polarised parton distributions is generally accepted in the literature. A discussion of the various models available can be found in [Abe 97a], e.g. In view of the rather ambiguous predictions, in this work an extrapolation based on Regge theory is chosen, according to the treatment in [Ell 96]. In this model, for low values of x the polarised structure functions $\Delta q(x)$ are proportional to $x^{-\alpha}$, where α denotes the intercept of the axial vector Regge trajectories. In [Ell 96] a value of $\alpha = -0.07\,^{+0.42}_{-0.32}$ has been obtained from a fit to EMC data. Here, the most simple case $\alpha = 0$ was chosen and a constant was fit to the polarised quark distributions for $x < 0.075$. This constant value was integrated from $x = 0$ to $x = 0.023$, and a relative uncertainty of 100% of the fitted constant was chosen as systematic uncertainty associated with the low–x extrapolation.

Note that the applicability of this theory has been questioned especially in the perturbative region $Q^2 \to \infty$ [Alt 97] as the rise of the unpolarised structure functions at low values of x is steeper than predicted by Regge theory. Hence the quoted systematic uncertainty is only justified in the chosen framework of Regge theory. Absolute upper limits on the integrals of the polarised structure functions may be obtained from the unpolarised structure functions. Using the CTEQ4LQ parametrisation, for the valence distributions these limits are $\int_0^{0.023} u_{\mathrm{v}}\,\mathrm{d}x = 0.40$ and $\int_0^{0.023} d_{\mathrm{v}}\,\mathrm{d}x = 0.26$ at $Q^2 = 2.5\,\mathrm{GeV}^2$. For the flavour decomposition, the corresponding limits are above 2.5 due to the contributions from sea quarks. Given the experimental observation that the polarised quark distributions do not seem to reach the positivity limits for small values of x (see Figs. 6.3 and 6.6) there is no reason to assume that the low–x extrapolation is close to these absolute limits.

Fortunately, the extrapolation to large values of x is less problematic. For values of $x > 0.6$ the integration in Eqn. (6.46) was performed over the functional forms given in Eqns. (6.29) – (6.31), which have been fitted to the extracted quark polarisations. The steep drop of the unpolarised quark densities in this kinematic region ensures that the integral contributions remain small. As a conservative estimate, a relative uncertainty of 100% on the integral value in the high–x range was assigned as systematic uncertainty.

In Tab. E.7 the first and second moments of the extracted polarised quark distributions in the measured range are listed together with the integrals from the low–x and high–x extrapolations. For brevity, the first moments $\Delta^{(1)}q_f(Q_0^2)$ of the quark distributions are referred to as $\Delta q_f(Q_0^2)$ everywhere. The total integrals are the sums of the three individual contributions. To obtain the errors of the total integrals the values of the low–x and high–x extrapolations are added quadratically with the systematic uncertainty from the measured region.

6.6 Comparison with Integrals and Theoretical Predictions

In this section, some of the obtained results are compared to theoretical predictions or other experimental results. Note that the results presented in this thesis differ from the values given in the publication [Ack 99c], as the input asymmetries and the purities used in this thesis are based on a slightly different analysis. Nevertheless, the results in [Ack 99c] are fully compatible with the values given here.

The only other measurement of polarised quark distributions was performed by the SM Collaboration [Ade 98a]. The extracted polarised valence quark distributions have already been compared in Fig. 6.6 with the SMC results, which have been evolved to the same scale of $Q^2 = 2.5\,\mathrm{GeV}^2$. Table 6.3 shows a comparison of the first and second moments calculated from the HERMES and evolved SMC data points in the common x–range of both experiments ($0.023 < x < 0.6$). As a technical detail, the integration of the SMC data points was performed using Eqn. (6.47), instead of the simpler expression

$$\Delta^{(n)}_{\mathrm{SMC}}\, q_f \;=\; \sum_i x^{n-1}\, \Delta q_f(x_i)\, \Delta x_i \qquad (6.48)$$

originally used by SMC [Pre 97], where the factor Δx_i denotes the width of the bin i. The first and second moments obtained from the SMC data are fully consistent with the values from this analysis. The lower statistical uncertainties on the moments of the u_v distribution reflect the higher statistical precision of the HERMES proton data.

Table 6.3: A comparison of integrals in the measured region with results from SMC. The SMC results for the polarised quark distributions [Ade 98a] have been evolved to a scale of $Q^2 = 2.5\,\mathrm{GeV}^2$ and integrated over the HERMES x–range of $0.023 < x < 0.6$.

	This analysis	SMC (at $Q^2 = 2.5\,\mathrm{GeV}^2$)
Δu_v	$0.45 \pm 0.05 \pm 0.03$	$0.59 \pm 0.08 \pm 0.07$
Δd_v	$-0.36 \pm 0.11 \pm 0.05$	$-0.33 \pm 0.11 \pm 0.09$
$\Delta \overline{u}$	$0.04 \pm 0.03 \pm 0.01$	$0.02 \pm 0.03 \pm 0.02$
$\Delta \overline{d}$	$0.05 \pm 0.04 \pm 0.01$	$0.02 \pm 0.03 \pm 0.02$
$\Delta^{(2)} u_\mathrm{v}$	$0.113 \pm 0.009 \pm 0.007$	$0.146 \pm 0.016 \pm 0.012$
$\Delta^{(2)} d_\mathrm{v}$	$-0.048 \pm 0.025 \pm 0.007$	$-0.053 \pm 0.024 \pm 0.015$

When comparing the experimental results to theoeretical predictions, model dependent correction factors have to be applied, which in general introduce an uncertainty on the value from the prediction. For instance, the triplet contribution Δq_3 is related to the Bjørken sum rule by

$$\Delta q_3(Q^2) = \left|\frac{g_\mathrm{A}}{g_\mathrm{V}}\right| \Delta\mathcal{C}_\mathrm{NS}(Q^2)\,, \tag{6.49}$$

where the Q^2–dependent first moment of the non–singlet coefficient function $\Delta\mathcal{C}_\mathrm{NS}(Q^2)$ is given in Eqn. (2.66). The computation of $\Delta\mathcal{C}_\mathrm{NS}(Q^2)$ requires the knowledge of the strong coupling constant $\alpha_\mathrm{s}(Q^2)$ at the scale Q^2. In [Ruh 99] a numerical value of $\Delta\mathcal{C}_\mathrm{NS}(2.5\mathrm{GeV}^2) = 0.795 \pm 0.045$ was derived using a value of $\alpha_\mathrm{s}^{(3)}(2.5\mathrm{GeV}^2) = 0.351 \pm 0.040$ for a number $n_f = 3$ of three active flavours. Together with the value for the neutron decay constant $|g_\mathrm{A}/g_\mathrm{V}| = 1.2670 \pm 0.0035$ [Cas 98] one obtains a value for the Bjørken sum rule prediction in Eqn. (6.49) of 1.01 ± 0.06, which agrees with the measured semi inclusive result of $\Delta q_3(2.5\,\mathrm{GeV}^2) = 0.88 \pm 0.07_\mathrm{stat} \pm 0.09_\mathrm{sys}$.

Table 6.4 shows a comparison of first moments from this work with an analysis of inclusive polarised DIS and hyperon decays, assuming $SU(3)_f$ symmetry [Ell 96]. As for the value of the Bjørken sum rule, the results from the $SU(3)_f$ analysis have been evolved to a scale of $2.5\,\mathrm{GeV}^2$, using Eqns. (2.66) and (2.67) together with the numerical value for $\alpha_\mathrm{s}^{(3)}(Q^2 = 2.5\,\mathrm{GeV}^2)$ from [Ruh 99]. For the results from the $SU(3)$ analysis two uncertainties are given: the first term gives the statistical uncertainty arising from the precision of the input data for the fit. The second term gives an estimate of the additional systematic uncertainty arising from higher–twist effects, the low–x extrapolation, etc. In [Ell 96] no numerical values for these additional systematic uncertainties are given, yet the authors estimate them to be of the same order as the statistic uncertainties.

The results for the first moments from the $SU(3)_f$ analysis agree for the up and down flavours, whereas there is a deviation for the first moment of the strange flavours.

Table 6.4: A comparison of first moments in the entire x–range to results from an $SU(3)_f$ analysis [Ell 96]. The values in [Ell 96] are given for $Q^2 \to \infty$. For the comparison with the measured values they have been evolved to a common fixed scale of $Q^2 = 2.5\,\mathrm{GeV}^2$.

	This analysis	$SU(3)_f$ analysis
$\Delta u + \Delta\overline{u}$	$0.58 \pm 0.02 \pm 0.05$	$0.66 \pm 0.03 \pm \mathcal{O}(0.03)$
$\Delta d + \Delta\overline{d}$	$-0.30 \pm 0.06 \pm 0.05$	$-0.35 \pm 0.03 \pm \mathcal{O}(0.03)$
$\Delta s + \Delta\overline{s}$	$0.05 \pm 0.04 \pm 0.01$	$-0.08 \pm 0.03 \pm \mathcal{O}(0.03)$
$\Delta\Sigma$	$0.33 \pm 0.06 \pm 0.06$	$0.23 \pm 0.04 \pm \mathcal{O}(0.04)$
Δq_3	$0.88 \pm 0.07 \pm 0.09$	$1.01 \pm 0.05 \pm \mathcal{O}(0.05)$
Δq_8	$0.17 \pm 0.09 \pm 0.07$	$0.46 \pm 0.03 \pm \mathcal{O}(0.03)$

However, one has to keep in mind that the result from this analysis does not represent a direct measurement of the strange quark contribution. The extracted strange spin contribution $\Delta s + \Delta\overline{s}$ is rather contrained by the $SU(3)_f$ symmetric polarisation model (see Sect. 6.4). The first moments of the extracted polarised quark distributions can also be converted to the expectation values of axial vector currents using Eqns. (2.70) – (2.72). There is agreement between the measured integrals with the results from the $SU(3)$ analysis for the matrix elements $a_0 \equiv \Delta\Sigma$ and $a_3 \equiv \Delta q_3$, with a difference for $a_8 \equiv \Delta q_8$. This deviation should not be interpreted as evidence for a breaking of $SU(3)_f$ symmetry, but is rather another manifestation of the strong bias of the extracted strange spin contribution by the sea model.

Table 6.5: First and second moments of the valence quark distributions compared to results from lattice QCD calculations. The measured values are given for a scale of $Q^2 = 2.5\,\mathrm{GeV}^2$, whereas the scales for the lattice calculations of the first [Göc 96] and second [Göc 97] moments are quoted in the table.

	This analysis	Lattice QCD	(Q^2/GeV^2)
Δu_v	$0.50 \pm 0.05 \pm 0.04$	0.83 ± 0.07	(5)
Δd_v	$-0.40 \pm 0.11 \pm 0.07$	-0.24 ± 0.02	(5)
$\Delta^{(2)} u_\mathrm{v}$	$0.13 \pm 0.01 \pm 0.01$	0.20 ± 0.01	(4)
$\Delta^{(2)} d_\mathrm{v}$	$-0.05 \pm 0.03 \pm 0.01$	-0.05 ± 0.03	(4)

Finally, Tab. 6.5 shows a comparison of the first and second moments of the valence spin contributions to results from lattice QCD calculations [Göc 96, Göc 97]. The extracted first and second moments of the u_v distribution are significantly lower than the results from lattice calculation, which was performed in the quenched approximation. Thus the quenched approximation might not be suited to yield reliable predictions of the nucleon's spin structure.

7 Summary

This section summarises the results obtained during the work for this thesis. The work was split in two parts, which comprise a hardware contribution and the analysis of data taken with the HERMES detector during the years 1996 and 1997. Parts of the results obtained in this thesis are published in [Ack 99c], a publication on the hardware contribution to the experiment is in preparation.

In the first part of this thesis work, the laser optical system of the Longitudinal Polarimeter was designed, built and tested. Since the LPOL became fully operational in 1997, the laser system has routinely been providing a circularly polarised laser beam which is guided in vacuum over a distance of about 80 metres to the interaction point with the HERA positron beam. During the transport, the degree of circular polarisation of the laser light is kept at a high level and its measurement is well understood. The LPOL provides a second, independent measurement of the beam polarisation, which helped to significantly reduce the losses of data due to the unavailability of a single polarimeter. Since 1999 the LPOL is being operated in a mode, which allows an absolute measurement of the beam polarisation without the necessity to calibrate the device using the method of rise–time measurements. As this calibration introduces the largest fraction of the systematic uncertainty on the measurement of the beam polarisation, the LPOL will substantially reduce this uncertainty and consequently also the uncertainty on the extracted polarised quark distributions.

In the second part, inclusive and semi inclusive virtual photon–nucleon cross section asymmetries were obtained from the analysis of 2.0 million deep inelastic scattering events taken on a polarised proton target. The data cover a kinematic range of $0.023 < x < 0.6$ and $1\,\mathrm{GeV}^2 < Q^2 < 10\,\mathrm{GeV}^2$. The inclusive asymmetries are compatible with results from SLAC experiments, and the semi inclusive asymmetries for charged hadrons were compared to the only other existing measurement from the SMC experiment. While taken at a much lower average value of $\langle Q^2 \rangle = 2.4\,\mathrm{GeV}^2$, the HERMES data are in agreement with the SMC results, which were obtained at an average value of $\langle Q^2 \rangle_{\mathrm{SMC}} \simeq 10\,\mathrm{GeV}^2$, thus confirming the approximate Q^2–independence of the virtual photon asymmetry A_1. The HERMES results provide a largely improved statistical precision over the published SMC data. Furthermore, also semi inclusive asymmetries for charged pions were extracted for the first time. Like the inclusive asymmetries, the semi inclusive asymmetries for positive and negative hadrons and identified pions are positive and increase for large values of x. While semi inclusive asymmetries contain additional information on the flavour of the struck quark, the dominance of scattering on the up quarks in the nucleon causes only moderate differences between the inclusive and semi inclusive asymmetries.

The purity formalism was introduced as a procedure to extract the polarised quark distributions in the nucleon from the measured semi inclusive asymmetries. Together with the results from another analysis of inclusive and semi inclusive asymmetries taken on a polarised ^{3}He target at HERMES, the polarisations of up, down, and sea quarks was determined from the asymmetries. The extracted polarisation of up quarks was found to be positive over the entire kinematic range of the experiment and increases up to about 0.5 for large values of x. In contrast the down flavours exhibit a negative polarisation, which is somewhat smaller in magnitude than for the up flavours. As for the up quarks, the absolute value of the polarisation increases with x. The polarisation of the sea was determined to be approximately zero in the measured range, despite the larger statistical uncertainties for the sea polarisation as compared to the results for the up and down flavours. Alternatively, the polarisation was extracted for valence and sea quarks. The latter results were found to be in agreement with an earlier measurement by the SMC experiment. Again, the polarisation of the valence up quarks is positive and grows for large values of x. The valence down quarks are negatively polarised with respect to the spin of the nucleon.

The extracted polarised quark distributions were extrapolated outside the measured kinematic region and first and second moments were calculated. As a key result, the Bjørken sum rule could be confirmed by this semi inclusive measurement and the fraction of the nucleon's spin carried by the quarks was determined to be about 1/3 at a scale of $Q^2 = 2.5\,\mathrm{GeV}^2$. Furthermore the results agree with an analysis of earlier inclusive measurements, using $SU(3)$ flavour symmetry, except for the axial octet matrix element a_8. The extracted value shows a deviation from the expectation based on $SU(3)$ symmetry by about 1.5 standard deviations. This difference may however not directly be interpreted as a violation of $SU(3)$ flavour symmetry due to strong bias of the extracted sea quark polarisation from sea up flavours in the chosen extraction method. A comparison of the first and second moments of the extracted polarised valence quark distributions with results from lattice QCD calculations revealed a large discrepancy for the valence up quarks, whereas the agreement for the valence down flavour is reasonable.

Since 1998 HERMES has been taking data on a polarised deuterium target. Coincident with the change of the target type, the threshold Čerenkov counter was replaced by a Ring Imaging Čerenkov detector. This RICH features the identification of pions, kaons and protons over almost the entire kinematical range of the experiment. Semi inclusive kaon–asymmetries will provide an enhanced sensitivity on the polarisation of strange sea quarks and will ultimately allow its direct determination. An extraction of the polarisation of the individual sea quark flavours will help to resolve the interesting question whether or not the observed deviation in the axial octet matrix element a_8 is due to a breaking of $SU(3)$ symmetry.

A Kinematics of Polarised Compton Scattering

In this Appendix, some formulae, which are required for calculation of the polarised Compton cross section in the laboratory system, are given. Unlike in the rest of this thesis, factors of $\hbar$ and c are explicitely written out here.

For the process of Compton scattering as shown in Fig. 4.3 the absolute values of the wave number vectors of the initial (k_i) and the scattered photon (k_f) in the rest system of the initial positron are given by:

$$k_i = \frac{(1+\beta\cos\epsilon)\gamma}{\hbar c}\cdot E_{\rm laser} \simeq \frac{2\gamma}{\hbar c}\cdot E_{\rm laser}\,, \tag{A.1}$$

$$k_f = \frac{1}{\lambdabar_{\rm c}(1-\cos\theta)+1/k_i}\,, \tag{A.2}$$

where $\beta = \sqrt{1-\gamma^{-2}}$ is the velocity of the positron rest system relative to the laboratory system and $\gamma = E_e/(m_e c^2)$ is the Lorentz factor of the positron. $E_{\rm laser} = hc/\lambda_{\rm laser}$ gives the energy of the initial photon in the laboratory frame and $\lambdabar_{\rm c} = \frac{\hbar}{m_e c} = 3.862\cdot 10^{-13}$ m is the reduced Compton wavelength of the positron. ϵ denotes the angle between the incident laser photon and the z axis, while θ is the scattering angle of the photon in the rest frame of the initial positron (see Fig. 4.3 for the definition of the coordinate system).

The approximation in Eqn. (A.1) is valid for the kinematics at the Longitudinal Polarimeter where the crossing angle of the laser photons with the positron beam $\epsilon = 8.7$ mrad and $\gamma = 53.9\cdot 10^3$ for a HERA beam energy of $E_e = 27.56$ GeV.

The polar scattering angle θ of the Compton photon in the rest frame of the initial positron is related to the energy E_e of the initial positron and the energy E_γ of the scattered photon, both in the laboratory frame, by:

$$\cos\theta = \frac{E_e - E_\gamma\left(1+\frac{1}{\lambdabar_{\rm c}k_i}\right)}{\beta E_e - E_\gamma} \simeq \frac{E_e - E_\gamma\left(1+\frac{m_e c^2}{2\gamma E_{\rm laser}}\right)}{E_e - E_\gamma} \quad \text{or} \tag{A.3}$$

$$E_\gamma = E_e\cdot\frac{1-\beta\cos\theta}{1+\frac{1}{\lambdabar_{\rm c}k_i}-\cos\theta} \simeq E_e\cdot\frac{1-\cos\theta}{1+\frac{m_e c^2}{2\gamma E_{\rm laser}}-\cos\theta}\,. \tag{A.4}$$

The Compton photon scattering angle $\theta_{\rm lab}$ in the laboratory system (see Fig. 4.3 for the definitions of the angles θ and $\theta_{\rm lab}$) is related to the scattering angle θ in the positron rest system by:

$$\theta_{\rm lab} \simeq \tan\theta_{\rm lab} = \frac{1}{\gamma}\cdot\frac{\sin\theta}{\beta-\cos\theta}\,. \tag{A.5}$$

For the special case of Compton scattering of completely circularly polarised laser light ($S_1 = 0, |S_3| = 1$) off longitudinally polarised positrons ($P_x = P_y = 0, P_z \neq 0$) the cross section $\frac{{\rm d}\sigma_c}{{\rm d}\Omega}$ in Eqn. (4.11) becomes independent of the azimuthal scattering angle ϕ and can be integrated over this degree of freedom:

$$\left|\frac{{\rm d}\sigma_c}{{\rm d}\theta}\right| = \int_0^{2\pi}{\rm d}\phi\,\sin\theta\,\frac{{\rm d}\sigma_c}{{\rm d}\Omega} = 2\pi\sin\theta\,\frac{{\rm d}\sigma_c}{{\rm d}\Omega}\,. \tag{A.6}$$

The Compton cross section in dependence of the energy E_γ of the scattered photon in the laboratory system is then given by:

$$\frac{\mathrm{d}\sigma_c}{\mathrm{d}E_\gamma} = \frac{\mathrm{d}\theta}{\mathrm{d}E_\gamma} \cdot 2\pi \sin\theta \cdot \frac{\mathrm{d}\sigma_c}{\mathrm{d}\Omega} \simeq \frac{2\pi E_e}{\lambda\!\!\!^{-}_{\mathrm{c}}\, k_i\, (E_e - E_\gamma)^2} \cdot \frac{\mathrm{d}\sigma_c}{\mathrm{d}\Omega}\,, \tag{A.7}$$

using

$$\frac{\mathrm{d}\theta}{\mathrm{d}E_\gamma} = \frac{(\frac{1}{\lambda\!\!\!^{-}_{\mathrm{c}} k_i}\beta + \beta - 1)\, E_e}{\sin\theta\, (\beta E_e - E_\gamma)^2} \simeq \frac{E_e}{\lambda\!\!\!^{-}_{\mathrm{c}}\, k_i\, \sin\theta (E_e - E_\gamma)^2}\,. \tag{A.8}$$

In Fig. A.1 the differential Compton cross section is shown for scattering unpolarised and fully circularly polarised laser photons off fully longitudinally polarised positrons ($P_x = P_y = 0, P_z = 1$). The cross section was calculated for photons with a wavelength of 532 nm hitting a positron beam with an energy of 27.56 GeV under a crossing angle of 8.7 mrad in the laboratory system. These parameters match the conditions at the Longitudinal Polarimeter (see Sect. 4.4).

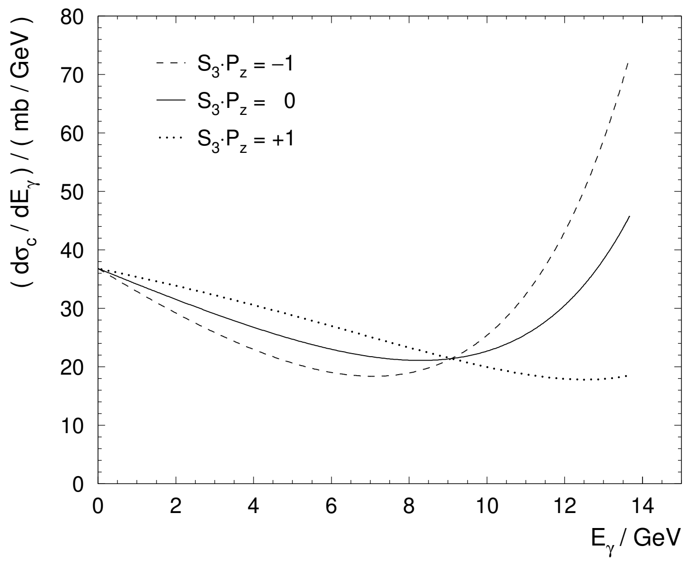

Figure A.1: The differential Compton cross section $\frac{\mathrm{d}\sigma_c}{\mathrm{d}E_\gamma}$ in dependence of the energy E_γ of the scattered photon in the laboratory frame. The full line corresponds to the unpolarised case, the dotted and the dashed lines give the cross sections for scattering fully circularly polarised laser light ($S_3 = \pm 1$) off longitudinally polarised positrons ($P_z = +1$).

B Measurement of the Laser Light Polarisation

The exact knowledge of the light polarisation is crucial for the operation of the Longitudinal Polarimeter as the measured positron polarisation scales directly with the difference $\Delta S_{\rm circ} = (|S^+_{\rm circ}| + |S^-_{\rm circ}|)/2$ in the degree of circular polarisation (see Eqn. (4.17)). At the Longitudinal Polarimeter the light polarisation can be measured at two different locations in the so–called *analyser boxes* AB1 and AB2. They are installed right behind the Pockels cell where the light becomes circularly polarised and behind the Compton I.P. at the end of the laser transport system in the HERA tunnel, respectively (see Fig. 4.4 on p. 51).

B.1 Setup of the "Analyser Boxes"

The two analyser boxes at the Longitudinal Polarimeter follow the same design idea, while their actual setup differs slightly in response to different geometrical boundary conditions. The measurement of the light polarisation is in principle performed by rotating an analyser and monitoring the transmitted light intensity in dependence of the rotation angle. Due to the high energy density of the pulses from the used laser, however, a setup had to be invented [Bur 96] which ensures that laser light is only absorbed in special beam dumps designed to withstand the high intensities. The setup of an analyser box is sketched in Fig. B.1.

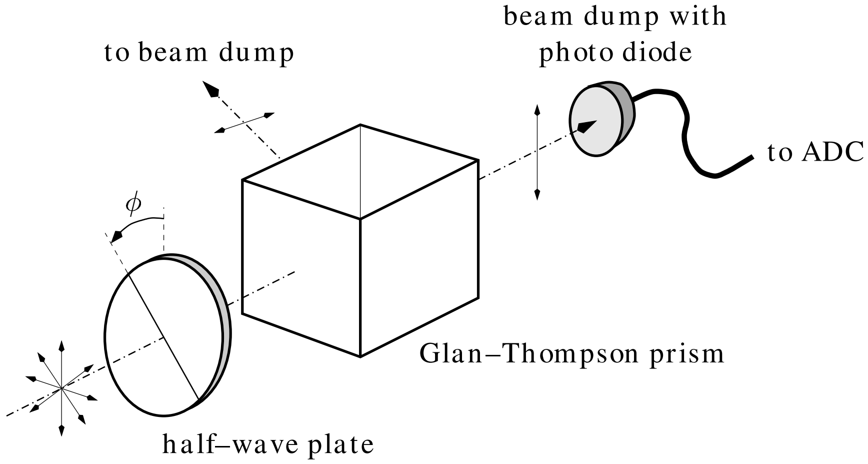

Figure B.1: Schematical setup of an analyser box used to measure the laser light polarisation.

In this sketch, the laser light is entering from the lower left side. It first passes through a half–wave plate which is mounted in a motorised rotary stage and can be rotated by any angle ϕ. Here, ϕ denotes the angle of the fast axis of the half–wave plate with respect to the vertical axis. Immediately behind the half–wave plate a Glan–Thompson prism is installed, which acts as an analyser, transmitting the light component with vertical linear polarisation straight through the prism while deflecting the component with horizontal linear polarisation sideways. The light beams emerging from either exit of the prism are absorbed in special beam dumps, designed to withstand the high energy densities of the laser pulses. A photo diode with an additional neutral density filter attached to a small opening at the rear side of one beam dump measures the intensity of the laser light which is transmitted through the Glan–Thompson prism. The signal from the photo diode is recorded by an ADC channel in the HERMES DAQ system, whereas the angle ϕ is recorded in the slow control system.

The above design has the advantage that the half–wave plate, which has very little weight, is the only rotational part. The "standard" approach to rotate the analyser (here the Glan–Thompson prism together with a beam dump) by itself would have required a much heavier and larger rotary stage.

B.2 Calculation of the Light Polarisation

The calculation of the light polarisation from the measured variation of the photo diode signal in dependence of the angular setting of the half–wave plate depends on the assumption that the light contains no unpolarised components, i.e. the light is fully linearly, circularly or elliptically polarised. For laser light this assumption is fulfilled with very good accuracy. This assumption can be expressed in terms of the Stokes parameters as

$$1 = S_0^2 = S_1^2 + S_2^2 + S_3^2 \,, \tag{B.1}$$

where the total intensity $I = S_0$ has been normalised to one. The definition of the Stokes parameters can be found e.g. in [Gue 90].

A fully polarised light wave with normalised intensity generally can be characterised by the linear and circular polarisation components:

$$\vec{S}_{\text{light}} = \begin{pmatrix} 1 \\ S_1 \\ S_2 \\ S_3 \end{pmatrix} = \begin{pmatrix} 1 \\ S_{\text{lin}} \cdot \cos(2\,\delta_{\text{lin}}) \\ S_{\text{lin}} \cdot \sin(2\,\delta_{\text{lin}}) \\ \pm\, S_{\text{circ}} \end{pmatrix} , \tag{B.2}$$

where δ_{lin} denotes the angle between the plane of linear polarisation and the 1–axis used in the definition of the Stokes vector. In our convention a negative value $S_3 < 0$ corresponds to left–handed circular polarisation S_{circ}^- and a positive value $S_3 > 0$ means right–handed circular polarisation S_{circ}^+. Together with Eqn. (B.1) this implies that the linear and circular polarisation are related to each other by

$$S_{\text{circ}} \;=\; +\sqrt{1 - S_{\text{lin}}^2} \,. \tag{B.3}$$

In order to describe quantitatively the effect of optical elements on the polarisation of a light wave described by a Stokes vector $\vec{S}$, the formalism of Mueller matrices [Mue 48] provides a useful tool. The Mueller matrices are real 4×4 matrices and the resulting Stokes vector for a light wave after the transmission through an optical system is obtained by the multiplication of the Mueller matrix $\mathbf{M}$ with the Stokes vector of the initial light wave:

$$\vec{S}_{\text{out}} = \mathbf{M}\,\vec{S}_{\text{in}} \,. \tag{B.4}$$

Table B.1 contains the definitions of Mueller matrices, which will be used in the following calculations.

Table B.1: Mueller matrices for a linear polariser, a quarter–wave and a half–wave retarder plate. The transmission axis of the linear polariser and the fast optical axes of the retarder plates are oriented vertically in these definitions [Gue 90]. This reference also contains a more complete list of Mueller matrices.

Linear polariser (Glan–Thompson prism)	$\mathbf{M}_{\text{G.T.}} = \frac{1}{2}\begin{pmatrix} 1 & -1 & 0 & 0 \\ -1 & 1 & 0 & 0 \\ 0 & 0 & 0 & 0 \\ 0 & 0 & 0 & 0 \end{pmatrix}$
Quarter–wave plate	$\mathbf{M}_{\lambda/4} = \begin{pmatrix} 1 & 0 & 0 & 0 \\ 0 & 1 & 0 & 0 \\ 0 & 0 & 0 & -1 \\ 0 & 0 & 1 & 0 \end{pmatrix}$
Half–wave plate	$\mathbf{M}_{\lambda/2} = \begin{pmatrix} 1 & 0 & 0 & 0 \\ 0 & 1 & 0 & 0 \\ 0 & 0 & -1 & 0 \\ 0 & 0 & 0 & -1 \end{pmatrix}$

For a retarder plate rotated by an angle ϕ the Mueller matrix $\mathbf{M}(\phi)$ is obtained from the definition at $\phi = 0$ by multiplication with the rotation matrices

$$\mathbf{M}(\phi) \;=\; \mathbf{D}_{-}(\phi)\,\mathbf{M}\,\mathbf{D}_{+}(\phi)\;, \tag{B.5}$$

using the definition:

$$\mathbf{D}_{\pm}(\phi) \equiv \begin{pmatrix} 1 & 0 & 0 & 0 \\ 0 & \cos(2\,\phi) & \pm\sin(2\,\phi) & 0 \\ 0 & \mp\sin(2\,\phi) & \cos(2\,\phi) & 0 \\ 0 & 0 & 0 & 1 \end{pmatrix}. \tag{B.6}$$

The Stokes vector $\vec{S}_{\text{p.d.}}$ of the light wave incident on the photo diode of the analyser box (see Fig. B.1) can be expressed as:

$$\vec{S}_{\text{p.d.}} \;=\; \mathbf{M}_{\text{perfect}}(\phi)\,\vec{S}_{\text{light}}\;, \tag{B.7}$$

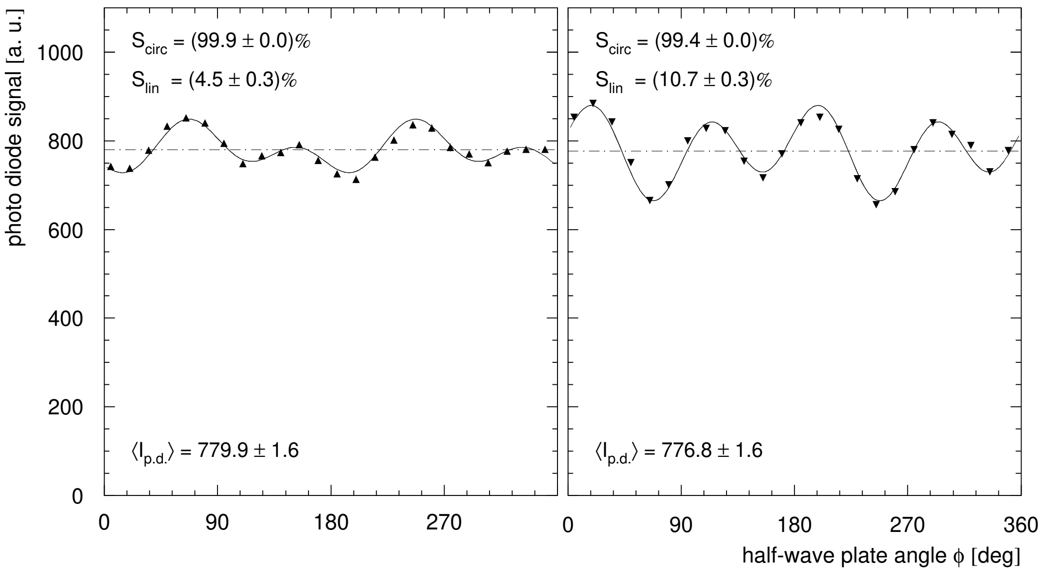

Figure B.2: A measurement of the laser light polarisation in the analyser box AB 2, located in the tunnel behind the Compton I.P. for left (▲) and right (▼) handed helicity. The dotted–dashed lines show the averaged intensity for each helicity state, the full line is the result of a fit to the data as described in the text.

with

$$\begin{aligned} \mathbf{M}_{\text{perfect}}(\phi) &= \mathbf{M}_{\text{G.T.}}\,\mathbf{M}_{\lambda/2}(\phi) \;=\; \mathbf{M}_{\text{G.T.}}\,\mathbf{D}_{-}(\phi)\,\mathbf{M}_{\lambda/2}\,\mathbf{D}_{+}(\phi) \\ &= \frac{1}{2}\begin{pmatrix} 1 & -\cos(4\,\phi) & -\sin(4\,\phi) & 0 \\ -1 & \cos(4\,\phi) & \sin(4\,\phi) & 0 \\ 0 & 0 & 0 & 0 \\ 0 & 0 & 0 & 0 \end{pmatrix} . \end{aligned} \tag{B.8}$$

Here, it is assumed that the Glan–Thompson prism and the half–wave plate are perfectly described by the Mueller matrices listed in Tab. B.1. Using Eqns. (B.7) and (B.8) the resulting Stokes vector is:

$$\vec{S}_{\text{p.d.}} = \frac{1}{2}\begin{pmatrix} 1 - \cos(4\,\phi + 2\,\delta_{\text{lin}})\,S_{\text{lin}} \\ -1 + \cos(4\,\phi + 2\,\delta_{\text{lin}})\,S_{\text{lin}} \\ 0 \\ 0 \end{pmatrix} . \tag{B.9}$$

The intensity $I_{\text{p.d.}}$ of the light incident on the photo diode is proportional to the 0–component of the Stokes vector $\vec{S}_{\text{p.d.}}$:

$$I_{\text{p.d.}} \propto 1 - \cos(4\,\phi + 2\,\delta_{\text{lin}}) \cdot S_{\text{lin}} \;, \tag{B.10}$$

so that one expects a sinusoidal variation of the intensity with a periodicity of 90 degrees when rotating the half–wave plate. The amplitude of this variation equals the linear polarisation component S_{lin}. Fig. B.2 shows a measurement of the light intensity on the photo diode versus the angle ϕ over a full turn of the half–wave plate. A variation of the measured intensity with a periodicity of 90 degrees is clearly visible, but the data points do not follow exactly a $\cos(4\,\phi)$ curve, as expected from Eqn. (B.10). In the following it is shown that this deviation from the expected curve can be explained by assuming a non–perfect half–wave plate.

A slight difference of the thickness of the plate due to temperature variations can cause a retardation of not exactly $\lambda/2$. The same effect can occur due to an inaccurate alignment of the normal axis of the retarder plate with the laser beam axis. These distortions can be effectively expressed by assuming a small admixture ϵ ($\epsilon \ll 1$) of a quarter–wave plate to the real "half–wave" plate. In order to accommodate this deviation into the above calculation the Mueller matrix $\mathbf{M}_{\text{perfect}}(\phi)$ in Eqn. (B.7) has to be replaced by the following expression:

$$\begin{aligned}\mathbf{M}_{\text{real}}(\phi) &= \mathbf{M}_{\text{G.T.}}\,\mathbf{D}_{-}(\phi)\,\left[(1-\epsilon)\,\mathbf{M}_{\lambda/2} + \epsilon\,\mathbf{M}_{\lambda/4}\right]\,\mathbf{D}_{+}(\phi) \\ &= \frac{1}{2}\begin{pmatrix} 1 & \left(\frac{\epsilon}{2}-1\right)\cos(4\,\phi)-\frac{\epsilon}{2} & \left(\frac{\epsilon}{2}-1\right)\sin(4\,\phi) & -\epsilon\,\sin(2\,\phi) \\ -1 & \left(1-\frac{\epsilon}{2}\right)\cos(4\,\phi)+\frac{\epsilon}{2} & \left(1-\frac{\epsilon}{2}\right)\sin(4\,\phi) & \epsilon\,\sin(2\,\phi) \\ 0 & 0 & 0 & 0 \\ 0 & 0 & 0 & 0 \end{pmatrix}.\end{aligned} \tag{B.11}$$

Analog to Eqn. (B.7), by multiplication of this matrix with the incident Stokes vector $\vec{S}_{\text{light}}$ one obtains the intensity $I_{\text{p.d.}}$ measured by the photo diode:

$$I_{\text{p.d.}} \propto 1 - \frac{\epsilon}{2}\cos(2\,\delta_{\text{lin}})\cdot S_{\text{lin}} - \epsilon\cdot S_{\text{circ}}\cdot\sin(2\,\phi) + \left(\frac{\epsilon}{2}-1\right)\cdot S_{\text{lin}}\cdot\cos(4\,\phi+2\,\delta_{\text{lin}})\,. \tag{B.12}$$

Using this model, a fit of the function

$$\begin{aligned}I_{\text{meas}}(\phi) = I_0\cdot\Big[1 &- \frac{\epsilon}{2}\cos(2\,\delta_{\text{lin}})\cdot S_{\text{lin}} - \epsilon\cdot\sqrt{1-S_{\text{lin}}^2}\cdot\sin(2\,\phi-\delta_0) \\ &+ \left(\frac{\epsilon}{2}-1\right)\cdot S_{\text{lin}}\cdot\cos(4\,\phi+2\,\delta_{\text{lin}}-\delta_0)\Big]\end{aligned} \tag{B.13}$$

to the data points with I_0, ϵ, δ_{lin}, δ_0 and S_{lin} as free parameters provides an excellent description of the data as shown in Fig. B.2. The additional degree of freedom δ_0 in the fit takes into account that the fast axis of the half–wave plate is not necessarily aligned with the zero degrees setting of the rotary stage. The circular polarisation S_{circ} is calculated from the fitted value of S_{lin} using Eqn. (B.3).

The fit to the data shown in Fig. B.2 yields values of $S_{\text{circ}} = 99.9\% \pm 0.01\%$ ($99.4\% \pm 0.03\%$), $\epsilon = 4.4\% \pm 0.3\%$ ($4.8\% \pm 0.3\%$) and $\delta_{\text{lin}} = -9.1^\circ \pm 2.6^\circ$ ($-6.3^\circ \pm 1.9^\circ$) for left (right) handed helicity of the light. Furthermore, the model underlying the fit gives consistent values for ϵ, δ_{lin} and for the averaged intensity $\langle I_{\text{p.d.}}\rangle \equiv I_0$ on the photo diode for both helicity states.

C Purity Fit Coefficients

The Coefficients for the Polarisation Symmetric Sea Assumption

For the assumption of a polarisation symmetric sea, which is defined in Eqn. (6.25), the following three quark polarisations are fitted in the *flavour decomposition*:

$$\frac{\Delta u + \Delta\overline{u}}{u+\overline{u}},\ \frac{\Delta d + \Delta\overline{d}}{d+\overline{d}},\ \frac{\Delta q_{\mathrm{s}}}{q_{\mathrm{s}}}. \tag{C.1}$$

Owing to Eqn. (6.25) the sea polarisation $\Delta q_{\mathrm{s}}/q_{\mathrm{s}}$ equals the polarisation $(\Delta s+\Delta\overline{s})/(s+\overline{s})$ of the strange flavours in this model, under the additional assumption that the unpolarised strange quark distribution is $SU(2)$ symmetric, $s(x) = \overline{s}(x)$.

Using Eqn. (6.7) the inclusive asymmetry A_1 can be expressed as

$$\begin{aligned}
A_1 \propto\ & P_u \cdot \frac{\Delta u}{u} + P_{\overline{u}} \cdot \frac{\Delta\overline{u}}{\overline{u}} + P_d \cdot \frac{\Delta d}{d} + P_{\overline{d}} \cdot \frac{\Delta\overline{d}}{\overline{d}} + P_s \cdot \frac{\Delta s}{s} + P_{\overline{s}} \cdot \frac{\Delta\overline{s}}{\overline{s}} \\
=\ & P_u \cdot \frac{\Delta u + \Delta\overline{u}}{u+\overline{u}} \cdot \frac{u+\overline{u}}{u} - P_u \cdot \frac{\Delta\overline{u}}{\overline{u}} \cdot \frac{\overline{u}}{u} + P_{\overline{u}} \cdot \frac{\Delta\overline{u}}{\overline{u}} \\
& + P_d \cdot \frac{\Delta d + \Delta\overline{d}}{d+\overline{d}} \cdot \frac{d+\overline{d}}{d} - P_d \cdot \frac{\Delta\overline{d}}{\overline{d}} \cdot \frac{\overline{d}}{d} + P_{\overline{d}} \cdot \frac{\Delta\overline{d}}{\overline{d}} + P_s \cdot \frac{\Delta s}{s} + P_{\overline{s}} \cdot \frac{\Delta\overline{s}}{\overline{s}} \\
=\ & \frac{\Delta u + \Delta\overline{u}}{u+\overline{u}} \cdot \left(P_u \cdot \frac{u+\overline{u}}{u}\right) + \frac{\Delta q_{\mathrm{s}}}{q_{\mathrm{s}}} \cdot \left(-P_u \cdot \frac{\overline{u}}{u} + P_{\overline{u}}\right) \\
& + \frac{\Delta d + \Delta\overline{d}}{d+\overline{d}} \cdot \left(P_d \cdot \frac{d+\overline{d}}{d}\right) + \frac{\Delta q_{\mathrm{s}}}{q_{\mathrm{s}}} \cdot \left(-P_d \cdot \frac{\overline{d}}{d} + P_{\overline{d}}\right) + \frac{\Delta q_{\mathrm{s}}}{q_{\mathrm{s}}} \cdot (P_s + P_{\overline{s}}) \\
=\ & \frac{\mathbf{\Delta u + \Delta\overline{u}}}{\mathbf{u+\overline{u}}} \cdot \left(P_u \cdot \frac{u+\overline{u}}{u}\right) + \frac{\mathbf{\Delta d + \Delta\overline{d}}}{\mathbf{d+\overline{d}}} \cdot \left(P_d \cdot \frac{d+\overline{d}}{d}\right) \\
& + \frac{\mathbf{\Delta q_s}}{\mathbf{q_s}} \cdot \left(-P_u \cdot \frac{\overline{u}}{u} + P_{\overline{u}} - P_d \cdot \frac{\overline{d}}{d} + P_{\overline{d}} + P_s + P_{\overline{s}}\right) ,
\end{aligned} \tag{C.2}$$

where the kinematic dependence of all quantities on x has been omitted. For each fitted quark polarisation in the above Eqn. (C.2) the coefficients are summarised:

$$\frac{\Delta u + \Delta\overline{u}}{u+\overline{u}} : \qquad P_u \cdot \frac{u+\overline{u}}{u} , \tag{C.3}$$

$$\frac{\Delta d + \Delta\overline{d}}{d+\overline{d}} : \qquad P_d \cdot \frac{d+\overline{d}}{d} , \tag{C.4}$$

$$\frac{\Delta q_{\mathrm{s}}}{q_{\mathrm{s}}} : \qquad - P_u \cdot \frac{\overline{u}}{u} + P_{\overline{u}} - P_d \cdot \frac{\overline{d}}{d} + P_{\overline{d}} + P_s + P_{\overline{s}} . \tag{C.5}$$

Similarly, for the *valence decomposition* one obtains the following coefficients for the fitted quark polarisations:

$$\frac{\Delta u_{\mathrm{v}}}{u_{\mathrm{v}}} : \qquad P_u \cdot \frac{u-\overline{u}}{u} , \tag{C.6}$$

$$\frac{\Delta d_{\mathrm{v}}}{d_{\mathrm{v}}} : \qquad P_d \cdot \frac{d-\overline{d}}{d} , \tag{C.7}$$

$$\frac{\Delta q_{\mathrm{s}}}{q_{\mathrm{s}}} : \qquad P_u \cdot \frac{\overline{u}}{u} + P_{\overline{u}} + P_d \cdot \frac{\overline{d}}{d} + P_{\overline{d}} + P_s + P_{\overline{s}} . \tag{C.8}$$

The Coefficients for the SU(3) Symmetric Sea Assumption

Assuming an $SU(3)_f$ symmetric sea as defined in Eqn. (6.23), in the *flavour decomposition* the same three quark polarisations are fitted as given in Eqn. (C.1). Here, the unpolarised sea quark distribution is defined as

$$q_\mathrm{s} := \frac{1}{6}\left(u_\mathrm{s} + \overline{u} + d_\mathrm{s} + \overline{d} + s + \overline{s}\right) = \frac{1}{3}\left(u_\mathrm{s} + d_\mathrm{s} + s\right) . \tag{C.9}$$

Note that the factor 1/6 in this definition is arbitrary, as the unpolarised sea distribution q_s will cancel out in Eqn. (C.10) below.

Again using Eqn. (6.7) the inclusive asymmetry A_1 can be expressed as

$$\begin{aligned}
A_1 \propto\; & P_u \cdot \frac{\Delta u}{u} + P_{\overline{u}} \cdot \frac{\Delta \overline{u}}{\overline{u}} + P_d \cdot \frac{\Delta d}{d} + P_{\overline{d}} \cdot \frac{\Delta \overline{d}}{\overline{d}} + P_s \cdot \frac{\Delta s}{s} + P_{\overline{s}} \cdot \frac{\Delta \overline{s}}{\overline{s}} \\
=\; & P_u \cdot \frac{\Delta u + \Delta \overline{u}}{u + \overline{u}} \cdot \frac{u + \overline{u}}{u} - P_u \cdot \frac{\Delta q_\mathrm{s}}{q_\mathrm{s}} \cdot \frac{q_\mathrm{s}}{u} + P_{\overline{u}} \cdot \frac{\Delta q_\mathrm{s}}{q_\mathrm{s}} \cdot \frac{q_\mathrm{s}}{\overline{u}} \\
& P_d \cdot \frac{\Delta d + \Delta \overline{d}}{d + \overline{d}} \cdot \frac{d + \overline{d}}{d} - P_d \cdot \frac{\Delta q_\mathrm{s}}{q_\mathrm{s}} \cdot \frac{q_\mathrm{s}}{d} + P_{\overline{d}} \cdot \frac{\Delta q_\mathrm{s}}{q_\mathrm{s}} \cdot \frac{q_\mathrm{s}}{\overline{d}} + P_s \cdot \frac{\Delta q_\mathrm{s}}{q_\mathrm{s}} \cdot \frac{q_\mathrm{s}}{s} + P_{\overline{s}} \cdot \frac{\Delta q_\mathrm{s}}{q_\mathrm{s}} \cdot \frac{q_\mathrm{s}}{\overline{s}} \\
=\; & \frac{\mathbf{\Delta u + \Delta \overline{u}}}{\mathbf{u + \overline{u}}} \cdot \left(P_u \cdot \frac{u + \overline{u}}{u}\right) + \frac{\mathbf{\Delta d + \Delta \overline{d}}}{\mathbf{d + \overline{d}}} \cdot \left(P_d \cdot \frac{d + \overline{d}}{d}\right) \\
& + \frac{\mathbf{\Delta q_s}}{\mathbf{q_s}} \cdot \left(-P_u \cdot \frac{q_\mathrm{s}}{u} + P_{\overline{u}} \cdot \frac{q_\mathrm{s}}{\overline{u}} - P_d \cdot \frac{q_\mathrm{s}}{d} + P_{\overline{d}} \cdot \frac{q_\mathrm{s}}{\overline{d}} + P_s \cdot \frac{q_\mathrm{s}}{s} + P_{\overline{s}} \cdot \frac{q_\mathrm{s}}{\overline{s}}\right) .
\end{aligned} \tag{C.10}$$

For each fitted quark polarisation in Eqn. (C.10) the coefficients are summarised:

$$\frac{\Delta u + \Delta \overline{u}}{u + \overline{u}} : \qquad P_u \cdot \frac{u + \overline{u}}{u} , \tag{C.11}$$

$$\frac{\Delta d + \Delta \overline{d}}{d + \overline{d}} : \qquad P_d \cdot \frac{d + \overline{d}}{d} , \tag{C.12}$$

$$\frac{\Delta q_\mathrm{s}}{q_\mathrm{s}} : \qquad -P_u \cdot \frac{q_\mathrm{s}}{u} + P_{\overline{u}} \cdot \frac{q_\mathrm{s}}{\overline{u}} - P_d \cdot \frac{q_\mathrm{s}}{d} + P_{\overline{d}} \cdot \frac{q_\mathrm{s}}{\overline{d}} + P_s \cdot \frac{q_\mathrm{s}}{s} + P_{\overline{s}} \cdot \frac{q_\mathrm{s}}{\overline{s}} . \tag{C.13}$$

Similarly, for the *valence decomposition* one obtains the following coefficients for the fitted quark polarisations:

$$\frac{\Delta u_\mathrm{v}}{u_\mathrm{v}} : \qquad P_u \cdot \frac{u - \overline{u}}{u} , \tag{C.14}$$

$$\frac{\Delta d_\mathrm{v}}{d_\mathrm{v}} : \qquad P_d \cdot \frac{d - \overline{d}}{d} , \tag{C.15}$$

$$\frac{\Delta q_\mathrm{s}}{q_\mathrm{s}} : \qquad P_u \cdot \frac{q_\mathrm{s}}{u} + P_{\overline{u}} \cdot \frac{q_\mathrm{s}}{\overline{u}} + P_d \cdot \frac{q_\mathrm{s}}{d} + P_{\overline{d}} \cdot \frac{q_\mathrm{s}}{\overline{d}} + P_s \cdot \frac{q_\mathrm{s}}{s} + P_{\overline{s}} \cdot \frac{q_\mathrm{s}}{\overline{s}} . \tag{C.16}$$

D Tables of Results: Semi Inclusive Asymmetries

Table D.1: Kinematical quantities and numbers of events for the 1996 inclusive and semi inclusive proton asymmetries. For each x–bin the mean values averaged over both target spin states are given; the event numbers are summed over all spin states. In case of the semi inclusive events, the kinematical quantities are given for the hadron asymmetries $A^{h^\pm}$, except for the mean values in z and the event numbers, which are also given for the pion asymmetries $A^{\pi^\pm}$. The values for $R(x, Q^2)$ and ϵ were calculated from the mean values in x and Q^2, using the parametrisation for $R(x, Q^2)$ given in [Abe 99].

Inclusive DIS events											
Bin	$\langle x\rangle$	$\langle Q^2\rangle$ (GeV^2)	$\langle W^2\rangle$ (GeV^2)	ϵ	$\langle\eta\rangle$	$\langle\gamma\rangle$	$\langle D\rangle$	R	$\frac{1}{1+\eta\gamma}$	$\frac{1+R}{1+\gamma^2}$	N_{events}
1	0.033	1.212	36.64	0.527	0.025	0.056	0.712	0.364	0.999	1.360	53164
2	0.047	1.465	30.41	0.689	0.043	0.075	0.585	0.350	0.997	1.343	63114
3	0.065	1.714	25.75	0.785	0.063	0.096	0.496	0.331	0.994	1.319	74542
4	0.087	1.991	21.87	0.847	0.087	0.121	0.428	0.306	0.989	1.287	75387
5	0.119	2.301	18.04	0.896	0.121	0.156	0.363	0.274	0.980	1.244	90259
6	0.168	2.651	14.12	0.934	0.172	0.208	0.298	0.238	0.963	1.187	92598
7	0.244	3.061	10.45	0.959	0.248	0.287	0.239	0.201	0.928	1.110	90693
8	0.342	3.754	8.10	0.969	0.318	0.361	0.211	0.161	0.891	1.027	40908
9	0.465	5.220	6.85	0.966	0.352	0.405	0.221	0.117	0.870	0.960	19551

Semi inclusive DIS events with positively charged hadrons												
Bin	$\langle x\rangle$	$\langle Q^2\rangle$ (GeV^2)	$\langle W^2\rangle$ (GeV^2)	ϵ	$\langle\eta\rangle$	$\langle\gamma\rangle$	$\langle D\rangle$	R	$\langle z_{h^+}\rangle$	N_{h^+}	$\langle z_{\pi^+}\rangle$	N_{π^+}
1	0.034	1.205	35.89	0.549	0.027	0.058	0.695	0.364	0.362	8818	0.367	5431
2	0.048	1.449	30.01	0.699	0.044	0.075	0.575	0.351	0.391	12251	0.432	6228
3	0.065	1.744	26.17	0.776	0.061	0.094	0.506	0.329	0.404	14635	0.474	6543
4	0.087	2.137	23.44	0.819	0.080	0.116	0.466	0.297	0.415	13969	0.499	5588
5	0.118	2.703	21.17	0.846	0.101	0.140	0.442	0.253	0.416	14083	0.521	4879
6	0.166	3.621	19.13	0.862	0.125	0.170	0.433	0.196	0.412	10097	0.529	3132
7	0.239	5.127	17.23	0.867	0.150	0.204	0.442	0.138	0.409	5380	0.541	1549
8	0.338	7.163	14.94	0.868	0.177	0.241	0.450	0.097	0.392	1305	0.538	341
9	0.449	9.798	12.84	0.858	0.196	0.272	0.474	0.071	0.376	298	0.575	62

Semi inclusive DIS events with negatively charged hadrons												
Bin	$\langle x\rangle$	$\langle Q^2\rangle$ (GeV^2)	$\langle W^2\rangle$ (GeV^2)	ϵ	$\langle\eta\rangle$	$\langle\gamma\rangle$	$\langle D\rangle$	R	$\langle z_{h^-}\rangle$	N_{h^-}	$\langle z_{\pi^-}\rangle$	N_{π^-}
1	0.033	1.203	35.99	0.547	0.026	0.057	0.698	0.364	0.351	5929	0.360	4116
2	0.047	1.452	30.23	0.694	0.043	0.075	0.580	0.351	0.376	7904	0.425	4677
3	0.065	1.761	26.44	0.770	0.060	0.094	0.512	0.328	0.392	9128	0.464	4779
4	0.087	2.163	23.78	0.812	0.079	0.115	0.474	0.296	0.397	7900	0.487	3712
5	0.118	2.730	21.35	0.843	0.100	0.139	0.447	0.252	0.398	7474	0.505	3079
6	0.165	3.725	19.67	0.853	0.121	0.167	0.448	0.192	0.391	4909	0.507	1883
7	0.237	5.160	17.52	0.862	0.147	0.201	0.449	0.138	0.382	2570	0.508	913
8	0.338	7.319	15.24	0.862	0.174	0.239	0.462	0.095	0.376	546	0.499	185
9	0.443	9.544	12.85	0.862	0.196	0.271	0.467	0.072	0.407	130	0.555	51

Table D.2: Kinematical quantities and numbers of events for the 1997 inclusive and semi inclusive proton asymmetries. See Table D.1 for more information on the quantities shown.

Inclusive DIS events											
Bin	$\langle x \rangle$	$\langle Q^2 \rangle$ (GeV^2)	$\langle W^2 \rangle$ (GeV^2)	ϵ	$\langle \eta \rangle$	$\langle \gamma \rangle$	$\langle D \rangle$	R	$\frac{1}{1+\eta\gamma}$	$\frac{1+R}{1+\gamma^2}$	N_{events}
1	0.033	1.211	36.65	0.526	0.025	0.056	0.712	0.364	0.999	1.360	120644
2	0.047	1.465	30.41	0.689	0.043	0.075	0.585	0.350	0.997	1.343	142204
3	0.065	1.710	25.71	0.786	0.063	0.096	0.495	0.331	0.994	1.319	166878
4	0.087	1.984	21.79	0.849	0.087	0.121	0.426	0.306	0.989	1.287	166604
5	0.119	2.293	17.98	0.897	0.121	0.156	0.362	0.275	0.980	1.244	198097
6	0.168	2.649	14.11	0.934	0.172	0.208	0.298	0.238	0.963	1.187	202111
7	0.245	3.039	10.36	0.960	0.250	0.288	0.236	0.202	0.927	1.110	198420
8	0.342	3.714	8.02	0.969	0.320	0.362	0.208	0.162	0.890	1.028	91419
9	0.466	5.135	6.75	0.968	0.356	0.408	0.217	0.119	0.868	0.959	45420

Semi inclusive DIS events with positively charged hadrons												
Bin	$\langle x \rangle$	$\langle Q^2 \rangle$ (GeV^2)	$\langle W^2 \rangle$ (GeV^2)	ϵ	$\langle \eta \rangle$	$\langle \gamma \rangle$	$\langle D \rangle$	R	$\langle z_{h^+} \rangle$	N_{h^+}	$\langle z_{\pi^+} \rangle$	N_{π^+}
1	0.033	1.207	36.02	0.546	0.026	0.057	0.698	0.364	0.362	19419	0.365	11991
2	0.048	1.452	30.09	0.697	0.044	0.075	0.577	0.351	0.388	26831	0.426	14080
3	0.065	1.739	26.13	0.777	0.061	0.094	0.505	0.330	0.407	32106	0.472	14692
4	0.087	2.129	23.36	0.820	0.080	0.116	0.464	0.298	0.417	29766	0.503	11957
5	0.118	2.682	20.98	0.850	0.102	0.141	0.437	0.254	0.419	29776	0.520	10577
6	0.166	3.636	19.23	0.861	0.124	0.169	0.436	0.196	0.418	20900	0.530	6841
7	0.238	5.096	17.20	0.868	0.150	0.204	0.440	0.139	0.412	11151	0.542	3417
8	0.338	7.109	14.83	0.871	0.178	0.242	0.446	0.097	0.395	2681	0.538	717
9	0.447	9.702	12.87	0.860	0.196	0.272	0.472	0.071	0.389	616	0.544	167

Semi inclusive DIS events with negatively charged hadrons												
Bin	$\langle x \rangle$	$\langle Q^2 \rangle$ (GeV^2)	$\langle W^2 \rangle$ (GeV^2)	ϵ	$\langle \eta \rangle$	$\langle \gamma \rangle$	$\langle D \rangle$	R	$\langle z_{h^-} \rangle$	N_{h^-}	$\langle z_{\pi^-} \rangle$	N_{π^-}
1	0.033	1.207	36.17	0.541	0.026	0.057	0.702	0.364	0.348	13337	0.354	9551
2	0.047	1.456	30.21	0.694	0.043	0.075	0.580	0.351	0.375	17123	0.419	10450
3	0.065	1.763	26.53	0.768	0.060	0.094	0.514	0.328	0.389	19308	0.459	10431
4	0.087	2.157	23.65	0.815	0.079	0.115	0.471	0.296	0.397	16821	0.486	8061
5	0.118	2.713	21.28	0.845	0.100	0.140	0.445	0.253	0.396	15667	0.498	6619
6	0.165	3.685	19.48	0.856	0.122	0.168	0.443	0.194	0.390	10558	0.502	4234
7	0.238	5.137	17.37	0.865	0.148	0.202	0.445	0.138	0.383	5143	0.512	1884
8	0.337	7.234	15.08	0.865	0.175	0.239	0.456	0.096	0.377	1187	0.518	419
9	0.443	9.547	12.82	0.863	0.197	0.271	0.466	0.072	0.352	261	0.520	75

Table D.3: Kinematical quantities and numbers of events for the inclusive and semi inclusive proton asymmetries, combined for 1996 and 1997 data. See Table D.1 for more information on the quantities shown.

Inclusive DIS events											
Bin	$\langle x \rangle$	$\langle Q^2 \rangle$ (GeV^2)	$\langle W^2 \rangle$ (GeV^2)	ϵ	$\langle \eta \rangle$	$\langle \gamma \rangle$	$\langle D \rangle$	R	$\frac{1}{1+\eta\gamma}$	$\frac{1+R}{1+\gamma^2}$	N_{events}
1	0.033	1.212	36.65	0.526	0.025	0.056	0.712	0.364	0.999	1.360	173808
2	0.047	1.465	30.41	0.689	0.043	0.075	0.585	0.350	0.997	1.343	205318
3	0.065	1.711	25.72	0.785	0.063	0.096	0.495	0.331	0.994	1.319	241420
4	0.087	1.986	21.82	0.848	0.087	0.121	0.427	0.306	0.989	1.287	241991
5	0.119	2.295	18.00	0.896	0.121	0.156	0.362	0.274	0.980	1.244	288356
6	0.168	2.650	14.11	0.934	0.172	0.208	0.298	0.238	0.963	1.187	294709
7	0.245	3.046	10.39	0.960	0.250	0.288	0.237	0.202	0.928	1.110	289113
8	0.342	3.726	8.05	0.969	0.319	0.362	0.209	0.162	0.890	1.027	132327
9	0.465	5.161	6.78	0.967	0.355	0.407	0.218	0.118	0.869	0.959	64971

Semi inclusive DIS events with positively charged hadrons												
Bin	$\langle x \rangle$	$\langle Q^2 \rangle$ (GeV^2)	$\langle W^2 \rangle$ (GeV^2)	ϵ	$\langle \eta \rangle$	$\langle \gamma \rangle$	$\langle D \rangle$	R	$\langle z_{h^+} \rangle$	N_{h^+}	$\langle z_{\pi^+} \rangle$	N_{π^+}
1	0.034	1.206	35.98	0.547	0.027	0.057	0.697	0.364	0.362	28237	0.366	17422
2	0.048	1.451	30.06	0.698	0.044	0.075	0.576	0.351	0.389	39082	0.428	20308
3	0.065	1.741	26.14	0.777	0.061	0.094	0.505	0.330	0.406	46741	0.473	21235
4	0.087	2.132	23.38	0.820	0.080	0.116	0.465	0.298	0.417	43735	0.501	17545
5	0.118	2.689	21.04	0.849	0.102	0.141	0.439	0.254	0.418	43859	0.521	15456
6	0.166	3.631	19.20	0.861	0.124	0.169	0.435	0.196	0.416	30997	0.530	9973
7	0.238	5.106	17.21	0.867	0.150	0.204	0.440	0.139	0.411	16531	0.542	4966
8	0.338	7.127	14.86	0.870	0.178	0.242	0.448	0.097	0.394	3986	0.538	1058
9	0.447	9.734	12.86	0.859	0.196	0.272	0.472	0.071	0.385	914	0.553	229

Semi inclusive DIS events with negatively charged hadrons												
Bin	$\langle x \rangle$	$\langle Q^2 \rangle$ (GeV^2)	$\langle W^2 \rangle$ (GeV^2)	ϵ	$\langle \eta \rangle$	$\langle \gamma \rangle$	$\langle D \rangle$	R	$\langle z_{h^-} \rangle$	N_{h^-}	$\langle z_{\pi^-} \rangle$	N_{π^-}
1	0.033	1.206	36.12	0.543	0.026	0.057	0.700	0.364	0.349	19266	0.356	13667
2	0.047	1.455	30.22	0.694	0.043	0.075	0.580	0.351	0.375	25027	0.421	15127
3	0.065	1.763	26.50	0.769	0.060	0.094	0.514	0.328	0.390	28436	0.460	15210
4	0.087	2.159	23.69	0.814	0.079	0.115	0.472	0.296	0.397	24721	0.486	11773
5	0.118	2.718	21.30	0.844	0.100	0.140	0.445	0.252	0.397	23141	0.500	9698
6	0.165	3.697	19.54	0.855	0.122	0.168	0.445	0.193	0.391	15467	0.504	6117
7	0.237	5.145	17.42	0.864	0.148	0.202	0.446	0.138	0.383	7713	0.511	2797
8	0.338	7.261	15.13	0.864	0.175	0.239	0.458	0.096	0.377	1733	0.512	604
9	0.443	9.558	12.83	0.862	0.196	0.271	0.467	0.072	0.371	391	0.535	126

Table D.4: The 1996 proton asymmetries $A_1^{(h/\pi)} = A_{\|}^{(h/\pi)} / [D\,(1+\eta\gamma)]$, including all corrections. For the semi inclusive case the mean values of the kinematical quantities x, y, and Q^2 are given for the hadron asymmetries $A_1^{h^\pm}$.

Bin	$\langle x\rangle$	$\langle y\rangle$	$\langle Q^2\rangle$ (GeV^2)	A_1 ± stat. ± sys.
1	0.033	0.715	1.212	0.104 ± 0.014 ± 0.008
2	0.047	0.599	1.465	0.098 ± 0.016 ± 0.007
3	0.065	0.514	1.714	0.097 ± 0.017 ± 0.007
4	0.087	0.444	1.991	0.192 ± 0.019 ± 0.014
5	0.119	0.376	2.301	0.205 ± 0.020 ± 0.015
6	0.168	0.307	2.651	0.229 ± 0.024 ± 0.018
7	0.244	0.244	3.061	0.331 ± 0.029 ± 0.027
8	0.342	0.212	3.754	0.369 ± 0.050 ± 0.033
9	0.465	0.216	5.220	0.483 ± 0.068 ± 0.047

Bin	$\langle x\rangle$	$\langle y\rangle$	$\langle Q^2\rangle$ (GeV^2)	$A_1^{h^+}$ ± stat. ± sys.	$A_1^{\pi^+}$ ± stat. ± sys.
1	0.034	0.700	1.205	0.108 ± 0.033 ± 0.008	0.123 ± 0.042 ± 0.009
2	0.048	0.591	1.449	0.118 ± 0.035 ± 0.009	0.106 ± 0.047 ± 0.008
3	0.065	0.522	1.744	0.112 ± 0.036 ± 0.008	0.120 ± 0.050 ± 0.009
4	0.087	0.477	2.137	0.161 ± 0.040 ± 0.012	0.217 ± 0.055 ± 0.016
5	0.118	0.444	2.703	0.228 ± 0.042 ± 0.017	0.236 ± 0.061 ± 0.017
6	0.166	0.423	3.621	0.275 ± 0.051 ± 0.020	0.356 ± 0.078 ± 0.026
7	0.239	0.415	5.127	0.479 ± 0.070 ± 0.035	0.391 ± 0.112 ± 0.029
8	0.338	0.410	7.163	0.491 ± 0.139 ± 0.036	0.742 ± 0.237 ± 0.054
9	0.449	0.421	9.798	0.606 ± 0.275 ± 0.046	1.039 ± 0.554 ± 0.076

Bin	$\langle x\rangle$	$\langle y\rangle$	$\langle Q^2\rangle$ (GeV^2)	$A_1^{h^-}$ ± stat. ± sys.	$A_1^{\pi^-}$ ± stat. ± sys.
1	0.033	0.702	1.203	0.142 ± 0.044 ± 0.011	0.135 ± 0.051 ± 0.010
2	0.047	0.595	1.452	0.139 ± 0.044 ± 0.010	0.146 ± 0.055 ± 0.011
3	0.065	0.528	1.761	0.054 ± 0.046 ± 0.004	0.050 ± 0.058 ± 0.004
4	0.086	0.484	2.163	0.176 ± 0.052 ± 0.013	0.196 ± 0.068 ± 0.014
5	0.118	0.449	2.730	0.207 ± 0.057 ± 0.015	0.159 ± 0.076 ± 0.012
6	0.166	0.435	3.725	0.298 ± 0.071 ± 0.022	0.218 ± 0.098 ± 0.016
7	0.237	0.421	5.160	0.373 ± 0.100 ± 0.027	0.327 ± 0.144 ± 0.024
8	0.338	0.419	7.319	0.589 ± 0.209 ± 0.043	0.332 ± 0.319 ± 0.025
9	0.442	0.416	9.544	0.400 ± 0.422 ± 0.032	1.031 ± 0.635 ± 0.075

Table D.5: The 1997 proton asymmetries $A_1^{(h/\pi)} = A_{\|}^{(h/\pi)}/\,[D\,(1+\eta\gamma)]$, including all corrections. For the semi inclusive case the mean values of the kinematical quantities x, y, and Q^2 are given for the hadron asymmetries $A_1^{h^\pm}$.

Bin	$\langle x\rangle$	$\langle y\rangle$	$\langle Q^2\rangle$ (GeV^2)	$A_1 \pm$ stat. $\pm$ sys.
1	0.033	0.715	1.211	$0.076 \pm 0.008 \pm 0.004$
2	0.047	0.599	1.465	$0.099 \pm 0.009 \pm 0.006$
3	0.065	0.513	1.710	$0.112 \pm 0.010 \pm 0.007$
4	0.087	0.443	1.984	$0.162 \pm 0.012 \pm 0.010$
5	0.119	0.375	2.293	$0.191 \pm 0.012 \pm 0.012$
6	0.168	0.307	2.649	$0.253 \pm 0.014 \pm 0.016$
7	0.245	0.242	3.039	$0.306 \pm 0.018 \pm 0.021$
8	0.342	0.210	3.714	$0.456 \pm 0.030 \pm 0.032$
9	0.466	0.213	5.135	$0.570 \pm 0.041 \pm 0.046$

Bin	$\langle x\rangle$	$\langle y\rangle$	$\langle Q^2\rangle$ (GeV^2)	$A_1^{h^+} \pm$ stat. $\pm$ sys.	$A_1^{\pi^+} \pm$ stat. $\pm$ sys.
1	0.034	0.702	1.207	$0.071 \pm 0.020 \pm 0.004$	$0.031 \pm 0.025 \pm 0.002$
2	0.047	0.592	1.452	$0.121 \pm 0.021 \pm 0.007$	$0.091 \pm 0.028 \pm 0.005$
3	0.065	0.522	1.739	$0.131 \pm 0.022 \pm 0.008$	$0.111 \pm 0.030 \pm 0.007$
4	0.087	0.476	2.129	$0.180 \pm 0.025 \pm 0.010$	$0.168 \pm 0.035 \pm 0.010$
5	0.118	0.440	2.682	$0.264 \pm 0.026 \pm 0.015$	$0.252 \pm 0.038 \pm 0.014$
6	0.166	0.425	3.636	$0.259 \pm 0.032 \pm 0.015$	$0.329 \pm 0.047 \pm 0.019$
7	0.238	0.414	5.096	$0.390 \pm 0.044 \pm 0.023$	$0.343 \pm 0.069 \pm 0.020$
8	0.338	0.407	7.109	$0.477 \pm 0.089 \pm 0.028$	$0.481 \pm 0.152 \pm 0.028$
9	0.447	0.419	9.702	$0.431 \pm 0.174 \pm 0.028$	$0.645 \pm 0.307 \pm 0.038$

Bin	$\langle x\rangle$	$\langle y\rangle$	$\langle Q^2\rangle$ (GeV^2)	$A_1^{h^-} \pm$ stat. $\pm$ sys.	$A_1^{\pi^-} \pm$ stat. $\pm$ sys.
1	0.033	0.706	1.207	$0.041 \pm 0.026 \pm 0.002$	$0.071 \pm 0.030 \pm 0.004$
2	0.047	0.595	1.456	$0.081 \pm 0.027 \pm 0.005$	$0.081 \pm 0.034 \pm 0.005$
3	0.064	0.530	1.763	$0.069 \pm 0.028 \pm 0.004$	$0.042 \pm 0.036 \pm 0.003$
4	0.087	0.482	2.157	$0.021 \pm 0.032 \pm 0.002$	$0.049 \pm 0.042 \pm 0.003$
5	0.118	0.447	2.713	$0.149 \pm 0.036 \pm 0.009$	$0.070 \pm 0.047 \pm 0.005$
6	0.166	0.431	3.685	$0.223 \pm 0.044 \pm 0.013$	$0.180 \pm 0.060 \pm 0.011$
7	0.238	0.418	5.137	$0.188 \pm 0.064 \pm 0.012$	$0.143 \pm 0.092 \pm 0.009$
8	0.337	0.414	7.234	$0.705 \pm 0.129 \pm 0.040$	$0.525 \pm 0.203 \pm 0.030$
9	0.443	0.415	9.547	$-0.056 \pm 0.271 \pm 0.014$	$-0.602 \pm 0.465 \pm 0.036$

Table D.6: The combined proton asymmetries $A_1^{(h/\pi)} = A_{\|}^{(h/\pi)} / [D\,(1+\eta\gamma)]$ from the 1996 and 1997 data taking periods, including all corrections. For the semi inclusive case the mean values of the kinematical quantities x, y, and Q^2 are given for the hadron asymmetries $A_1^{h^\pm}$.

Bin	$\langle x \rangle$	$\langle y \rangle$	$\langle Q^2 \rangle$ (GeV^2)	A_1 ± stat. ± sys.
1	0.033	0.715	1.211	0.084 ± 0.007 ± 0.005
2	0.047	0.599	1.465	0.099 ± 0.008 ± 0.006
3	0.065	0.513	1.711	0.108 ± 0.009 ± 0.007
4	0.087	0.443	1.986	0.170 ± 0.010 ± 0.011
5	0.119	0.375	2.295	0.195 ± 0.011 ± 0.013
6	0.168	0.307	2.650	0.246 ± 0.012 ± 0.016
7	0.245	0.243	3.045	0.313 ± 0.015 ± 0.023
8	0.342	0.211	3.725	0.433 ± 0.026 ± 0.033
9	0.465	0.214	5.158	0.547 ± 0.035 ± 0.046

Bin	$\langle x \rangle$	$\langle y \rangle$	$\langle Q^2 \rangle$ (GeV^2)	$A_1^{h^+}$ ± stat. ± sys.	$A_1^{\pi^+}$ ± stat. ± sys.
1	0.034	0.702	1.206	0.080 ± 0.017 ± 0.005	0.055 ± 0.022 ± 0.004
2	0.047	0.592	1.451	0.120 ± 0.018 ± 0.007	0.095 ± 0.024 ± 0.006
3	0.065	0.522	1.740	0.126 ± 0.019 ± 0.008	0.113 ± 0.026 ± 0.007
4	0.087	0.476	2.131	0.175 ± 0.021 ± 0.011	0.182 ± 0.029 ± 0.012
5	0.118	0.442	2.688	0.254 ± 0.022 ± 0.016	0.248 ± 0.032 ± 0.015
6	0.166	0.424	3.632	0.263 ± 0.027 ± 0.016	0.336 ± 0.041 ± 0.021
7	0.238	0.414	5.105	0.415 ± 0.037 ± 0.026	0.356 ± 0.059 ± 0.022
8	0.338	0.408	7.125	0.481 ± 0.075 ± 0.030	0.557 ± 0.128 ± 0.035
9	0.447	0.420	9.730	0.481 ± 0.147 ± 0.033	0.738 ± 0.269 ± 0.047

Bin	$\langle x \rangle$	$\langle y \rangle$	$\langle Q^2 \rangle$ (GeV^2)	$A_1^{h^-}$ ± stat. ± sys.	$A_1^{\pi^-}$ ± stat. ± sys.
1	0.033	0.705	1.206	0.068 ± 0.022 ± 0.005	0.088 ± 0.026 ± 0.006
2	0.047	0.595	1.455	0.097 ± 0.023 ± 0.006	0.098 ± 0.029 ± 0.007
3	0.064	0.529	1.762	0.065 ± 0.024 ± 0.004	0.044 ± 0.030 ± 0.003
4	0.087	0.482	2.159	0.064 ± 0.028 ± 0.005	0.089 ± 0.035 ± 0.006
5	0.118	0.447	2.718	0.166 ± 0.030 ± 0.011	0.094 ± 0.040 ± 0.007
6	0.166	0.432	3.696	0.244 ± 0.038 ± 0.016	0.190 ± 0.051 ± 0.012
7	0.237	0.419	5.144	0.242 ± 0.054 ± 0.016	0.197 ± 0.078 ± 0.014
8	0.338	0.416	7.258	0.673 ± 0.110 ± 0.041	0.469 ± 0.171 ± 0.029
9	0.443	0.415	9.546	0.077 ± 0.228 ± 0.020	−0.033 ± 0.375 ± 0.050

Table D.7: The 1995 ^{3}He asymmetries $A_1^{(h/\pi)} = A_\parallel^{(h/\pi)} / [D\,(1+\eta\gamma)]$, including all corrections. These data are taken from [Tip 99].

Bin	$\langle x \rangle$	$\langle y \rangle$	$\langle Q^2 \rangle$ (GeV^2)	A_1 ± stat. ± sys.
1	0.033	0.710	1.211	$-0.036 \pm 0.012 \pm 0.004$
2	0.047	0.600	1.459	$-0.012 \pm 0.014 \pm 0.003$
3	0.065	0.505	1.697	$-0.029 \pm 0.015 \pm 0.004$
4	0.087	0.432	1.945	$-0.031 \pm 0.017 \pm 0.004$
5	0.119	0.361	2.220	$-0.040 \pm 0.019 \pm 0.004$
6	0.168	0.291	2.524	$-0.038 \pm 0.022 \pm 0.004$
7	0.245	0.225	2.844	$-0.011 \pm 0.028 \pm 0.003$
8	0.342	0.199	3.526	$0.067 \pm 0.046 \pm 0.006$
9	0.465	0.206	4.964	$-0.032 \pm 0.063 \pm 0.007$

Bin	$\langle x \rangle$	$\langle y \rangle$	$\langle Q^2 \rangle$ (GeV^2)	$A_1^{h^+}$ ± stat. ± sys.	$A_1^{\pi^+}$ ± stat. ± sys.
1	0.033	0.710	1.211	$-0.046 \pm 0.033 \pm 0.007$	$0.121 \pm 0.101 \pm 0.011$
2	0.047	0.600	1.459	$-0.002 \pm 0.034 \pm 0.006$	$-0.058 \pm 0.109 \pm 0.007$
3	0.065	0.505	1.697	$-0.034 \pm 0.035 \pm 0.006$	$0.071 \pm 0.117 \pm 0.008$
4	0.087	0.432	1.945	$-0.048 \pm 0.039 \pm 0.007$	$-0.253 \pm 0.134 \pm 0.020$
5	0.119	0.361	2.220	$-0.017 \pm 0.041 \pm 0.006$	$-0.077 \pm 0.147 \pm 0.008$
6	0.168	0.291	2.524	$0.017 \pm 0.049 \pm 0.006$	$-0.213 \pm 0.184 \pm 0.017$
7	0.245	0.225	2.844	$-0.135 \pm 0.065 \pm 0.011$	$0.418 \pm 0.267 \pm 0.030$
8	0.342	0.199	3.526	$-0.116 \pm 0.131 \pm 0.010$	$-0.595 \pm 0.750 \pm 0.042$
9	0.465	0.206	4.964	$-0.178 \pm 0.243 \pm 0.015$	$1.407 \pm 2.089 \pm 0.100$

Bin	$\langle x \rangle$	$\langle y \rangle$	$\langle Q^2 \rangle$ (GeV^2)	$A_1^{h^-}$ ± stat. ± sys.	$A_1^{\pi^-}$ ± stat. ± sys.
1	0.033	0.710	1.211	$-0.079 \pm 0.038 \pm 0.008$	$-0.268 \pm 0.114 \pm 0.021$
2	0.047	0.600	1.459	$0.032 \pm 0.040 \pm 0.006$	$0.133 \pm 0.125 \pm 0.012$
3	0.065	0.505	1.697	$-0.013 \pm 0.042 \pm 0.006$	$0.241 \pm 0.140 \pm 0.019$
4	0.087	0.432	1.945	$0.025 \pm 0.049 \pm 0.006$	$-0.125 \pm 0.168 \pm 0.011$
5	0.119	0.361	2.220	$0.051 \pm 0.053 \pm 0.007$	$-0.195 \pm 0.183 \pm 0.015$
6	0.168	0.291	2.524	$-0.023 \pm 0.065 \pm 0.006$	$0.604 \pm 0.241 \pm 0.044$
7	0.245	0.225	2.844	$0.048 \pm 0.090 \pm 0.006$	$0.450 \pm 0.385 \pm 0.032$
8	0.342	0.199	3.526	$-0.169 \pm 0.187 \pm 0.013$	$0.409 \pm 1.242 \pm 0.029$
9	0.465	0.206	4.964	$0.866 \pm 0.379 \pm 0.062$	$0.000 \pm 0.000 \pm 0.000$

Table D.8: Systematic error contributions for the 1996 proton inclusive and semi inclusive hadron asymmetries. For each x–bin the individual contributions and the total systematic error, which is the quadratic sum of the individual terms, are given.

Inclusive asymmetry A_1							
Bin	**Total**	P_{Beam}	P_{Target}	$R(x,Q^2)$	$g_2(x,Q^2)$	Smear. Corr.	Rad. Corr.
1	0.0077	0.0036	0.0066	0.0012	0.0004	0.0010	0.0001
2	0.0072	0.0033	0.0062	0.0013	0.0008	0.0009	0.0000
3	0.0073	0.0033	0.0061	0.0013	0.0014	0.0009	0.0000
4	0.0143	0.0066	0.0121	0.0023	0.0023	0.0019	0.0000
5	0.0154	0.0070	0.0129	0.0021	0.0037	0.0019	0.0000
6	0.0178	0.0078	0.0144	0.0019	0.0065	0.0019	0.0000
7	0.0266	0.0113	0.0209	0.0021	0.0117	0.0025	0.0001
8	0.0331	0.0125	0.0232	0.0021	0.0196	0.0030	0.0001
9	0.0472	0.0164	0.0304	0.0032	0.0319	0.0027	0.0001

Semi inclusive asymmetry $A_1^{h^+}$						
Bin	**Total**	P_{Beam}	P_{Target}	$R(x,Q^2)$	$g_2(x,Q^2)$	Smear. Corr.
1	0.0079	0.0037	0.0068	0.0013	0.0004	0.0008
2	0.0087	0.0040	0.0074	0.0016	0.0009	0.0009
3	0.0083	0.0038	0.0071	0.0014	0.0014	0.0008
4	0.0119	0.0055	0.0101	0.0018	0.0020	0.0010
5	0.0168	0.0078	0.0144	0.0022	0.0029	0.0012
6	0.0203	0.0094	0.0173	0.0021	0.0040	0.0012
7	0.0349	0.0163	0.0302	0.0026	0.0057	0.0015
8	0.0363	0.0167	0.0309	0.0022	0.0087	0.0015
9	0.0458	0.0206	0.0382	0.0025	0.0143	0.0024

Semi inclusive asymmetry $A_1^{h^-}$						
Bin	**Total**	P_{Beam}	P_{Target}	$R(x,Q^2)$	$g_2(x,Q^2)$	Smear. Corr.
1	0.0107	0.0048	0.0089	0.0018	0.0004	0.0027
2	0.0104	0.0047	0.0087	0.0019	0.0009	0.0024
3	0.0043	0.0018	0.0034	0.0007	0.0014	0.0009
4	0.0131	0.0060	0.0111	0.0020	0.0020	0.0021
5	0.0153	0.0071	0.0131	0.0020	0.0028	0.0016
6	0.0218	0.0101	0.0188	0.0022	0.0038	0.0016
7	0.0273	0.0127	0.0235	0.0021	0.0055	0.0015
8	0.0432	0.0200	0.0371	0.0025	0.0085	0.0024
9	0.0320	0.0136	0.0252	0.0017	0.0140	0.0016

Table D.9: Systematic error contributions for the 1997 proton inclusive and semi inclusive hadron asymmetries. For each x–bin the individual contributions and the total systematic error, which is the quadratic sum of the individual terms, are given.

Inclusive asymmetry A_1							
Bin	**Total**	P_{Beam}	P_{Target}	$R(x,Q^2)$	$g_2(x,Q^2)$	Smear. Corr.	Rad. Corr.
1	0.0044	0.0026	0.0034	0.0009	0.0004	0.0008	0.0001
2	0.0058	0.0034	0.0044	0.0013	0.0008	0.0010	0.0000
3	0.0066	0.0038	0.0049	0.0015	0.0014	0.0010	0.0000
4	0.0096	0.0055	0.0071	0.0019	0.0023	0.0016	0.0000
5	0.0116	0.0065	0.0084	0.0020	0.0038	0.0017	0.0000
6	0.0158	0.0086	0.0111	0.0022	0.0065	0.0021	0.0000
7	0.0210	0.0104	0.0135	0.0020	0.0119	0.0023	0.0001
8	0.0325	0.0155	0.0201	0.0026	0.0199	0.0038	0.0001
9	0.0457	0.0194	0.0251	0.0038	0.0325	0.0032	0.0001

Semi inclusive asymmetry $A_1^{h^+}$						
Bin	**Total**	P_{Beam}	P_{Target}	$R(x,Q^2)$	$g_2(x,Q^2)$	Smear. Corr.
1	0.0041	0.0024	0.0031	0.0009	0.0004	0.0005
2	0.0070	0.0041	0.0053	0.0016	0.0009	0.0009
3	0.0076	0.0044	0.0057	0.0017	0.0014	0.0010
4	0.0105	0.0061	0.0079	0.0021	0.0020	0.0012
5	0.0152	0.0090	0.0116	0.0026	0.0029	0.0011
6	0.0151	0.0088	0.0114	0.0020	0.0039	0.0011
7	0.0226	0.0133	0.0172	0.0022	0.0057	0.0012
8	0.0280	0.0162	0.0210	0.0021	0.0088	0.0014
9	0.0279	0.0147	0.0190	0.0018	0.0142	0.0013

Semi inclusive asymmetry $A_1^{h^-}$						
Bin	**Total**	P_{Beam}	P_{Target}	$R(x,Q^2)$	$g_2(x,Q^2)$	Smear. Corr.
1	0.0025	0.0014	0.0018	0.0005	0.0004	0.0008
2	0.0049	0.0028	0.0036	0.0011	0.0009	0.0014
3	0.0043	0.0023	0.0030	0.0009	0.0014	0.0011
4	0.0023	0.0007	0.0009	0.0002	0.0020	0.0003
5	0.0090	0.0051	0.0066	0.0014	0.0028	0.0011
6	0.0132	0.0076	0.0098	0.0017	0.0039	0.0012
7	0.0119	0.0064	0.0083	0.0010	0.0056	0.0008
8	0.0403	0.0240	0.0310	0.0031	0.0086	0.0021
9	0.0144	0.0019	0.0025	0.0002	0.0141	0.0002

Table D.10: Correlation coefficients for the asymmetries A_1 on a proton target in the HERMES kinematics. These numbers are extracted from measured particle multiplicities and averaged over both spin states.

$\langle x \rangle$	Cor (A^{e^+}, A^{h^+})	Cor (A^{e^+}, A^{h^-})	Cor (A^{e^+}, A^{π^+})	Cor (A^{e^+}, A^{π^-})	Cor (A^{h^+}, A^{h^-})	Cor (A^{π^+}, A^{π^-})
0.033	0.367	0.307	0.292	0.261	0.145	0.110
0.047	0.410	0.332	0.302	0.262	0.144	0.084
0.065	0.420	0.329	0.289	0.244	0.138	0.072
0.087	0.408	0.311	0.263	0.217	0.122	0.063
0.119	0.377	0.276	0.228	0.181	0.109	0.057
0.168	0.313	0.226	0.182	0.144	0.096	0.054
0.245	0.232	0.159	0.130	0.097	0.077	0.036
0.342	0.168	0.113	0.088	0.067	0.064	0.029
0.466	0.114	0.076	0.060	0.041	0.039	0.009

Table D.11: Correlation coefficients for the asymmetries A_1 on a ^{3}He target in the HERMES kinematics. These numbers are taken from [Fun 98].

$\langle x \rangle$	Cor (A^{e^+}, A^{h^+})	Cor (A^{e^+}, A^{h^-})	Cor (A^{e^+}, A^{π^+})	Cor (A^{e^+}, A^{π^-})	Cor (A^{h^+}, A^{h^-})	Cor (A^{π^+}, A^{π^-})
0.033	0.367	0.319	0.207	0.187	0.125	0.025
0.047	0.404	0.339	0.205	0.180	0.131	0.017
0.065	0.407	0.332	0.189	0.161	0.124	0.014
0.087	0.391	0.311	0.167	0.139	0.113	0.014
0.119	0.372	0.287	0.148	0.119	0.099	0.011
0.168	0.359	0.269	0.135	0.104	0.088	0.006
0.245	0.342	0.246	0.120	0.089	0.072	0.006
0.342	0.324	0.224	0.108	0.076	0.047	0.004
0.466	0.325	0.213	0.109	0.079	0.035	0.000

E Tables of Results: Polarised Quark Distributions

Table E.1: Extracted quark polarisations in the flavour decomposition using a model of an $SU(3)_f$ polarisation symmetric sea.

$\langle x \rangle$	$\langle Q^2 \rangle$	$\frac{\Delta u + \Delta \bar{u}}{u + \bar{u}}$ ± stat. ± sys.	$\frac{\Delta d + \Delta \bar{d}}{d + \bar{d}}$ ± stat. ± sys.	$\Delta q_s / q_s$ ± stat. ± sys.
0.033	1.211	0.100 ± 0.012 ± 0.007	−0.140 ± 0.046 ± 0.026	0.147 ± 0.095 ± 0.022
0.047	1.463	0.108 ± 0.014 ± 0.007	−0.084 ± 0.055 ± 0.018	0.071 ± 0.106 ± 0.039
0.065	1.707	0.134 ± 0.015 ± 0.009	−0.141 ± 0.061 ± 0.018	0.007 ± 0.123 ± 0.060
0.087	1.973	0.197 ± 0.016 ± 0.014	−0.181 ± 0.073 ± 0.019	−0.066 ± 0.165 ± 0.132
0.119	2.271	0.228 ± 0.018 ± 0.013	−0.259 ± 0.090 ± 0.028	0.165 ± 0.242 ± 0.143
0.168	2.608	0.267 ± 0.021 ± 0.018	−0.262 ± 0.120 ± 0.045	0.609 ± 0.444 ± 0.122
0.245	2.981	0.351 ± 0.028 ± 0.022	−0.310 ± 0.191 ± 0.058	0.027 ± 1.163 ± 0.499
0.342	3.665	0.408 ± 0.046 ± 0.027	0.452 ± 0.386 ± 0.095	—
0.465	5.106	0.649 ± 0.065 ± 0.038	−0.965 ± 0.767 ± 0.124	—

Table E.2: The correlations among the extracted quark polarisations in the flavour decomposition. The last column shows the minimum value of χ^2 from the fit in each bin according to Eqn. (6.10).

Bin	$\langle x \rangle$	Cor $\left(\frac{\Delta u + \Delta \bar{u}}{u + \bar{u}}, \frac{\Delta d + \Delta \bar{d}}{d + \bar{d}}\right)$	Cor $\left(\frac{\Delta u + \Delta \bar{u}}{u + \bar{u}}, \frac{\Delta q_s}{q_s}\right)$	Cor $\left(\frac{\Delta d + \Delta \bar{d}}{d + \bar{d}}, \frac{\Delta q_s}{q_s}\right)$	$\chi^2_{\mathrm{min}}/\mathrm{ndf}$
1	0.033	−0.687	−0.093	−0.383	1.50
2	0.047	−0.680	−0.047	−0.400	0.54
3	0.065	−0.679	−0.036	−0.412	0.15
4	0.087	−0.638	−0.043	−0.427	2.43
5	0.119	−0.637	−0.007	−0.468	1.44
6	0.168	−0.595	−0.051	−0.459	0.92
7	0.245	−0.518	−0.226	−0.440	2.08
8	0.342	−0.706	—	—	1.63
9	0.465	−0.735	—	—	1.60

Table E.3: Systematic uncertainties on the quark polarisations $(\Delta u + \Delta\overline{u})/(u+\overline{u})$, $(\Delta d + \Delta\overline{d})/(d+\overline{d})$, and $\Delta q_{\rm s}/q_{\rm s}$. For each x–bin the individual contributions and the total systematic uncertainty are given. The total uncertainty is the quadratic sum of the individual contributions.

Bin	**Total**	$P_{\rm Beam}$	$P_{\rm Target}$	Yield Fluc.	$R(x,Q^2)$	$g_2(x,Q^2)$	Smear. Corr.	Rad. Corr.	Frag. Model	Unpol. PDF	$\Delta q_{\rm s} \overset{x\geq 0.3}{=} 0$
Systematic uncertainties on $(\Delta u + \Delta\overline{u})/(u+\overline{u})$											
1	0.0075	0.0035	0.0037	0.0022	0.0033	0.0005	0.0027	0.0005	0.0025	0.0007	0.0000
2	0.0074	0.0036	0.0043	0.0022	0.0014	0.0005	0.0026	0.0005	0.0025	0.0017	0.0000
3	0.0091	0.0045	0.0052	0.0020	0.0006	0.0007	0.0028	0.0005	0.0036	0.0030	0.0000
4	0.0137	0.0067	0.0083	0.0020	0.0002	0.0012	0.0035	0.0005	0.0064	0.0038	0.0000
5	0.0134	0.0077	0.0093	0.0022	0.0005	0.0014	0.0034	0.0005	0.0034	0.0018	0.0000
6	0.0178	0.0090	0.0111	0.0022	0.0008	0.0015	0.0030	0.0005	0.0079	0.0057	0.0000
7	0.0215	0.0119	0.0159	0.0022	0.0010	0.0019	0.0029	0.0005	0.0069	0.0018	0.0000
8	0.0270	0.0139	0.0208	0.0022	0.0013	0.0028	0.0028	0.0004	0.0081	0.0010	0.0034
9	0.0382	0.0220	0.0287	0.0022	0.0015	0.0029	0.0050	0.0003	0.0083	0.0057	0.0029
Systematic uncertainties on $(\Delta d + \Delta\overline{d})/(d+\overline{d})$											
1	0.0262	0.0067	0.0061	0.0118	0.0163	0.0001	0.0038	0.0086	0.0050	0.0093	0.0000
2	0.0177	0.0038	0.0034	0.0113	0.0076	0.0001	0.0020	0.0080	0.0002	0.0058	0.0000
3	0.0176	0.0067	0.0062	0.0114	0.0036	0.0002	0.0030	0.0075	0.0011	0.0042	0.0000
4	0.0190	0.0086	0.0078	0.0120	0.0012	0.0002	0.0033	0.0073	0.0039	0.0005	0.0000
5	0.0276	0.0122	0.0110	0.0138	0.0036	0.0003	0.0038	0.0073	0.0072	0.0130	0.0000
6	0.0454	0.0114	0.0100	0.0165	0.0063	0.0003	0.0029	0.0076	0.0269	0.0270	0.0000
7	0.0578	0.0123	0.0107	0.0204	0.0101	0.0003	0.0025	0.0083	0.0398	0.0299	0.0000
8	0.0954	0.0230	0.0219	0.0239	0.0144	0.0006	0.0031	0.0089	0.0772	0.0001	0.0356
9	0.1243	0.0346	0.0333	0.0316	0.0226	0.0029	0.0074	0.0108	0.1048	0.0003	0.0215
Systematic uncertainties on $\Delta q_{\rm s}/q_{\rm s}$											
1	0.0215	0.0054	0.0052	0.0065	0.0083	0.0012	0.0040	0.0017	0.0160	0.0043	—
2	0.0390	0.0031	0.0031	0.0067	0.0044	0.0020	0.0017	0.0020	0.0377	0.0023	—
3	0.0605	0.0036	0.0058	0.0069	0.0024	0.0015	0.0001	0.0024	0.0593	0.0059	—
4	0.1322	0.0076	0.0140	0.0085	0.0010	0.0036	0.0012	0.0031	0.1237	0.0426	—
5	0.1429	0.0133	0.0165	0.0126	0.0039	0.0025	0.0024	0.0047	0.1404	0.0077	—
6	0.1223	0.0218	0.0231	0.0178	0.0090	0.0037	0.0069	0.0068	0.1039	0.0514	—
7	0.4986	0.0366	0.0595	0.0265	0.0214	0.0095	0.0002	0.0114	0.4425	0.2157	—

Table E.4: Extracted quark polarisations in the valence decomposition using a model of an $SU(3)_f$ polarisation symmetric sea.

$\langle x \rangle$	$\langle Q^2 \rangle$	$\Delta u_\mathrm{v}/u_\mathrm{v}$ ± stat. ± sys.	$\Delta d_\mathrm{v}/d_\mathrm{v}$ ± stat. ± sys.	$\Delta q_\mathrm{s}/q_\mathrm{s}$ ± stat. ± sys.
0.033	1.211	$0.043 \pm 0.124 \pm 0.026$	$-0.760 \pm 0.291 \pm 0.172$	$0.147 \pm 0.095 \pm 0.022$
0.047	1.463	$0.140 \pm 0.099 \pm 0.039$	$-0.349 \pm 0.276 \pm 0.109$	$0.071 \pm 0.106 \pm 0.039$
0.065	1.707	$0.215 \pm 0.083 \pm 0.046$	$-0.344 \pm 0.263 \pm 0.117$	$0.007 \pm 0.123 \pm 0.060$
0.087	1.973	$0.316 \pm 0.078 \pm 0.068$	$-0.308 \pm 0.285 \pm 0.187$	$-0.066 \pm 0.165 \pm 0.132$
0.119	2.271	$0.246 \pm 0.075 \pm 0.049$	$-0.628 \pm 0.325 \pm 0.165$	$0.165 \pm 0.242 \pm 0.143$
0.168	2.608	$0.211 \pm 0.080 \pm 0.030$	$-0.822 \pm 0.415 \pm 0.116$	$0.609 \pm 0.444 \pm 0.122$
0.245	2.981	$0.375 \pm 0.099 \pm 0.048$	$-0.454 \pm 0.663 \pm 0.286$	$0.027 \pm 1.163 \pm 0.499$
0.342	3.665	$0.420 \pm 0.048 \pm 0.041$	$0.569 \pm 0.486 \pm 0.310$	—
0.465	5.106	$0.656 \pm 0.066 \pm 0.041$	$-1.097 \pm 0.872 \pm 0.212$	—

Table E.5: The correlations among the extracted quark polarisations in the valence decomposition. The last column shows the minimum value of χ^2 from the fit in each bin according to Eqn. (6.10).

Bin	$\langle x \rangle$	Cor $\left(\frac{\Delta u_\mathrm{v}}{u_\mathrm{v}}, \frac{\Delta d_\mathrm{v}}{d_\mathrm{v}}\right)$	Cor $\left(\frac{\Delta u_\mathrm{v}}{u_\mathrm{v}}, \frac{\Delta q_\mathrm{s}}{q_\mathrm{s}}\right)$	Cor $\left(\frac{\Delta d_\mathrm{v}}{d_\mathrm{v}}, \frac{\Delta q_\mathrm{s}}{q_\mathrm{s}}\right)$	$\chi^2_\mathrm{min}/\mathrm{ndf}$
1	0.033	0.748	−0.968	−0.872	1.50
2	0.047	0.718	−0.958	−0.865	0.54
3	0.065	0.690	−0.947	−0.861	0.15
4	0.087	0.683	−0.934	−0.869	2.43
5	0.119	0.698	−0.928	−0.886	1.44
6	0.168	0.728	−0.928	−0.904	0.92
7	0.245	0.775	−0.935	−0.928	2.08
8	0.342	−0.706	—	—	1.63
9	0.465	−0.735	—	—	1.60

Table E.6: Systematic uncertainties on the quark polarisations $\Delta u_{\mathrm{v}}/u_{\mathrm{v}}$, $\Delta d_{\mathrm{v}}/d_{\mathrm{v}}$, and $\Delta q_{\mathrm{s}}/q_{\mathrm{s}}$. For each x–bin the individual contributions and the total systematic uncertainty are given. The total uncertainty is the quadratic sum of the individual contributions.

Bin	**Total**	P_{Beam}	P_{Target}	Yield Fluc.	$R(x,Q^2)$	$g_2(x,Q^2)$	Smear. Corr.	Rad. Corr.	Frag. Model	Unpol. PDF	$\Delta q_{\mathrm{s}} \overset{x\geq 0.3}{=} 0$
Systematic uncertainties on $\Delta u_{\mathrm{v}}/u_{\mathrm{v}}$											
1	0.0261	0.0016	0.0025	0.0031	0.0029	0.0010	0.0012	0.0032	0.0252	0.0021	0.0000
2	0.0394	0.0049	0.0074	0.0019	0.0012	0.0012	0.0034	0.0027	0.0379	0.0039	0.0000
3	0.0461	0.0073	0.0108	0.0011	0.0005	0.0002	0.0045	0.0023	0.0435	0.0061	0.0000
4	0.0680	0.0110	0.0160	0.0009	0.0002	0.0029	0.0057	0.0021	0.0647	0.0031	0.0000
5	0.0493	0.0086	0.0135	0.0009	0.0005	0.0012	0.0036	0.0020	0.0455	0.0091	0.0000
6	0.0297	0.0072	0.0097	0.0004	0.0006	0.0012	0.0024	0.0017	0.0262	0.0064	0.0000
7	0.0478	0.0130	0.0196	0.0003	0.0006	0.0028	0.0031	0.0014	0.0342	0.0233	0.0000
8	0.0415	0.0144	0.0213	0.0022	0.0014	0.0029	0.0029	0.0004	0.0084	0.0008	0.0311
9	0.0413	0.0222	0.0291	0.0022	0.0015	0.0029	0.0050	0.0003	0.0084	0.0078	0.0140
Systematic uncertainties on $\Delta d_{\mathrm{v}}/d_{\mathrm{v}}$											
1	0.1721	0.0319	0.0276	0.0511	0.0703	0.0028	0.0208	0.0310	0.0192	0.1361	0.0000
2	0.1090	0.0157	0.0142	0.0423	0.0280	0.0037	0.0084	0.0250	0.0641	0.0636	0.0000
3	0.1170	0.0200	0.0208	0.0364	0.0118	0.0024	0.0072	0.0211	0.0793	0.0678	0.0000
4	0.1871	0.0230	0.0275	0.0348	0.0036	0.0040	0.0055	0.0190	0.1454	0.1047	0.0000
5	0.1649	0.0338	0.0335	0.0373	0.0101	0.0028	0.0092	0.0178	0.1356	0.0681	0.0000
6	0.1164	0.0323	0.0289	0.0386	0.0161	0.0029	0.0093	0.0168	0.0927	0.0307	0.0000
7	0.2858	0.0289	0.0327	0.0404	0.0235	0.0037	0.0037	0.0167	0.2456	0.1302	0.0000
8	0.3097	0.0290	0.0276	0.0301	0.0181	0.0007	0.0039	0.0112	0.0971	0.0026	0.2890
9	0.2124	0.0394	0.0379	0.0360	0.0257	0.0033	0.0084	0.0122	0.1191	0.0102	0.1601
Systematic uncertainties on $\Delta q_{\mathrm{s}}/q_{\mathrm{s}}$											
1	0.0215	0.0054	0.0052	0.0065	0.0083	0.0012	0.0040	0.0017	0.0160	0.0043	—
2	0.0390	0.0031	0.0031	0.0067	0.0044	0.0020	0.0017	0.0020	0.0377	0.0023	—
3	0.0605	0.0036	0.0058	0.0069	0.0024	0.0015	0.0001	0.0024	0.0593	0.0059	—
4	0.1322	0.0076	0.0140	0.0085	0.0010	0.0036	0.0012	0.0031	0.1237	0.0426	—
5	0.1429	0.0133	0.0165	0.0126	0.0039	0.0025	0.0024	0.0047	0.1404	0.0077	—
6	0.1223	0.0218	0.0231	0.0178	0.0090	0.0037	0.0069	0.0068	0.1039	0.0514	—
7	0.4986	0.0366	0.0595	0.0265	0.0214	0.0095	0.0002	0.0114	0.4425	0.2157	—

Table E.7: The first and second moments of various combinations of polarised quark distributions. All integrals are given at a scale $Q^2 = 2.5\,\mathrm{GeV}^2$. Note that the values for $\Delta s + \Delta\overline{s}$ do not represent a direct measurement of the properties of the strange sea, as explained in the text. For the integrals in the measured range and for the total integrals the statistical (systematic) uncertainties are given by the first (second) term behind the value.

	Measured x–range	Low x–range	High x–range	**Total integral**
$\Delta u + \Delta\overline{u}$	$0.519 \pm 0.018 \pm 0.031$	0.038	0.018	$0.575 \pm 0.018 \pm 0.052$
$\Delta d + \Delta\overline{d}$	$-0.265 \pm 0.059 \pm 0.036$	−0.035	−0.002	$-0.301 \pm 0.059 \pm 0.050$
$\Delta s + \Delta\overline{s}$	$0.049 \pm 0.036 \pm 0.027$	0.005	0.000	$0.054 \pm 0.036 \pm 0.027$
Δu_{v}	$0.453 \pm 0.047 \pm 0.029$	0.028	0.018	$0.499 \pm 0.047 \pm 0.044$
Δd_{v}	$-0.356 \pm 0.107 \pm 0.048$	−0.046	−0.001	$-0.403 \pm 0.107 \pm 0.067$
$\Delta\overline{u}$	$0.037 \pm 0.025 \pm 0.006$	0.005	0.000	$0.042 \pm 0.025 \pm 0.007$
$\Delta\overline{d}$	$0.052 \pm 0.042 \pm 0.009$	0.006	0.000	$0.058 \pm 0.042 \pm 0.010$
$\Delta\Sigma$	$0.303 \pm 0.059 \pm 0.042$	0.008	0.016	$0.328 \pm 0.059 \pm 0.046$
Δq_3	$0.784 \pm 0.067 \pm 0.055$	0.073	0.020	$0.876 \pm 0.067 \pm 0.094$
Δq_8	$0.156 \pm 0.086 \pm 0.062$	−0.007	0.017	$0.166 \pm 0.086 \pm 0.065$
$\Delta^{(2)} u_{\mathrm{v}}$	$0.113 \pm 0.009 \pm 0.007$	0.000	0.012	$0.125 \pm 0.009 \pm 0.014$
$\Delta^{(2)} d_{\mathrm{v}}$	$-0.048 \pm 0.025 \pm 0.007$	−0.001	−0.001	$-0.049 \pm 0.025 \pm 0.007$

Table E.8: The correlation matrix among the first moments of the quark distributions in the flavour decomposition.

	$\Delta u + \Delta\overline{u}$	$\Delta d + \Delta\overline{d}$	$\Delta s + \Delta\overline{s}$
$\Delta u + \Delta\overline{u}$	1	−0.68	−0.20
$\Delta d + \Delta\overline{d}$	−0.68	1	−0.35
$\Delta s + \Delta\overline{s}$	−0.20	−0.35	1

Table E.9: The correlation matrix among the second moments of the quark distributions in the flavour decomposition.

	$x\,(\Delta u + \Delta\overline{u})$	$x\,(\Delta d + \Delta\overline{d})$	$x\,(\Delta s + \Delta\overline{s})$
$x\,(\Delta u + \Delta\overline{u})$	1	−0.77	−0.10
$x\,(\Delta d + \Delta\overline{d})$	−0.77	1	−0.20
$x\,(\Delta s + \Delta\overline{s})$	−0.10	−0.20	1

Acknowledgements

Having been fascinated by reports on the huge, ingenious experiments in elementary particle physics since my days at high school, it was very challenging when I finally got the chance to take part in such an experiment. Working for almost five years in the international environment of the HERMES Collaboration has been a great pleasure for me and I am grateful for many invaluable experiences I could gather here. I have benefitted from the help of a large number of people, many more than I could mention here individually.

First of all, I would like to thank my advisor Prof. Kay Königsmann for the freedom to pursue my personal preferences and his generous support of my visits to national and international schools and trips to numerous other foreign destinations. Furthermore, I very much appreciated his understanding and patience during times when private issues significantly reduced my efficiency. In the same place I want to sincerely thank Prof. Klaus Rith for his continued interest and support after he had procured me from his group to Freiburg.

During the conceptual phase of the LPOL the expertise of Otto Häusser, Peter Schüler and Michael Spengos was invaluable to avoid many pitfalls which already had been experienced by our colleagues at the TPOL. Sadly, Otto was not granted any more to see the fruits of his advice himself.

The construction of the LPOL would have been impossible without the devoted contributions by Wilhelm Beckhusen, Dieter Bremer, Norbert Meyners, the MEA Hallendienst, and the very professional work of the Freiburg engineer Rainer Fastner with his crew Fränk Großmann, Bertram Rudmann, Armin Ruh, and Klaus Wilfert. Work in Hamburg would have been much harder without the organisational efforts of Horst Fischer. For their unweary labour in endless nights in the tunnel below the Hamburger Volkspark, I am indebted to Stephan Brauksiepe, Florian Burkart, Martin Kestel, Wolfgang Lorenzon, and Andreas Most.

In the analysis part I benefitted a lot from the very inspiring work with Balijeet Bains, Hideyuki Kobayashi, Mike McAndrew, and Bryan Tipton during the tedious investigations of the semi inclusive 1997 data. Thanks are also due to Antje Brüll, Holger Ihssen, Felix Menden, Naomi Makins, and Michael Ruh for numerous valuable hints on this topic, and especially to Marc–André Funk for his analysis code and to Erik Volk for his patient advice and help with software problems of all kinds. I am grateful to Yvo Gärber, Andreas Gute, Delia Hasch, and Uta Stösslein, who let me benefit frequently from their detailled work on the inclusive analysis.

I very much appreciated the warm and friendly atmosphere in the entire Freiburg group, be it at DESY or in Freiburg. I would like to express my special thanks to Heiko Lacker, Paolo Sereni, Martin Kestel, Andreas Grünemaier, Thomas Schmidt, Marc Niebuhr, and Lars Hennig for the always nice welcome, for hosting me sometimes, and for numerous unforgettable "events" during my stays in Freiburg. In particular I would like to thank my office mates Stephan Brauksiepe and Felix Menden for many inspiring discussions on physics as well as on unrelated topics. The latter sometimes blossomed in legendary photo sessions with the most incredible results ...

I am also indebted to Jürgen Franz, who was always a reliable attorney for the "Hamburg guys", not only in finding agreeable solutions for the organisation of the famous *Ferienpraktikum*. Thanks are also due to Sabine Krohn, Ramona Matthes, Edith Jordan, Angela Göller, and Gisela Mössner for their efficient and flexible help with many organisational issues.

The inspiring working atmosphere in the good spirited HERMES group has always been a great motivation. Too many people to mention contributed to this atmosphere with their very personal styles. Yet, events like the unforgotten "Bastille Day" party, barbecues at the Elbe beach, or the Offsite Meetings provided a necessary compensation for the sometimes long and hard working days in the *Blasenkammer*. I am very grateful that I met so many interesting people from different nations at these occasions.

Furthermore, I am indebted to Felix Menden and in particular to Armand Simon for their very careful reading of the manuscript and numerous suggestions and amendments to the text.

Desweiteren geht ein Dankeschön an Familie Ruttmann mit Skipper für die sehr nette Aufnahme in Hamburg, und insbesondere an Tina und Jan Ruttmann, Karin und Michi v. Appen, Birgit und Marc Gemkow, Peechen und Jörn Wille und Christine und Moritz v. Appen für viele sehr nette Erlebnisse, die einem Nichthamburger oft nicht zugänglich sind.

Dagmar, ich danke Dir für den grossen Rückhalt, den Du mir über Jahre hinweg geben konntest und dafür, dass ich trotz meiner ständigen Reisen in die entfernten Ecken Deutschlands meinen Lebensmittelpunkt lange in Erlangens Umgebung gefunden hatte.

Für Dein geduldiges und sehr liebevolles Verständnis in der sehr anstrengenden Schlussphase dieser Arbeit möchte ich Dir ganz herzlich danken, Uli.

Schliesslich möchte ich besonders meinen Eltern für die fortwährende Unterstützung und das viele Verständnis danken, auch wenn ich bei meinen oftmals kurzen "Gastaufenthalten" nur schnell die schmutzige Wäsche ablud oder keine befriedigende Antworten geben konnte, ob denn soviel Aufwand nötig wäre . . .

Bibliography

[Abe 97a] K. Abe *et al.*, The E154 Collaboration, *Precision Determination of the Neutron Spin Structure Function g_1^n*, Phys. Rev. Lett. **79** (1997) 26.

[Abe 97b] K. Abe *et al.*, The E154 Collaboration, *Measurement of the neutron spin structure function g_2^n and asymmetry A_2^n*, Phys. Lett. **B 404** (1997) 377.

[Abe 97c] K. Abe *et al.*, The E154 Collaboration, *Next–to–leading order QCD analysis of polarized deep inelastic scattering data*, Phys. Lett. **B 405** (1997) 180.

[Abe 98] K. Abe *et al.*, The E143 Collaboration, *Measurements of the proton and deuteron spin structure functions g_1 and g_2*, Phys. Rev. **D 58** (1998) 112003.

[Abe 99] K. Abe *et al.*, The E143 Collaboration, *Measurements of $R = \sigma_L/\sigma_T$ for 0.03 $< x <$ 0.1 and fit to world data*, Phys. Lett. **B 452** (1999) 194.

[Ack 97] K. Ackerstaff *et al.*, The HERMES Collaboration, *Measurement of the Neutron Spin Structure Function g_1^n with a Polarised ^{3}He Internal Target*, DESY 97–085, Phys. Lett. **B 404** (1997) 383.

[Ack 98a] K. Ackerstaff *et al.*, The HERMES Collaboration, *The HERMES Spectrometer*, DESY 98–057, Nucl. Instr. Meth. **A 417** (1998) 230.

[Ack 98b] K. Ackerstaff *et al.*, The HERMES Collaboration, *Flavor Asymmetry of the Light Quark Sea from Semi–inclusive Deep–Inelastic Scattering*, DESY 98–078, Phys. Rev. Lett. **81** (1998) 5519.

[Ack 99a] K. Ackerstaff *et al.*, The HERMES Collaboration, *Beam–Induced Nuclear Depolarisation in a Gaseous Polarised–Hydrogen Target*, DESY 98–058, Phys. Rev. Lett. **82** (1999) 1164.

[Ack 99b] K. Ackerstaff *et al.*, The HERMES Collaboration, *Observation of a Coherence Length Effect in Exclusive ρ^0 Electroproduction*, DESY 98–178, Phys. Rev. Lett. **82** (1999) 3025.

[Ack 99c] K. Ackerstaff *et al.*, The HERMES Collaboration, *Flavor decomposition of the polarized quark distributions in the nucleon from inclusive and semi–inclusive deep–inelastic scattering*, DESY 99–048, Phys. Lett. **B 464** (1999) 123.

[Ack 00] K. Ackerstaff *et al.*, The HERMES Collaboration, *Nuclear effects on $R = \sigma_L/\sigma_T$ in deep–inelastic scattering*, DESY 99–150, Phys. Lett. **B 475** (2000) 386.

[Ada 94] D. Adams *et al.*, The Spin Muon Collaboration, *Spin asymmetry in muon–proton deep inelastic scattering on a transversely–polarized target*, Phys. Lett. **B 336** (1994) 125.

[Ada 95] D. Adams *et al.*, The Spin Muon Collaboration, *A new measurement of the spin–dependent structure function $g_1(x)$ of the deuteron*, Phys. Lett. **B 357** (1995) 248.

[Ada 96] M.R. Adams *et al.*, The E665 Collaboration, *Proton and deuteron structure functions in muon scattering at 470 GeV*, Phys. Rev. **D 54** (1996) 3006.

[Ada 97] D. Adams *et al.*, The Spin Muon Collaboration, *Spin structure of the proton from polarized inclusive deep–inelastic muon–proton scattering*, Phys. Rev. **D 56** (1997) 5330.

[Ade 98a] B. Adeva *et al.*, The Spin Muon Collaboration, *Polarised quark distributions in the nucleon from semi–inclusive spin asymmetries*, Phys. Lett. **B 420** (1998) 180.

[Ade 98b] B. Adeva *et al.*, The Spin Muon Collaboration, *Spin asymmetries A_1 and structure functions g_1 of the proton and the deuteron from polarized high energy muon scattering*, Phys. Rev. **D 58** (1998) 112001.

[Ade 98c] B. Adeva *et al.*, The Spin Muon Collaboration, *Next–to–leading order QCD analysis of the spin structure function g_1*, Phys. Rev. **D 58** (1998) 112002.

[Adl 69a] S.L. Adler, *Axial–Vector Vertex in Spinor Electrodynamics*, Phys. Rev. **177** (1969) 2426.

[Adl 69b] S.L. Adler, W.A. Bardeen, *Absence of Higher–Order Corrections in the Anomalous Axial–Vector Divergence Equation*, Phys. Rev. **182** (1969) 1517.

[Adl 97] C. Adloff *et al.*, The H1 Collaboration, *Measurement of event shape variables in deep inelastic e p scattering*, Phys. Lett. **B 406** (1997) 256.

[Aid 96] S. Aid *et al.*, The H1 Collaboration, *A measurement and QCD analysis of the proton structure function $F_2(x,Q^2)$ at HERA*, Nucl. Phys. **B 470** (1996) 3; C. Adloff *et al.*, The H1 Collaboration, *A measurement of the proton structure function $F_2(x,Q^2)$ at low x and low Q^2 at HERA*, Nucl. Phys. **B 497** (1997) 3.

[Air 98] A. Airapetian *et al.*, The HERMES Collaboration, *Measurement of the proton spin structure function g_1^p with a pure hydrogen target*, DESY 98–072, Phys. Lett. **B 442** (1998) 484.

[Air 00] A. Airapetian *et al.*, The HERMES Collaboration, *Evidence for a Single–Spin Azimuthal Asymmetry in Semi–Inclusive Pion Electroproduction*, DESY 99–149, Phys. Rev. Lett. **84** (2000) 4047.

[Ako 97] N. Akopov *et al.*, The HERMES g_1^n Group, *Determination of the 1995 Data Quality and the Extraction of the Spin Structure Function of the Neutron*, HERMES Internal Report 97–007 (1997).

[Aku 94] I. Akushevich, N. Shumeiko, *Radiative effects in deep inelastic scattering of polarized leptons by polarized light nuclei*, J. Phys. **G 20** (1994) 513.

[Aku 97] I. Akushevich *et al.*, *POLRAD 2.0. FORTRAN code for the radiative corrections calculation to deep inelastic scattering of polarized particles*, Comp. Phys. Comm. **104** (1997) 201.

[Aku 99] I. Akushevich, Private Communication, (1999).

[Alt 77] G. Altarelli, G. Parisi, *Asymptotic Freedom in Parton Language*, Nucl. Phys. **B 126** (1977) 298.

[Alt 82] G. Altarelli, *Partons in Quantum Chromodynamics*, Phys. Rep. **81** (1982) 1.

[Alt 97] G. Altarelli *et al.*, *Determination of the Bjorken sum and strong coupling from polarized structure functions*, Nucl. Phys. **B 496** (1997) 337.

[And 83] B. Anderson *et al.*, *Parton Fragmentation and String Dynamics*, Phys. Rep. **97** (1983) 31.

[Ans 95] M. Anselmino, A. Efremov, E. Leader, *The theory and phenomenology of polarized deep inelastic scattering*, Phys. Rep. **261** (1995) 1; Erratum *ibid.* **281** (1997) 399.

[Ant 96] P.L. Anthony *et al.*, The E142 Collaboration, *Deep inelastic scattering of polarized electrons by polarized ^{3}He and the study of the neutron spin structure*, Phys. Rev. **D 54** (1996) 6620.

[Ant 99a] P.L. Anthony *et al.*, The E155 Collaboration, *Measurement of the proton and deuteron spin structure functions g_2 and asymmetry A_2*, Phys. Lett. **B 458** (1999) 529.

[Ant 99b] P.L. Anthony *et al.*, The E155 Collaboration, *Measurement of the deuteron spin structure function $g_1^d(x)$ for $1\,(GeV/c)^2 < Q^2 < 40\,(GeV/c)^2$*, Phys. Lett. **B 463** (1999) 339.

[Arn 84] M. Arneodo *et al.*, The European Muon Collaboration, *Quark and Diquark Fragmentation into Neutral Strange Particles as Observed in Muon–Proton Interactions at 280 GeV*, Phys. Lett. **B 145** (1984) 156.

[Arn 86] M. Arneodo *et al.*, The European Muon Collaboration, *Investigation of the W and Q^2 Dependence of Charged Pion Distributions in $\mu\, p$ Scattering*, Z. Phys. **C 31** (1986) 1.

[Arn 95] M. Arneodo *et al.*, The New Muon Collaboration, *Measurement of the proton and the deuteron structure functions, F_2^p and F_2^d*, Phys. Lett. **B 364** (1995) 107.

[Asc 99] E. Aschenauer, K. Negodaeva, Private Communication, (1999).

[Ash 88] J. Ashman *et al.*, The European Muon Collaboration, *A measurement of the spin asymmetry and determination of the structure function g_1 in deep inelastic muon–proton scattering*, Phys. Lett. **B 206** (1988) 364.

[Att 93] C.C. degli Atti *et al.*, *Nuclear effects in deep inelastic scattering of polarized electrons off polarized ^{3}He and the neutron spin structure functions*, Phys. Rev. **C 48** (1993) R968.

[Ava 98] H. Avakian *et al.*, *Performance of the electromagnetic calorimeter of the HERMES experiment*, Nucl. Instr. Meth. **A 417** (1998) 69; H. Avakian *et al.*, *Performance of F101 radiation resistant lead glass shower counters*, Nucl. Instr. Meth. **A 378** (1996) 155.

[Bai 99] B. Bains, M. Beckmann, H. Ihssen, H. Kobayashi, M. McAndrew, M. Ruh, H. Tallini, *Determination of the charged hadron asymmetries from the 1997 data*, HERMES Internal Report 99–015 (1999).

[Bar 78] W.A. Bardeen *et al.*, *Deep–inelastic scattering beyond the leading order in asymptotically free gauge theories*, Phys. Rev. **D 18** (1978) 3998.

[Bar 93] D.P. Barber *et al.*, *The HERA polarimeter and the first observation of electron spin polarization at HERA*, Nucl. Instr. Meth. **A 329** (1993) 79.

[Bar 94] D.P. Barber *et al.*, *High spin polarization at the HERA electron storage ring*, Nucl. Instr. Meth. **A 338** (1994) 166.

[Bar 97] D.P. Barber, Private Communication, (1997).

[Bau 83] G. Baum *et al.*, The E130 Collaboration, *New Measurement of Deep–Inelastic e–p Asymmetries*, Phys. Rev. Lett. **51** (1983) 1135.

[Bau 98] Ch. Baumgarten, Private Communication, (1998).

[Bec 97a] M. Beckmann, *Test of the new 37–layer CVI mirrors for the Longitudinal Polarimeter*, HERMES Internal Report 97–006 (1997).

[Bec 97b] M. Beckmann, *Summary of Systematic Studies performed between June 3 and July 8, 1997 on the Longitudinal Polarimeter*,
HERMES Internal Polarimeter Report IPR–97–08 (1997),
http://www-hermes.desy.de/polarimeter/reports/ipr-97-08.ps.gz;
S. Brauksiepe, M. Ruh, *Summary of systematic studies at the Long. Polarimeter in June and July 1997*,
HERMES Internal Polarimeter Report IPR–97–09 (1997),
http://www-hermes.desy.de/polarimeter/reports/ipr-97-09.ps.gz

[Bel 69] J.S. Bell, R. Jackiw, *A PCAC Puzzle: $\pi^0 \to \gamma\gamma$ in the σ–Model*, Nuovo Cimento **60 A** (1969) 47.

[Ben 89] A.C. Benvenuti *et al.*, The BCDMS Collaboration, *A High Statistics Measurement of the Proton Structure Functions $F_2(x, Q^2)$ and R from Deep Inelastic Muon Scattering at High Q^2*, Phys. Lett. **B 223** (1989) 485.

[Ben 98] T. Benisch, *Polarisierte Bhabha–Streuung und Luminositätsmessung im HERMES–Experiment*, Dissertation, Friedrich–Alexander–Universität Erlangen–Nürnberg (1998).

[Ber 98] S. Bernreuther *et al.*, *The HERMES back drift chambers*, Nucl. Instr. Meth. **A 416** (1998) 45;
S. Bernreuther *et al.*, *Design and performance of the large HERMES drift chambers*, Nucl. Instr. Meth. **A 367** (1995) 96.

[Bin 95] J. Binnewies, B.A. Kniehl, G. Kramer, *Next–to–leading order fragmentation functions for pions and kaons*, Z. Phys. **C 65** (1995) 471.

[Bjø 66] J.D. Bjørken, *Applications of the Chiral $U(6) \otimes U(6)$ Algebra of Current Densities*, Phys. Rev. **148** (1966) 1467.

[Bjø 69a] J.D. Bjørken, *Asymptotic Sum Rules at Infinite Momentum*, Phys. Rev. **179** (1969) 1547.

[Bjø 69b] J.D. Bjørken, E.A. Paschos, *Inelastic Electron–Proton and γ–Proton Scattering and the Structure of the Nucleon*, Phys. Rev. **185** (1969) 1975.

[Blo 99] J. Blouw *et al.*, *Design and performance of a large microstrip gas tracker for HERMES*, Nucl. Instr. Meth. **A 434** (1999) 227.

[Böt 99] H. Böttcher, Y. Gärber, U. Stösslein, *Results on the Top/Bottom Detector Alignment for the 1997 Data*, HERMES Internal Report 99–053 (1999).

[Bra 96a] S. Brauksiepe, *COP: A Graphical Interface to Control and Monitor the Longitudinal Polarimeter at HERA*, Contribution to the 12th International Symposium on High Energy Spin Physics, Amsterdam, Sept. 1996 (World Scientific, eds. C.W. de Jager *et al.*), 771.

[Bra 96b] B. Braun, *Polarization of the HERMES Hydrogen Target*, Contribution to the 12th International Symposium on High Energy Spin Physics, Amsterdam, Sept. 1996 (World Scientific, eds. C.W. de Jager *et al.*), 241;
B. Braun, *The HERMES Polarimeter*, Contribution to the 7th International Workshop on Polarized Gas Targets and Polarized Beams, Urbana–Champaign, Aug. 1997, (AIP, eds. R.J. Holt, M.A. Miller), 156.

[Bre 99] J. Breitweg *et al.*, The ZEUS Collaboration, *Measurement of mulitplicity and momentum spectra in the current and target regions of the Breit frame in Deep Inelastic Scattering at HERA*, Eur. Phys. J. **C 11** (1999) 251.

[Bur 96] F. Burkart, *Messung der Stokes–Parameter am Laserstrahl des HERA–Polarimeters*, Wissenschaftliche Arbeit, Albert–Ludwigs–Universität Freiburg i. Brsg. (1996).

[Cal 69] C.G. Callan, D.J. Gross, *High–Energy Electroproduction and the Constitution of the Electric Current*, Phys. Rev. Lett. **22** (1969) 156.

[Cas 98] C. Caso *et al.*, The Particle Data Group, *Review of Particle Physics*, Eur. Phys. Jour. **C 3** (1998) 1.

[CER 93] CERN Programming Techniques Group, *ADAMO — Entity–Relationship Programming System, Users Guide, Version 3.3*, CERN, Geneva (1993);
S.M. Fisher, P. Palazzi, *The ADAMO Data System, Programmers Manual*, CERN, Geneva (1993).

[CER 94] CERN CN Application Software Group, *GEANT — Detector Description and Simulation Tool*, CERN, Geneva (1994).

[Cis 97] E. Cisbani *et al.*, *Proposal for a Dual Radiator RICH for HERMES*, HERMES Report 97–003 (1997),
http://www-hermes.desy.de/notes/pub/97-LIB/jackson.97.003.ps.gz;
E. Cisbani, *The Dual Radiator RICH for the HERMES Experiment at DESY*, Contribution to the 6th International Conference on Adv. Technology and Particle Physics, Como, Italy, Oct. 1998.

[Coh 95] Coherent Laser Group, *Infinity 40–100 Nd:YAG Laser Operator's Manual*, Coherent Inc., Santa Clara (CA) (1995).

[Col 63] F.D. Colegrove, L.D. Schearer, G.K. Walters, *Polarization of ^{3}He Gas by Optical Pumping*, Phys. Rev. **132** (1963) 2561.

[COM 96] The COMPASS Collaboration, *Proposal for a Common Muon and Proton Apparatus for Structure and Spectroscopy*, CERN/SPSLC 96–14, SPSC/P 297 (1996).

[Der 73] Ya.S. Derbenev, A.M. Kondratenko, *Polarization kinetics of particles in storage rings*, Sov. Phys. JETP **37** (1973) 968.

[Der 96] M. Derrick *et al.*, The ZEUS Collaboration, *Measurement of the F_2 structure function in deep inelastic e^+p scattering using 1994 data from the ZEUS detector at HERA*, Z. Phys. **C 72** (1996) 399;
J. Breitweg *et al.*, The ZEUS Collaboration, *Measurement of the proton structure function F_2 and $\sigma_{\mathrm{tot}}^{\gamma^* p}$ at low Q^2 and very low x at HERA*, Phys. Lett. **B 407** (1997) 432.

[DeS 98] D. DeSchepper *et al.*, *The HERMES polarized ^{3}He internal gas target*, Nucl. Instr. Meth. **A 419** (1998) 16.

[Dok 77] Y.L. Dokshitser, *Calculation of structure functions of deep–inelastic scattering and e^+e^- annihilation by perturbation theory in quantum chromodynamics*, Sov. Phys. JETP **46** (1977) 641.

[Dol 93] B. Dolgoshein, *Transition radiation detectors*, Nucl. Instr. Meth. **A 326** (1993) 434.

[Dre 99] B. Dressler *et al.*, *Flavor asymmetry of polarized antiquark distributions and semi–inclusive DIS*, RUB–TPII–12/99, hep–ph/9909541.

[Dür 95] M. Düren, *The HERMES Experiment: From the Design to the First Results*, Habilitation Thesis, DESY HERMES–95–02, Friedrich–Alexander–Universität Erlangen–Nürnberg (1995).

[Ell 74] J. Ellis, R. Jaffe, *Sum rule for deep–inelastic electroproduction from polarized protons*, Phys. Rev. **D 9** (1974) 1444; Erratum *ibid.* **D 10** (1974) 1669.

[Ell 96] J. Ellis, M. Karliner, *The strange spin of the nucleon*, Phys. Lett. **B 341** (1995) 397.

[Fer 97] M. Ferstl, *Polarisierte tiefinelastische Streuung an einem ^{3}He –Target im HERMES–Experiment*, Dissertation, Friedrich–Alexander–Universität Erlangen–Nürnberg (1997).

[Fey 69] R.P. Feynman, *Very High–Energy Collisions of Hadrons*, Phys. Rev. Lett. **23** (1969) 1415.

[Fie 78] R.D. Field, R.P. Feynman, *A Parametrization of the Properties of Quark Jets*, Nucl. Phys. **B 136** (1978) 1.

[Flo 98] D. de Florian, O.A. Sampayo, R. Sassot, *Next–to–leading order analysis of inclusive and semi–inclusive polarized data*, Phys. Rev. **D 57** (1998) 5803.

[Fri 72] J.I. Friedman, H.W. Kendall, *Deep Inelastic Electron Scattering*, Ann. Rev. Nucl. Part. Sci. **22** (1972) 203.

[Fri 90] J.L. Friar *et al.*, *Neutron polarization in polarized ^{3}He targets*, Phys. Rev. **C 42** (1990) 2310.

[Fun 98] M.A. Funk, *A Measurement of the Polarised Parton Densities of the Nucleon in Deep–Inelastic Scattering at HERMES*, Dissertation, Universität Hamburg (1998).

[Gär 00] Y. Gärber, *Messung des Strukturfunktionsverhältnisses g_1^p/F_1^p bei kleinen Q^2 und Bjorken–x mit dem Hermes–Experiment*, Dissertation, Humboldt–Universität Berlin (2000).

[Geh 95] T. Gehrmann, W.J. Stirling, *Spin–dependent parton distributions from polarized structure function data*, Z. Phys. **C 65** (1995) 461.

[Geh 96a] T. Gehrmann, W.J. Stirling, *Polarized parton distributions in the nucleon*, Phys. Rev. **D 53** (1996) 6100.

[Geh 96b] T. Gehrmann, W.J. Stirling, *Analytic approaches to the evolution of polarised parton distributions at small x*, Phys. Lett. **B 365** (1996) 347.

[Gei 98] Ph. Geiger, *Measurement of Fragmentation Functions at HERMES*, Dissertation, Ruprecht–Karls–Universität Heidelberg (1998).

[Gel 64] M. Gell–Mann, *A Schematic Model of Baryons and Mesons*, Phys. Lett. **8** (1964) 214.

[Glü 95] M. Glück, E. Reya, A. Vogt, *Dynamical parton distributions of the proton and small–x physics*, Z. Phys. **C 67** (1995) 433.

[Glü 96] M. Glück, E. Reya, M. Stratmann, W. Vogelsang, *Next–to–leading–order radiative parton model analysis of polarized deep inelastic lepton–nucleon scattering*, Phys. Rev. **D 53** (1996) 4775.

[Göc 96] M. Göckeler *et al.*, *Polarized and unpolarized nucleon structure functions from lattice QCD*, Phys. Rev. **D 53** (1996) 2317.

[Göc 97] M. Göckeler *et al.*, *A lattice determination of the second moment of the polarised valence quark distribution*, Phys. Lett. **B 414** (1997) 340.

[Gol 96] A. Golendoukhin, *The HERMES Polarised Proton Target at HERA*, Contribution to the 12th Int. Symposium on High Energy Spin Physics, Amsterdam, Sept. 1996 (World Scientific, eds. C.W. de Jager *et al.*), 331; J. Stewart, *The HERMES Polarized Hydrogen Internal Gas Target*, Contribution to the 7th Int. Workshop on Polarized Gas Targets and Polarized Beams, Urbana–Champaign, Aug. 1997, (AIP, eds. R.J. Holt, M.A. Miller), 69.

[Gri 72] V.N. Gribov, L.N. Lipatov, *Deep inelastic ep scattering in perturbation theory*, Sov. J. Nucl. Phys. **15** (1972) 438.

[Gri 87] D.J. Griffiths, *Introduction to Elementary Particles*, John Wiley, New York (1987).

[Gue 90] R.D. Guenther, *Modern Optics*, John Wiley, New York (1990).

[Gut 99a] A. Gute, *Messung der polarisierten Strukturfunktion g_1^p des Protons im HERMES–Experiment*, Dissertation, Friedrich–Alexander–Universität Erlangen–Nürnberg (1999).

[Gut 99b] A. Gute, Private Communication, (1999).

[Has 99] D. Hasch, *Messung der polarisierten Strukturfunktion $g_1(x, Q^2)$ des Protons mit dem HERMES–Experiment*, Dissertation, Humboldt–Universität Berlin (1999).

[Haw 98] E.A. Hawker *et al.*, The E866 Collaboration, *Measurement of the Light Antiquark Flavor Asymmetry in the Nucleon Sea*, Phys. Rev. Lett. **80** (1998) 3715.

[HER 93] The HERMES Collaboration, *HERMES Technical Design Report*, DESY–PRC 93/06, MPIH–V20–1993 (1993).

[Hen 99] M. Henoch, *Interpretation der Polarisationsmessungen am polarisierten Wasserstofftarget des HERMES–Experiments am DESY in Hamburg*, Diploma Thesis, Universität Münster (1999).

[Hen 00] M. Henoch, *The sampling correction on α_r for 1997*, HERMES Internal Report 00–004 (2000).

[HMC 96] The HERMES Collaboration, *The HERMES Monte Carlo*, http://www-hermes.desy.de/hmc/ (1996).

[Hol 00] B. Holzer, DESY –M– Group, Private Communication, (2000).

[Hug 99] E.W. Hughes, *Polarized Deep Inelastic Lepton–Nucleon Scattering: Inclusive Results*, Proceedings of the 7$^{\text{th}}$ Int. Workshop on Deep Inelastic Scattering and QCD, Zeuthen 19–23 April 1999, Nucl. Phys. **B** (Proc. Suppl.) **79** (1999) 511.

[Ihs 96] H. Ihssen, Private Communication, (1996).

[Ihs 98] H. Ihssen, Private Communication, (1998).

[Ing 97] G. Ingelman, A. Edin, J. Rathsman, *LEPTO 6.5 — A Monte Carlo generator for deep inelastic lepton–nucleon scattering*, http://www3.tsl.uu.se/thep/lepto/, Comp. Phys. Comm. **101** (1997) 108.

[Jac 83] J.D. Jackson, *Klassische Elektrodynamik*, 2$^{\text{nd}}$ Edn., Walter de Gruyter, Berlin (1983), pp. 661 ff.

[Jaf 97] R.L. Jaffe, *Spin, Twist and Hadron Structure in Deep Inelastic Processes*, in *Lectures on QCD, Applications* (Lecture Notes in Physics, eds. F. Lenz, H. Grießhammer, D. Stoll), Springer, Berlin (1997).

[Jon 91] C.T. Jones *et al.*, The WA21 Collaboration, *Inclusive ρ^0(770) meson production in νp and $\overline{\nu}p$ charged current interactions*, Z. Phys. **C 51** (1991) 11.

[Kai 97a] R. Kaiser, *Particle Identification at HERMES*, HERMES Internal Report 97–025 (1997).

[Kai 97b] R. Kaiser, F. Menden, M. Vetterli, *Probability Analysis of the TRD Response and the Contribution of Flux Ratios to HERMES Particle Identification*, HERMES Internal Report 97–036 (1997).

[Kod 79] J. Kodaira *et al.*, *QCD higher order effects in spin–dependent deep inelastic electroproduction*, Nucl. Phys. **B 159** (1979) 99;
J. Kodaira *et al.*, *Quantum–chromodynamic effects in polarised electroproduction*, Phys. Rev. **D 20** (1979) 627.

[Kol 98] H. Kolster, *The HERMES Gaseous Internal Polarized Proton Target and its use in the HERA Positron Storage Ring*, Dissertation, Ludwig–Maximilians–Universität München (1998).

[Kol 00] H. Kolster, Private Communication, (2000).

[Lac 98] W. Lachnit, *Die hinteren HERMES–Driftkammern und ihr Einfluß auf systematische Fehler von Asymmetriemessungen*, Dissertation, Friedrich–Alexander–Universität Erlangen–Nürnberg (1998).

[Lai 97] H.L. Lai *et al.*, The CTEQ Collaboration, *Improved parton distributions from global analysis of recent deep inelastic scattering and inclusive jet data*, Phys. Rev. **D 55** (1997) 1280.

[Lam 95] B. Lampe, *Trends in polarized lepton nucleon scattering*, Fortsch. Phys. **43** (1995) 673.

[Lar 94] S.A. Larin, *The next–to–leading QCD approximation to the Ellis–Jaffe sum rule*, Phys. Lett. **B 334** (1994) 192.

[Lip 75] L.N. Lipatov, *The parton model and perturbation theory*, Sov. J. Nucl. Phys. **20** (1975) 94.

[Man 92] L. Mankiewicz *et al.*, *PEPSI — a Monte Carlo generator for polarized leptoproduction*, Comp. Phys. Comm. **71** (1992) 305.

[Men 99] F. Menden, Private Communication, (1999).

[Mer 96] R. Mertig, W.L. van Neerven, *The calculation of the two–loop spin splitting functions $P_{ij}^{(1)}(\alpha)$*, Z. Phys. **C 70** (1996) 637.

[Mue 48] H. Mueller, J. Opt. Soc. Am. **38** (1948) 661.

[Nic 98] J.M. Niczyporuk, E.E.W. Bruins, *Quark flavor tagging in polarized hadronic processes*, Phys. Rev. **D 58** (1998) 091501.

[Pen 98] J.C. Peng *et al.*, The E866 Collaboration, *$\overline{d}/\overline{u}$ asymmetry and the origin of the nucleon sea*, Phys. Rev. **D 58** (1998) 092004.

[Pla 00] *Densimet* is a registered trademark of PLANSEE GmbH, D–86983 Lechbruck.

[Pre 92] W.H. Press *et al.*, *Numerical Recipes in C: The Art of Scientific Computing*, 2^{nd} Edn., Cambridge University Press, Cambridge (1992).

[Pre 97] J. Pretz, *Messung der polarisierten Quarkverteilungen in semi–inklusiver Myon–Nukleon–Streuung*, Dissertation, Johannes–Gutenberg Universität Mainz (1997).

[Rit 97] K. Rith, *Quark–Gluon Structure of the Nucleon*, in *Lectures on QCD, Applications* (Lecture Notes in Physics, eds. F. Lenz, H. Grießhammer, D. Stoll), Springer, Berlin (1997).

[Roo 82] M. Roos *et al.*, The Particle Data Group, *Review of Particle Properties*, Phys. Lett. **111 B** (1982) 1.

[Ruh 99] M. Ruh, *Measurement of the Polarised Quark Distributions of the Nucleon at HERMES*, Dissertation, Albert–Ludwigs–Universität Freiburg i. Brsg. (1999).

[Sjö 94] T. Sjöstrand, *High–energy–physics event generation with PYTHIA 5.7 and JETSET 7.4*, Comp. Phys. Comm. **82** (1994) 74.

[Sok 64] A.A. Sokolov, I.M. Ternov, *On Polarization and Spin Effects in the Theory of Synchrotron Radiation*, Sov. Phys. Dokl. **8** (1964) 1203.

[Tal 98] H. Tallini, *A measurement of the quark spin distributions of the nucleon at HERMES*, PhD Thesis, University of Liverpool (1998).

[Tip 98] B. Tipton, F. Dashevsky, *Investigations of Strange Sea Polarization in the HERMES 96–97 Data*, HERMES Internal Report 98–073 (1998).

[Tip 99] B. Tipton, *Measurement of Polarized Parton Distributions With Spin–dependent Deep–inelastic Scattering*, PhD Thesis, Massachusetts Institute of Technologie, Boston (1999).

[Vog 96] W. Vogelsang, *Rederivation of the spin–dependent next–to–leading order splitting functions*, Phys. Rev. **D 54** (1996) 2023.

[Wan 77] S. Wandzura, F. Wilczek, *Sum Rules for Spin–Dependent Electroproduction — Test of Relativistic Constituent Quarks*, Phys. Lett. **B 72** (1977) 195.

[Wan 95] W. Wander, *DAD — Distributed ADAMO Database System at HERMES*, Proc. of CHEP '95, Rio de Janeiro, Sept. 1995.

[Wan 96] W. Wander, *Rekonstruktion hochenergetischer Streuereignisse im HERMES Experiment*, Dissertation, Friedrich–Alexander–Universität Erlangen–Nürnberg (1996).

[Whi 92] L.W. Whitlow *et al.*, *Precise measurements of the proton and deuteron structure functions from a global analysis of the SLAC deep inelastic electron scattering cross sections*, Phys. Lett. **B 282** (1992) 475.

[Zij 94] E.B. Zijlstra, W.L. van Neerven, *Order–α_s^2 corrections to the polarized structure function $g_1(x, Q^2)$*, Nucl. Phys. **B 417** (1994) 61.